AN ISOTHERMAL STUDY OF GAS TURBINE COMBUSTOR FLOWS

P. KOUTMOS
DIPL. ING.

Thesis submitted for the degree of
Doctor of Philosophy
in the University of London
and for the
Diploma of Membership of the Imperial College

Imperial College of Science and Technology
(Department of Mechanical Engineering)

July, 1985

To my parents

ABSTRACT

Research work is described which comprises a theoretical and an experimental investigation of a flow configuration relevant to aero-engine gas turbine combustion systems.

In the experimental study, LDA measurements are obtained of the three mean velocity components and the corresponding turbulence intensities in a water model of a can-type combustor made up of a swirl-driven primary zone, annulus fed rows of primary and dilution jets and an exit contraction nozzle. The effect of the variation of the flow split between swirler, primary and dilution holes and the influence of the swirler geometry on the flow pattern are investigated. At low swirler flow rates, a toroidal recirculation is formed in the primary zone and high levels of turbulence energy are generated due to primary jet impingement. As the swirler flow rate increases, the stength of the vortex weakens and the recirculation region shifts off centre allowing a forward velocity to be established on the combustor axis. These changes have a smaller effect on the combustor exit profiles due to strong mixing in the dilution zone.

The theoretical study is based upon the numerical solution of the time-averaged transport equations for momentum, turbulence kinetic energy and energy dissipation rate using a finite-difference formulation. The computational investigations include the calculation of isothermal flow fields external as well as internal to the combustion chamber. In the former case, the flow in annular combustor dump diffuser geometries is calculated. The comparison between predicted results and measurements available from a separate study shows that the variation in the overall pressure recovery and loss coefficient with changes in diffuser design features (eg inner/outer annulus flow split or dump gap) can be predicted to within 7% of the inlet dynamic head.

For the case of internal combustor flow fields, the measurements obtained inside the current water model are calculated. The combustor geometry is split into two zones and the computation of the flow in the exit contraction nozzle is made possible by using a general method for treating complex geometries with finite-difference methods based on simple (cartesian, cylindrical-polar) co-ordinate systems. The predicted mean velocity distributions show favourable agreement with the measurements in the primary and intermediate zones, although the discrepancies increase in the dilution region. Predicted levels of turbulence kinetic energy are too low in regions of high anisotropy. A parametric study for the range of flow patterns observed in the experiments illustrates the usefulness and acceptable quantitative accuracy of this type of numerical approach for practical combustion chamber design at least under isothermal conditions. Finally, it is demonstrated that such methods can be applied conveniently and economically to the complex geometries found in practice.

ACKNOWLEDGEMENTS

I have been fortunate in having received the assistance and encouragement of a number of people for the preparation of this thesis and it gives me pleasure to acknowledge this.

I am deeply indebted to my supervisor, Dr. J. J. McGuirk, who provided me with sound advice, valuable criticism and maintained a constant interest in my work.

I am obliged to Professor J. H. Whitelaw for introducing me to the research team at Imperial College and for many helpful discussions throughout my work. I would also like to thank Professor D. Papailiou, of the University of Patras, Greece, for initiating my interest in research in this field.

The work has also benefited by being part of a larger overall research collaboration between Imperial College and industry. I would like to thank particularly: Dr. W. P. Jones of the Department of Chemical Engineering and Chemical Technology at Imperial College, Mr. A. Sotheran of Rolls-Royce Ltd, Bristol and Mr. D. C. Dryburgh of Rolls-Royce Ltd, Derby for many interesting and informative discussions; Dr. C. H. Priddin of Rolls-Royce Ltd, Derby for his assistance with the calculations of the nozzle; Mr. D. M. Snape of Rolls-Royce Ltd, Derby for useful discussions on the Spey combustor; finally, Mr. J. B. Jamieson, Mr. R. Cottington and Dr. C. Coats of the National Gas Turbine Establishment for continued interest and support.

I have also benefited from my association with all my colleagues, particularly Dr. A. M. K. P. Taylor, Dr. C. Arcoumanis, Mr. C. Vafidis, Dr. B. E. Thompson, Mr. D. Adair, Mr. M. V. Heitor, Mr. T. Dakos and Mr. A. J. Marquis.

My thanks go to Messrs. H. Avis, W. Crew, O. Vis, J. Laker for their execution of, and help with, the experimental apparatus. Mr. G. Tindall, Mr. S. Bedley and Miss E. Archer have also been most helpful. I would also like to thank Miss L. Micklem for typing this thesis.

I also welcome the opportunity to acknowledge the financial support provided by the Ministry of Defence.

Finally, I deeply appreciate the love and support of my parents.

TABLE OF CONTENTS

LIST OF TABLES

CHAPTER I

CHAPTER II

CHAPTER III

CHAPTER IV

CHAPTER V

LIST OF FIGURES

CHAPTER I

CHAPTER II

CHAPTER III

CHAPTER IV

CHAPTER V

NOMENCLATURE

Roman characters

A	area of control volume face, equation (3.12)
A	subscripted (N, S, E, W) coefficients of finite-difference equation, equation (3.37)
A	cross-sectional area
AR	area ratio
a	coefficient in finite-difference equation, equations (3.14), (3.15), (3.26), (3.43)
a	aspect ratio, equation (3.33)
b	coefficient in finite-difference equation, equation (3.26)
b, b_o	diameters of laser beam at e^{-2} intensity level, equation (2.7)
b_x, b_y	measuring volume dimensions, equations (2.5), (2.6)
C_μ, C_1, C_2	constants of the k-ϵ turbulence model, equations (3.7), (3.8), (3.9)
C_P	static pressure recovery coefficient, Chapter IV
C	chord length, Figure 2.4a
D_C	internal diameter of water model combustor
D	diameter of containing tube
D_{SW}	diameter of swirler
D_G	dump gap, Chapter IV

E	constant in the law of the wall equations (3.19), (3.21), (3.22)
F	weighting factor used in finite-difference equation, equation (3.12)
FL	flux through hole, equations (3.46), (3.47), (3.48)
f	function of surface, Figure 3.4
f_D	Doppler frequency, equations (2.3), (2.9)
f_S	Doppler shift frequency, equations (2.4), (2.10), (2.11), (2.12)
$\tilde{f}_V$	instantaneous Doppler frequency caused by particle motion, equations (2.10), (2.11)
$f_{1,2,3}$,	focal lengths of lenses used in LDA system, equation (2.7)
G_{esw}	axial flux of azimuthal momentum at swirler exit, equation (2.1)
G_{xsw}	axial flux of axial momentum at swirler exit, equation (2.1)
G_{pr}	radial flux of radial momentum of primary hole fluid, Table 2.1
h	annulus height, Figure 4.2
J	Jacobian, equation (3.29)
k	turbulent kinetic energy
L	prediffuser length, Figure 4.2, Table 4.1
$L_{1,2,3,4}$	lenses used in the LDA system, Figure 2.6

l	local length scale
$l_{1,2,3}$	metric coefficients in ζ_1, ζ_2, ζ_3 direction, equation (2.41)
$\dot{m}$	mass flow rate
N	number of line pairs on radial diffraction grating, equation (2.4), Table 2.2
n	perpendicular distance from wall, equations (3.17), (3.45)
Pe_e	local Peclet number, equation (3.13)
P	pressure
$\tilde{P}_t$	mass-weighted mean total pressure, Chapter IV
$\tilde{P}_s$	mass-weighted mean static pressure, Chapter IV
PD	perpendicular distance from the node to the boundary surface, equation (3.45)
p'	pressure correction
$\dot{q}$	local mass flux, equations (3.12), (3.13)
R_c	radius of combustor, Figure 4.1
R	radial distance between inner and outer casing in dump diffuser geometry, Figure 4.6
Re	Reynolds number
r	cylindrical polar co-ordinate (radial direction)
S	linearised source term

S	mass flow split in dump diffuser geometry $(=\dot{m}_o/\dot{m}_i)$
s	space between vanes of swirler, Figure 2.4a
U	axial velocity
U_b	bulk velocity
U_{max}	maximum velocity in cross-section
U^+	non-dimensional velocity used at the law of the wall
$U_{1,2,3}$	velocity components in ζ_1, ζ_2, ζ_3 directions, equation (3.41)
$\sqrt{\overline{u^2}}$	axial turbulence intensity
$\overline{u_i u_j}$	time-mean of cross-correlation
V	radial velocity
$\widetilde{V}_1$	tracker voltage output, equations (2.10), (2.11), (2.12)
$\widetilde{V}_2$	tracker voltage output, equations (2.10), (2.11), (2.12)
V_o	offset voltage, equations (2.10), (2.11), (2.12)
VBNS	boundary cell velocity component normal to the boundary surface, Chapter III
VBT	boundary cell velocity component lying in the plane of the boundary surface, Chapter III
VPNS	node velocity component normal to the boundary surface, Chapter III
VPPS	node velocity component parallel to the boundary surface, Chapter III

$\sqrt{\overline{v^2}}$	radial turbulence intensity
W	azimuthal velocity
$\sqrt{\overline{w^2}}$	azimuthal turbulence intensity
x	cartesian co-ordinate (streamwise-direction)
x	cylindrical polar co-ordinate (axial direction)
y	cartesian co-ordinate (cross-stream direction)
y	distance from the wall
y^+	variable in law of the wall, equation (3.18)
z	cartesian co-ordinate (spanwise direction)
z	swirler exit height, Figure 2.4a

Greek characters

α	quadratic function, equation (3.31)
α	velocity profile energy coefficient, equation (4.2)
β	quadratic function, equation (3.31)
Γ	diffusion coefficient, equation (3.10), (3.11)
γ	quadratic function, equation (3.31)
$\Delta\widetilde{P}_t$	mass-weighted mean total pressure loss, equation (4.3)
Δx	local mesh spacing in axial direction
δ_{ij}	kronecker's delta

Ω	r.m.s fluctuation of Ω, Table 2.2
ϵ	isotropic rate of dissipation of turbulent kinetic energy
ϵ_w	value of ϵ at the wall
$\zeta_1, \zeta_2, \zeta_3$	general orthogonal curvilinear co-ordinates
η	refractive index of medium, equation (3.13)
θ	half angle of beam intersection, Figure 2.6
θ	swirler vane outlet angle
θ	cylindrical polar co-ordinate (azimuthal direction)
κ	Von Karman's constant, equations (2.19), (2.21), (2.23)
λ	wavelength of laser light, Chapter II
λ	total pressure loss coefficient, Chapter IV
ν_t	turbulent viscosity
ν	kinematic viscosity
ρ	density of fluid
σ_ϕ	effective turbulent Prandtl number for variable ϕ
τ_w	wall shear stress, equations (3.20), (3.21)
ϕ	surrogate variable for U, V, W, pressure correction, k and ϵ
ϕ	velocity potential, equation (3.27)
ϕ	prediffuser wall angle, Figure 4.1

ψ	stream function, equation (3.27)
Ω	angular velocity of rotating grating, equation (2.4)

Operators

P(...)	production of Reynolds stresses, equation (2.14)
$\overline{...}$	time-averaged value
$\widetilde{...}$	*mass weighted mean value,* Chapter IV
Σ	summation

Subscript

B	boundary, boundary cell value
H	value of hole
CH	corrected hole value, equation (3.47)
N, S, E, W, R, L, P	values appropriate to nodes marked in Figure 3.1
N, S, E, W, P	values appropriate to nodes marked in Figure 3.3
n, s, e, w, l, r	values appropriate to control volume faces shown in Figure 3.1
U, V, W, P, k, ϵ, θ	pertaining to each variable or ϕ
last	last
inlet	inlet

sw	pertaining to swirler
pr	pertaining to primary holes
int	pertaining to intermediate zone
d	pertaining to dilution holes
tr	pertaining to wall transpiration cooling
w	pertaining to wall
tot	total
o	outer annulus flow field, Chapter IV
i	inner annulus flow field, Chapter IV
1,2,3,4	stations along dump diffuser, Figure 4.1
1-4	between station 1 and 4
s	pertaining to static pressure, Chapter IV
t	pertaining to total pressure, Chapter IV

<u>Superscripts</u>

B	boundary value
k, k+1	values at the outlet boundary and the preceding grid line, equation (4.8)
ϕ	pertaining to any variable (U, V, W, pressure correction, k and ϵ)
P	internal value at node P

CHAPTER I

INTRODUCTION

1.1 Gas turbine engine combustion chambers - types, nomenclature and design criteria

1.1.1 Preliminary remarks

The gas turbine engine has evolved rapidly in the past twenty-five years and today it plays a dominant role in the industrial world, being a major component in a range of aeronautical, marine and land-based applications. This development has been achieved largely due to advances in the aircraft gas turbine, and non-aeronautical engines have greatly benefited from the technical lead given by aero-engines. In recent years, the demand for improved performance, conservation of fossil fuels and an increased concern for the growing atmospheric pollution have drawn particular attention to the operation of the combustion chamber, the gas turbine engine component primarily related to the above aspects of operation. The combustor is an essential part of the gas turbine engine, its function being to burn fuel under conditions that are conducive to the optimum operation of the engine. A comprehensive description of the operation and the design principles of the gas turbine combustion system can be found in Lefebvre (1983).

As the operation of the combustor depends on complex physical, chemical and aerothermodynamic processes it was soon realised that improved design requires fundamental understanding of these phenomena. This desire for more detailed and better knowledge combined with the advances in computational fluid dynamics and the advent of powerful computers has promoted the adoption of a more fundamental approach to design which is intended to reduce development time and costs. The work reported here was undertaken with the aim of contributing to this type of approach.

1.1.2 Combustor types

There are three basic types of combustor employed in aircraft engines, namely tubular, annular and tuboannular.

(1) The tubular chamber shown in Figure 1.1 was used in most of the early gas turbine engines. It comprises a cylindrical flame-tube (also called "can" or "liner") mounted concentrically inside a cylindrical casing. From seven up to sixteen chambers may be arranged circumferentially between compressor and turbine. The chambers use interconnectors to facilitate ignition and commonly introduce the fuel through an injector located on the combustor centre line in the head of the can. The compressor air enters the chamber via several routes: i) through a swirler device in the front of the can to help create a flame-stabilising recirculating flow region in the zone where the fuel is to be burned (primary zone); (ii) via discrete round holes on the periphery of the liner to control the air-fuel ratio and to dilute the hot gases to a level demanded by turbine blade-life considerations (intermediate and dilution zones).

(2) The annular chamber shown in Figure 1.2 is an annular liner mounted concentrically inside an annular casing. Although details of the fuel injection and dilution air addition differ from type (1), the essential features and internal flow patterns remain very similar.

(3) The tuboannular chamber, Figure 1.3, represents a compromise between the tubular and annular chamber; the can-type flametubes are retained, but are located in a single annular casing. Again, air flow entry routes may differ from type (1) in terms of number, size and location of holes, but no fundamental differences appear.

1.1.3 Basic design requirements

The basic requirements of all gas turbine combustion chambers can be listed as follows:

High combustion efficiency
Stable operation over a wide variety of conditions
Low pressure loss
Suitable temperature profiles at exit as demanded by turbine blade design
Smooth and reliable ignition
Low emission of pollutants

Durability

Size and shape acceptable for practical engine arrangement.

Combustor designs which can achieve at least some of the above requirements are best described with reference to various sub-zones (Figure 1.1) within the total combustor which play different roles in the overall operation of the system.

(i) A diffuser and annular feed are required to control the entry of the air into the combustor itself. These should efficiently decelerate the high velocity air delivered by the compressor and distribute it in prescribed amounts to the various combustor zones. Uniform and controlled distribution of flow through the various entry routes is essential for stable operation of the liner to minimize the pressure loss and to enable efficient flame tube cooling.

(ii) The primary zone should contain a stable recirculation region for good flame-holding and provide sufficient residence time, temperature and turbulence so that at least 90% combustion completion of the fuel can be achieved in this region. The formation of carbon monoxide and oxides of nitrogen (which are important from pollution considerations) has been found to be sensitive to the local flow pattern and temperature distribution in this region (Niedzwiecki and Jones, 1974).

(iii) The intermediate zone completes the combustion to about 99% and initiates dilution, completed in the dilution zone to provide a desired radial temperature profile for optimum turbine blade life.

Considerable effort is required by the combustion chamber designer to satisfy the above demands while maintaining pace with the development and advances of other engine components.

1.2 Scope and subject of the present work

From the above description, it is clear that aerodynamic processes play an important role in the design and performance of gas turbine combustion systems. For example, the flame stabilising properties of the primary zone depend on the size and strength of the recirculation region and the overall length of the combustor is governed by the fluid mechanics of the rapid mixing promoted by the inflowing dilution air jets. Although there are several types of combustion chambers, differing in size, concept and method of fuel and air injection. It is fortunately the case that the aerodynamic features are common to all systems. In addition, since typical Reynolds numbers for practical combustion systems are of the order of 10^6, the flow is highly turbulent and quantitative and qualitative understanding of the turbulent transport processes which influence internal aerodynamics is of primary importance (Lefebvre, 1968).

In the past, advances in combustion chamber design have been guided predominantly by experimental work. In recent years, however, this has led to expensive and time-consuming design procedures. As a consequence, the exploitation of theoretical approaches for the evaluation of the aerothermochemical processes is becoming increasingly attractive. Therefore, the credibility of a theoretical approach (usually numerical modelling) and the degree to which it can confidently complement experimental investigations is currently the subject of rigorous testing (Jones and Priddin, 1978; Jones and McGuirk, 1979; Bruce et al, 1979; Swithenbark et al, 1979).

The work in this thesis aims to contribute to the testing of such a numerical prediction procedure. In order to select the particular areas in which the contribution may most fruitfully be concentrated, the following section describes relevant previous work on combustor flow field investigations; this provides the background necessary for formulating the precise purpose and nature of the present work.

1.3 Previous work

Research work into gas turbine combustion chamber design and performance can be categorised under three headings: global empirical correlations, more detailed experimental work and numerical modelling. The following review concentrates on the internal flow field of combustion chambers, but some consideration of combustor entry section design is included in the numerical modelling section.

1.3.1 Empirical correlations

Continuous advances in combustor technology brought on by increasing demands on performance created the need for the designer to be able to correlate the performance of different combustor types.

This encouraged the exploitation of a systematic approach based on simple (usually one- or zero- dimensional) analysis and global or overall experimental results. A comprehensive description of the formulation adopted in this type of approach together with examples of its application may be found in several NASA reports (NASA CR-72374 and CR-72375, 1968). In the present review, only a brief description of the method will be given together with an assessment of its capabilities and weaknesses. Further relevant work is included in Table 1.1.

In the context of an empirical theory, the geometry to be calculated is usually simplified and the flow in the combustion system broken down into distinct but interacting regions (eg diffuser/annulus region, primary zone, dilution region etc). The flow in the diffuser and annulus is assumed uniform and isentropic and is calculated from one-dimensional equations for the conservation of mass, momentum and energy. This calculation thus provides the amounts of air that enter the combustor through the cooling slots and dilution holes (combustion chamber air flow distribution or flow split). Inside the combustor in the primary zone the velocity, pressure and temperature are calculated assuming steady one-dimensional flow. Mixing and burning in this zone are considered to occur instantaneously (ie the primary zone is assumed to be a "stirred reactor"). The amount of primary jet air which recirculates in this region (primary jet recirculation ratio) and the penetration of the dilution jets are estimated from empirical formulae based on the correlation of experimental data. The overall calculation proceeds by dividing the combustor into axial control volumes and solving the appropriate set of equations at successive stations; overall continuity is imposed by superposition and adjustment in an iterative cycle. The approach allows the estimation of parameters such as overall pressure drop, temperature distribution at the outlet and on the combustor wall for a given combustor geometry.

A major criticism of this approach is that spatial variation in dependent variables such as velocity and temperature are largely ignored and no attempt is made to calculate the local features of the flow. It can also not provide accurate information in three-dimensional and recirculating regions. In addition, when these methods are extrapolated too far from the data on which they were based, they can not predict accurately even gross operational characteristics such as blow out, relight, mixing rates and emission of pollutants (Osgerby, 1974).

These deficiencies have given rise to a demand for more detailed experiments or a more general analytical approach based upon fundamental fluid mechanics and physical modelling.

1.3.2 Experimental research

Experimental investigations reported in the literature range from simple air and water model flow visualization to high pressure combustion tests at full load. For confidentiality reasons there are relatively few publications on complete, specific design combustion chamber flows. Papers found in the open literature tend to concentrate on model chambers, usually with simplified geometries and running at atmospheric pressure. The work cited in Table 1.2 ranges from isothermal to combusting flows in practical and model combustors and is representative of the ongoing research.

The flow patterns in the primary zone of practical production-type combustion chambers were investigated by Clarke et al (1963) and Youssef (1968). Both isothermal and combusting conditions were used to assess the qualitative and quantitative correlation between the hot and cold flow inside the combustor. In the former investigation, restricted measurements of velocity and local air-fuel ratio were obtained in a full scale can-type combustor operating with both gaseous and liquid fuels. Comparisons between these results and similar measurements obtained in the same combustor operating with air and in a water model identical to the metal chamber showed that the primary zone recirculating flow pattern remained essentially similar in both isothermal and burning situations. Slight quantitative differences in the profiles were attributed to small changes in static pressure, density and secondary jet angles due to combustion. In the work of Youssef probe-based measurements of velocity and pressure were also obtained under isothermal and reacting conditions. Comparisons between the profiles indicated that although combustion reduced the strength of the reverse flow, it had a smaller effect on the size of the recirculation. Profiles of the axial and angular velocities were generally similar except in the negative velocity region near the swirler. In this region however, the accuracy of the five-hole pressure probe used can be called into question due to the high swirl and the associated pressure gradients. More recently, Bicen and Jones (1985) investigated a can-type propane fuelled combustor. LDA measurements of the axial and azimuthal mean and fluctuating velocities were obtained under isothermal and reacting conditions. The data, however, were restricted to traverses at the exit and through the jet holes (the only positions where the laser beams could access the internal combustor volume). Good qualitative similarity between the hot and cold flow profiles was observed in the primary zone especially at air-fuel ratios as encountered in gas turbine practice. Quantitative differences were attributed to density and static pressure changes due to combustion and were most evident in the dilution zone.

Although the comparisons performed in the above investigations were based on a limited number of measurements, they nevertheless show that the similarities between hot and cold flow, at least in the primary zone, are sufficiently encouraging to support the use of isothermal models for providing useful and cheap information.

As the concern for gas turbine generated pollutants grew and new legislation was proposed, a wide range of experimental work on combustor exhaust emissions was undertaken. Here, by way of illustration, two investigations that drew attention to the advantages of swirl in reducing levels of pollutants are mentioned. Mularz et al (1975, 1975a) and Niedzwiecki and Jones (1974) measured pollutant levels of oxides of nitrogen, unburnt hydrocarbon and carbon monoxide at the exit of experimental tuboannular and annular combustors. These employed single swirlers or several swirlers positioned in circumferential rows on the combustor head. The results demonstrated that this approach helped to reduce levels of oxides of nitrogen and this was attributed to rapid mixing of combustion gases with dilution air over a short length together with more uniform fuel distributions due to the swirler. Although no measurements were taken inside the combustor which would allow direct interpretation of the data, this and other encouraging investigations stimulated the interest for more comprehensive information. Coupled with the desire for suitable data which would allow the testing and development of mathematical models of combustors, this created the need for more detailed information. However, comprehensive measurements inside a complex practical combustor geometry are difficult to obtain because of limited access and the often ambiguous interpretation of the data due to uncertainties in the proportions of flow entering the cooling slots and dilution holes. For this reason, investigators have so far concentrated on a particular flow region and simplified geometries where the flow conditions would be more easily controlled.

Altgeld et al (1983), Vu et al (1982) and Rhode et al (1983) restricted attention to the primary zone and examined the changes in the flow structure caused by the introduction and variation of swirl in idealised combustor models without dilution jets. These works provided useful detailed information on the kind of swirling flow fields to be expected in combustion systems, but neglected any influences due to interaction between swirler and primary jet flows. The existence of a vortex breakdown phenomenon and its subsequent development on the presence of a downstream contraction was investigated by Escudier and Keller (1985) but only for an axisymmetric geometry. In the same vein, many experiments have examined only the downstream dilution region and the behaviour of rows of jets in a cross-flow (eg Khan et al, 1981).

A step further towards realistic combustor flows was made by Green and Whitelaw (1983) who included both primary and dilution regions in the same facility but the upstream (combustor head) and downstream (exit nozzle) geometry were greatly simplified and the effect of swirl was neglected. LDA measurements were restricted to one component of velocity but did show the effect of primary jet trajectory on the primary vortex. Measurements in a realistic combustor have been reported by Jones and Toral (1983) who investigated the same can-type geometry as Bicen and Jones (1985). These data, however, were restricted to detailed temperature and gas composition maps for various air-fuel ratios.

In summary then, although a range of detailed measurements of velocity and turbulence properties have been obtained in simplified (usually axisymmetric) chambers a comprehensive mapping of the flow field inside a practical combustion chamber has not yet been achieved. Despite the difficulty of performing such measurements inside an actual combustor, this type of information could be conveniently obtained in a water model whilst retaining an acceptable level of geometrical and flow similarity to an actual chamber.

1.3.3 Numerical modelling

The numerical modelling approach is based upon the numerical solution of the governing conservation equations of mass, momentum and energy complemented by suitable physical models. The equations are solved in their time-averaged form because of the turbulent nature of the flows and various aspects of the flow such as turbulence and combustion have to be modelled and require some empirical input. Space does not allow a complete description of the details of the modelling adopted by the various investigators, rather an indication is given of what has been attempted so far, and to what extent the models have been tested and successful predictions obtained; relevant work is summarised in Table 1.3.

Serag Eldin and Spalding (1979) used a finite-difference technique with a two-equation turbulence model and a combustion model which assumes instantaneous reaction to investigate the reacting flow in a can-type gaseous fuelled model combustor containing both a swirler and dilution jets. Comparison of calculated results with experiment was limited to temperature profiles downstream of the air supply holes and showed correct prediction of trends. Quantitative discrepancies were mainly attributed to the poor performance of the combustion model in regions where the rate of reaction might not be diffusion-controlled. This could imply that the discrepancy would increase further in the region upstream of the dilution holes. Jones and Priddin (1978) investigated the reacting flow in two can-type gaseous and liquid fuelled research combustors. The predictions for the gaseous fuelled combustor were tested against measurements and showed overestimation of species such as carbon monoxide, unburnt hydrocarbon and nitric oxide. The few velocity measurements obtained with a seven-hole pressure probe showed that the predictions overestimated the recirculation lengths. It was commented that full interpretation of the results and appraisal of the models was not possible due to lack of suitable data. However, it was concluded that the model provided useful indications, for design purposes, of the regions of maximum pollutant formation and consumption. Similar techniques were used by Jones and McGuirk (1979) to investigate a two-dimensional isothermal and reacting flow in a gaseous fuelled model combustor and a three-dimensional reacting flow in a liquid fuelled chamber. Comparison of probe measurements in the two-dimensional axisymmetric chamber with numerical results showed underestimation of recirculation lengths and temperature levels; the discrepancy between predicted and measured temperature distributions increased in the three-dimensional calculations. The disagreement was attributed to uncertainties in the inlet boundary conditions and the poor performance of the turbulence model under strongly swirling conditions. The difficulty of obtaining grid independent solutions in three-dimensional calculations was also emphasised. A slightly different approach was employed by Swithenbank et al (1979) who modelled the three-dimensional two-phase flow inside a model can combustor. They used a finite-difference technique to obtain velocity, turbulence and temperature data and empirical stirred reactor models to predict total pollutant emission levels. Limited comparisons with experiment were made inside the combustor, but the predicted exit profiles of velocity, turbulence intensity and temperature agreed well with measurements. The authors supported hybrid modelling of this type as the only way, at present, to make quantitative pollutant emission predictions due to time and cost penalties of more complex models.

The direct application of numerical methods in the design and development of gas turbine combustion chambers was demonstrated by Bruce et al (1979) and Sturgess et al (1981). The former work used a combination of empirical methods and three-dimensional numerical modelling to design two full scale reverse flow annular combustors. A one-dimensional annulus flow model was employed to calculate the pressure loss, air flow distribution, jet velocities and efflux angles at the various holes on the combustor walls and these were used as boundary conditions for the three-dimensional reacting calculation inside the combustor. The program was tested and developed against experimental work and applied to assess the effect of detailed design changes on combustor performance. Sturgess et al (1981) simulated numerically the flow pattern inside an experimental combustor for a large scale turbo fan engine. The modelling enabled the authors to pinpoint quickly and economically the cause of changes in dome and liner pressure drop.

The ability of numerical methods, when applied to simplified model combustors, to provide results that can usefully be extrapolated to actual designs is indicated in the investigations of Novick et al (1979, 1979a) and Green and Whitelaw (1983). Novick et al examined the isothermal and reacting flow in axisymmetric geometries. The comparison between numerical calculations and measurements, for reacting flows, is confined to one temperature map and shows good agreement. The calculated results show the effects of swirl, recirculation zone amplification and laterally induced secondary air supply on the flow field development. A more systematic appraisal of the numerical technique was attempted by Green and Whitelaw (1983) in a three-dimensional isothermal model combustor. Predicted results were compared with detailed LDA measurements of one velocity component over the whole combustor and 10-40% discrepancies were found. The maximum error was obtained in calculations which attempted to include the annulus region in the main calculation and was attributed to an incorrectly predicted flow division in the annulus. The turbulence model was also criticised although the numerical inaccuracy was estimated to be equally important.

The above discussion illustrates that although direct comparison between prediction and measurement has been realised over a range of operating conditions, a comprehensive evaluation against detailed and complete data of all three velocity components, turbulence kinetic energy and concentration has yet to be demonstrated. It is further evident that testing of the method has largely been restricted to simple geometries conforming to simple systems of co-ordinates. The application of the numerical approach in combustors of practical geometry with complex boundaries has also not yet been achieved.

The investigations by Bruce et al (1979) and Green and Whitelaw (1983) demonstrated that the prediction of gas turbine combustion systems requires a calculation procedure which can calculate the flow field both outside and inside the combustor, the results of the former calculation providing the boundary conditions for the latter. Although empirical theory and zero- and one-dimensional models have been successfully used for the prediction of the flow inside the diffuser and annulus, recently developed arrangements require more fundamental treatment. This has created an interest in assessing the capability of numerical modelling to predict the flow inside currently preferred diffuser geometries. Examples of numerical modelling of diffusers (in relation to the combustion system) are therefore summarised in Table 1.3.

An early contribution was made by Livesey et al (1960) who investigated the flow in tube type combustion chamber entry sections. Theoretical analysis of the flow in the entry section under the assumption of irrotationality did not yield useful quantitative results. It was concluded, however, that even the ideal flow solution could indicate the trends. More recently, diffusers of wide angle followed by a downstream sudden expansion ("dump") were considered by Habib and Whitelaw (1982) who used a body fitted co-ordinate mesh to allow proper treatment of the near wall regions. Detailed comparison between calculations and measurements showed up to 14% discrepancies in the predicted mean axial velocity profiles while the turbulent kinetic energy was underestimated by up to 30%. The authors believed that numerical inaccuracies did not contribute significantly and the error was attributed mainly to the performance of the turbulence model. Improved finite-difference techniques and turbulence models have been used by Hah (1983) to investigate the effect of the variation of the inlet conditions on the performance of planar, conical and annular diffusers. The comparison between predictions and measurements showed that the results were of acceptable accuracy for engineering purposes and this was used to justify the adoption of more complex turbulence models.

The application of numerical methods for predicting the flow in simple diffusers has provided useful information about the problems and levels of attainable accuracy to be expected in the study of the actual combustion system. However, it would also be of interest to examine how well the combined diffuser and annular supply duct system can be predicted when influences such as the flow division between inner and outer annulus and the presence of the combustor are introduced.

1.4 Assessment

To achieve significantly increased performance, such large departures from conventional design may be necessary that extrapolation from empirical knowledge of current systems is dangerous and fundamental understanding of combustor operation is required. Clearly, this can only be achieved through detailed knowledge of the aerodynamic processes within the liner and how these interact with the combustion process.

Traditionally, this knowledge has been gained via a great deal of experimentation and very little recourse to numerical modelling. This can be attributed to the fact that the capability and the assessment of calculation methods has been demonstrated predominantly on simplified geometrical configurations and flows with simple boundary conditions. From the designer's point of view, this detracts from the potential usefulness of the method and the confidence with which it can be applied to real problems. The application of these methods in realistic configurations, with boundary conditions appropriate to gas turbine practice will provide a more convincing demonstration of their potential. Because of the detailed information provided by numerical methods, a rigorous assessment can only be performed by comparing with complete three-dimensional velocity data taken in a realistic configuration.

Finally, given the comments above on the comparative similarity between isothermal and reacting flow fields, this comparison may reasonably be performed in isothermal flows.

1.5 Present contribution

On the basis of previous remarks, the contributions of this thesis may be separated into three categories:

(i) To provide detailed laser Doppler anemonetry measurements of the three-dimensional velocity and turbulence fields in an isothermal model, scaled from a current production can-type combustor, retaining as far as possible all geometrical features. The geometry chosen is identical to that in the reacting experiments of Jones and Toral (1983) and Bicen and Jones (1985) with the only omission being the wall cooling arrangements (the combusting experiments use transpiration cooled walls); the geometry has close similarity to the combustor used in the Rolls-Royce Spey engine (Gradon and Miller, 1968). Although the reacting flow field will differ in certain respects from the isothermal flow, it is likely that dominance of the dilution jet flows in creating the flow pattern (at least in the primary zone) encourages the retention of the isothermal flow type of experiment. This alleviates the optical access problems to the extent that measurements should be possible over practically the whole internal volume of the combustor. The detailed mapping of the flow field thus obtained (for a variety of flow splits between swirler, primary and dilution jets) will provide the detailed information required for adequate numerical model assessment as described above. At the same time, useful information about the primary jet recirculation ratio and the interaction between swirler and primary jets can be obtained.

(ii) To apply to the chosen flow configuration a calculation method for combustion chamber flows using a finite-difference numerical model. In particular, the work should examine the extent to which the model can predict changes in the flow pattern brought about by alterations in the geometry and boundary conditions. Attention should also be paid to the treatment of complex geometries with arbitrary boundaries which do not conform to a simple system of co-ordinates such as cartesian or cylindrical-polar. Such geometries always occur in practice and a sufficiently flexible method for handling this problem within the numerical method is necessary for general applicability.

(iii) The above internal flow field calculations will use information obtained in the experimental study as boundary conditions. As a first step to providing these boundary conditions as the output of a numerical model, calculations of the flow external to the combustor in the upstream diffuser and surrounding annular ducts should be performed. For this study, because of the current interest in such systems and the readily available experimental data in the literature, a dump diffuser system for an annular combustor has been chosen for investigation.

1.6 Outline of Thesis

The remainder of the thesis is presented in five chapters. Chapter II describes the water flow tunnel, the model combustor, the laser Doppler measuring technique and includes an assessment of the errors incurred in the measurements. The results are then presented and discussed with particular reference to the effect of the flow split between swirler, primary and dilution holes and the influence of swirler geometry on the flow field development.

Chapter III outlines the partial differential equations and the procedure for the solution of the corresponding finite-difference equations. Three methods which enable the application of the numerical method to the calculation of flow configurations with complex geometries are described. Finally, an assessment of the limitations in the physical models and numerical accuracy is provided.

Chapter IV discusses the relevance of dump diffuser geometries to gas turbine combustion systems and describes the flow configuration chosen for the numerical investigation and the performance parameters of this type of diffuser. Numerical error estimates are provided and the results are compared with available measurements.

Chapter V is devoted to the numerical calculation of the flows of Chapter II. The approaches adopted for the efficient and economic calculation of the flow inside the complex model combustor geometry are described and the details of the application of the numerical model and the numerical accuracy of the calculations are discussed. The calculated results are then presented and compared with experiments. The extent of correspondence between calculations and measurements is discussed with particular reference to the ability of the method to predict correctly the variations in the flow pattern observed experimentally.

Chapter VI concludes the thesis by summarising the present work and providing some suggestions for further research.

TABLE 1.1
EMPIRICAL CORRELATION

Reference	Type of Study	Remarks
NASA CR-72374 and CR-72375 (1968)	Description of calculation procedures accompanied by complete computer program for predicting the performance of an annular combustor.	The analysis calculates the performance of the diffuser, the airflow distribution, pressure and temperature on the liner walls using empirical formulae based on the one-dimensional equations for mass, momentum and energy complemented by experimental results. The limitations of the procedure are also discussed.
Tacina and Grobman (1969)	The effect of changes in combustor geometry and Mach number on the total pressure loss and airflow distribution were investigated with procedures similar to those used above.	Results correlate airflow distribution, pressure ratio, area ratio, total temperature for various geometries in tubular and annular chambers.
Verduzio and Campanaro (1971)	Determination of primary jet recirculation ratio.	Compares upstream recirculation ratio in a simple can-type geometry with a simple empirical analysis. Parametric study of primary jet-hole size and number is included.
Novick et al (1980)	Description of an analysis for the calculation of dilution zone configurations.	A three-dimensional analysis predicts the trajectories of dilution jets through the dilution zone and contracting section of the combustor nozzle. The method predicts the effects of the variation of the rate of lateral jet spread as well as the interaction between jets.
Odgers (1979)	A review of design approaches using empirical models.	Discusses relevance of a range of models (0-3-dimensions) and the implications of the strong three-dimensional nature of the flow in the primary zone.

TABLE 1.2
EXPERIMENTAL RESEARCH

Reference	Type of Study	Remarks
Clarke et al (1963)	3-d isothermal study with air and water; reacting study with gaseous and liquid fuels at atmospheric pressures in a can-type geometry.	Measurements of axial velocity and local concentration of air-fuel ratios in air, water and reacting flows are compared and similarities between isothermal and reacting flow are emphasized.
Youssef (1968)	3-d isothermal and reacting study using gaseous fuel at atmospheric pressures in a can-type model combustor.	Compares measurements of velocity, pressure and temperature within the primary zone. Discusses similarities and differences between isothermal and reacting profiles.
Bicen and Jones (1985)	3-d isothermal and reacting study of a can-type gaseous fuelled model combustor.	LDA measurements of velocity were obtained through primary and dilution holes and at the exit. The effect of air-fuel ratio and fuel injection were investigated. Similarities between isothermal and reacting flow were found in the primary zone.
Mularz et al (1975, 1975a)	3-d reacting study with liquid fuel. Evaluation of a number of swirl can combustors at simulated gas turbine operation.	Exhaust pollutants were measured with a gas sample probe. Results showed that swirl can combustors reduce levels of oxides of nitrogen.
Altgeld et al (1983)	2-d isothermal study of an axisymmetric swirl stabilised combustor.	LDA measurements of the velocity and turbulence fields were obtained and the effect of fuel injection and exit contraction were investigated.
Vu and Gouldin (1982)	2-d isothermal study with air of an axisymmetric model combustor composed of two confined co-axial swirling jets.	Velocity measurements of the axial and azimuthal components and their normal stresses were obtained with hot wire and pitot probe. The effects of the coswirl and counter swirl on the strength of the recirculation and on the turbulence levels are discussed.

TABLE 1.2 (CONTINUED)

Reference	Type of Study	Remarks
Rhode et al (1983)	2-d isothermal study of an axisymmetric model combustor with swirl.	Probe measurements of velocity were performed to examine the effect of the angle of the expansion downstream the swirler and of the swirler vane angle on the flow field.
Green and Whitelaw (1983)	Isothermal study of the three-dimensional flow in a model can-type combustor with simplified upstream and downstream sections.	LDA measurements of velocity were obtained and the interaction between annulus and flame tube and the effect of primary jet trajectory on the upstream recirculation were discussed.
Jones and Toral (1983)	3-d reacting study of a propane fuelled can-type combustor.	Detailed measurements of temperature and gas composition fields were obtained at various cross-sections of the combustor and for various air-fuel ratios.

TABLE 1.3
NUMERICAL MODELLING

Reference	Type of Study	Remarks
COMBUSTOR FLOWS		
Serag Eldin and Spalding (1979)	3-d study of the reacting flow inside a gaseous fuelled can-type model combustor made up of a swirler and a single row of dilution jets.	The numerical model used was tested against measurements by *Serag-Eldin* (1977) and the limited comparison between calculated and measured temperature profiles showed correct prediction of trends. Quantitative disagreement was attributed to the combustion model.
Jones and Priddin (1978)	3-d studies of gaseous and liquid fuelled reacting flows in two model can combustors.	Probe measurements compared with numerical results showed overestimation of recirculation lengths and combustion species such as HC, CO, NO.
Jones and McGuirk (1979)	2-d isothermal and reacting study with gaseous fuel and 3-d reacting study with liquid fuel.	Probe measurements of velocity, temperature and gas composition obtained in the 2-d axisymmetric chamber were compared with numerical results. Underestimation of recirculation lengths and temperature were found.
Swithenbank et al (1979)	3-d study of a model can combustor under isothermal and combusting conditions.	A combination of finite-difference techniques and empirical reactor models were used to predict the velocity, turbulence, temperature and total pollutant emission levels. Limited comparison with experiment at the combustor exit showed good agreement.
Bruce et al (1979)	Extensive 3-d study of isothermal and reacting flows in practical combustors.	Two reverse flow annular combustors were designed using a combination of empirical correlation and numerical modelling. Goals such as a more durable and fuel efficient system were achieved while reducing development time and cost.

TABLE 1.3 (CONTINUED)

References	Type of Study	Remarks
Sturges et al (1981)	3-d reacting study of an experimental combustor for a large turbojet engine.	The numerical modelling approach enabled the investigators to identify quickly and economically the cause of changes in pressure drop and dome overheating.
Novick et al (1979, 1979a)	2-d study of isothermal and reacting (premixed gas-air) flows in axisymmetric combustors.	Calculated results show the effects of combustor design parameters such as degree of swirl, recirculation zone amplification and laterally induced secondary air supply on the flow field development.
Green and Whitelaw (1983)	Isothermal study in 3-d water model can-type combustors.	Predictions were compared with available detailed LDA measurements of one component of velocity and 10-40% discrepancies were found depending on location.
<u>DIFFUSER FLOWS</u>		
Livesey et al (1960)	An early theoretical analysis of component pressure losses in tube-type gas turbine combustion chamber entry sections.	The analysis of the two-dimensional flow at the diffuser entry section, under the assumption of irrotationality did not yield useful quantitative results.
Habib and Whitelaw (1982)	Numerical investigation of straight walled diffusers up to 45° half-angle followed by a downstream sudden expansion.	A body-fitted mesh was used to allow proper treatment of the near wall region. Detailed comparison of the results with available measurements shows maximum discrepancies of 14% in the mean axial velocity and underestimation of the turbulence kinetic energy by up to 30%.
Hah (1983)	Numerical investigation of the effect of the variation of the inlet conditions on the performance of planar, conical and annular diffusers.	Improved finite-difference techniques and turbulence models yielded results of acceptable accuracy for engineering design purposes.

CHAPTER II

EXPERIMENTAL PROCEDURE AND MODEL COMBUSTOR FLOW FIELDS

2.1 Introduction

This chapter describes the experimental investigation undertaken on the model combustor to obtain measurements of the three mean velocity components and the corresponding turbulence intensities. Experiments were carried out, for two swirlers, over a variety of flow splits between swirler, primary and dilution ports representative of current practice.

The first section gives details of the experimental method and considers, in turn, the flow configuration, the laser Doppler velocimeter and the errors incurred in the measurements. Section 2.3 presents the results for each operating condition and is followed by a discussion, in Section 2.4, of the influence of the swirler/primary jets mass flow ratio and the effect of the swirler geometry on the flow patterns. The final section, 2.5, presents a summary of the main findings and conclusions of the experimental programme.

2.2 Experimental method

2.2.1 Flow configuration

The model chamber was inserted in a closed-circuit water tunnel shown schematically in Figure 2.1. The combustor, Figure 2.2, was manufactured from cast acrylic and consisted of a hemispherical head section attached to a cylindrical central barrel of 74 mm internal diameter, which terminated in a circular to rectangular contraction nozzle. The curved vane aerodynamic swirlers were attached to the head with their central hub blocked off. The model was located concentrically in a larger diameter tube so that an evenly spaced surrounding annular passage was formed. Six primary holes 10 mm in diameter and equispaced around the combustor were located 46 mm downstream of the swirler (this distance was 49 mm when the combustor was operating with swirler 2 in position). A second row of 12 equispaced holes (also 10 mm) was placed a further 80 mm downstream. In what follows, the first row of holes will be referred to as primary holes and the second row of holes as dilution holes.

A single constant head tank (A) supplied fluid to the larger containing tube to feed both hole rows via the annulus which was blocked off at the retaining flange at the farthest downstream end. The swirler was fed separately from another constant head tank (D) via a rotameter to allow control and regulation of the flow rate of the swirler fluid. The outflow from the combustor entered (via a free overflow, B) a large sump tank (C) from where it was pumped to the two constant head tanks. Photographs of the water flow rig and the model combustor are shown in Figures 2.3a and b respectively.

The above geometrical characteristics were conceived by scaling down a current production can-type combustor (Rolls-Royce Spey engine, as reported by Gradon and Miller, 1968). However, devices such as wall cooling arrangements, plunged holes or additional trimmer holes and nozzle guide vane bleed were omitted. This does not preclude them from future work as discussed later. Similarly, the two swirlers used for the investigation were also taken from production chambers (Bhangu et al, 1983). The geometry of the two swirlers is depicted in Figure 2.4b. The definition of swirl number most commonly accepted (Beer and Chigler, 1972; Mathur and Maccalum, 1967; Gupta et al, 1984) is

$$SN = \frac{2G_{\theta sw}}{G_{xsw} \cdot D_{sw}} \qquad (2.1)$$

where:

$G_{\theta sw}$ = axial flux of azimuthal momentum

G_{xsw} = axial flux of axial momentum

D_{sw} = exit radius (see Figure 2.4a)

For an annular vaned swirler assuming uniform profiles, equation 2.1 leads to

$$SN = \frac{2}{3} \, \frac{1-(D_h/D_{sw})^3}{1-(D_h/D_{sw})^2} \tan\theta \qquad (2.2)$$

From the above expression, swirl numbers of 0.74 and 0.85 were evaluated for swirlers 1 and 2 respectively. (A more accurate value for the swirl number of swirler 1, obtained from measurements close to the swirler exit is 0.87. Due to lack of similar measurements for swirler 2, however, and for the sake of comparison in performance between the two swirler types, hereafter only the swirl numbers obtained from the geometrical characteristics will be referred to.)

Qualitative and quantitative investigations were carried out for the two swirlers over a range of flow splits between swirler, primary and dilution ports. This was achieved by varying the swirler flow rate while the annulus flow rate was kept constant. The range of operating conditions and the corresponding Reynolds numbers (based on the individual bulk velocity and the internal combustor diameter) are given in Table 2.1. The swirler flow rate was metered with a rotameter (see Figure 2.1) while the annulus flow rate was evaluated from the integration of the measured axial velocity profile in the annular gap between the swirler feed and the large containing tube upstream of the combustor. The method of determination of the flow split between the primary and dilution holes and the reason for its variation with swirler flow, as indicated in Table 2.1, will be discussed in conjunction with the presentation of the measurements of the annulus flow field in subsection 2.3.2.

The use of water, rather than air, as the working fluid has two advantages when using laser-Doppler velocimetry. Naturally occurring particles in the water are suitable for use as scattering particles so that seeding of the flow is usually unecessary. Secondly, sufficiently high Reynolds numbers can be achieved at bulk velocities of about 1 m/sec corresponding to frequencies (several hundred kilohertz) which can conveniently be demodulated by a frequency tracker. The use of air would result in frequencies larger by an order of magnitude which are too high for use with a frequency tracking system (Taylor, 1981).

2.2.2 Velocimeter configuration, signal processing system and measurement technique

Velocimeter configuration

The optical arrangement of the laser-Doppler velocimeter used in the measurements is shown in Figure 2.6. It was operated in a symmetric heterodyne, forward-scatter mode (dual beam mode) with light "frequency shifting" provided by the rotation of a radial diffraction grating. The principles and practice of laser-Doppler velocimetry are

TABLE 2.1
COMBUSTOR OPERATING CONDITIONS IN TERMS OF FLOW SPLITS

	$\dot{m}_{tot}$ (kgr/ sec)	$\dot{m}_{sw}/\dot{m}_{tot}$ (%)	$\dot{m}_{pr}/\dot{m}_{tot}$ (%)	$\dot{m}_{d}/\dot{m}_{tot}$ (%)	$\dot{m}_{sw}/\dot{m}_{pr}$	$\dot{m}_{d}/\dot{m}_{pr}$	G_{xsw}/G_{pr}	Reynolds Number ($\times 10^6$)	V_{pr}/U_{sw}	V_d/U_{int}	SWIRLER TYPE
CASE 1	3.11111	10	34.84	55.16	0.287	1.58344	0.03637	5.4	7.899	5.641	SWIRLER 1
CASE 2	3.29425	15	32.90	52.10	0.456	1.58344	0.09180	5.7	4.967	4.986	SWIRLER 1
CASE 3	3.5	20	30.30	49.70	0.660	1.640887	0.19242	6.02	3.430	4.519	SWIRLER 1
CASE 4	3.73333	25	28.40	46.60	0.8802	1.640887	0.34209	6.42	2.573	3.991	SWIRLER 1
CASE 5	3.88888	28	27.26	44.74	1.026	1.640887	0.46562	6.7	2.205	3.703	SWIRLER 1
CASE 6	3.7	35	24.63	40.37	1.416	1.640887	0.89275	6.4	1.593	3.118	SWIRLER 1
CASE 7	3.11111	10	34.84	55.16	0.287	1.58344	0.08584	5.4	3.340	5.641	SWIRLER 2
CASE 8	3.29425	15	32.90	52.10	0.456	1.58344	0.216	5.7	2.104	4.986	SWIRLER 2
CASE 9	3.5	20	30.30	49.70	0.660	1.640887	0.454	6.02	1.453	4.519	SWIRLER 2

NB. (I) $\dot{m}_{annulus}$ = $\dot{m}_{pr} + \dot{m}_d$ was held constant at 2.8 kgr/sec except for case 6 when it was 2.405 kgr/sec.

(II) $\dot{m}_{tot}$ = $\dot{m}_{sw} + \dot{m}_{annulus}$

(III) G_{xsw} = axial flux of axial momentum at swirler exit: $\rho U^2_{sw} A_{sw}$ (assuming a flat axial velocity profile)

G_{pr} = radial flux at radial momentum at primary holes: $\rho V^2_{pr} . 6 . A_{pr}$

(IV) V_{pr}, V_d are the mean radial jet velocities
U_{sw} is the mean axial velocity at swirler exit
U_{int} is the mean axial velocity at a cross-section upstream of the dilution jets.

extensively described in a number of texts (eg Melling, 1975; Durst et al, 1981; Drain, 1980) and therefore only a description of the features and advantages of the present design will be given here.

The basis of the dual beam anenometer is the intersection of two equally intense, coherent light beams to form a measuring probe known as the "scattering volume". The scattering volume is a region of interference between two electromagnetic waves producing areas of high and low energy within the region. As the light intensity of the beams is Gaussian in radial distribution the measuring volume is an ellipsoid in shape with boundaries usually defined as a fraction ($^1/e^2$) of the maximum intensity, and shown in Figure 2.6. A particle passing through the measuring volume with velocity V in the plane of the beams in the direction of the minor axis, produces a periodic variation in the scattered light intensity due to the interference of the light beams. The Doppler frequency f_D of the periodic scattered light intensity is given by (Durst et al, 1981):

$$f_D = \frac{2V.\sin\theta}{\lambda} \qquad (2.3)$$

where 2θ is the angle of the beams and λ the wave length (Figure 2.6). Hence, the velocity of the particle is linearly related to the frequency of the scattered light intensity and the constant of proportionality is uniquely defined by parameters that are independent of the flow (assuming no variation in wave length due to density changes). Natural contaminants found in water lie within a suitable size range for use as scattering particles whose instantaneous velocity faithfully represents that of the water (Melling and Whitelaw, 1973).

A major advantage of the laser-Doppler velocimeter is the provision of direction sensitivity essential in flows with regions of recirculation. This is achieved by arranging a frequency difference between the two beams which form the symmetric heterodyne velocimeter. A comprehensive review of frequency shifting techniques is given by Durst and Zare (1974). For the magnitude of the Doppler frequencies encountered in this experiment (several hundred kilohertz) the frequency shift is conveniently derived from the frequency difference between the first order maxima of a rotating radial diffraction grating. The grating provides the frequency shift and splits the incident beam to create the two channels of the velocimeter, Figure 2.6.

Two further advantages concerning the demodulation of the Doppler signal can be mentioned. The first is that frequency shifting increases the separation, in frequency space, between the shifted frequency and the pedestal frequency, associated with the time of crossing of a particle across the light beams (Durst and Zare, 1974). The second advantage is that it provides the ability to select a range of the Doppler frequency demodulator, which can accommodate the spread (due to turbulence) of the velocity probability density distribution at every point in the flow by varying the magnitude of the frequency shift which is applied (see also under "Doppler signal processing").

The frequency shift applied by the grating is, for the first order maxima:

$$f_s = 2.N.\Omega \qquad (2.4)$$

where Ω is the angular velocity of the rotating grating in hertz.

The transmission phase diffraction grating used in the present design was manufactured by the Technische Physische tho-th, Holland, designated "type H". The principal characteristics are summarised in Table 2.2 and further information is given by Oldengarm, Van Krieken and Raterink (1976).

The velocimeter incorporates three lenses which are shown in Figure 2.6. The function of these lenses can be summarised as follows:

Lens L1: focuses the laser beam on the grating to minimize distortion of the first order diffracted beams. Its focal length influences the size of the fringe volume and determines the number of fringes that are in it.

Lens L2: makes the diffracted laser beams parallel. Its focal length determines the beam separation S and the beam expansion ratio ($b'o/bo$).

Lens L3: focuses the two beams at the focal region of the beams thus forming the scattering volume. Its focal length influences the size of the scattering volume and determines the intersection angle.

The measuring volume has the form of an ellipsoid with major (b_y) and minor (b_x) axes (Figure 2.6), defined at the e^{-2} level of intensity, of length:

$$b_x = \frac{b}{\cos\theta} \qquad (2.5)$$

$$b_y = \frac{\eta b}{\sin\theta} \qquad (2.6)$$

where:

$$b = \frac{4\lambda . f_1 . f_3}{\pi . b_o . f_2} \qquad (2.7)$$

and η is the refractive index of water. The fringe spacing δx is:

$$\delta x = \frac{\lambda}{2\sin\theta} \qquad (2.8)$$

The Table 2.3 summarises the principal characteristics of the laser-Doppler velocimeter.

Doppler signal processing

The function of the signal processing system of a laser-Doppler velocimeter is to process the Doppler signal produced, via the photomultiplier (in the present work of type RCA 4836), by the optical system into a form that may be statistically analysed. The range of electronic devices that are capable of processing this type of signal includes frequency analysers, frequency counters, frequency trackers, filterbanks and photon correlators. The details, advantages and disadvantages of each of these processing systems are described in detail by Durst et al (1981). In turbulent water flows one of the most convenient methods of signal processing is by using a frequency tracker and this was used for all present measurements.

The frequency tracker operates in the frequency domain providing real time demodulation of the Doppler signals and yielding an analogue signal continually proportional to the velocity of the fluid, suitable for further statistical processing. The operation of the frequency tracker employed in the present work (Cambridge consultants CC01) has been described in detail by Taylor (1981). Consequently,

TABLE 2.2

PRINCIPAL CHARACTERISTICS OF THE RADIAL DIFFRACTION (TRANSMISSION PHASE) GRATING

Number of line pairs (N)		16384
Spacing	(μm)	6.08 (±0.14)
Diffraction angle for first order maxima for wavelength of 632.8 nm	(degrees)	5.98 (±0.14)
Disc diameter	(mm)	35
Efficiency of diffraction for first order maxima	(each)	25-30%
Long term stability		0.1%
Short term stability ($\delta\Omega$)	(r.m.s.)	0.2%
Shift frequency	(MHz)	2

TABLE 2.3

PRINCIPAL CHARACTERISTICS OF THE LASER-DOPPLER VELOCIMETER

5mw He-Ne laser	$\lambda = 632.8$ nm
Focal length of lenses:	
L1 (nominal)	$f_1 = 110$ mm
L2 (nominal)	$f_2 = 300$ mm
L3 (nominal)	$f_3 = 300$ mm
Beam diameter bo, at e^{-2} intensity of laser	0.8 mm
Half angle of intersection, θ (in air)	5.98 degrees
Fringe separation	3.037 μm
Intersection volume diameter at e^{-2} intensity level (in water)	0.111 mm
Intersection volume length at e^{-2} intensity level (in water)	1.416 mm
Calculated number of fringes within e^{-2} intensity level with no frequency shift	37
Velocimeter transfer constant (MHz/msec^{-1}) with no frequency shift	0.329

only the general characteristics of its operation will be described below with emphasis placed upon the precautions taken for the correct demodulation of the Doppler signals.

The concentration of the naturally-occurring scattering points, which give rise to Doppler signals, in water is such that the probability of finding more than one particle in the measuring volume of the velocimeter is small. Consequently, the occurence of Doppler signals is a discrete, rather than a continuous process. The correct operation of the tracker depends on being able to distinguish the presence of a valid signal from the noise base line and on a sufficiently low drop out rate of the signal. The criterion of a suitable signal is based on comparing the amplitude of the signal at the input with that of a variable-level comparator. The level of the comparator is set so that this is larger than the noise level at the input. In addition, frequency trackers are designed to detect signal drop out and to hold the previous measured frequency. Thus, high drop out rates distort any further statistical processes such as true integration to determine the mean frequency, Taylor (1981). Although the drop out rate in water flows is not normally significant, seeding of the flow with minute quantities of milk increases the scattering particle concentration and thereby increases the scattering particle arrival rate.

A further restriction in the operation of the tracker is that of the "tracking range" which requires that the Doppler frequency to be demodulated lies within the selected tracking range at all times. This can be expressed as a maximum permissible turbulence intensity which is a function of the mean Doppler frequency (see Durst et al, page 228) and is a potential limitation in highly turbulent flows. In addition, the rate at which the tracker can follow a highly fluctuating signal is also limited by its dynamic response and maximum slew rate (ie the maximum rate of change of frequency with time that can be followed). These limitations can usually be avoided by using optical frequency shifting to reduce the overall "turbulence intensity" to less than 15%, ie:

$$\frac{\sqrt{\overline{f_D{}^2}}}{\overline{f_D}+f_s} < \frac{\sqrt{\overline{f_D{}^2}}}{\overline{f_D}} \qquad (2.9)$$

The voltage analogue of the Doppler frequency was processed by a true integrator (for the mean velocity; DISA model 52B30) and an RMS meter (DISA model 55D35) and their output was read on a digital voltmeter (Solartron LM1450). A schematic diagram of the processing equipment is given in Figure 2.7, including the wave forms of the Doppler signal at each stage.

Measurement techniques

In order to traverse the model with the laser-Doppler anemometer, the optical components and the photomultiplier were mounted on a rigid mild steel optical bench which in turn was bolted to a three-dimensional traversing bed. The optical orientation of the velocimeter for the measurement of *axial, azimuthal and radial velocities* is shown in Figure 2.8. The effects of refraction of the laser beams on passing through the curved tube walls due to the different retractive indices of air, water (η = 1.33) and perspex (η = 1.49), were minimised by immersing the model and the containing round tube in a plane walled trough filled with distilled water.

Measurements of the axial, azimuthal and radial velocities and the corresponding turbulence intensities were obtained for various θ planes passing through the centre line of the combustor at a total of 13 axial locations spanned by the positions where beam interference was experienced either by the curved combustor head near the swirler or the nozzle geometry. The measurement points and the system of co-ordinates are shown in Figure 2.9. Due to the circumferential distribution of the first and second row of holes every 60^o and 30^o respectively, the combustor cross-section (excluding the nozzle section) may be divided into six geometrically identical sectors, ie the geometry repeats itself every 60^o. Consequently, the flow is expected to exhibit cyclic repetition over a 60^o sector at least up to the position whereby the nozzle will disrupt this behaviour. To investigate the extent of this periodic behaviour of the flow, radial planes at $\theta = 0^o, 15^o, 30^o, 60^o$ were studied and measurements were obtained over the whole diameter so that two opposing sectors were in fact examined (see Figure 2.9). The whole internal combustor geometry could be rotated using the rear retaining flange to bring the relevant θ plane into position. Further comments on the cyclic nature of the flow patterns will be made in the presentation of the experimental results. The actual θ planes and the axial locations on which measurements were made for each operating condition are shown in Table 2.4.

TABLE 2.4

MEASUREMENT LOCATIONS FOR EACH OPERATING CONDITION

OPERATING CONDITION	MEASUREMENT POSITION	θ PLANE
CASE 1	b,c,d,f,h,k,l,m	0°
CASE 2	a,b,c,d,f,g,h,i,j,k,l,m	$0^{\circ}, 15^{\circ}, 30^{\circ}, 60^{\circ}$
CASE 3	b,c,d,f,h,k,l,m	0°
CASE 4	b,c,d,f,h,k,l,m	0°
CASE 5	b,c,d,f,h,k,l,m	0°
CASE 6	c,d,f,h,k,l,m	0°
CASE 7	b,c,d,f,g,h,i,j,k,l,m	0°
CASE 8	b,c,d,f,g,h,i,j,k,l,m	0°, 30°
CASE 9	b,c,d,f,g,h,i,j,k,l,m	0°

A limitation lay in the measurement of the radial velocity which became progressively more difficult as the measuring volume approached the pipe wall because of the increasing refraction and dispersion at solid-liquid interfaces. The furthest position at which measurements could be reliably obtained corresponded to about 80% of the radius. The deterioration in the signal quality of the radial velocity as the measuring volume lies further off axis impairs the reliability of demodulation. As a consequence, V velocity measurements within the curved combustor head were not obtained and, in the rest of the profiles, some values far from the pipe axis have been deleted in the presentation of the results on the grounds that they were unreliable.

2.2.3 Limitations in the accuracy of the measuring technique

This section presents the errors incurred in the measurements of the velocities and turbulence intensities. The sources of broadening of the velocity probability density are briefly discussed and quantified.

Estimates of the systematic and random errors of measurement are also included.

Doppler broadening

The Doppler frequency probability density is affected by sources other than true velocity fluctuations at a point. These sources increase the variance of the Doppler frequency probability density (and hence increase the measured values of normal stress) with the effect that the distribution is broader than that of the velocity. The most significant of these errors in relation to the present measuring system are finite transit time broadening, mean velocity gradient broadening, instrument noise and short-term fluctuations in the rotation of the grating.

Finite transit time broadening of the Doppler spectrum arises because signals from individual scattering particles last only for the time required to traverse the scattering volume and the random arrivals and departures of individual particles into and out of the scattering volume cause phase and frequency fluctuations which give a finite width to the measured Doppler spectrum. Melling (1975) and George and Lumley (1973) have given formulae for the evaluation of this error, in accordance with other workers (Edwards et al, 1971).

Mean velocity gradient broadening occurs when a mean velocity gradient exists across a finite-size scattering volume and may be present in both laminar and turbulent flows. The variation of velocity is proportional to the gradient and to the dimension of the volume parallel to the gradient. A simple method of evaluating this broadening error has been proposed by Melling (1975).

The analogue output of the tracker has a noise component associated with it, so that even if a continuous sine wave of constant frequency is applied to the tracker input, the output has a small root mean square component referred to as "instrument noise" broadening. Finally, deterioration in the quality of signals obtained with a rotating grating as compared to, for example, a beam splitter, stem mainly from imperfections in the manufacturing process (bleaching) and inherent vibrations caused by its rotation.

The various sources of broadening are summarised in Table 2.5, together with formulae for their magnitude and estimates of the contribution in the flows of this chapter.

Measurement errors

Apart from the above described sources, errors arise in the evaluation of the mean velocity and turbulence intensity in relation to the accuracy of the voltage output of the tracker (which affects the mean voltage) and through the averaging of voltages corresponding to Doppler frequencies (voltage output of mean and RMS meter). The accuracy (systematic error) of the voltage output of the tracker is quoted by the manufacturer as 1% of full scale deflection and this error is removed by calibration to the level of the random error in the measurement of the mean velocity. The systematic error originates as an offset in the calibration curve of the tracker output. The voltage output of the tracker is:

$$\widetilde{V}_1 = (\widetilde{f}_V + f_s)\, G_T + V_o \qquad (2.10)$$

where:

$\widetilde{V}_1$ is the tracker voltage output
G_T is the transfer function
V_o is the offset voltage giving rise to systematic errors.

If the direction of the frequency shift is reversed then, assuming $f_s > \widetilde{f}_V$:

$$\widetilde{V}_2 = (f_s - \widetilde{f}_V)\, G_T + V_o \qquad (2.11)$$

Hence:

$$V_o = \frac{\widetilde{V}_1 + \widetilde{V}_2}{2} + G_T . f_s \qquad (2.12)$$

and thus the systematic error is reduced to the precision (random error) of measuring $\widetilde{V}_1$ and $\widetilde{V}_2$ (Taylor, 1981). This has been included in the systematic error for $\overline{U}$, $\overline{V}$, $\overline{W}$ quoted in Table 2.6. Random errors in the true integrator output are ±1% of the mean voltage measured. Random errors in the output of the r.m.s unit are 1% of full scale deflection corresponding to a maximum of 3% for the smallest value measured in any one range.

TABLE 2.5
SOURCES AND MAGNITUDE OF NON TURBULENT DOPPLER BROADENING

SOURCE	FORMULA	MAGNITUDE
Gradient of mean velocity (effect on mean)	$\frac{1}{2}\left(\frac{b_y}{4}\right)^2\left(\frac{\partial^2 U}{\partial r^2}\right)$ Melling (1975)	$\simeq 10^{-4}\, U_b$
Gradient of mean velocity (effect on variance)	$\frac{1}{2}\left(\frac{b_y}{4}\right)^2\left(\frac{\partial U}{\partial r}\right)^2$ Melling (1975)	$\simeq 4 \times 10^{-3}\, U_b^2$
Finite transit time (effect on variance)	$\left\{\frac{U/2\pi}{2(b_x/4)}\,\frac{\lambda}{2\sin\theta}\right\}^2$ George and Lumley (1973)	$\simeq 5 \times 10^{-5}\, U_b^2$
Tracker instrument noise (effect on variance)	from direct measurement Durao and Whitelaw (1974)	$(1.2\times10^{-2})^2$ $(m^2\ s^{-2})$
Grating jitter (short term stability, see Table 2.2) (effect on variance)	$\left\{\delta\Omega\, f_s\, \frac{\lambda}{2\sin\theta}\right\}^2$ Manufacturer's specification	. . . $(1.2\times10^{-2})^2$ $(m^2\ s^{-2})$

TABLE 2.6
SYSTEMATIC AND RANDOM ERRORS IN MEASURED QUANTITIES

QUANTITY	SYSTEMATIC ERROR	RANDOM ERROR
$\bar{U}$, $\bar{V}$, $\bar{W}$	up to 0.04 U_b	± 1%
$\frac{\sqrt{\overline{u^2}}}{U_b}$, $\frac{\sqrt{\overline{v^2}}}{U_b}$, $\frac{\sqrt{\overline{w^2}}}{U_b}$	$\angle$ 0.003	± 1% to ± 3%
$\frac{k}{U_b^2}$	$\angle$ 0.006	± 3% to ± 8%
x	0.4 mm	± 0.02 mm
r	0.3 mm	± 0.03 mm

Detailed analysis of the errors involved in the instrumentation as used in the present work are given by Melling (1975). Table 2.6 summarises the estimates of accuracy (systematic error) and precision (random error) associated with the measurements presented in the present chapter.

2.3 Results

This section describes the flow visualization studies and the experimental results for each of the operating conditions described in Table 2.1. Radial profiles of mean velocity and turbulence intensity are presented for the two swirlers and the range of flow splits between swirler, primary and dilution holes. Contours of the mean axial velocity and turbulence intensity at the exit from the nozzle are also provided.

2.3.1 Flow visualization studies

A qualitative picture of the flow field, for the various swirler mass flow rates was obtained using flow visualization via hydrogen bubbles produced from a 1 mm stainless steel wire inserted through tappings in the larger containing tube and entering the combustor through the primary or dilution holes. A vertical sheet of light 2 mm thick was produced from a light source and photographs of the bubble streaklines were taken with shutter speeds ranging from $^1/_{60}$ to $^1/_4$ sec. The film rated at ASA 400 was then overdeveloped. In addition, flow patterns were investigated with dye injected through a small hole in the perspex plug which blocked off the hub of the swirler.

These investigations revealed that very different flow patterns could be created inside the combustor with variation in the level of swirler flow. For cases 1 and 2, a stable and symmetric toroidal vortex was identified upstream of the axis of the primary ports (Figure 2.10a). The entry angle of the primary jets was close to 90^o and their contribution to the upstream recirculation can be clearly seen. Although the trajectory of the dilution jets is less steep than that of the primary jets, they are still able to create a small but weak recirculation on the can centre line as depicted by the few hydrogen bubbles found upstream of the wire, in Figure 2.10b. Dye injected at low forward velocity via a 1.5 mm hole on the combustor centre line in the swirler hub confirmed in case 2 the strong backflow by being rapidly dispersed and mixed throughout the primary zone (Figure 2.10c). This pattern is highly desirable in combustion chambers as it ensures rapid mixing of the injected fuel with primary zone fluid.

The general flow patterns for 15%, 20% and 25% swirler flow levels, as deduced from the flow visualization, are shown schematically in Figure 2.11. As the swirler mass flow rate increased, the dominance of the primary vortex was reduced, giving rise to a double vortex structure as depicted in Figure 2.11c. Vortex B is mainly the result of the flow separation caused by the swirler hub and is influenced by the strong swirl and the downstream flow pattern. Although the primary jets do not penetrate fully along their geometric axis (as in cases 1, 2), the low pressure in the primary zone causes strong curvature of the local streamlines with the result that some of the jet fluid travels upstream in this region. Part of this fluid contributes to the formation of Vortex A (Figure 2.11c) while the rest exits from the primary zone through the region near the centre line. Due to the higher swirl momentum in this case, the primary jets are aslo deflected circumferentially so that primary jet fluid can mix in the upstream and downstream direction on planes other than its entry plane. At this swirler flow level, a precessing motion could be identified on the combustor centre line but this was suppressed downstream of the dilution holes.

At even higher swirler flow rates, case 6, a filament of fluid exists in the vicinity of the combustor axis which hardly mixes with the surrounding flow as the dye picture in Figure 2.10d indicates. This filament is obviously related to the existence of a precessing vortex core on the can centre line. Such a feature has been observed previously (eg Rhode et al, 1983); the present flow seems to be slightly different however in that the vortex core appears without the flow first undergoing large scale vortex breakdown as was the case for instance in the measurements of Rhode et al. Flow visualization studies at this level of swirler flow rate with the primary jet holes completely blocked off, revealed the existence of a large recirculation region downstream of the swirler and no evidence of a forward flow in the vicinity of the centre line within the primary zone as indicated above. Apparently, the interaction between swirler fluid and primary jet fluid influences the nature of the vortex breakdown considerably. As Figure 2.10d shows, the vortex core in this case emanates from within the primary zone;

this flow pattern would have an adverse effect on the distribution of fuel in this region and should be clearly avoided in gas turbine combustor design.

Investigations of the same type carried out for swirler 2 showed similar results. However, flow patterns obtained with the first swirler at a certain flow rate could be reproduced with the second swirler at a lower flow. This can be related to the fact that the second swirler due to its higher swirl number and decreased area imparts higher axial and azimuthal momentum to the incoming flow. Comparison of the performance of the two swirlers on the basis of swirler/primary jets momentum ratio rather than mass flow ratio (Table 2.1) readily explains the above behaviour.

The above description of the observed flow fields will now be quantified using the measured velocity data which are presented in the next two sections for the various operating conditions.

2.3.2 The flow patterns upstream of the combustor and in the annulus

Axial velocity and turbulence intensity data were obtained at $x/D_C = -0.74$ (D_C = internal combustor diameter) upstream of the model and are depicted in Figure 2.12 for case 2; these are representative of all operating conditions because they did not change qualitatively with variation in the swirler flow rate. Axisymmetric profiles with flat velocity distributions and low turbulence levels were measured in the annulus supply tube. Inside the separate feed for the swirler, the velocity profiles were significantly peakier, this being caused by the upstream effect of the swirler, the lower pressure near the centre line causing the fluid to accelerate in this region of the supply pipe. (Note that the radial co-ordinate in the figures of this and all subsequent sections has been non-dimensionalised using the inside diameter of the larger containing tube (D = 160 mm) and the velocity used for non-dimensionalization is the bulk velocity for the particular case under consideration.)

The behaviour of the flow in the annulus itself is of direct relevance in practical cases since the local static pressure distribution determines the proportions of mass flow through the ports. In addition, flow patterns in the vicinity of the ports are important in identifying local regions of low velocity with implications for wall heat transfer and formation of high temperature spots.

Radial profiles of the axial velocity and turbulence intensity in the annulus are presented in Figure 2.13 for case 2 and $\theta = 0^{\circ}$ (in line with primary holes), 15° and 30° (mid-way between primary holes). Examination of the annulus flow development in these three planes indicates that three-dimensionalities occur mainly in the immediate vicinity of the primary and dilution ports (planes c, d, e and j, k). Local acceleration of the flow is evident at stations c($\theta = 0^{\circ}$) and k($\theta = 0^{\circ}, 30^{\circ}$) upstream of the entry to the ports, while a low velocity region is formed downstream of the primary holes (station e, $\theta=0^{\circ}$). As the flow develops dowstream, transfer of momentum from other θ planes compensates for this low velocity region so that an axisymmetric velocity distribution is found at plane g (about 2.5 hole diameters away from the axis of the holes). Half-way between the ports, the developed axial velocity profiles show a bias in the location of the maximum velocity towards the combustor wall which is consistent with turbulent annular flows (Brighton and Jones, 1964). In this middle region of the annular passage where the flow was axisymmetric and uniform, the axial velocity profile at plane h was integrated to obtain the mass flow split between primary and dilution holes and the calculated values are included in Table 2.1. As shown in Figure 2.13, the turbulence levels in the annular flow were low and of the same magnitude as in the upstream section.

Measurements obtained for other swirler flow levels showed that the changes in the flow pattern inside the combustor (discussed in the next section) with variation in the swirler flow rate, exerted only a small influence on the annulus flow in the immediate vicinity of the ports. The change in the flow split between primary and dilution holes (as indicated by the values quoted in Table 2.1) is related to the change in the flow conditions at the hole as a result of the above effect. In general, the above depicted flow behaviour in the annulus is considered to be representative of all operating conditions.

2.3.3 Model combustor flow fields

The velocity and turbulence fields for the various operating conditions and for the two swirlers will now be described in terms of profiles along a diameter at the successive axial measuring locations defined in Figure 2.9.

Swirler 1

Case 1 ($\dot{m}_{sw}$ = 10%, $\dot{m}_{pr}$ = 34.84%, $\dot{m}_d$ = 55.16%, $\dot{m}_{sw}/\dot{m}_{pr}$ = 0.28)

Figure 2.14a shows radial profiles of the axial velocity and turbulence intensity for case 1. Within the primary zone, planes b, c, a backflow region is formed by the combined action of the swirl and the primary jets. The length of this recirculation deduced from axial velocity measurements on the combustor centre line agreed well with the flow visualization discussed above. At plane d, through the geometric axis of the primary holes, the still negative velocity on the combustor axis indicates the contribution of the jets in the upstream vortex. The centre line velocity increases rapidly up to plane f as the jets merge and travel downstream. A local recirculation region is formed at this plane near the combustor wall as the main flow is entrained into the low pressure region behind the jets. The shallower trajectory of the dilution jets is evident from the off centre line peaks in the axial profiles at planes l and m. The shallow penetration is due to the lower velocity ratio (jet/cross-flow) for the dilution jets as compared to the primary jets (see Table 2.1). The blockage associated with this penetration is still sufficient to create a small recirculation near the centre line (also identified in the flow visualization).

Swirl velocities, Figure 2.14b, within the toroidal vortex are low compared to those downstream. The maximum W location changes position from the middle of the can radius at station b progressively moving towards the axis at planes c and d as the inflowing jets carry some swirling fluid towards smaller radii. The deep penetration of the primary jets and the associated blockage effect force the majority of the swirling fluid to exit from the primary zone at planes other than those containing jets and away from the impingement point. As this fluid passes downstream, it is also entrained into the low pressure regions behind the jets leading to a swirl profile shape as seen on plane f. The profile shape then remains close to solid body rotation with slowly decaying levels of maximum swirl velocity until the shallow entry of the dilution jets again forces swirling fluid towards the centre line. This movement to smaller radii is one reason for the enhancement of the W component as illustrated in Figure 2.14b, plane l. Another reason contributing to this increase is the slight non-cyclic behaviour of the dilution jets which is depicted in the axial velocity profile at the same station. These deviations from the cyclic pattern are thought to be related to annulus flow disturbance caused by the presence of a *recirculation zone in the annulus downstream* of the holes due to the blocked off area at the rear retaining flange. The presence of this recirculation in combination with the low velocities in the annulus has been found to lead to unsteady annulus flow with random circulations about both the can axis and the axis of the hole (Gradon and Miller, 1968; Lefebvre, 1983). Although in actual production chambers this problem is usually remedied by the use of splitters across the dilution hole and flow bleed downstream in the annulus, in the present model this would have rendered a large part of the dilution zone region inaccessible to the laser beams. Since the mode of measurement of the W component is to traverse along a diameter of the combustor, it is expected that if this plane does not coincide with the plane on which $\partial V/\partial r = 0$ then large W components may be measured.

Radial velocity profiles are depicted in Figure 2.14c. The dominance of the primary jets in the formation of the primary vortex is evident from the presence of the strong inward V velocities, typically 1.5 times the maximum axial velocity, over most of the diameter at plane d. These high V velocities disappear rapidly upstream (plane c) and *downstream* (planes f, h) of the entry plane, so that large pressure gradients and strong curvature of the local "streamlines" can be expected. Radial velocities in the dilution jets ($x/D_c = 1.70$) do not disappear as quickly in the axial direction ($x/D_c = 1.87$) as would be expected from their less steep trajectory.

Nearly uniform levels of axial turbulence intensity (Figure 2.14a) are found within the recirculation region while at plane d large axial gradients and the impingement of opposing jets gives rise to higher values on the centre line. The maximum value of the RMS of the swirl component was measured in this position and is twice that of the axial turbulence intensity, indicating the strong anistropy of turbulence in this region (this will be further discussed in subsection 2.4.1). The radial turbulence intensities (Figure 2.14c) exhibit similar behaviour to the azimuthal ones with similar centre line values and rates of decay except at the entry plane of the dilution jets.

Case 2 ($\dot{m}_{sw}$ = 15%, $\dot{m}_{pr}$ = 32.90%, $\dot{m}_d$ = 52.10%, $\dot{m}_{sw}/\dot{m}_{pr}$ = 0.456)

More detailed measurements were obtained for this case over the whole internal flow field at 0°, 15°, 30° and 60° in order to investigate the extent of the expected cyclic behaviour of the flow. As mentioned earlier, flow patterns in the combustor are expected to repeat for every 60° sector (up to the position whereby the nozzle will distort this behaviour). This is further discussed at the end of this presentation in the light of the experimental results.

The main features of the flow patterns for this case, illustrated in Figure 2.15, are very similar to those found in the previous case. The toroidal vortex found previously is again sustained in the primary zone by the still impinging primary jets (Figure 2.15a; planes a, b, c, d). However, due to the higher axial and azimuthal momentum of the swirler flow, the strength of impingement has been reduced as is evident from a decrease in the maximum negative axial velocity by about 20%. The persistence of very low swirl velocities in the vicinity of the primary ports (Figure 2.15b) underlines the dominance of jet fluid. Although in case 1 these low values were found in the region $0.16<2r/D<0.5$ now they extend over a radial distance of only $0.3<2r/D<0.5$, implying a somewhat shallower penetration. The jets, however, still produce an effective blockage so that the swirl velocity profile downstream is similar to that obtained in the lower swirler flow rate (solid body rotation). A similar type of swirl velocity profile has been measured by Altgeld et al (1983) in their investigation of a swirl stabilised model combustor.

Compared with the rapid changes occurring near the impingement point, the flow develops relatively slowly in the intermediate zone (x/D_c = 0.82 - 1.50) as radial transfer of momentum compensates for the low axial velocities in the near wall regions; velocity gradients, however, are still high since the centre line axial velocity has halved between stations g and k, a distance of only 0.5 D_c. In the dilution zone, the double S shape of the axial velocity profile at plane m is typical of that measured in several rows of jets in cross-flow experiments (eg Khan et al, 1981). The levels of anisotropy in the turbulence field at the plane of the primary jet entry and the subsequent development of the three turbulence intensities are similar to that of the previous case.

Figures 2.16 and 2.17 present, in a similar format, the velocity and turbulence fields at the 15^o and 30^o planes respectively. Examination of the profiles of the three velocity components in these planes reveals axisymmetric behaviour of the flow well within the primary zone (x/D_c = 0.13 - 0.27) and in the intermediate zone (x/D_c = 0.95 - 1.50). Three-dimensionalities start to intrude only in the vicinity of the primary and dilution ports. This is clearly depicted in the very different distributions of the radial velocity between 0^o, 15^o and 30^o planes at station d and between 0^o and 15^o planes at station l. Due to the impingement of the primary jets, primary zone fluid can only exit from this region through the $15^o$and 30^o planes, resulting in the local acceleration of the flow in the near wall region at planes c, d and f, illustrated in Figures 2.16a and 2.17a. This is accompanied by an increase in the swirl velocities near the wall (Figure 2.17b; plane d) leading progressively to the solid body rotation type of profile. Deviations from axisymmetry are less evident in the turbulence field, apart from differences exhibited in the distributions of the three intensities at the entry planes of the jets.

The extensive measurements obtained for the present case confirmed cyclic behaviour of the flow over a 60^o sector up to plane l, where noticeable deviations occur. This is unlikely to be caused by the nozzle (which ultimately destroys the cyclic behaviour) as good repeatability is observed again at plane m. One possible cause is the asymmetric behaviour of the dilution jets previously discussed. Further examination of the upstream effect of the nozzle will be undertaken with the help of the theoretical approach in Chapter V.

Case 3 ($\dot{m}_{sw}$ = 20%, $\dot{m}_{pr}$ = 30.30%, $\dot{m}_d$ = 49.70%, $\dot{m}_{sw}/\dot{m}_{pr}$ =0.660)

Radial profiles of the three velocity components and their turbulence intensities for the 20% swirler flow case are shown in Figure 2.18. At this level of flow split between swirler and ports, significant changes have started to appear, especially in the primary zone. It should be noted that although the change in swirler flow represents only a 5% increase in terms of the bulk flow, it constitutes a much higher increase in terms of swirler/primary jets mass flow ratio (Table 2.1). The maximum axial negative velocity at station b (Figure 2.18a) now occurs near the middle of the radius, while on the centre line the value is only $-0.1\ U_b$ as compared to $-1.5\ U_b$ in case 2. (Since bulk velocities between consecutive swirler flow levels are different by only 5%, comparisons on the basis of nondimensional quantities between such cases is valid.) Although at the lower swirler flow rates of 10% and 15% the backflow was clearly influenced strongly by the upstream contribution of the jets, this contribution seems now to be restricted to the near entry region, as indicated by the higher negative axial velocities found at planes c and d. The associated shallower trajectory of the primary jets is depicted in the radial velocity distributions in Figure 2.18c. At plane d, the radial gradient of the V component has been reduced by about 25% (over that of the previous case) while at $x/D_c = 0.48$, positive V velocities were measured over the whole radius. This lack of impingement leads to shapes of axial velocity profiles with off centre line peaks (Figure 2.18a, planes c and f). The absence of these peaks, however, at $x/D_c = 1.09$ indicates that the primary jet fluid finally did penetrate to the axis of the combustor but at some distance within the intermediate zone ($x/D_c \simeq 1.0$). Maximum positive axial velocities are now of order U_b as compared to $2\ U_b$ in case 2.

Swirl velocities within the primary zone (Figure 2.18b, planes b, c) show overall an increase but follow trends similar to those found in the lower swirler flow cases. At plane d, the insufficient penetration of the primary jets allows swirling fluid to exit from the primary zone region in the vicinity of the centre line, resulting in the azimuthal velocity distribution seen at plane f. The swirl peak near the centre line, however, is quickly destroyed by the continuing off axis penetration of the primary jets, eventually giving rise to the familiar solid body rotation type of profile at plane h. In the dilution zone, the absence of the small backflow found in the lower swirler flow rates at $x/D_c = 1.70$ is the result of the further increase in the cross-flow now being able to completely deflect the dilution jets. In all other aspects, the flow distribution in this region has been little affected by the primary zone flow changes.

The above described mean flow variations influence the turbulence field in a consistent manner. In the primary zone, due to the weaker impingement of the jets, all three turbulence intensities have been reduced, the greater effect being on the azimuthal and radial components: $\sqrt{\overline{w^2}}$ and $\sqrt{\overline{v^2}}$ still have their maxima on the combustor axis at planes c, d and f but their magnitude is now significantly reduced; for example, at plane d their centre line value is only 1.1 U_b, representing a reduction of 40% over the levels of the previous case. In the dilution zone, the absence of the small recirculation has led to a decrease in the turbulence kinetic energy production on the centre line. Turbulence is now generated primarily in the shear layers between the bulk flow and the incoming jets.

Case 4 ($\dot{m}_{sw}$ = 25%, $\dot{m}_{pr}$ = 28.40%, $\dot{m}_d$ = 46.60%, $\dot{m}_{sw}/\dot{m}_{pr}$ = 0.88)

The flow development for the 25% swirler flow level is presented in Figure 2.19. Examination of the axial velocity profiles in Figure 2.19a shows a further decrease in the levels of the primary zone negative axial velocities, confirming the trend underlined in the previous case. The maximum negative axial velocity in this region has now moved from plane c (where it was found in case 3) to plane d and is only −0.5 U_b, representing a reduction of 50% compared with case 3. In addition, a low positive axial velocity has now emerged on the can centre line at station b (as observed in the flow visualization) progressively increasing at station c and leading to a value of 0.25 U_b at plane d (as opposed to a value of − U_b found in this position in case 3). The presence of vortex B, as observed in the flow visualization, is not evident from the axial velocity field distribution because measurements very near the swirler hub were not obtained, due to beam interference with the curved walls. The decreasing trajectory of the primary jets is illustrated in the profiles of the radial component in Figure 2.19c, where now at the jet entry plane zero V velocity fluid fills the central core up to 30% of the radius. Consequently, the primary jet fluid does not have the necessary momentum to reach the centre line throughout the whole length of the intermediate zone and eventually mixes with the bulk flow to produce a relatively flat profile at plane k. The radial distribution of the tangential velocity in the present case is of Rankine type (combined free-forced vortex; Beer and Chigier, 1972), as shown in Figure 2.19b (planes f to k) and this is now retained throughout the intermediate zone as a result of the complete lack of primary jet penetration. The distinct centre line peaks found in the distributions of all three turbulence intensities at planes h, k and l are related to the non-turbulent contribution (Bradshaw, 1976) as it is from the periodic rotation of the mean flow within the central processing core. These peaks, however, are reduced at station m as the processing core is disturbed by the strong mixing and the pressure effects of the dilution jets (see also subsection 2.3.1).

Case 5 ($\dot{m}_{sw}$ = 28%, $\dot{m}_{pr}$ = 27.26%, $\dot{m}_d$ = 44.74%, $\dot{m}_{sw}/\dot{m}_d$ = 1.026)
Case 6 ($\dot{m}_{sw}$ = 35%, $\dot{m}_{pr}$ = 24.63%, $\dot{m}_d$ = 40.37%, $\dot{m}_{sw}/\dot{m}_d$ = 1.416)

Figures 2.20 and 2.21 illustrate the flow distributions for the 28% and 35% swirler flow rates respectively. In both cases, the flow development is quicker than that of the 25% swirler flow level, as is shown by the rapid changes in the axial velocity distributions at planes f, h and k (Figures 2.20a, 2.21a). As the angular momentum of the flow eventually increases, the onset of a central precessing core shifts farther upstream so that at 35% swirler flow rate it emanates from within the primary zone. This is illustrated by the centre line maxima found in the mean and turbulent components of the axial and azimuthal velocities at planes c, d and f (Figure 2.21a).

In both cases, turbulence levels remain similar to those found at the 25% swirler flow case, apart from the centre line region which is influenced by the precessing core. The winged shape of the profile of the azimuthal turbulence intensity at plane d (Figure 2.21a, b) has also been found under isothermal and combusting conditions by Bicen and Jones (1985) in their investigation of a similar model combustor. In general, fewer measurements were obtained in the above swirler flow cases since they exceed swirler flow levels likely to be found in current practice.

Swirler 2

The performance of the second swirler will now be investigated under operating conditions similar to those of swirler 1. At this stage, it is useful to summarise the major differences between the two swirlers. These are:

(1) The larger number of vanes employed by swirler 2 (20 as compared to 18 of swirler 1). This, in effect, results in an increase in space/chord ratio (Figure 2.4a).

(2) The geometry of swirler 2 corresponds to a ratio of $D_{sw}/D_h = 1.5$, while that of swirler 1 corresponds to $D_{sw}/D_h = 2.6$. As a consequence, swirler 2 has a smaller outlet area by about 57%.

(3) The swirl number of swirler 2 (based on the geometry) is 0.85, while that of swirler 1 is 0.74.

Comparison of the axial and azimuthal velocity distributions within the primary zone between Figures 2.14 and 2.22 (depicting the flow fields obtained from each of the swirlers operating at 10% swirler flow rate) reveals that the higher axial and azimuthal momentum imparted to the swirler flow in case 7 has resulted in a decrease in the maximum negative axial velocity (by about 20%) and an increase in the swirl levels (by about 30%). As the swirler flow increases to 15%, the differences in swirler geometry influence the primary zone flow patterns significantly as comparison between Figure 2.15 (case 2) and Figure 2.23 (case 8) indicate. Swirler 2 has now incurred a reduction in the magnitude of the maximum negative axial velocity of about 50% (plane c) and has shifted its location away from the centre line, denoting the considerable lateral spread of the primary jets due to their shallow entry (Figure 2.23c, plane d). As a result of the different primary jet trajectories, the flow development at the initial stages of the intermediate zone is very different between cases 8 and 2 (compare axial and swirl velocity profiles at plane f) but thereafter efficient mixing and the effectiveness of the dilution jets result in very similar distributions at plane m. Similar variations are encountered in the flow patterns of case 9 (Figure 2.24). At this level of swirler flow, swirler 2 produces a positive velocity within the primary zone (Figure 2.24a, plane c) and encourages the onset of a central precessing core (Figure 2.24a, planes h, i), features which were obtained with swirler 1 at the higher swirler flow level of 25%. The similarities and differences between the flow patterns obtained with the two swirlers will be discussed in more detail in subsection 2.4.2.

Levels of turbulence generated in the primary zone under operation with swirler 2 are significantly reduced over those of swirler 1, as indicated by the reduction in $\sqrt{\overline{w^2}}$ and $\sqrt{\overline{v^2}}$ (plane d) by about 42% and 50% at swirler flow levels of 15% and 20% respectively.

Exit conditions

Since exit conditions from the combustor are important in engineering terms (they affect the performance of downstream components such as nozzle guide vanes and turbine blades), a complete mapping of the axial velocity and turbulence intensity fields was undertaken. Figure 2.25 shows contours of the axial velocity at the exit for swirler flows up to 25% including results from both swirlers, while Figure 2.26 depicts the corresponding axial turbulence intensity contours.

Figure 2.25 shows that non-uniformities in the axial velocity field spanning a factor of 2.2 remain for the lower swirler flow cases (1, 2, 3, 7 and 8) while this factor reduces to 1.9 for higher swirler flows. When the dilution jets penetrate sufficiently and mix rigorously with the bulk flow (low swirler flows), they lose their identity and do not contribute any individual features at the exit field (Figure 2.25, a, b, e, f). In contrast, the kidney-like shape of the contours in Figures 2.25c and 2.25d, similar to the well documented shape found in various jet in cross-flow investigations (Atkinson et al, 1980), is likely to be the result of some individual contribution from the dilution jets at the exit field. As the angular momentum of the flow in the can increases further, a minimum can be identified in the centre of the nozzle (Figure 2.25g). This is thought to be related to the central precessing vortex core which, although strongly accelerating inside the combustor, being detached and hardly mixing with the main flow, cannot follow the sudden acceleration of the bulk flow, due to the contraction of the nozzle, and retains its velocity. A similar minimum in the combustor exit axial velocity profiles has also been found in the isothermal study of a similar model by Bicen and Jones (1985). In general, the spanwise asymmetries which occur (the model geometry itself is symmetrical about a vertical plane through the nozzle centre) are caused by the swirling nature of the flow as it enters the nozzle.

The axial turbulence intensities at the exit, Figure 2.26, exhibit a spanwise variation of about 1.8 for all cases. Maximum levels are encountered near the centre of the nozzle with maximum local turbulence intensities $\sqrt{\overline{u^2}}/U_{local}$ of about 20% except in case 9 (Figure 2.26g), where the precession gives rise to values of the order of 40%.

2.4 Discussion

Several further aspects of the flow field are of interest in this study because of their importance to the design of combustion chambers; these include: the size and strength of large recirculation regions, interactions between jets and local recirculations, the influence of swirl on the development of the flow and the levels of turbulence that are generated. Further, the distribution of the mean and turbulence field at the chamber exit are important since they would influence the quality of the exit temperature traverse (pattern factor). The following three subsections discuss these aspects in more detail.

2.4.1 Influence of flow split between swirler and ports

It is evident from the descriptions of the flow patterns in subsection 2.3.3 that the most dramatic effect of the variation in the flow split between swirler, primary and dilution ports is on the flow distribution in the primary zone. (Although the total flow rate through the combustor was varied at the same time, this merely produces a change in the overall Reynolds number of the flow; this was, however, always sufficiently high ($5.4 - 6.7 \times 10^4$) to lie in a Reynolds number independent flow regime.) The effects can best be explained as the result of the variations in the trajectory, depth of penetration and strength of impingement of the primary jets, all of which are observed to be strongly dependent on the ratio of swirler to primary jets mass flow.

The different flow patterns obtained with the variation of the above ratio are summarised in Figure 2.27a, which combines the axial velocity profiles in the primary zone (planes c, d) for 15%, 20% and 25% swirler flow level and Figure 2.30a, which displays the centre line development of the axial velocity for swirler 1 and a variety of flow splits. As the swirler/primary jets mass flow ratio increases from 0.45 to 0.66 and then to 0.88, the location of the maximum negative velocity at station c (Figure 2.27a) moves from $2r/D = 0$ to $2r/D = 0.1$ and then to $2r/D = 0.26$ respectively. This is accompanied by a sharp decrease in its value from $2.34\ U_b$ (case 2) to $0.3\ U_b$ (Case 4), representing a reduction of about 85% in terms of absolute velocity. This change is in accord with a reduction in the primary jet trajectory, as illustrated by the steep decrease in the axial velocity gradient on the centre line at plane d in Figure 2.30a.

These variations are expected to influence significantly the primary zone recirculation ratio, a parameter important in describing the performance of primary zone configurations (Green, 1981). The magnitude of this parameter for recirculations induced solely by an opposed jet system may be estimated from empirical formulae proposed by Way (1956), Rosenthal (1959) and Verduzio and Campanaro (1971). However, accurate information is lacking on recirculation ratios for primary zones which utilize a combination of swirler and opposed jets (Lefebvre, 1983). In the present investigation, this quantity has been determined by integration of the negative part of the axial velocity profile at plane c:

$$\dot{m}_r = \int_0^{r_{u=0}} \rho U dA \qquad (2.13)$$

This station was chosen because of its proximity to the eye of the primary vortex (deduced from the flow visualization) so that the above integration yields, as close as possible, a maximum estimate of the recirculating fluid within the vortex. Figure 2.28 shows the variation in the recirculation ratio $\dot{m}_r/(\dot{m}_{sw} + \dot{m}_{pr})$ with increase in the swirler mass flow ratio $\dot{m}_{sw}/\dot{m}_{pr}$ for the range of flow splits (swirler 1). The curve indicates an almost linear decrease with increasing $\dot{m}_{sw}/\dot{m}_{pr}$ in the region $0.2<\dot{m}_{sw}/\dot{m}_{pr}<1.0$. At low levels of swirler flow ($\dot{m}_{sw}/\dot{m}_{pr}\approx 0.3$), up to 74% of the total ($\dot{m}_{sw}+ \dot{m}_{pr}$) participates in the toroidal vortex. Assuming that all of the swirler fluid in this case contributes to the recirculation, then the contribution of the primary jets amounts to about 64%. For this case (with jet trajectory near 90^o) empirical formulae would yield a value of 50% (Rosenthal, 1959). Consequently, one can estimate that the extra 15% is due to the influence of the swirler. At higher swirler flow ratios ($\dot{m}_{sw}/\dot{m}_{pr} > 1.0$), $\dot{m}_r/(\dot{m}_{sw} + \dot{m}_{pr})$ can be severely reduced to less than 10%.

The primary zone flow patterns discussed above have also been found by Bicen and Jones (1985) in their investigation of a geometrically similar chamber under combusting conditions. They provided LDA measurements of the axial and tangential mean velocities and turbulence intensities at planes through the ports. Their results with the combustor operating at flow splits similar to those of case 5 of the present investigation exhibited good qualitative and quantitative similarity with the results of the present work in the primary zone. This can be seen in Figure 2.29, taken from Bicen and Jones (1985), which depicts the axial velocity distribution along the primary jet axis under combusting conditions with gaseous propane fuel and at an air-fuel ratio of 70. It clearly shows that all qualitative features found in the similar profiles of the present study (see for example Figure 2.20a, plane d) are also identified under combusting conditions. It is likely then that the variations in the primary zone flow patterns observed here would influence combustor performance, since under reacting conditions parameters such as mean residence times, blow out velocity and heat release rates are directly related to the mean flow velocity and recirculation ratio.

The flow behaviour in the intermediate zone is also of interest in the design of combustion chambers. The near wall flow development and localized stagnation regions are critical in determining the location of wall cooling arrangements and additional trimmer holes for improved chamber durability (Lefebvre, 1983). The location of the small recirculation regions just downstream of the primary holes and the slow axial development of the flow near the combustor wall in the intermediate zone in cases 1 and 2 coincides with the location of hot spots identified in an experimental production chamber reported by Bhangu et al (1983). The rate of flow development and the maximum axial and angular velocities in this region are a measure of the mixing which is essential for the complete destruction of any hot streaks remaining in the primary zone efflux. Inspection of the profiles at station k (Figures 2.14 to 2.24) indicates that deviations from a uniformly flat distribution are a minimum at this plane in all cases. This, in the lower swirler flows, can be attributed partly to the swirl (in the intermediate zone) and primarily to the deep penetration of the dilution jets while at the higher swirler flows, it is the strongly swirling flow field that leads to rapid development at the early stages of the intermediate zone. In either case, the primary zone flow variations have a smaller effect on the dilution zone profiles as illustrated in Figure 2.27a (planes l, m) with the result that the velocity profile at plane m is quite similar under all conditions.

The central processing core identified near the centre line for swirler flows higher than 25% (swirler 1) has also been found by other workers under isothermal and combusting conditions (Syred and Beer, 1974; Bicen and Jones, 1985). Its occurrence can be related to the stability of the swirling flow field according to the radial distribution of the angular momentum (Gupta et al, 1984). The Rayleigh criterion states that a swirling flow is stable if W.r increases with r and unstable if W.r decreases with r. At low swirler flows (cases 1, 2, 3), the former is true and no precession was identified. At 28% and 35%

swirler flow levels, however, the Rankine vortex type of distribution of the angular momentum implies that most of the profile is unstable and in these cases a precessing vortex core was observed.

The levels of turbulence generated throughout the combustor are important since they affect the entrainment rates in the primary zone, the penetration of the jets and the mixing rates in the dilution zone. Under combusting conditions, they influence the stability limits, combustion efficiency and ignition performance (Lefebvre, 1983). Turbulence kinetic energy profiles evaluated from the three individual turbulence intensities are depicted in Figure 2.31 for various operating conditions. At the lower swirler flows (cases 1 and 2), the turbulence fields are very similar with maximum turbulence production occurring in the primary jet impingement position (Figure 2.31a, b; planes c, d, f). The very high values of turbulence kinetic energy at this position are related to the large values of $\sqrt{\overline{w^2}}$ and $\sqrt{\overline{v^2}}$. The anisotropy of the turbulence field at the region of impingement (where $\sqrt{\overline{w^2}}$, $\sqrt{\overline{v^2}} \simeq 2.5\sqrt{\overline{u^2}}$) can be explained by examination of the exact equations for the transport of the individual normal stresses (Rodi, 1970; Bradshaw, 1976) and, in particular, those terms which express the generation of each component. For a three-dimensional flow, these read:

$$P(\overline{u^2}) = -2\left\{\underline{\overline{u^2}\frac{\partial U}{\partial x}} + \overline{uv}\frac{\partial U}{\partial r} + \overline{uw}\frac{\partial U}{r\partial\theta}\right\}$$

$$P(\overline{v^2}) = -2\left\{\overline{uv}\frac{\partial V}{\partial x} + \underline{\overline{v^2}\frac{\partial V}{\partial r}} + \overline{vw}\frac{\partial V}{r\partial\theta}\right\} + 2\frac{V}{r}\overline{vw} \qquad (2.14)$$

$$P(\overline{w^2}) = -2\left\{\underline{-\frac{V}{r}\overline{w^2}} + \overline{uw}\frac{\partial W}{\partial x} + \overline{vw}\frac{\partial W}{\partial r} + \overline{w^2}\frac{\partial W}{r\partial\theta}\right\}$$

At the impingement position both $\partial U/\partial x$ and $\partial V/\partial r$ are very large. The production term for $\overline{u^2}$ on the centre line is $-2\,\overline{u^2}\,\partial U/\partial x$ (only the underlined terms are non zero on the axis) which is a sink while the counterpart production terms for $\overline{v^2}$ and $\overline{w^2}$ are $\overline{v^2}\,\partial U/\partial x$ and $\overline{w^2}\,\partial U/\partial x$ ($\partial U/\partial x = -2\partial V/\partial r$ on the axis) which have large positive values (sources). The high anisotropy observed in this position can thus be interpreted as the result of relatively large values of $P(\overline{u^2})$ and $P(\overline{w^2})$ (or $P(\overline{v^2})$) with opposite signs. The absence of large convective transport near the impingement position is important in allowing the production terms to dominate, giving rise to centre line maxima of $\overline{u^2}$, $\overline{v^2}$, $\overline{w^2}$ and k. Similar behaviour of the three normal stresses has been observed by Taylor and Whitelaw (1984) at the rear stagnation point of recirculation regions behind bluff bodies. At higher swirler flows $\partial U/\partial x$ (and hence $\partial V/\partial r$) are smaller near the centre line (Figure 2.30a). The radial position of the maxima of the three normal stresses now lies in the region of large $\partial U/\partial r$ and $\partial U/r\partial \theta$ (Figure 2.19a, b, c, plane d). Production of turbulence now occurs predominantly in the curved shear layers through shear stress ~ shear strain interaction and this gives rise to maximum values of turbulence kinetic energy away from the centre line (Figure 2.31d, e; plane d). This, however, shoud not be taken to imply that the entire production of turbulence occurs due to shear since the maximum values of $\sqrt{\overline{v^2}}$ and $\sqrt{\overline{w^2}}$ are still related to relatively high values of $\partial V/\partial r$ away from the axis of the can (Figure 2.19c; plane d). The variation in the turbulence kinetic energy field, portrayed in Figure 2.27b which gathers the turbulence kinetic energy profiles for 15%, 20% and 25% swirler flows and in Figure 2.30b which displays the centre line development are in agreement with the arguments of the above paragraph.

Since the dominant production of turbulence, for the lower swirler flows, in the impingement region is mainly by normal stress ~ normal strain interaction calculation of these flows using the k-ϵ turbulence model may be inaccurate (at least for the turbulence in this region) because scalar effective viscosity models do not adequately represent normal stresses. On the other hand, according to the above arguments, this deficiency should be less severe in the calculation of the higher swirler flows.

2.4.2 Influence of swirler geometry

The variations in the flow distributions obtained by the two swirlers accrue mainly from the differences in geometry which were summarised in subsection 2.3.3. The effect of the swirler geometry on the flow patterns is depicted in Figure 2.32a, b which combines the axial velocity and turbulence kinetic energy profiles in the primary (planes c, d) and dilution (planes l, m) zones for 15% swirler flow rate. As a result of its smaller outlet area and higher swirl number (implying higher axial and azimuthal momentum imparted to the swirler flow), swirler 2 reduces the primary jet trajectory and the strength of the primary vortex. In accord with the weaker impingement, levels of turbulence in the primary zone are also reduced (Figure 2.32b, planes c, d). As discussed in subsection 2.4.1, due to effective mixing in the intermediate and dilution zones, dilution zone flow patterns are less affected by the primary zone variations (Figure 2.32a, b, plane l, m).

The performance of the primary zone operating with each of the swirlers can be examined by comparing the recirculation ratios produced in each case. Figure 2.33 (displaying the recirculation ratios for swirler 1 and 2 plotted together) shows that for $\dot{m}_{sw}/\dot{m}_{pr}$ less than 0.55 swirler 1 produces higher levels of $\dot{m}_r/(\dot{m}_{sw}+\dot{m}_{pr})$ by about 8% while for $\dot{m}_{sw}/\dot{m}_{pr} > 0.55$ both swirlers yield similar values. This can be explained as follows: At low swirler flows, the main contribution to this ratio is made by the primary jets. As swirler 2 produces a flow with higher axial momentum, it is able to counteract strongly the upstream contribution of the jets. When the swirler flow rate increases, the swirling flow plays a more dominant role in the primary zone flow pattern. Since the second swirler possesses a greater entraining capability than swirler 1 (due to the higher swirl number, larger number of vanes, higher vane aspect ratio and space/chord ratio (Kilik, 1976)) it is expected to be able to balance the adverse influence of the axial momentum on the primary jet contribution. This is demonstrated in Figure 2.33b where the recirculation ratio is plotted against the swirler/primary jets momentum ratio. In this graph, which depicts an almost linear relationship between the recirculation ratio and the momentum ratio, the higher entrainment rates of swirler 2 at the higher swirler flow rates are clearly evident and confirm the above arguments.

Two interesting features can be mentioned with regard to the performance of the two swirlers. The first is that swirler 2 causes a greater variation on the flow patterns, over a smaller range of swirler flows, than swirler 1. This is clearly depicted by the centre line development of the axial velocity and turbulence intensity produced by swirler 2 (Figure 2.34a, b). Comparison between Figures 2.34 and 2.30 reveals that the level of variation on the centre line profiles of U and k obtained with swirler 2 by changing the input flow from 10% to 20% can only be obtained with the first swirler in position if its input flow is varied by 15% (eg from 10% to 25%). The second feature concerns the overall performance of swirler 2 and follows from the considerations of the above paragraph. It seems possible that flow patterns obtained with swirler 1 at a certain flow rate (eg 20%) can be "reproduced" with swirler 2 in position at a lower flow rate (eg 15%) for the range of measured flow splits. This is not so suprising if one relates these changes in flow split between swirler and primary ports to changes in input momentum. In Table 2.1, the ratio $\dot{m}_{sw}/\dot{m}_{pr}$ has been translated to a ratio of swirler to primary jets momentum. Inspection of these figures readily explains the above findings; for example, the momentum ratio for case 7 is very similar to case 3. It follows from the above discussion that in order to increase the entrainment rates of the primary zone recirculation in the present configuration it may be preferable, for stabler operation, to increase the vane outlet angle instead of decreasing the ratio D_{sw}/D_{hub}. In production chambers, however, the choice of swirler geometry is also affected by the requirements of the injection system.

2.4.3 Exit conditions

The presentation of the axial velocity distributions at the exit from the nozzle in subsection 2.3.3 showed that nonuniformities spanning a factor of 2 remained for almost all cases. In the lower swirler flows (10%, 15%), these arise mainly from the low velocities near the upper corners of the cross-section and the high velocities occurring in the lower surface of the nozzle (Figure 2.25 a, b, e, f). The former is related to the velocity deficit near the wall at station m (Figure 2.27a) and the locally expanding cross-section of the nozzle (local separation cannot be excluded and this is further discussed in Chapter V) while the latter is caused by the sudden cross-stream elevation of the geometry. At higher swirler flows (20%, 25%), the decreased trajectory of the dilution jets reduces the width of this low velocity region (Figure 2.27a; plane m) while the stronger swirl encourages mixing, resulting in a mild improvement as seen in Figures 2.25d, g. Comparison of the quantity $(U_{max}-U_{min})/U_b$ between station m and the exit can give an estimate of the effectiveness of the nozzle in suppressing any nonuniformities originating in the dilution zone. This has a value of 2 at plane m (for all cases) while at the exit its value is 1.5 at low swirler flows (cases 1, 2, 7, 8) and 1.1 at higher swirler flow rates (cases 3, 4, 9).

Turbulence intensities at this position are also of interest; damping of the fluctuations is achieved by promoting intense mixing in the dilution zone leading to a reduction of the turbulence intensities at the exit. Comparison of the maximum value of $\sqrt{\overline{u^2}}$ between the exit and plane m indicates that turbulence intensity levels at the exit have been reduced by about 45%.

2.5 Summary

This section provides a summary of the most important findings and conclusions of this chapter.

1. The primary zone flow distribution is strongly dependent on the flow split between swirler and primary ports. Variation of the swirler/primary jets mass flow ratio showed that:

   a) At low swirler flows ($\dot{m}_{sw}/\dot{m}_{pr} \leqslant 0.456$), a large and stable recirculation is formed within the primary zone with maximum attained negative axial velocities of order 2.5 U_b.

   b) At intermediate swirler flows ($\dot{m}_{sw}/\dot{m}_{pr} \approx 0.666$), the primary jet trajectory is decreased with subsequent weakening of the primary vortex. Maximum negative axial velocities are reduced to 1 U_b.

   c) As the swirler flow increases further ($\dot{m}_{sw}/\dot{m}_{pr} \geqslant 0.880$), the primary jets fail to penetrate to the centre line of the combustor. The primary zone is now occupied by a double vortex system with maximum negative axial velocities of 0.5 U_b.

   d) The decrease in swirler flow rate results in a steep reduction in the primary zone recirculation ratio $\dot{m}_r/(\dot{m}_{sw}+\dot{m}_{pr})$. The decrease is almost linear for $0.2<\dot{m}_{sw}/\dot{m}_{pr}<1.0$ (swirler 1).

   e) A precessing core is established on the centre line throughout most of the combustor length for $\dot{m}_{sw}/\dot{m}_{pr} \geqslant 1.026$ and its onset is closely related to the distribution of the angular momentum of the flow.

   f) Levels of turbulence kinetic energy production throughout the combustor are related to interactions between incoming jets and the mainstream flow. Highest turbulence levels were generated in the primary zone under conditions of strong impingement of the primary jets and were of order 3.5 U^2_b ($\dot{m}_{sw}/\dot{m}_{pr} \leqslant 0.456$) while at higher swirler flows ($\dot{m}_{sw}/\dot{m}_{pr} \geqslant 0.880$) these were reduced to 1 U^2_b. Examination of the Reynolds stress transport equations showed that different terms dominate the equations in each case.

2. The influence of swirler geometry on the primary zone flow pattern was examined by comparison of the flow fields obtained with each of the two swirlers used. The investigation showed that:

   a) Swirler 2 (possessing a smaller outlet area and higher swirl number as compared to swirler 1) weakened the primary zone recirculation, incurring reductions in the maximum negative axial velocity of about 20% at 10% swirler flow rate, and 40% at 15% and 20% swirler flows. Maximum levels of turbulence kinetic energy were also reduced by about 50% and 20%, for swirler flow rates of 15% and 25% respectively.

   b) In general, swirler 2 produced a greater variation in the primary zone flow, over a smaller range of changes in the input flow, than swirler 1.

3. The severe changes in the primary zone are reflected in the flow development at the initial stages of the intermediate zone but efficient mixing throughout the rest of the intermediate zone and the interaction between the dilution jets and the bulk flow results in a smaller effect on the profiles of the dilution zone.

4. Nonuniformities in the axial velocity profiles at the exit span a factor of two for all cases. Maximum turbulence intensities at this position were of the order 0.5 U_b, representing a reduction of about 50% over those emerging from the dilution region.

5. As discussed in subsection 2.4.1, the flow fields obtained in the present investigations are representative of the reacting flow in similar geometries, at least in the primary zone. Consequently, under combusting conditions, the primary zone flow variations may influence combustor performance through their effect on air-fuel ratio, mixing rates and heat release rates. Although, in general, these changes were not readily apparent on the dilution zone and exit flow patterns, it should be noted that features of operation under combustion, such as emission of pollutants, are related to the history of the flow at exit from the primary zone.

6. Since the flow splits used in this investigation are typical of those encountered in traditional and current combustor designs and the flow behaviour obtained is similar to that observed in rig testing of full-scale production chambers (Gradon and

Miller, 1968), the flow patterns obtained in the water model are representative of the aerodynamic behaviour of practical combustion systems. Although the above underlined trends can be found in similar can-type chambers (to be discussed in Chapter V), the absolute levels of swirler/primary jets mass flow ratio at which the described variations occur and the relative effect of the swirler flow rate on the flow pattern are also determined by the geometric configuration and may vary from one arrangement to the other. Finally, the comprehensive measurements presented here are suitable data against which the results of numerical calculation schemes may be compared. The ability to predict this isothermal flow accurately would represent a significant step in the appraisal of a real combustor prediction procedure.

CHAPTER III

THE CALCULATION PROCEDURE

3.1 Introduction

This chapter presents the details of the calculation methods used to obtain predictions presented in subsequent chapters. Section 3.2 describes the governing partial differential equations and the turbulence closure used. The appropriate boundary conditions and the procedure for the numerical integration of the above equations on a finite-difference grid are also described. Section 3.3 considers the application of the numerical procedure to the calculation of complex geometries and discusses three methods used in conjunction with the present work. In Section 3.4, the accuracy of the calculation methods is discussed in terms of the limitations imposed by the turbulence model, by the numerical techniques and by the approximations involved in the assumed boundary conditions.

3.2 Description of the equations

3.2.1 The governing equations

The general equations which describe the flow of an incompressible, constant property, Newtonian fluid, expressed in cartesian tensor form, are:

Mass conservation:

$$\frac{\partial U_i}{\partial x_i} = 0 \qquad (3.1)$$

Transport equations for momentum:

$$\frac{\partial U_i}{\partial t} + \frac{\partial}{\partial x_j}(U_i U_j) = -\frac{1}{\rho}\frac{\partial P}{\partial x_i} + \nu\frac{\partial^2 U_i}{\partial x_j \partial x_j} \qquad (3.2)$$

where U_i is, in general, a function of three space co-ordinates and time.

Although these instantaneous equations represent a closed set, the spatial and temporal resolution which would be required of the numerical integration for an accurate solution for a flow of engineering interest is far greater than currently available computer storage. This is because such flows possess characteristically very high Reynolds numbers, they therefore are generally turbulent. The number of mesh points which must be used to resolve all important length scales is of the order (Reynolds number)$^{3/4}$ in one direction (Tennekes and Lumley, 1972) and therefore high Reynolds number three-dimensional calculations are not possible. The standard approach is to decompose the dependent variables into mean and fluctuating components and to average the equations statistically. For constant density flows, a convenient decomposition and averaging may be represented by:

$$U_i = \overline{U_i} + u_i \qquad (3.3)$$

where

$$\overline{U_i} = \lim_{T \to \infty} \frac{1}{T} \int_{t_o}^{t_o + T} U_i dt$$

with

$$\overline{u_i} = 0$$

The equations 3.1 and 3.2 may then be re-written in averaged form to give (for steady mean flows):

$$\frac{\partial \bar{U}_i}{\partial x_i} = 0 \qquad (3.4)$$

$$\frac{\partial(\bar{U}_i \bar{U}_j)}{\partial x_j} = - \frac{1}{\rho} \frac{\partial \bar{P}}{\partial x_i} + \frac{\partial}{\partial x_j} \left(\nu \frac{\partial \bar{U}_i}{\partial x_j} - \overline{u_i u_j} \right) \qquad (3.5)$$

Due to the non-linearity of equations 3.1 and 3.2, the decomposition and averaging procedure produces a set of equations (Reynolds averaged equations) 3.4 and 3.5 that are no longer closed. The excess of unknowns over available equations is referred to as the closure problem and requires the determination of the Reynolds stress tensor $\overline{u_i u_j}$ via a turbulence model; this is dealt with in the next subsection.

3.2.2 The turbulence model

Exact transport equations for $\overline{u_i u_j}$ may be derived from the instantaneous equations, but contain correlations of even higher order (eg $\overline{u_i u_j u_k}$) which must be modelled if a closed set of equations is to be obtained. Much work has been invested in recent years (eg Launder et al (1975), Bradshaw (1976)) in attempting to formulate a suitable closure for the transport equations for the Reynolds stresses (second order closure). Since this work is still in progress and no clearly superior model has yet emerged and bearing in mind the computational expense involved in such a model (involving in three-dimensional flows the solution of six extra partial differential equations), only simpler levels of closure are considered appropriate at this stage for the kind of three-dimensional flows under consideration here.

A first order closure of equations 3.4 and 3.5, where transport equations for the $\overline{u_i u_j}$ are not directly solved, depends upon the introduction of an eddy viscosity concept (Boussinesq, 1877) where the Reynolds stress tensor is related to the mean rate of strain via:

$$-\overline{u_i u_j} = \nu_t \left(\frac{\partial \bar{U}_i}{\partial x_j} + \frac{\partial \bar{U}_j}{\partial x_i}\right) - \frac{2}{3} k \,\delta_{ij} \qquad (3.6)$$

where ν_t is a scalar eddy viscosity and δ_{ij} is the kronecker delta.

Various models have been suggested for describing ν_t (Gibson et al, 1984), but the one which offers (for the type of problem studied here) the best compromise of maximum realism and acceptable cost is the so-called two-equation level of closure. The best tested model at this level is the k-ϵ model which describes ν_t via the following set of equations:

$$\nu_t = C_\mu \frac{k^2}{\epsilon} \qquad (3.7)$$

$$\frac{\partial}{\partial x_i}(\bar{U}_i k) = \frac{\partial}{\partial x_i}\left(\frac{\nu_t}{\sigma_k}\frac{\partial k}{\partial x_i}\right) - \overline{u_i u_j}\frac{\partial \bar{U}_i}{\partial x_j} - \epsilon \qquad (3.8)$$

$$\frac{\partial}{\partial x_i}(\bar{U}_i \epsilon) = \frac{\partial}{\partial x_i}\left(\frac{\nu_t}{\sigma_\epsilon}\frac{\partial \epsilon}{\partial x_i}\right) - C_1 \frac{\epsilon}{k}\overline{u_i u_j}\frac{\partial \bar{U}_i}{\partial x_j} - C_2 \frac{\epsilon^2}{k} \qquad (3.9)$$

where k (= $\overline{u^2_i}/2$) is the turbulence kinetic energy and ϵ is its rate of dissipation. The above are modelled equations and therefore contain empirical constants whose value must be calibrated against experimental data. The full set of constants for equations 3.7 to 3.9 is given below and was obtained by optimisation of the model's performance against a range of two-dimensional shear flows (Launder and Spalding, 1974):

$$C_\mu = 0.09,\ C_1 = 1.44,\ C_2 = 1.92,\ \sigma_k = 1.0,\ \sigma_\epsilon = 1.3.$$

In what follows in this thesis, this version of the model and its constants will be used in unaltered form. Further information on the model and its derivation may be found in Bradshaw (1976) and Gibson et al (1984). The set of equations 3.4 to 3.9 now form a soluble set.

3.2.3 The finite-difference formulation

The numerical solution of the above partial differential equations is achieved by using a standard finite-difference method as has been described by Patankar (1980). The following subsection briefly outlines the derivation of the finite-difference equations and introduces the type of differencing used; a more detailed description may be found in Patankar (1980). The finite-difference forms of the partial differential equations governing the flow are derived with reference to a suitably discretised calculation domain which usually extends to the boundaries of the flow. The method of discretisation uses a staggered grid which involves pressure and scalar quantities being stored at nodes placed between the velocity storage locations. This facilitates the formulation of the finite-difference equations and helps to avoid spatially oscillatory pressure fields to which an unstaggered system is prone (Patankar, 1980). However, this necessitates the adoption of different control volumes for the velocities and pressure (see Figure 3.1).

The transport equations may be transformed into the general framework (after multiplying by the density):

$$\frac{\partial}{\partial x_j}(\rho \bar{U}_j \phi) = \frac{\partial}{\partial x_j}\left(\Gamma_\phi \frac{\partial \phi}{\partial x_j}\right) + S_\phi \qquad (3.10)$$

where ϕ can be 1, U, V, W, k or ϵ (overbars are now omitted and upper case letters indicate time-averaged quantities); $\Gamma_\phi = \rho \nu_t / \sigma_\phi$ is the appropriate diffusion coefficient and σ_ϕ is the appropriate turbulent Prantl number. S_ϕ represents all remaining terms as the "source" of property ϕ. For a general variable ϕ the finite-difference equation is derived by integration of equation 3.10 over a control volume; this is illustrated below in two-dimensional cartesian form:

$$\int_{vol} \left\{\frac{\partial(\rho U\phi)}{\partial x} + \frac{\partial(\rho V\phi)}{\partial y}\right\} dvol - \int_{vol} \left\{\frac{\partial}{\partial x}\left(\Gamma_\phi \frac{\partial \phi}{\partial x}\right) + \frac{\partial}{\partial y}\left(\Gamma_\phi \frac{\partial \phi}{\partial y}\right)\right\} dvol = \int_{vol} \{S_\phi\}\, dvol \qquad (3.11)$$

or, in finite-difference terms:

$$\begin{aligned} & A_e\, \dot{q}_e\, \{(1-F_e)\, \phi_E + F_e\, \phi_P\} - A_w\, \dot{q}_w\, \{F_w\, \phi_W + (1-F_w)\, \phi_P\} \\ & + A_n\, \dot{q}_n\, \{(1-F_n)\, \phi_N + F_n\, \phi_P\} - A_s\, \dot{q}_s\, \{F_s\, \phi_S + (1-F_s)\, \phi_P\} \\ & \qquad = (S_U^{\phi} + S_P^{\phi}\, \phi_P)\, Vol \qquad (3.12) \end{aligned}$$

where A_e is the east face area of the control volume
$\dot{q}_e$ is the east face mass flux ($= \rho_e U_e$), and
F_e is the east weighting factor for differencing used in the convection terms.

The type of differencing used is the "hybrid" scheme (Spalding, 1972) which consists of a combination of upstream and central differencing, being chosen according to the ratio (for any cell face) of the convective flux to the diffusive flux (Peclet number) thus:

$$F_e = \frac{1}{2} + \frac{1}{Pe_e} \quad \text{for } |Pe_e| < 2 \text{ (central differencing)}$$

$$F_e = \begin{cases} 1 \text{ for } Pe_e \geqslant 2 \\ 0 \text{ for } Pe_e \leqslant -2 \end{cases} \quad \text{(upwind differencing)} \qquad (3.13)$$

where eg:

$$Pe_e = \frac{\dot{q}_e \Delta x}{\Gamma_e}$$

and Δx is the local mesh spacing in the x direction at the east face. The source term in equation 3.11 has been integrated over the control volume and linearised to enhance numerical stability (Patankar, 1980). The transport equation for ϕ in finite-difference form is then re-arranged and with the help of the continuity equation re-written as:

$$\left(\sum_{i=1,N} a_i^{\Phi} - S_P^{\Phi} \right) \Phi_P = \sum_{i=1,N} a_i^{\Phi} \Phi_i + S_U^{\Phi} \qquad (3.14)$$

where $\sum\limits_{i=1,N}$ represents summation over all cell faces (N =6 in three-dimensional problems). The transport equation for a velocity U can be expressed as:

$$\left(\sum_{i=1,N} a_i^{u} - S_P^{u} \right) U_P = \sum_{i=1,N} a_i^{u} U_i + A_W \left(P_W - P_P \right) \qquad (3.15)$$

where the pressure gradient acting upon Up enters the finite-difference equation as a source term and is an unknown; its determination will be discussed in subsection 3.2.5.

3.2.4 The boundary conditions

Equations similar to 3.10 are of the elliptic type. Elliptic partial differential equations must be supplied with conditions on the variables at all points on a closed boundary surrounding the field. The specification of these conditions varies according to the type of boundary and the dependent variable under consideration.

(i) Inlet boundary

The values for each variable are assigned for each grid node at the entry plane. These can be deduced from knowledge of the particular situation which is being modelled, eg from experimental measurements; any values not available from prior knowledge must be guessed.

(ii) Symmetry plane

At a symmetry plane, or an axis of symmetry, both diffusion and convection fluxes normal to the boundary are zero.

(iii) Cyclic boundary

In can-type combustor problems, it is usual, due to the distribution of the dilution ports, for a section of the flow domain to exhibit a periodic repetition around the can periphery (Figure 3.2a).

For such cases, the integration domain need only cover one of these repeated sections, thereby reducing the size of the calculation domain; cyclic boundary conditions must then be prescribed at the boundaries of the periodic section. Cyclic boundary conditions imply that (Figure 3.2b):

$$\Phi_1 = \Phi_m$$
$$\Phi_2 = \Phi_{m+1} \qquad (3.16)$$

A convenient method for dealing with this type of boundary in can combustor situations is described in Serag-Eldin (1977).

(iv) Wall Boundary

The physical boundary conditions for velocity at a solid wall are zero normal and tangential velocity. Further, the turbulent kinetic energy and the normal gradient of the energy dissipation are zero:

$$U = V = W = k = \frac{\partial \epsilon}{\partial n} = 0 \qquad (3.17)$$

Two important features result from these conditions and distinguish near wall regions from other parts of the flow. Firstly, very steep gradients prevail in the direction normal to the surface. Secondly, viscous effects can be important and the presence of the wall influences the eddy structure so that small-scale turbulence is no longer isotropic. As a consequence, the assumptions made in the high Reynolds number version of the k-ϵ turbulence model described above are no longer applicable. It is possible to account for these effects by using closely spaced grid nodes to resolve the gradients and by modifying the turbulence model so that low Reynolds number phenomena are more appropriately modelled (see Jones and Launder, 1973); this does, however, incur a high penalty in computational cost due to the grid fineness. In many cases, algebraic prescriptions known as "wall functions" (Launder and Spalding, 1974) can obviate the need for a fine grid to resolve the distributions near the viscous sublayer while allowing for the effect of the wall on the remaining of the flow.

The empirical law of the wall (Schlichting, 1968; Townsend, 1980) can be used to bridge between the wall condition and the dependent variable outside the viscous sublayer. The semi-empirical relation given by:

$$U^+ = y^+ \qquad (3.18)$$

can be used in the viscous sublayer and the universal law of the wall given by:

$$U^+ = \frac{1}{\kappa} \ln (Ey^+) \qquad (3.19)$$

can be used for matching in the inertial sublayer. The dimensionless velocity and distance are defined as follows:

$$U^+ = U/(\frac{\tau_w}{\rho})^{1/2}$$

$$(3.20)$$

$$y^+ = \rho.y.\ (\frac{\tau_w}{\rho})^{1/2}\ /\mu$$

where τ_w is the wall shear stress, U is the velocity parallel to the wall and y is the perpendicular distance from the wall. The complex nature of the near wall region is thus represented by just two zones: viscous ($0 \leqslant y^+ \leqslant 11.5$) and inertial ($11.5 \leqslant y^+$).

A convenient way of implementing the law of the wall for calculations involving flow separation is through a modified version suggested by Launder and Spalding (1974) which reduces to the above under local equilibrium conditions:

$$\frac{\rho U C_\mu^{1/4} k^{1/2}}{\tau_w} = \frac{1}{\kappa} \ln (Ey^+) \qquad (3.21)$$

where now

$$y^+ \simeq \frac{\rho.k^{1/2}.C_\mu^{1/4}.y}{\mu}$$

The generation of turbulence kinetic energy in the wall region also requires the grid to resolve steep gradients; this is avoided by use of a modified form of the generation term incorporated into the source term in an approximate form, eg:

$$S_u^k = \frac{C_\mu^{1/2}\ \rho k\ U}{y \ln (Ey^+)} \quad \text{(for a horizontal wall)} \qquad (3.22)$$

The near wall values of energy dissipation rate are prescribed using the definition of turbulence length scale near the wall and the assumption of a local equilibrium region (Gibson et al, 1984):

$$l = \frac{k^{3/2}}{\epsilon} = C_\mu^{-3/4} \kappa y \qquad (3.23)$$

Hence:

$$\epsilon_w = \frac{C_\mu^{3/4} k^{3/2}}{\kappa y} \qquad (3.24)$$

ϵ_w is fixed at a near wall mesh node by altering the appropriate source terms as follows:

$$S_u^\epsilon = G \epsilon_w$$
$$S_p^\epsilon = -G \qquad (3.25)$$

where G is a large number (see discussion in subsection 3.3.2).

(v) Outlet boundary

At an outlet boundary, it is assumed that zero gradient conditions exist in the direction normal to the outlet plane.

3.2.5 The solution of the finite-difference equations

The solution of algebraic relations of the form of equation 3.14 is required at each grid node internal to the area of integration for each dependent variable. The method of solution used here is an implicit, iterative technique (the SIMPLE technique (Patankar and Spalding, 1972)) which makes successive adjustments to the velocity and pressure field until a set of values which simultaneously satisfy momentum and continuity is obtained. The method involves a guess and correct procedure for the pressure and the derivation of a pressure correction equation which replaces the continuity equation. This algorithm is described in detail in several places in the literature (eg Patankar and Spalding, 1972; Patankar, 1980) and is, therefore, not reported here.

The equations for all variables, including the pressure correction, reduce to the same algebraic form, ie:

$$\phi_p = \sum_{i=1,N} a_i\phi_i + b_p \qquad (3.26)$$

Solution of equation 3.26 is obtained, assuming a_i and b_p to be known, by means of line-by-line application of the standard tri-diagonal matrix algorithm (Roache, 1976). The assumption of known coefficients is necessary to linearise the equations; iteration of each equation is then not pursued to convergence but merely to obtain improved estimates of ϕ (Patankar, 1980). The improved estimates are then used to calculate new values of a_i and b_p and the application of the above algorithm is repeated until convergence of the whole set of algebraic equations is obtained.

3.3 Methods for calculating complex geometries with arbitrary boundaries

The calculation of flow systems of practical engineering interest often requires that the numerical procedure is capable of representing the flow in complex geometries whose boundaries do not readily conform to any simple frame of co-ordinates such as cartesian or cylindrical polar systems. The numerical computation of such geometries with irregularly shaped boundaries poses difficulties related to the accurate formulation and implementation of boundary conditions and the efficient and economical use of the grid nodes of the specified mesh. Methods to overcome these problems and endow the finite-difference technique with geometrical flexibility may be summarised under the headings of conforming and non-conforming grid meshes.

The former approach involves the use of curvilinear grid systems (orthogonal or non-orthogonal), usually generated numerically, whose co-ordinate lines are coincident with all boundaries (boundary fitted meshes). The partial differential equations 3.4 and 3.5 in order to be solved on such a mesh are themselves transformed and can take on very complex forms. An extensive description of grid generation methods and the appropriate solution algorithms, their advantages, disadvantages and limitations is given by Thompson (1982).

In the methods which adopt non-conforming meshes, the flow domain is usually overlaid by a regular orthogonal co-ordinate mesh (cartesian or cylindrical polar); the differential equations therefore retain their simple form. The specification of the boundary shape and the implementation of boundary conditions in regions where the boundary surface is irregular to the mesh depends on the particular treatment of the boundary cells. The application of both of the above methods in the calculation of fluid flow problems, their merits and drawbacks are discussed by Gosman and Issa (1984).

The three following sections present three methods that have been used for the calculation of the flows presented in Chapters IV and V. Section 3.3.1 describes a procedure for the generation of a curvilinear orthogonal grid while sections 3.3.2 and 3.3.3 discuss two methods that fall into the second category of the above classification.

3.3.1 A method for generating curvilinear orthogonal meshes

In two-dimensional geometries, conformal meshes equivalent to a potential flow solution for the problem under study are widely popular and have been used by various workers (Thom and Apelt, 1971; Johns, 1980; Thompson, 1984). Winslow (1967) started from the two Laplace equations for the velocity potential and stream function of an irrotational flow in the geometry under consideration:

$$\frac{\partial^2\phi}{\partial x^2} + \frac{\partial^2\phi}{\partial y^2} = 0 \quad , \quad \frac{\partial^2\psi}{\partial x^2} + \frac{\partial^2\psi}{\partial y^2} = 0 \qquad (3.27)$$

so that the boundaries of the flow are described by lines of constant stream function or constant velocity potential. The inverse form of 3.27 is more convenient for numerical calculation and is derived by using the general transformations:

$$\frac{\partial\phi}{\partial x} = -\frac{1}{J}\frac{\partial y}{\partial\psi} \quad ; \quad \frac{\partial\psi}{\partial x} = \frac{1}{J}\frac{\partial y}{\partial\phi}$$

$$\frac{\partial\phi}{\partial y} = \frac{1}{J}\frac{\partial x}{\partial\psi} \quad ; \quad \frac{\partial\psi}{\partial y} = -\frac{1}{J}\frac{\partial x}{\partial\phi} \qquad (3.28)$$

where the Jacobian J of the transformation is given by

$$J = \frac{\partial x}{\partial\psi}\frac{\partial y}{\partial\phi} - \frac{\partial x}{\partial\phi}\frac{\partial y}{\partial\psi} \qquad (3.29)$$

This yields:

$$\alpha \frac{\partial^2 x}{\partial\phi^2} - 2\beta \frac{\partial^2 x}{\partial\phi\partial\psi} + \gamma \frac{\partial^2 x}{\partial\psi^2} = 0$$

$$\alpha \frac{\partial^2 y}{\partial\phi^2} - 2\beta \frac{\partial^2 y}{\partial\phi\partial\psi} + \gamma \frac{\partial^2 y}{\partial\psi^2} = 0 \qquad (3.30)$$

Here, α, β, γ are the quadratic functions:

$$\alpha = \left(\frac{\partial x}{\partial\psi}\right)^2 + \left(\frac{\partial y}{\partial\psi}\right)^2$$

$$\beta = \frac{\partial x}{\partial\phi}\frac{\partial x}{\partial\psi} + \frac{\partial y}{\partial\phi}\frac{\partial y}{\partial\psi} \qquad (3.31)$$

$$\gamma = \left(\frac{\partial x}{\partial\phi}\right)^2 + \left(\frac{\partial y}{\partial\phi}\right)^2$$

It should be noted that orthogonality requires satisfaction of the Cauchy-Rieman equations which under general transformation become:

$$\frac{\partial x}{\partial\psi} = a\frac{\partial y}{\partial\phi} \quad ; \quad \frac{\partial y}{\partial\psi} = -a\frac{\partial x}{\partial\phi} \qquad (3.32)$$

where a is the aspect ratio given by:

$$a^2 = \frac{\gamma}{\alpha} \qquad (3.33)$$

For an orthogonal mesh equation 3.30 then reduces to:

$$\frac{\partial^2 x}{\partial\phi^2} + a^2\frac{\partial^2 x}{\partial\psi^2} = 0$$

$$\frac{\partial^2 y}{\partial\phi^2} + a^2\frac{\partial^2 y}{\partial\psi^2} = 0 \qquad (3.34)$$

the central term being eliminated by the orthogonality condition.

The method followed in the present work is that of Gosman and Johns (1979) who solve the inverse equations 3.34. This is done so as to avoid the need for interpolation of the ϕ-ψ solution in order to obtain the x, y co-ordinates of the iso-ϕ and iso-ψ lines which would be required if equations 3.27 were solved directly. Gosman and Johns (1979) expressed the equations 3.34 in finite-difference form using second order central differences with constant step sizes (although the values of $\Delta\phi$ and $\Delta\psi$ may be different) eg:

$$\alpha \frac{(x_E - 2x_P + x_W)}{\Delta\phi^2} + \gamma \frac{(x_N - 2x_P + x_S)}{\Delta\psi^2} = 0 \qquad (3.35)$$

where the five point numerical scheme is shown in Figure 3.3. The associated functions α and γ can also be expressed via central differences as:

$$\alpha = \left(\frac{x_N - x_S}{2\Delta\psi}\right)^2 + \left(\frac{y_N - y_S}{2\Delta\psi}\right)^2$$

$$\gamma = \left(\frac{x_E - x_W}{2\Delta\phi}\right)^2 + \left(\frac{y_E - y_W}{2\Delta\phi}\right)^2 \qquad (3.36)$$

Equation 3.35 may be then expressed in the form

$$A_P x_P = A_N x_N + A_S x_S + A_E x_E + A_W x_W \qquad (3.37)$$

and an equation similar to this may be derived with y as the dependent variable.

Boundary conditions are required to ensure that the co-ordinate intersections on the boundaries are linked to internal grid points with a line that is orthogonal to the boundaries (except in singularities on the surface). The boundary must first be specified in the physical plane with a discrete or continuous description of its co-ordinates. Initially, the co-ordinates of the intersections on the boundary are guessed and are then refined through subsequent iteration with the equation expressing the orthogonality conditions. The method requires that the boundary is continuous and explicit in the first derivative over the region of interest. This is arranged when the boundary is specified as discrete points by fitting a piecewise parametric cubic polynomial to the boundary co-ordinates. Gosman and Johns propose an iterative equation to express the boundary condition. A straight line is passed from the boundary point through the first internal grid node which, for a near horizontal boundary may be expressed by the equations:

$$y^P = -\left(\frac{dy}{dx}\right)_B^{-1} x^P + C$$

$$y^B = -\left(\frac{dy}{dx}\right)_B^{-1} x^B + C \qquad (3.38)$$

where the superscripts P and B refer to the internal and boundary values respectively (Figure 3.4). The slope of the boundary curve $(dy/dx)_B$ is obtained with first order accuracy from the equation:

$$\left(\frac{dy}{dx}\right)_B = \frac{y^E - y^B}{x^E - x^B} \qquad (3.39)$$

where the superscript E indicates the estimated value from the previous iteration (Figure 3.4). After eliminating C and y^B the corrected location for the co-ordinate point x^B is obtained from the iterative formula:

$$x^B = \frac{y^E - y^P - x^E \left(\frac{dy}{dx}\right)_B - x^P \left(\frac{dy}{dx}\right)_B^{-1}}{-\left(\frac{dy}{dx}\right)_B - \left(\frac{dy}{dx}\right)_B^{-1}} \qquad (3.40)$$

The value of x^B may be updated several times with this equation before the internal nodes are recalculated. Once the value of x^B is found, the curve describing the boundary is used to obtain y^B. For a near vertical boundary equation 3.40 is replaced by a similar one for y^B obtained in an analogous fashion. The above procedure has been described here in some detail because it was used to generate the meshes employed in the calculations of Chapter IV.

In practical application of the above method, situations often arise where the boundary configuration does not strictly fulfil all the criteria required for a perfectly orthogonal mesh. It is possible, for example, for the boundary intersections at the four corners of the domain over which equations 3.34 are solved, to be non-orthogonal and in this case local orthogonality errors arise. In addition, deviations from orthogonality occur in the vicinity of singularities where the requirement that the boundary must be continuous in the first derivative is violated. This problem arose in the calculations reported here and is referred to in Chapter IV.

The meshes generated in the above manner correspond ideally to an orthogonal curvilinear system of co-ordinates and the governing equations transformed to this new system can be written in the common form:

$$\frac{\partial}{\partial\zeta_1}(l_2\ l_3\ \rho\ U_1\ \phi) + \frac{\partial}{\partial\zeta_2}(l_1\ l_3\ \rho U_2\ \phi) =$$

$$\frac{\partial}{\partial\zeta_1}\left(l_2\ l_3\ \frac{\Gamma_\phi}{l_1}\frac{\partial\phi}{\partial\zeta_1}\right) + \frac{\partial}{\partial\zeta_2}\left(l_1\ l_3\ \frac{\Gamma_\phi}{l_2}\frac{\partial\phi}{\partial\zeta_2}\right) + l_1\ l_2\ l_3\ S_\phi \qquad (3.41)$$

In this equation, ϕ represents any of the dependent variables, U_1 and U_2 are the mean velocities in directions 1 and 2 (Figure 3.5) and Γ_ϕ is the corresponding diffusivity. l_1, l_2, l_3 are the metric coefficients which relate increments in the co-ordinates to increments in physical space (Gosman and Johns, 1979) and ζ_1, ζ_2 are the co-ordinates corresponding to lines of constant stream function and velocity potential obtained as discussed above (Figure 3.5). The metric coefficients were obtained from the mesh generation program using cubic polynomials to connect the constant potential or stream function locations. They were incorporated into the flow solution program using surface integrals to obtain the cell face areas, volumes, arc lengths and radii of curvature (which are linked to the variation of the angle β, Figure 3.5, through the metric coefficients, Gosman et al (1969)). The detailed procedure for the estimation of these geometric parameters is presented by Gosman and Johns (1979).

The major advantages of the above method are that wall boundary conditions are easier to implement and that it allows better control over the grid distribution than methods which use non-conforming grids. However, the need to generate the mesh may in some cases be a major task and the increased complexity of the finite-difference equations due to extra co-ordinate curvature terms requires considerably additional effort and storage requirement. Further, the above method is restricted to two-dimensional geometries (or three-dimensional configurations whose third direction is formed by rotating the system about an axis) due to restrictions in the generation of curvilinear-orthogonal grids in fully three-dimensional geometries (see Thompson 1982, p 201); for example, the model combustor of Figure 2.1 could not be handled in its entirety because of the exit nozzle.

3.3.2 The castellated approximation

This subsection discusses a method widely used for representing irregular geometries where the irregular surface is restricted to a small area of the flow domain while most of the system conforms to a simple frame of co-ordinates. In such cases, it is possible to employ a regular grid and improvise on the finite-difference formulation so that it can handle the irregularly shaped boundary while avoiding the need for generating a special mesh. The incorporation of the solid boundary within the calculation domain is accomplished by rendering inactive (or "blocking off") some of the control volumes of the regular grid so that the remaining active control volumes approximate the irregular boundary (Figure 3.6). The "blocking off" operation consists of modifications in the finite-difference equations so that, when solved, the result is appropriate to the value that the dependent variable would attain inside the solid boundary. For example, all fluid velocities are zero beyond a confining wall. The method used is then to express the source terms for such grid nodes in the form:

$$S_u^{\Phi} = G\ \phi_W$$

$$S_p^{\Phi} = -G \qquad (3.42)$$

where G is a large number ($\rightarrow\infty$) and ϕ_W is zero. Then equation 3.14 can be re-written as:

$$\left(\sum_{i=1}^{4} a_i^{\Phi} + G\right)\phi_P = \sum_{i=1}^{4} a_i^{\Phi}\ \phi_i + G\ \phi_W \qquad (3.43)$$

The solution of 3.43 for a velocity located at node P within the wall would be:

$$\phi_P = \frac{\Sigma a_i^{\Phi}\phi_i + G\phi_W}{\Sigma a_i^{\Phi} + G} = \frac{G\phi_W}{G} = 0 \qquad (3.44)$$

It is necessary also to specify the wall functions for these internal walls in the same manner as for calculation domain boundary walls.

This method is usually employed in two-dimensional geometries as in fully three-dimensional geometries the difficulty of properly indexing the blocked off cells to represent as accurately as possible the irregular surface and the necessity of specifying wall functions for each of the resulting steps makes the method less attractive. A futher disadvantage of the method is its lack of flexibility and inefficiency in terms of grid node distribution (since nodes outside the flow domain are wasted). Although a variety of flow configurations have been successfully calculated with the above approach, there are situations where large errors can be introduced by the castellation and this is further discussed in Chapter IV.

3.3.3 A general method for fully three-dimensional geometries with arbitrary boundaries

This section introduces a more general method for calculating fully three-dimensional geometries of arbitrary shape. The procedure makes use of a non-conforming orthogonal mesh (cartesian or cylindrical polar system of co-ordinates) so that the boundaries of the flow domain may intersect the mesh at irregular positions resulting in irregular shapes and sizes of boundary cells. In the present approach, the crudity of the castellated approach is avoided by allowing different types of boundary cells to exist. Each boundary cell possesses its own finite-difference formulation and boundary condition, depending on its shape and position relatively to the solid surface. This approach has been used previously in three-dimensional boundary layer type flows (McGuirk and Spalding, 1973) but not for fully elliptic flows as studied here. A computer program which incorporated the basic methodology described below was available (Priddin, 1979) but had not been fully debugged and was insufficiently developed to enable it to be applied to the kind of complex geometry represented by the nozzle of the model combustor described in the previous chapter. The further development, testing and application to this problem was achieved during the work presented in this thesis.

Definition of geometry

The geometry of the flow system to be calculated is specified in the finite-difference code by providing the intersections of the grid lines with the boundary surface. The description of the surface can either be given in a continuous form (eg as an algebraic function in simple cases) or, generally, as discrete points which can be input into a surface fitting routine which then provides the continuous specification of the boundary. Although there are four separate grids (scalar, U, V, W) there are only three independent sets of boundary intersections since staggering along a grid line does not change the point of intersection of that grid line with the surface.

Since a cartesian or cylindrical polar grid mesh is retained, it is likely that the grid covers areas outside the flow domain. In the present method, the undesirable staircase shape of the castellated approximation is avoided by allowing four different types of boundary cells. The corners of all cells are first allocated an identifying tag according to whether it lies inside or outside the flow domain. This enables the classification of cells as follows (Figure 3.7):

1) fully internal cells - all corners lie completely inside the flow domain (Type A);

2) boundary cells, further subdivided into three categories:

a) cells which are fully external to the flow domain (Type B; all corners outside)

b) cells intersected by the boundary whose node lies inside the flow domain (Type C)

c) cells intersected by the boundary whose node lies outside the flow domain (Type D).

The above formulation helps to apply the appropriate boundary condition to each of the boundary cells. The part of the boundary surface contained within a boundary cell is approximated as a plane surface (equivalent to a piecewise linear fit to a curve in two-dimensions). In general, a finer mesh is usually needed to resolve highly convoluted boundary surfaces.

The boundary intersections are used to calculate the geometric quantities, related to the boundary cells, which are needed for the finite-difference formulation. These are the cell face area of that part of the cell lying inside the boundary (this value normalised by the total face area is actually stored), the perpendicular distance from the grid node to the boundary, the direction cosines of the normal to the boundary and the area of that part of the boundary contained within the cell (Figure 3.7).

Finite-difference modifications

Each boundary cell in the discretised domain is treated in a different way according to its classification. The appropriate modifications in the finite-difference formulation for the three types of boundary cells are:

a) For fully external cells (Type B) the value appropriate to the dependent variable in this position is fixed in a manner similar to that described in subsection 3.3.2.

b) In the case of boundary cells of Type C, the correct fluxes at the faces of this cell are obtained by multiplying each flux term calculated in the normal way by the values of the normalised areas appropriate to each cell face.

c) When the cell node falls outside the boundary (Type D) as in Figure 3.8, a special practice is adopted. The fluxes for these cells (A in Figure 3.8) are calculated and added to an adjoining cell whose node is internal to the flow domain, so that the conservative property of the finite-difference formulation is retained. In the example shown in Figure 3.8, the flux at the south face of cell A cancels the flux at the north face of cell B and the new cell "abef" is used to determine the value of the dependent variable at P. Those "add-on" cells are transferred to those adjoining cells with which they have the largest contact area. The only exception to the above approach is in the formulation and solution of the pressure correction equation. In this case, a value for the pressure correction is calculated at Q, based on the mass source for cell A. This is because, for the configuration of Figure 3.8, the velocity at SN will be corrected by $(P_P'-P_Q')$ and so although P is external to the flow domain, V is internal and hence the pressure correction is required. In this example, cell B would not normally have been treated as a boundary cell of Type C as it is not intersected by the boundary, but the addition of cell A to it causes it to be treated as a Type C cell.

Boundary conditions

The boundary conditions required for the solution of the finite-difference equations formulated in the manner described above are generally those presented in subsection 3.2.4. However, the implementation of the wall functions deserves special attention. The procedure allows each boundary cell to have associated with it a value for each dependent variable; for the present problem this is required due to the existence of holes with through flow at the boundary. The components of the boundary velocities in the grid directions (U_B, V_B, W_B) are interpolated using area weighting for staggered cells. These velocities are then resolved into a component normal to the boundary (VBNS) and one lying in the plane of the boundary (VBT) (see Figure 3.9). If VBNS is non zero, that portion of the wall is treated as an inflow region (see below). If not, the wall is assumed solid and the standard log-law expressions are used (see subsection 3.2.4 iv). For the velocity components, the wall shear terms are incorporated into the algebraic equations using an effective wall viscosity (Γ_B). The velocity components at the near wall node are also resolved into components, normal to the boundary (VPNS) and parallel to the boundary VPPS so that the velocity gradient normal to the wall may be calculated from:

$$\frac{\partial U}{\partial n} = \frac{(\mathrm{VPPS-VBT})}{\mathrm{PD}} \qquad (3.45)$$

where PD is the perpendicular distance from the node to the boundary surface.

A special practice was also necessary for the implementation of through flow via dilution holes on the boundary surface; the following paragraphs describe the procedure adopted in the context of the present method. In general, the boundary values for each dependent variable can be used to represent the velocity and turbulence properties of the fluid entering through the surface. However, if the plane of the hole (and consequently the boundary surface in this region) does not coincide with the mesh surface, the resultant velocity component normal to the boundary (VBNS) will not necessarily (due to the interpolation involved) be of the correct magnitude. As a result, the calculated influx of any property ϕ through the boundary:

$$FL_H = \rho_B \ VBNS \ A_B \ \phi_H \qquad (3.46)$$

will also not correspond to the desired influx specified from the boundary conditions, when summed over all cells adjacent to the hole. In this expression, ρ_B is the density of the entering fluid, A_B is the area of the boundary surface contained within the cell and ϕ_H is the value of the dependent variable at the hole. The above discrepancy can be corrected by using a density modified by a factor defined as follows:

$$\rho_B{}' = \rho_B \ \frac{FL_{CH}}{FL_H} \qquad (3.47)$$

where FL_{CH} is the required influx and FL_H is the numerically interpolated one. This task is performed at the beginning of the iteration cycle so that at subsequent iterations the flux at this position is determined by the expression:

$$FL_H = \rho_B{}' \ VBNS \ A_B \ \phi_H \qquad (3.48)$$

which is then introduced into the finite-difference equations through the source term.

Although the complex geometry technique described above was developed with the purpose of calculating the exit nozzle of the model combustor (Figure 2.1) and similar systems it provides a general capability of calculating fully three-dimensional geometries of any arbitrary shape. Its advantage over methods that use conforming non-orthogonal meshes is the reduced computational effort involved in solving the simpler partial differential equations. Its main drawback is its inefficiency in terms of grid node distribution. Since the grid covers areas outside the flow domain grid refinement in important regions may result in many redundant nodes in irrelevant parts of the mesh.

Particular details of the application of the methods described in the previous subsections to the flows of Chapters IV and V are discussed in the related chapters.

3.4 Limitations of the calculation approach

The method of calculating turbulent flows outlined in the previous sections may now be applied to the flows of interest here and compared against experimental data. If differences between predictions and measurements arise, it is important to remember that inaccuracies may be due to several quite different sources of error. Differences between experiment and calculation may be seen as the result of (i) deficiencies in the turbulence model, (ii) numerical inaccuracy in the finite-difference technique, (iii) uncertainties in the boundary conditions and (iv) approximations related to the specification of the grid and the geometry. These are further discussed below.

3.4.1 Limitations of the turbulence model

The two-equation k-ϵ turbulence model described in subsection 3.2.2 is the most extensively used and tested turbulence model in a variety of flows that range from unconfined developing wake regions (Pope and Whitelaw, 1976) to strongly confined recirculating flows (McGuirk and Whitelaw, 1983). A consistent underprediction of recirculation lengths and peak turbulence kinetic energy levels has been observed in two-dimensional flows and has been attributed to the inability of the k-ϵ model to represent flows with strong streamline curvature or highly anisotropic trubulence. The flow visualisation and experimental data presented in Chapter II indicate that both of these phenomena are present in the current flows. The effect of streamline curvature in turbulent flows alters the local turbulence structure and, consequently, the development of the mean flow (Bradshaw, 1973). Most experimental investigations have been with two-dimensional curved wall boundary layers (Irwin and Arnot-Smith, 1975) and it has been observed that turbulent transport decreases if the angular momentum of the flow increases with radius and vice-versa. This influences also the division of the turbulence energy between its components (the normal stresses) and is not included in the standard k-ϵ model, as a result of the eddy viscosity hypothesis and the approximations in the derivation of the modelled k and ϵ equations (Taylor, 1981). Several changes in the model have been proposed for two-dimensional flows in order to account for the desired effect upon the turbulence transport. Launder et al (1977) suggested a modification to the energy dissipation rate equation decay term so that an increase in angular momentum with radius would increase the local dissipation rate and hence lower the turbulent transport. An alternative to the eddy viscosity is the use of an algebraic stress model (Launder, 1982) this being an intermediate stage between eddy viscosity closures and full transport equation closures. Calculations with this approach have been reported for two-dimensional recirculating flows involving streamline curvature effects (Leschziner and Rodi, 1981) and these methods exhibit better agreement with experiment than the standard k-ϵ model. The possible merits of algebraic-stress modelling, however, are likely to be restricted to two-dimensional recirculating flows where they can be applied in a local streamline co-ordinate system. In these circumstances, the model reduces to an eddy viscosity type with a variable C_μ coefficient (Leschziner and Rodi, 1981). In more complex flows, the existence of multiple non-negligible strain rates and the non-existence of a stream function with which to analyse the flow locally imply that all six non-zero Reynolds stresses require consideration and the non-linearity of the algebraic equations gives rise to the possibility of non-unique solutions and numerical solution difficulties (McGuirk and Whitelaw, 1983).

A more fundamental allowance for the effects of streamline curvature involves the use of a Reynolds stress model in which modelled transport equations for all Reynolds stresses as well as for ϵ are solved (see, for example, Launder, Reece and Rodi, 1975). The use of this model results in qualitatively accurate prediction of the curvature effects on turbulence (Gibson and Rodi, 1981) and automatically ensures the separate consideration of normal stress normal strain interaction. This model, however, has not been extensively tested in complex recirculating flows and is substantially more expensive than the two-equation model.

For internal flows requiring solution of the full three-dimensional equations, it is not yet clear how significant is the streamline curvature effects on the turbulent structure as far as its influence on the mean flow is concerned. Regions of large streamline curvature in the current flow are also regions of large pressure gradients and the relative importance of the turbulence terms may be less than in two-dimensional curved boundary layers. It is, therefore, probable that the two-equation model represents the best current compromise. In strongly confined recirculating flows, where the physical boundaries or conditions dictate, for example, the mean size of the recirculation the defects of the standard k-ϵ model are not so great (Green, 1981).

Further comments on the performance of the k-ϵ model will be given in the discussion of Chapters IV and V.

3.4.2 Limitations of the finite-difference technique

The optimum method of discretising the terms in the partial differential equations governing the flow (Equations 3.4 to 3.5) is by no means clear when the convective terms are considered. For dominantly convective flows, the simplest method, known as "upwind differencing" (Gosman et al, 1969; Roache, 1976) estimates the convection by assuming a stepwise variation between nodes to calculate the value of a flow variable at the cell face; which nodes are used depends upon the direction of the prevailing velocity at this face. The central differencing scheme assumes a linear variation between nodes when estimating convection and, in general, is more accurate. Central differencing, however, when used in calculations of highly convective flows, leads to unstable numerical behaviour (Roache, 1976). Upstream differencing although stable in highly convective flows gives rise to a first order truncation error (proportional to grid node spacing) which is of the form of an erroneous diffusional flux or "false diffusion". This tends to smear the local gradients of a flow variable, especially in flows with strong flow to grid line skewness and can dominate the true physical diffusion (Raithby, 1976; Spalding, 1972). The hybrid scheme (Gosman et al, 1969) used in the present work is a combination of upwind and central differencing depending on the ratio of the convective to the diffusive flux (local Peclet number, Equation 3.13). However, it still retains the inherent weakness of upwind differencing in that large numerical diffusion effects are possible.

McGuirk et al (1981) have shown that the solution of the finite-difference equations may be viewed as a solution of a partial differential equation which is made up of the original equation plus additional terms due to the truncation errors involved in the differencing approximations. The numerical accuracy of the solution depends upon the relative importance of the added terms to the original terms in the differential equation. It is the truncation error of the upwind differencing scheme which gives most cause for concern. McGuirk et al (1981) present a method for estimating the effect of the additional numerical truncation error terms due to upwind differencing by evaluating an out-of-balance residual using (a posteriori) central-difference approximations to the terms in the governing equations. Details of the method may be found in the above reference, here only the methodology involved is discussed.

The accuracy of the solution can be improved by increasing the number of grid points within the regions where the out-of-balance residual is a large term in the algebraic equations and this may be estimated by examining the balance between all terms in the equation on a physical basis (eg nett convection, pressure gradient, nett physical diffusion, false diffusion). McGuirk and Rodi (1978) have also used this method in a two-dimensional recirculating flow.

Improvements in the accuracy of the numerical calculations have also been attempted by using higher order finite-difference schemes. Higher order approximations to the convection terms (Leonard, Leschziner and McGuirk, 1978; Leschziner, 1980) are more accurate because the leading term in the truncation error is a higher power of grid spacing. Another method is the skew-upwind differencing procedure (Raithby, 1976) which is derived by extending the concept of upwind differencing in streamline co-ordinates. The application of these differencing schemes is still under development and both can exhibit under and overshoots in the solution requiring special attention to ensure physically realistic values (eg no negative turbulence kinetic energy values). One disadvantage is the greater complexity in the specification of the boundary conditions. These methods are, therefore, not readily applicable to geometries with wall boundaries specified within the calculation domain (Green, 1981) and have not been considered ready for application to the current problem.

3.4.3 Boundary condition approximations

Errors in the calculation can also arise from assumptions in the boundary conditions such as those involved in the derivation of the empirical wall functions described in subsection 3.2.4. These were originally formulated for two-dimensional boundary layer flows in the absence of a pressure gradient. The log-law approach assumes that the resultant velocity parallel to the wall is in the direction of the resultant shear stress and this has been called into question for three-dimensional wall boundary layer flows. More refined wall laws have been suggested, for example by Van de Berg (1975), where account is taken of the variation of the shear stress vector near the wall and the local pressure gradient. However, there is little evidence to justify their use at present and even these are only valid when the deviations from the simple law are not large. Use of any of these laws for calculation at points involving separation along a wall surface where they are not valid (Simpson, 1976) will create errors in local mean velocity gradients through wrongly prescribed shear stress distributions.

Inaccuracies in the numerical solution may also stem from uncertainties in the boundary conditions, such as those related to the symmetric behaviour of the dilution jets discussed in subsection 2.3.3. Further errors can be introduced due to the specification of the grid and geometry. The errors associated with the non-orthogonality of the grid lines in the meshes generated with the procedure described in subsection 3.3.1 and the castellated approximation are discussed in Chapter IV. The accuracy of the boundary description and the implementation of the boundary conditions in the numerical method presented in subsection 3.3.3 are examined in more detail in Chapter V.

3.5 Summary

The time-averaged Navier-Stokes equations together with a two-equation $k-\epsilon$ turbulence model have been presented for incompressible, constant propertry flow. A description of a numerical procedure used to solve the above set of equations in finite-difference form has also been given. Three methods which endow the finite-difference procedure with geometrical flexibility and make possible the calculation of complex two- and three-dimensional geometries have also been described. Finally, the limitations of the calculation method were discussed in terms of errors introduced from various sources.

CHAPTER IV

THE CALCULATION OF THE FLOW FIELD EXTERNAL TO COMBUSTION CHAMBERS

4.1 Introduction

This chapter presents calculations of the flow external to a combustor, this being part of the task of an overall combustor prediction procedure as mentioned in Chapter I. An annular combustor dump diffuser geometry has been chosen for the calculations and the numerical techniques described in Chapter III applied to the chosen configuration. Section 4.2 discusses the relevance of dump diffusers to gas turbine combustion chamber systems; the flow configuration chosen and the parameters which describe its performance are also outlined. Section 4.3 presents the finite-difference meshes employed and two approaches used to simulate the combustion chamber body; the boundary conditions and the numerical error incurred in the predictions are also described. In the following section, the results of the calculations are presented and the discrepancies between measurements and predictions discussed. Finally, Section 4.5 provides a summary of the main findings and conclusions drawn.

4.2 Annular combustion chamber dump diffuser systems

4.2.1 Relevance to gas turbine combustion chambers

In the combustion system of a gas turbine, it is necessary to use a diffuser upstream of the combustor to decelerate the high velocity air stream delivered by the compressor to avoid high total pressure losses (Lefebvre, 1983). A typical aircraft gas turbine combustion system using a "faired" diffuser is shown in Figure 4.1a. High velocity air supplied by the compressor passes through an initial diffuser A and is then divided into three streams: two main streams pass through diffusers C and D and are then fed to the inner and outer annuli to enter the liner through primary and dilution ports; a third stream comprising a small proportion of the total airflow passes into the primary zone via the so-called snout (B). It is important that the annulus flow has sufficient static pressure to achieve adequate penetration of the dilution jets and that the correct proportions of air enter the combustor through the dome and the various ports to maintain stable operation and good quality outlet conditions.

In a faired diffuser system thick boundary layers can form on the walls of diffusers C and D as a result of the adverse pressure gradients; asymmetries can also appear due to the turning of the flow. These factors increase the possibility of undesirable features such as separation and large non-uniformities in the annulus flow (Stevens and Fry, 1973). Another disadvantage of the faired system is its sensitivity to the non-uniformities of the compressor outlet velocity profile (Lefebvre, 1983). In modern high by-pass ratio engines where a relatively low gas generator flow is compressed, relatively small annulus heights are used in the diffusers feeding the inner and outer annuli. Manufacturing tolerances and differential thermal expansion and distortion during operation can then give rise to significant variations in diffuser geometry with consequent effects on performance (Fishenden, 1974).

In an attempt to overcome these problems, modern engines are moving towards the use of the "dump" diffuser system shown in Figure 4.1b. This system has four components in which diffusion takes place, A, B, C, D, which can be compared directly with Figure 4.1a. The flow is initially decelerated in a short prediffuser and then discharged into the dump region where a free surface diffusion continues in the regions C and D. These regions are bounded on one side by the head of the flame tube and on the other by the boundary S-S of the vortices in the corners of the dump region. In this system, the sharp-edged splitters of the faired system have been replaced by the blunt combustor head and this is thought to render the system less sensitive to variations in the approach flow (Fishenden, 1974). In addition, this geometry is simpler to manufacture and has fewer critical dimensions than the faired system.

The performance of dump diffuser systems was examined experimentally by Klein et al (1974) who focussed attention on the effect of the compressor exit conditions on the overall performance. They found that the overall loss coefficient of the system was increased with simulated compressor exit non-uniformities (blade wakes). Fishenden and Stevens (1977) have undertaken a more extensive investigation of dump diffuser flows. The overall static pressure recovery and total pressure loss were evaluated and the influence of the prediffuser geometry, the division of the flow between the two annuli and the distance between the flame tube and the prediffuser exit were investigated. No theoretical investigations of this diffuser type have been reported and the numerical investigation of axisymmetric wide angle diffusers followed by a downstream sudden expansion by Habib and Whitelaw (1982) is of little direct relevance to the complete annular system since it did not include the presence of the combustor body.

The choice of acceptable diffuser shapes and optimum outer to inner annulus mass flow split for a given combustor size and shape is currently based on experience or experimental information. Furthermore, knowledge of the more standard faired-type diffuser performance is of little use as the flow patterns in the two diffusers are radically different. Prediction methods employing simple analysis, used for the evaluation of faired systems (see, for example, NASA CR-72374; Adkins, 1978) are not directly applicable due to the greater complexity of the flow development in the dump system. Fundamental knowledge of the flow behaviour in these systems is therefore required if designs are to be realised efficiently and economically. The aim of the present investigation is to use existing measurements to develop and appraise a calculation method for the turbulent flow fields in dump diffuser systems.

4.2.2 Flow configuration chosen for the numerical investigation

The flow configuration chosen for the present study is that of Fishenden (1974) since this work provides data over a range of variations in geometric and flow variables. The geometry is shown in Figure 4.2 and represents an axisymmetric annular system which comprises an initial prediffuser, equal inner and outer annulus heights and a combustor with a semi-circular head.

Numerical investigations of simple wide angle diffusers have been undertaken by various workers (for example, Sala et al (1980) and Hah (1983)) and the possibility of calculating the flow properties and the effects of the variation of the inlet conditions on the performance has been considered in some detail. The present investigation does not include the prediffuser section and is concerned with aspects of the flow related to the fluid dynamic behaviour in the dump region (2-3) and the settling length (3-4) of the system of Figure 4.2. Attention is focussed on examining the extent to which the theoretical model is capable of describing the detailed flow development in these regions and the variation of the overall performance parameters with changes in geometry and flow conditions. In particular, the effects of the flow division between the two annuli (flow split: $S = \dot{m}_o/\dot{m}_i$) and the distance between the combustor and the prediffuser exit (dump gap: D_G) are studied. The performance parameters of the initial section (1-2, Figure 4.2) were taken from the experimental investigation (Fishenden, 1974) and added to the predicted behaviour for section (2-4) so that the overall performance (1-4) could be evaluated and compared with measurements. The range of investigated cases is given in Table 4.1.

TABLE 4.1

INVESTIGATED DUMP DIFFUSER CONFIGURATIONS

Dump gap (D_G/h_2)	Flow split (S)	Prediffuser data		
		A_2/A_1	2ϕ	L/h_1
1.0	1.3, 1.72, 2.57	1.4	12°	1.900
1.5	0.882, 1.473, 2.303	1.6	12°	2.850
0.5	1.199, 1.71, 2.485	1.6	12°	2.850

As in the experimental work, no bleed flow for cabin air or into the combustor via film cooling rings or dilution ports has been simulated in the calculations. Their inclusion, however, in future work is not precluded and this is further discussed in Chapter VI.

4.2.3 Performance parameters

The performance parameters of a branched duct system as investigated here are defined in the same way as for simple diffusers. The equations for the present system, however, must take into account the variation in the division of the flow (Fishenden, 1974).

For incompressible, spatially non-uniform flow, the mass-weighted mean total pressure at any cross-section can be written (Sovran and Klomp, 1967):

$$\tilde{P}_t = \tilde{P}_s + \alpha\ 1/2\rho\ \bar{U}^2 \qquad (4.1)$$

where $\tilde{P}_s$ and α are the mass-weighted mean static pressure and the velocity profile energy coefficient and are defined as follows:

$$\tilde{P}_s = 1/\dot{m}\int^{A} P_s d\dot{m}$$

$$\alpha = 1/\dot{m}\int^{A} (\frac{U}{\bar{U}})^2\ d\dot{m} \qquad (4.2)$$

with $\bar{U}$ as the bulk mean velocity (= $\dot{m}/\rho A$). Designating $\Delta\tilde{P}_{t1-4}$ as the mean total pressure loss between station 1 and 4, the energy equation for the system may be written (Fishenden and Stevens, 1977):

$$\dot{m}_1\ (\tilde{P}_s + \alpha\ \rho/2\ \bar{U}^2)_1 = \dot{m}_{4i}\ (\tilde{P}_s + \alpha\ \rho/2\ \bar{U}^2)_{4i} + \dot{m}_{4o}\ (\tilde{P}_s + \alpha\ \rho/2\ \bar{U}^2)_{4o} + \dot{m}_1\ \Delta\tilde{P}_{t1-4} \qquad (4.3)$$

Defining

$$C_{p1-4} = \frac{\dot{m}_{4i}\ \tilde{P}_{s4i} + \dot{m}_{4o}\ \tilde{P}_{s4o} - \dot{m}_1\ \tilde{P}_{s1}}{\dot{m}_1\ \alpha_1\ \rho/2\ \bar{U}_1^2} \qquad (4.4)$$

(static pressure recovery coefficient)

and

$$\lambda_{1-4} = \frac{\Delta\tilde{P}_{t1-4}}{\alpha_1\rho/2\bar{U}_1^2} \qquad (4.5)$$

(total pressure loss coefficient)

we obtain

$$C_{p1-4} = 1 - \frac{\dot{m}_{4i}(\alpha\rho/2\bar{U}^2)_{4i} + \dot{m}_{4o}(\alpha\rho/2\bar{U}^2)_{4o}}{\dot{m}_1\ \alpha_1\ \rho/2\ \bar{U}_1^2} - \lambda_{1-4} \qquad (4.6)$$

Introducing the flow split S = $(\dot{m}_o/\dot{m}_i)_4$ and the area ratios $AR_o = A_{4o}/A_1$ and $AR_i = A_{4i}/A_1$ this equation may be rewritten:

$$C_{p1-4} = 1 - \frac{1}{\alpha_1(1+S)^3}\ (\frac{\alpha_{4o}.S^3}{AR_o^2} + \frac{\alpha_{4i}}{AR_i^2}) - \lambda_{1-4} \qquad (4.7)$$

The second term on the the right hand side of equation 4.7 shows that the overall pressure recovery of this system depends on the geometry (AR_o and AR_i), the division of flow (S) and the exit velocity profile distortion (α_{4o} and α_{4i}) and represents the reduction in static pressure recovery due to inefficient diffusion, ie excessive kinetic energy flux remaining at the exit (Fishenden, 1974). The third term represents a loss term due to viscous effects.

4.3 Details of the calculation

4.3.1 Finite-difference meshes used

Although most of the geometry in the dump region and the settling length fully conforms to a rectilinear system of co-ordinates, the combustion chamber requires special attention due to the presence of the curved section. Initially, a cylindrical polar grid was used and the curved combustor head was simulated in a castellated fashion according to the method of subsection 3.3.2. A typical cylindrical polar mesh is shown in Figure 4.3, together with the approximation of the head surface. The second approach employed body-fitted curvilinear orthogonal meshes which conformed to the irregular shape of the chamber and were generated with the method discussed in subsection 3.3.1. The procedure was first to generate a mesh which included the upper half of the dump region up to the beginning of the parallel walled section. Such a mesh of 50 x 50 (ζ_1, ζ_2) grid nodes is shown in Figure 4.4. This mesh was then reflected to include the lower half and subsequently extended in the downstream direction to include the flow in the annuli. The resulting grids being excessively fine (up to 100 x 100 grid nodes) were computationally expensive and selection of grid lines, based on either empirical knowledge of regions of steep gradients and angled streamlines or systematic examination of the truncation errors in previously performed calculations (see subsection 4.3.3), was necessary to obtain the meshes finally used. Two such grids of 31 x 42 and 80 x 92 grid nodes produced with the above method are shown in Figure 4.5 a, b. Other meshes were also generated to accommodate the changes in configuration due to the variation in the dump gap (see Koutmos and McGuirk, 1983).

4.3.2 The boundary conditions

The boundary conditions for the numerical solution were taken, where available, from the measurements of Fishenden (1974) and were as follows:

(i) Zero velocities were assigned at all solid surfaces and wall functions used to connect the first internal node to the wall. These wall-laws were applied to the curved combustor head in both the stepwise approximation and the body-fitted meshes.

(ii) Zero gradient conditions were applied at the outlet which was located at one annulus gap downstream of station 4. Tests were performed with the outlet boundary further removed from station 4, but no sensitivity of the solution to the location of the zero gradient condition was found. The appropriate flow split in the two annuli was obtained in the following way: the outlet velocity in the streamwise direction was corrected at every cell in both annuli, ie:

$$\begin{aligned} U_{4o}^{k+1} &= U_{4o}^{k} + U_{4o}^{inc} \quad \text{(outer annulus)} \\ U_{4i}^{k+1} &= U_{4i}^{k} + U_{4i}^{inc} \quad \text{(inner annulus)} \end{aligned} \qquad (4.8)$$

where the superscripts k+1 and k refer to the velocity of the outlet boundary and in the preceding grid line respectively. The value of the correction increment was obtained by balancing the overall continuity equation according to the flow split in the two annuli:

$$\begin{aligned} U_{4o}^{inc} &= \frac{(\dot{m}_o - \dot{m}_{last,o})}{\rho A_{4o}} \\ U_{4i}^{inc} &= \frac{(\dot{m}_i - \dot{m}_{last,i})}{\rho A_{4i}} \end{aligned} \qquad (4.9)$$

where

$$\begin{aligned} \dot{m}_o &= \frac{S.\dot{m}_{inlet}}{(1+S)} \\ \dot{m}_i &= \frac{\dot{m}_{inlet}}{(1+S)} \end{aligned} \qquad (4.10)$$

where $\dot{m}_{inlet}$ is the total mass flow rate at the inlet and $\dot{m}_{last}$ represents the mass flow rate before correction. When the solution is converged U^{inc} should have a negligible value and implies that the gradient of U is zero at the outlet while the appropriate flow split is assured.

(iii) The mean velocity at the prediffuser inlet (1) was 26 m/sec, giving rise to a Reynolds number based on the hydraulic diameter of 1.6×10^5. To test the influence of Reynolds number, the mass flow rate was reduced by 30%, but this did not have any influence on non-dimensional velocity profiles. The axial velocity profile at the exit of the prediffuser was available for each case (Table 4.1) from the experimental investigation and was used as boundary condition at the inlet of the calculation domain (plane 2, Figure 4.2). The turbulence kinetic energy at station 1 was estimated from measurements of the axial normal stress assuming isotropy. The turbulence kinetic energy at station 2 was then estimated by assuming a level of increase between station 1 and 2 similar to that found experimentally by Habib and Whitelaw (1982) in their investigation of wide angle conical diffusers followed by a downstream sudden expansion. This gave a value of k inlet of $\sqrt{k}/U_2 = 0.08$. Variation of this value by ±20% did not have any appreciable effect on overall performance or on the details of the flow. The energy dissipation rate at the inlet was calculated using a mixing length formulation based on the dimensions of the prediffuser exit (equation 3.23).

4.3.3 The application of the numerical model

The governing equations were solved in two-dimensional form using the numerical scheme outlined in Chapter III. The iterative cycle of the solution procedure was terminated using a convergence criterion based upon the ratio of the integrated continuity errors in all cells and the total mass flow rate. The solution was considered to be converged when this ratio was less than 10^{-4}.

The influence of the number and location of grid nodes was determined by performing calculations with different grid arrangements and the grid refinement process was aided by the method outlined in subsection 3.4.3. The cylindrical polar grids used ranged from 25 x 25 (x, r) to 45 x 58 grid nodes (Figure 4.3) but further grid refinement was not pursued due to the poor results obtained with this method (see subsection 4.4). The investigation with the boundary-fitted meshes encompassed levels of grid fineness of 31 x 42, 52 x 62 and 80 x 92 (ζ_1, ζ_2) grid nodes and these meshes required computer times to obtain convergence of about 2, 7 and 28 CPU minutes, respectively (on an AMDHAL V8). The finer grid distributions were arrived at by examination of the local Peclet numbers and evaluation of the truncation errors associated with upwind-differencing in the numerical solution. The out-of-balance term was determined using the method of McGuirk et al (1981). This was then plotted against the remaining convection, diffusion and source terms in the equation under investigation to assess its relative importance. Figure 4.6 a, b shows radial profiles of the out-of-balance term in the axial momentum equations, plotted for the 80 x 92 mesh at two axial locations where the errors were found to be typical. Half-way in the dump gap ($x/D_G=0.47$) the error is minimum inside the recirculation regions and slightly increases in the shear layers bordering the two vortices, as the flow in these regions is deflected by the combustor head and is not aligned with the grid. Truncation errors are of order of 23% of the true diffusion in the centre core flow as it emanates from the prediffuser. This is not surprising since as shown in Figure 4.6a in this region convection almost balances pressure gradients and any level of numerical diffusion would be large compared with that of the small physical diffusion. At $x/D_G \simeq 1.75$ (Figure 4.6b) similar profiles are plotted in the two branches of the system near station 3 (Figure 4.2). The distributions show that in this region the errors are unimportant but in relative terms are larger in the inner branch where the maximum error is of order 5% of the physical diffusion.

In general, truncation errors were sufficiently small, as demonstrated above, to be considered unimportant over most of the calculation domain. The region causing most cause for concern is the central core region approaching the combustor head; this demonstrates the unsuitability of solving the full elliptic equations in a region where the Euler equations are closer to reality (Thompson, 1984). Further improvement would require excessively fine meshes with consequences on computer-run time and storage. The effectiveness of the grid refinement undertaken here and the acceptability of the finest mesh predictions was also determined by the relative changes found in the solutions obtained by repeated mesh refinement. On the basis of the above, the 80 x 92 mesh was then employed in the calculation of the geometries with a dump gap of 1.0 whereas for the configurations with dump gaps of 0.5 and 1.5 the 52 x 62 mesh was considered acceptable (as will be demonstrated below) to examine trends in predicted behaviour.

Errors in the numerical solution can also arise due to the non-orthogonality of the grid lines evident in the region near the centre of the combustor head (maximum errors were 40^o, Figures 4.4, 4.5). This deviation from orthogonality is the result of the presence of a singularity in the geometry of the surface which bounds the domain in which the mesh was generated (Figure 4.4). As discussed in subsection 3.3.1, accurate solution of the inverse Laplace equations requires specification of a boundary which is continuous in the first derivative; this requirement is violated at the leading edge of the combustor head. Further, the implication of first-order accuracy in equation 3.39 for locating intersections with the boundary is that the orthogonality constraints are less rigidly applied at boundary cells than at internal nodes where the second order accurate scheme of equation 3.37 is applied (although the condition of orthogonality of the grid line intersections with the boundary itself is strongly applied). Equation 3.37 is not applicable at boundary intersections because it would require the use of nodes outside the calculation domain.

Estimation of this type of error was attempted by comparing the calculated results obtained from one of the above meshes against those obtained with a grid with improved orthogonality (Figure 4.7b). The improved mesh had maximum non-orthogonality errors of 10^o (and this at only a few cells near the centre of the head) which corresponded to a significant reduction of non-orthogonality compared with the original mesh in the region of interest. The improved mesh was achieved by generating a very fine grid and then selecting and adjusting the grid lines in the region of interest. The same number of grid nodes in both meshes were distributed in a similar manner so that any differences in the results could be related to the improved orthogonality. Further quantification of the orthogonality errors would require adoption of a non-orthogonal treatment of the governing partial differential equations (see Demirdzic, 1982).

The two meshes yielded very similar results in most regions of the flow; the main discrepancies were concentrated, not surprisingly, at the leading edge of the combustor head. Figure 4.7c shows the static pressure distribution around the head obtained with the two grids and compared against measurements for the configuration with dump gap 1.0 and flow split 1.3. The static pressure at the wall was extrapolated from the field values with a third order polynomial fitted to the pressure values at the first three internal nodes. Although no improvements in the stagnation static pressure were obtained, it is evident that mesh 1 distorts the pressure distribution around the flame tube, especially in the initial stages of the curved head. The predicted position where the flow starts to decelerate around the head is similar in both cases while the levels of minimum static pressure are lower in mesh 2. The static pressure recovery is steeper in the calculations with mesh 2, resulting in an improvement in the overall static pressure recovery of about 0.01 of the inlet dynamic head (mesh 2 produced an overall static pressure coefficient of 0.33 against 0.32 of mesh 1). The lengths of the recirculation regions in the two corners, the subsequent flow development in the settling lengths and the outlet profiles (except the levels of static pressure) were very similar in both cases. In general, it was found that the errors were contained locally in the region of the non-orthogonal cells around the combustor head and their effect was seen to be largest in the static pressure distribution. The level of error and the discrepancies in the detailed comparisons between the two grids are considered to be small. Consequently, the grids generated without special adjustment to minimise orthogonality errors in the significant region were considered adequate for the purposes of the present investigation.

4.4 Results and discussion

The calculated flow pattern with the cylindrical polar grid and the castellated approximation of the combustor head (Figure 4.3) is illustrated in Figure 4.8a in the form of a plot of the stream function contours for a dump gap of 1.0 and flow split of 1.3. The recirculation regions formed at the dump cross-section are clearly identified and the influence of the flow split is evidenced by the slight upward inclination of the streamline which impinges on the combustor head and the different recirculation lengths of the two corner vortices. Although this flow pattern is certainly qualitatively correct as confirmed by experimental observations (Fishenden, 1974), it seems that the recirculation regions are too small. The experiments show that the separation streamline in the branch with the higher flow reattaches on the horizontal casing wall almost level with the end of the curved combustor and not half-way round as shown here. This level of disagreement is much larger than that usually found in recirculating flow calculations using similar numerical techniques and turbulence models (eg 15-20% discrepancy in sudden expansion flows; Gupta et al (1984)) and will be further discussed below.

The predicted static pressure distributions around the combustor are plotted against the measurements in Figure 4.8b; although the location of the maximum static pressure at the stagnation point is predicted well, its magnitude is underpredicted by 20%. Further comparison between the predicted and measured location of the minimum static pressure indicates that in the measurements the flow accelerates from the stagnation point to about two thirds of the way round the head before diffusing into the surrounding annuli while in the predictions diffusion is initiated at a distance of only one third of the way round the curve. The jumps in the static pressure distribution in this region coincide with the castellation in the approximated head shape and provide evidence of further disadvantages of this kind of approach for complex geometries where the flow direction is towards the boundary wall. The differences between the predicted and measured velocity and static pressure profiles at station 3 (Figure 4.8c) plotted along the extension of the combustor head radius (Figure 4.2), confirm the excessive amount of diffusion present in the predictions. It is noteable, however, that this is not accompanied by a static pressure rise and, consequently, total head loss results. In the calculation, the flow is unable to gain any more static pressure up to the exit from the settling length and this results in an underestimation of the overall static pressure recovery by about 57% with attendant total pressure losses about 78% higher than the measured value. The predicted velocity profiles at station 4 (Figure 4.8d) are qualitatively incorrect with the maximum in the velocity profile located away from the combustor wall in stark contrast to the measurements.

The above discrepancies between measurements and calculations in both overall performance and in the details of the flow are clearly related to the poor prediction of the flow development in the region around the combustor head. Inspection of the various terms in the axial momentum equation with the residual balance technique of McGuirk et al (1981) (see subsection 4.3.3) showed that the relative importance of the truncation errors remaining in the castellated solution was similar to that of the truncation errors in the solution obtained with the 31 x 42 boundary -fitted mesh. The examination, however, also showed that in the vicinity of the stepped approximation physically unrealistic gradients in the velocity and pressure field (Koutmos and McGuirk, 1983) led to steep reductions in total pressure as indicated by the above discussion. Although the stepped approximation has been used with some success in various flows, in the present configuration it is positioned adjacent to a strongly accelerating layer of flow that approaches the steps (which can perhaps be thought of as acting as excessive surface roughness) thus resulting in total head loss. A similar approximation of the sloping walls of wide angle diffusers was used by Sala et al (1980) and the marked increase in the discrepancies between measured and predicted static pressure profiles near the castellation implies effects similar to the above. Although the representation of the curved walls with the above method will improve as the grid is further refined, the approach is definitely inefficient in terms of grid node distribution and not worthwhile pursuing in view of the improvements obtained with coarser boundary-fitted meshes which offer significant advantages over the cylindrical polar grids in controlling numerical diffusion errors due to better alignment of the flow streamlines with the grid lines.

A plot of the predicted stream function contours obtained with the boundary-fitted mesh of figure 4.5b for the same configuration and flow split is illustrated in Figure 4.9a. This calculation now produces corner eddies with recirculation lengths of 2 and 1.4 dump gaps (D_G) for the outer and inner vortex respectively which represent an improvement of about 18% over the results of the previously discussed calculation. Both finer grids used (52 x 62 and 80 x 92) produced the same reattachment lengths, being 8% longer than those obtained with the 31 x 42 grid, indicating the diminishing influence of grid density. It is extremely important in this flow for the calculation method to be able to represent adequately the two recirculation regions as the fluid captured in them is useful in the design process when cabin air bleed is utilised in an engine environment or in the development of the vortex-controlled diffuser systems where flow suction is attempted to achieve improved performance (Smith, 1979). Furthermore, the size and shape of the two stationary vortices defines the size and shape of the region between the separation streamline and the combustor head which influences the amount of turning, acceleration and subsequent diffusion of the flow. The recirculating fluid for the above configuration flow split was found to be 11% and 6% of the total mass flow rate for the outer and inner vortex respectively.

The predicted and measured static pressure distributions around the flame tube are shown in Figure 4.9b, where the effect of grid refinement is also included. The magnitude of the predicted minimum static pressure is now much closer to the measurements while its position lies half-way around the head, implying an earlier static pressure rise than the measurements. The consistent underprediction of the stagnation static pressure on the combustor head (which is thought to be associated with the remaining truncation errors in this region, Figure 4.6a) could influence the flow development around the head and contribute to the above discrepancy; in addition, the performance of the turbulence model can be called into question in this region where streamline curvature effects on the flow are possible as discussed below. The calculated static pressure recovery is overestimated up to the end of the flame tube head but underpredicted in the later stages of the settling length subsequent to the flow turning in the axial direction. The predicted overall static pressure recovery and loss coefficient have now significantly improved and the results of the 80 x 92 mesh show levels of agreement within 7% of the inlet dynamic head (or 14% in terms of absolute values). The strong acceleration of the flow around the head is represented well with the boundary-fitted mesh (Figure 4.9c) and the static pressure profile is now consistent with flow over a convex surface with $\partial P/\partial h_3 > 0$. As implied by the coincidence of the location of the zero velocity in the measurements and calculations, the size of the recirculation in this position is predicted well. Although the initial velocity profiles at entry to the annulus (Figure 4.9d, profile (a)) are different in each branch due to the different recirculation lengths, efficient mixing over the settling length produces inner and outer profiles of similar shapes at station 4 (Figure 4.9d, profile (b)). The biasing in the location of the maximum velocity towards the combustor wall, in the developed profile, is consistent with turbulent annular flows (Brighton and Jones, 1964) and with the measurements of Chapter II and is borne out by the predictions. Once again, the diminishing returns aspect of the grid refinement is illustrated in the velocity profile predictions.

Figure 4.10a shows the static pressure distribution for the same dump gap and a flow split of 2.57. As the flow in the outer annulus increases, the higher acceleration of the flow near the head causes a more severe decrease in pressure in this branch, resulting in an asymmetric C_p distribution in both the measurements and the calculations. As the dump gap increases by 50% (D_G/h_2=1.5), the flow is allowed to initially decelerate in the dump region and turns around the head with a reduced dynamic head so that a lower adverse pressure gradient (Figure 4.10b) results. Asymmetries in the C_p distribution in this case are generally reduced in both measured and predicted results.

The influence of the variation of the flow split on the overall performance for a dump gap of 1.0 is illustrated in Figure 4.11. The effect is small in the region of flow splits between 1.0 and 2.0 with the maximum predicted and measured C_p obtained at a flow split of about 1.7. The greater loss incurred at flow splits higher than 2.3, is the result of a steeper decrease in static pressure (Figure 4.10a). The severe adverse pressure gradient on the combustor walls does not cause local separation, however a large pressure loss is generated in the adjacent region where the flow diffuses rapidly. Since in most cases both the measured and predicted velocity profile energy coefficients are very close to unity (Figure 4.11b), they do not contribute significantly to the difference between the actual and ideal pressure recovery and the major loss of available energy is due to internal mixing and viscous effects (λ_{1-4}). In general, the trends in the variation of C_p and λ are closely followed by the predictions and the level of agreement with measurement is maintained at about 7% of the inlet dynamic head. This compares well with the results of Sala et al (1980) and Habib and Whitelaw (1982) who used similar finite-difference techniques and turbulence models in their investigation of simpler configurations.

The predicted variation in performance with changes in flow split for the configurations with dump gaps of 0.5 and 1.5 and the effect of changes in the dump gap on the overall static pressure recovery and loss coefficient for a constant flow split of 2.48 are depicted in Figure 4.12. The trends identified in these graphs can be explained by detailed examination of the predicted flow field. For small dump gaps, there is strong acceleration around the head and the calculated results show that the velocities in the higher flow branch (outer) rise to values approximately 1.5 times those at station 2. The steep radial gradients which then exist under these conditions imply high generation of turbulence and, consequently, high transfer of momentum and energy towards the vortex. As the flow split increases, the strength of the vortex increases and the above process is enhanced. The above factors combined with the high dynamic pressure at station 3 which causes steep adverse pressure gradients, accounts for the increase in loss as the dump gap decreases (Figure 4.12c). At large dump gaps, the flow diffuses in the dump region prior to acceleration around the combustor head and creates milder adverse pressure gradients (Figure 4.10b) thus resulting in the trends of Figure 4.12c. In general, at large dump gaps the overall loss coefficient is insensitive to flow split variations as Figure 4.12b indicates. The overall level of agreement between measurements and calculations in the above configurations is of the order of 10% of the inlet dynamic head (for the grid of 52 x 62 grid nodes) and the deterioration in the case of dump gap of 0.5 is attributed to the higher truncation errors due to the increased difficulty of aligning the flow with the grid lines in this geometry.

Although no turbulence data are available from the measurements, some comments on the performance of the turbulence model can be made in terms of the predicted results. Levels of turbulence kinetic energy were 60% higher than the inlet value in the shear layers formed between the vortex and the core flow emanating from the prediffuser while inside the recirculation region they were 20% higher than the inlet value. In all investigated cases, the maximum levels of turbulence were found in the high branch flow near station 3, where the strongly accelerating fluid borders the recirculation and were of order $3k_{inlet}$. As the flow turns around the combustor head in the vicinity of stagnation (Figure 4.9a; flow concave to head) and then downstream of station 3, returns to the axial direction (flow convex to head) extra strain rates are introduced due to the curvature whose effects are known not to be well predicted by the $k-\epsilon$ turbulence model as discussed in Chapter III. Further, the effective viscosity hypothesis is unable to represent asymmetric flows where the position of zero velocity gradient and zero shear stress do not coincide (Reece, 1976). However, neither of these effects seems to be dominant in the present flow pattern where large pressure gradients and convective flows were seen to dominate (Figure 4.6). A full assessment of the performance of the $k-\epsilon$ turbulence model can only be undertaken on the basis of detailed comparisons with turbulence data and after the remaining truncation errors in the vicinity of the stagnation on the combustor head have been completely removed.

In general, the results could be improved with respect to the turbulence model performance by using an algebraic stress model (Launder, 1982) or the specification of empirical formulae for the constants in the k-ϵ model as functions of the Richardson number (Launder et al, 1977; Rodi, 1979) which have been shown to yield improved results (Rodi, 1979; Hah, 1983). It is clear, however, that in order to exploit completely the merits of such improved turbulence models a higher order numerical scheme that responds more efficiently to grid refinement should be used in parallel and the results of Rodi (1980) and Hah (1983) certainly confirm this. This is especially required in the present complex geometry where it is almost impossible to align a priori the mesh with streamlines over most of the flow domain and very fine meshes are necessary to obtain an acceptable level of grid independent solutions as the above investigation has shown. Nevertheless, the numerical study has highlighted the practical problems in the calculation of this flow and provided useful insight into the details of the flow and the influence of such parameters as the dump gap and flow split. Most importantly, it should be emphasised that although absolute values were in error, the trends in overall performance caused by changes in the above parameters were reproduced faithfully by the present numerical method - a most important consequence for engineering design calculations.

4.5 Summary

The numerical prediction of turbulent flows in branched annular dump diffuser systems showed that:

(i) The choice of co-ordinates and the representation of the curved combustor head are very important in the calculation of this flow system. The use of a cylindrical polar co-ordinate mesh and a castellated approximation of the curved head caused excessive total pressure loss in the vicinity of discontinuities in the approximated surface and resulted in underestimation of the recirculation lengths (by about 40%) and the overall static pressure recovery (by about 57%).

(ii) The use of a boundary-fitted mesh helped to represent the flame tube head accurately and enabled significant improvements in the prediction of the overall performance and the detailed development of the flow to be achieved at a much lower level of grid density. Solutions obtained with the 80 x 92 mesh produced corner recirculation lengths 18% longer than those of the cylindrical polar grid while the overall static pressure recovery and loss coefficient were predicted to within 7% of the inlet dynamic head. Detailed comparisons between measurements and predictions showed that the calculation method represents well the velocity and static pressure profiles at the initial stages of the settling length and the exit. Parametric studies over a range of operating conditions indicated that the effect of the variation of the flow split and dump gap can be predicted.

(iii) In view of the high grid density required to obtain acceptable grid independent solutions with the hybrid-differencing scheme employed in the above investigations, it is suggested that the calculation can be improved by adopting a higher order finite-difference method which will minimise numerical diffusion at a lower computational cost. Further improvements can also be brought about by the exploitation (after the above has been implemented) of a turbulence model which represents better than the k-ϵ model the effect of the streamline curvature.

(iv) Despite the remaining discrpancies between measured and calculated results, the calculation method is capable of providing results for dump diffuser flow systems which are of sufficient accuracy for engineering purposes. The predicted results in the annulus are also of sufficient accuracy to be used as boundary conditions for the calculation of the flow inside the combustion chamber.

CHAPTER V

THE CALCULATION OF THE FLOW FIELD INTERNAL TO COMBUSTION CHAMBERS

5.1 Introduction

This chapter presents the application of the numerical techniques described in Chapter III to the calculation of flow fields internal to a combustion chamber. The study is mainly concerned with the flows encountered inside the water model combustor of Chapter II, but the isothermal flow fields in different geometric configurations of practical interest are also considered. The following section describes the approaches adopted for the efficient calculation of the complex model combustor geometry and provides details of the finite-difference meshes used. The boundary conditions and the details of the application of the numerical model are also discussed. The series of calculations of the flows of Chapter II are presented in section 5.3, while section 5.4 provides a brief assessment of the capabilities of the model in relation to the discrepancies between measurements and predictions. Section 5.5 presents calculations of the isothermal flow fields inside a geometry different to the model used here, but representative of a current production can-type combustion chamber. Finally, a summary of the main findings and conclusions of the investigations is given in section 5.6.

5.2 The calculation details

5.2.1 Arrangement of the calculation and finite-difference meshes used

The flow configuration of interest in the present investigation is the internal flow region of the water model combustor of Figure 2.2. As discussed in Chapter I, in most practical cases the flow development and the local pressure gradients in the annulus determine the jet trajectories and mass flow through the ports. The accurate numerical prediction of the internal combustor flow field requires the specification of accurate jet entry boundary conditions and this in the absence of experimental data, often necessitates the calculation of the annulus flow.

In the present study, however, reliable and accurate information about the *primary and dilution jet entry* conditions was available from the measurements of Chapter II so that attention could be focussed on the internal flow, thereby eliminating the uncertainties that can accrue from the calculation of the annulus (Green and Whitelaw, 1983).

The efficient calculation of this model combustor (which comprises three distinct geometric sections), necessitated the adoption of an approach which allowed the correct representation of the interacting flow regions encountered inside the various combustor sections, whilst minimising computational effort. The detailed experimental investigation of Chapter II and the available techniques for treating complex geometries described in Chapter III provided useful directions as to the manner in which the above task could best be achieved. The measurements indicated the consistent cyclic behaviour of the flow over a 60^o sector up to the second row of holes (plane l) where asymmetries started to appear in the profiles. It was therefore decided to adopt a zonal approach where the whole combustor flow domain was split into two overlapping zones (Figure 5.1). Zone A comprised the hemispherical head of the combustor and the cylindrical barrel and zone B which included the downstream portion of the can containing the second row of holes and the circular to rectangular nozzle. In this arrangement, zone A can be calculated with a cylindrical polar grid which reduces the number of grid nodes to those required to resolve the flow domain in the 60^o sector. The inclusion of the dilution jets in this domain is necessary in order to introduce their effect on the upstream flow in the latter stages of the intermediate zone. A cartesian mesh can then be employed to calculate zone B with the use of the method described in subsection 3.3.3. Starting the calculation of zone B at a cross-section in the intermediate zone well upstream of the dilution holes allows for any non-cyclic behaviour of the dilution jets due to the upstream effect of the nozzle. The results of the calculation of zone A were used as boundary conditions at the inlet plane of zone B which is located at plane j (Figure 2.9). Numerical tests with the calculation of zone B starting downstream of the dilution holes (plane m) yielded results inferior to those obtained with the above arrangement which was considered to be optimum in terms of economy, accuracy and resolution of the flow field. The dilution jets could be neglected in zone A which would then terminate at the beginning of zone B but in this case simultaneous solution of the two domains would be required, resulting in excessive storage requirements and possible uncertainties in the boundary conditions needed to link the two calculation regions. At this stage, only a one-way coupling has been taken into account (ie the calculations in zone A influence those in zone B but not vice versa). Further testing involving a two-way coupling and repeated calculations in the two zones will be undertaken when the results of the present calculation are fully analysed.

The range of finite-difference meshes used for the calculation of zone A are shown in Figure 5.2. The influence of the representation of the hemispherical combustor head geometry was examined by comparing the numerical solutions for the flow in zone A, obtained with two different approaches while using the same finite-difference mesh (grid 1, Figure 5.2). In the first, the curved combustor head was simulated with the castellated approximation of subsection 3.3.2 while in the second, the general arbitrary boundary method discussed in subsection 3.3.3 was used. The comparison showed that both methods yielded identical results in all regions of the flow and, in particular, in the vicinity of the curved combustor head. The above tests suggested that the stepped approximation of the curved walls, in the present flow, does not incur errors as important as those found in Chapter IV; the reason is thought to be that the flow in this case is directed predominantly away from the irregular boundary. In addition, the comparison provided a further confirmation about the correctness of the assumptions employed in the boundary cell treatment of the general arbitrary boundary method. As a result of the above tests, and because of the higher computer storage requirements of the general arbitrary boundary code (by about 10% in the above tests), all further computations of this zone were performed with the cylindrical polar grids of Figure 5.2 and the castellated approximation of the curved combustor head surface.

The finite-difference mesh used for the calculations of zone B is shown in Figure 5.3. According to the requirements of the general arbitrary boundary method, the whole geometry to be calculated was contained within the rectangular box comprising the mesh, as indicated in Figure 5.3. The dimensions of the nozzle were measured directly from the water model combustor and the description of the nozzle cross-section at several successive axial locations (Figure 5.4a) was input to a surface fitting routine which constructed the surface of the nozzle and the adjoining can section from the discretised data (Figure

5.4b). The intersections of the grid lines with the surface were then obtained and used to calculate all near boundary quantities required by the arbitrary boundary flow calculation code as described in subsection 3.3.3.

Due to the limitations of the cartesian and cylindrical polar systems, the simulation of the primary and dilution holes required special attention. In the cartesian mesh used in conjunction with the general arbitrary boundary method, the procedure described in subsection 3.3.3 was used to obtain the correct fluxes through the dilution holes. In the cylindrical polar grids used in the calculation of zone A, the method applied is similar in concept to that described in subsection 3.3.3, but is formulated in a simpler manner due to the coincidence of the grid surface with the plane of the holes. The actual hole shape (in this case circular) is used to determine which control volume faces, in the plane of the hole, either lie completely inside or are intersected by the hole surface. The flow variables in these cells are then ascribed boundary values appropriate to the boundary conditions in the hole and the correct fluxes are obtained by multiplying the density of the jet fluid at these nodes by an area ratio as follows:

$$\rho_B = \rho_{fluid} \cdot \frac{A_i}{A_{total}} \qquad (5.1)$$

In the above formula, A_i is the area of that part of the cell face which lies inside the hole and A_{total} is the total cell face area (Figure 5.5). The area ratio is one for cells lying completely inside the hole and in the grids 2 and 3 in Figure 5.2 its value was about 1.1 - 1.2 for cells intersected by the hole surface. Further comments about the use of correction factors of this type will be made in subsection 5.2.3. In general, the above procedure allows a better simulation of the hole shape, this simulation improving as the grid is refined; it represents a more accurate method of introducing dilution holes into the calculation domain than those used by Green and Whitelaw (1983) and Bruce *et al* (1979).

5.2.2 The boundary conditions

The boundary conditions for the calculation were mainly taken from the measurements and their implementation is according to the discussion of subsection 3.2.4. These for the calculation of zone A were as follows:

(i) Zero slip velocities on all solid walls and the wall functions described in subsection 3.2.4 were used for the near wall nodes.

(ii) On the combustor centre line, boundary conditions appropriate to a symmetry axis were applied (see subsection 3.2.4ii).

(iii) The periodic nature of the flow over a 60^o sector allowed the cyclic boundary conditions, described in subsection 3.2.4iii, to be used for all variables at the edges of the periodic domain (Figure 3.2b).

(iv) At the swirler inlet, uniform axial, azimuthal and zero radial velocity profiles were specified. The axial velocity was determined from the appropriate mass flow rate through the separate feed for the swirler. The tangential velocity was calculated from the definition of the swirl number (equation 2.1) assuming uniform axial and azimuthal velocity distributions at the swirler exit. The magnitude of the swirl number for swirler 1 was available from measurements close to the swirler exit (cases 1 to 5, table 2.1) while for swirler 2 (cases 7 to 9) the swirl number was evaluated from the swirler geometry. Numerical tests made with non-uniform velocity distributions and non-zero radial velocities at the swirler exit (by using triangular profiles with peak values of 1.5 times the mean axial velocity corresponding to the bulk flow through the swirler for the U and W and 0.6 times this value for the V component) did not show any improvements in the predicted flow field mainly due to the intense mixing in the primary zone caused by the primary jets. No measurements of the mean and turbulent quantities were obtained in the vicinity of the swirler inside the combustor due to the refraction of the laser beams on their passage through the hemispherical combustor head. Detailed profiles of the three normal stresses were, however, obtained immediately upstream of the swirler inside the separate feed and the turbulence kinetic energy distribution deduced from these was used as the inlet boundary condition. A 20% variation in the inlet turbulence kinetic energy boundary condition was found to have no effect on the calculated turbulence kinetic energy distributions downstream of the swirler due to the very high levels of turbulence generation in the primary zone region. The boundary conditions for the energy dissipation rate at the swirler exit were evaluated from the turbulence kinetic energy values assuming a length scale proportional to the swirler exit height (equation 3.23).

(v) At the primary and dilution holes, the axial and azimuthal velocities were available from measurements and were used as boundary conditions at the plane of the hole. The radial velocity at the jet entry was calculated from the mass flow rate at each hole. The measured values of the axial and azimuthal normal stresses were also used to determine the kinetic energy boundary condition (assuming $\sqrt{\overline{v^2}}=\sqrt{\overline{w^2}}$) and from that the energy dissipation rate was calculated with the assumption of a length scale proportional to the hole diameter. A variation of the radial velocity by about 6% (representing a percentage which is similar to the estimated error in the integration performed to obtain the flow split between the holes) had no significant qualitative effect on the flow pattern. A 40% increase in the turbulence kinetic energy boundary condition increased the maximum turbulence kinetic energy found in the primary jet impingement position by about 3% and decreased the maximum negative velocity by about 1.5%.

(vi) *Zero* gradient conditions ($\partial\phi/\partial x=0$) were applied for all variables at the outlet plane. The solution was not sensitive to the variation in the location of the outlet plane from 3 (for grid 1, Figure 5.2) to 6 (for grid 3) hole diameters downstream of the dilution jets.

The boundary conditions for zone B are similar to those for zone A with the inlet boundary conditions for this zone provided by the calculation of zone A at the beginning of the overlap of the two zones. Again, uniform dilution jet entry conditions around the periphery of the can were used for the dilution jets in the calculation of this zone. A representative set of the boundary conditions for the calculation of the flow in case 2 (Table 2.1) is given in Table 5.1.

TABLE 5.1

BOUNDARY CONDITIONS USED FOR THE CALCULATION OF CASE 2

	U(m/sec)	V(m/sec)	W(m/sec)	$k(m^2/sec^2)$	$\epsilon(m^2/sec^3)$
swirler exit	0.463	0	0.55	7×10^{-4}	3.46×10^{-3}
primary holes	0.15	2.3	0.08	9.5×10^{-4}	2.9×10^{-3}
dilution holes	0.27	1.82	0.18	1.33×10^{-3}	4.85×10^{-3}

5.2.3 The application of the numerical model

The equations for velocity, pressure, turbulence kinetic energy and energy dissipation rate were solved in finite-difference form, in the three-dimensional domain using the numerical techniques outlined in Chapter III. A convergence criterion similar to that described in subsection 4.3 was used and the iterative process was terminated when the overall continuity error was less than 10^{-4} of the total mass flow. The influence of grid node distribution and mesh size was determined by performing calculations with different grid arrangements. The range of cylindrical polar grids used encompassed 18 x 9 x 9, 34 x 14 x 12 and 45 x 18 x 15 (x, r, θ) grid nodes (Figure 5.2) with storage and computer run time requirements at each level of grid fineness given in Table 5.2.

TABLE 5.2

COMPUTER STORAGE AND EXECUTION TIME REQUIREMENTS (AMDAHL V8)

GRID SIZE	STORAGE	TIME
18 x 9 x 9	352 k	6 min
34 x 14 x 12	900 k	30 mins
45 x 18 x 15	1900 k	74 mins

The level of increase in grid lines was greater in the axial direction where the largest gradients were identified in the experimental results (90% and 32% increase in grid lines in the first and second level of grid refinement). The increase was smaller in the azimuthal direction as three-dimensionalities were small away from the primary and dilution jets (30% and 25% increase in grid lines in the first and second level of grid refinement).

The difficulty associated with grid refinement in three-dimensions, due to limitations in computer storage capacity and the high cost of computer time, has been discussed by Jones and McGuirk (1979). However, confidence in the solution can be gained by inspection of the relative changes occurring in the solutions obtained in the successively refined meshes. The effectiveness of the grid refinement process is illustrated in Figure 5.6, which shows radial profiles of the axial velocity and turbulence kinetic energy obtained with the three grids of Figure 5.2 and plotted at five axial planes which exhibited the greatest sensitivity (profiles presented in this and all subsequent subsections in this chapter have been non-dimensionalised and plotted similarly to those in Chapter II and the plane numbers are the same as those in Figure 2.9). The changes in the axial velocity profiles as the grid node density increased from 18 x 9 x 9 to 34 x 14 x 12 (representing an average increase in grid lines in all directions of 60%) were about 30% in most stations with the maximum effect at plane d where the results changed by more than 70%. The turbulence kinetic energy distributions showed greater sensitivity than other variables (particularly in the vicinity of the primary jet impingement position) with overall changes in the first level of grid refinement of about 60% at most stations. At the second level of grid refinement to 45 x 18 x 15 grid nodes (representing an average increase in grid lines of 30%) the changes in the mean axial velocity were about 1.5% while in the turbulence kinetic energy they were about 3%. This clearly demonstrates the diminishing influence of the grid node density on the solution. As both the finer grids gave essentially similar solutions, as indicated by the distributions of Figure 5.6, the results of the 34 x 14 x 12 mesh were considered acceptable in terms of economy and accuracy. Consequently, this mesh was used to obtain the calculated results of zone A presented in subsection 5.3.

The cartesian mesh of 12 x 10 x 9 grid nodes shown in Figure 5.3 was used to perform all the calculations for zone B. No further grid refinement was pursued due to time limitations. The favourable comparison between the calculated results obtained with this mesh and those obtained with the finer cylindrical polar grids in the regions where they overlap and the dominance of large pressure gradients in creating the flow pattern in the dilution region (as discussed below) could suggest that this level of grid node density is likely to represent the flow qualitatively accurately. A fuller assessment of numerical errors in this region can only be made by using a significantly finer mesh as has been done for the zone A calculations.

The higher efficiency of the grid refinement process inside the combustor (at least in zone A) as compared to the same process undertaken in the calculations of the dump diffuser can be attributed to the dominance of the primary and dilution jets in creating the flow pattern in this type of combustor. This results in large pressure gradients which have been found to dominate most regions of this type of flow (Green, 1981; Serag Eldin, 1977). In the present investigation, the axial pressure gradient term was found to dominate by about two orders of magnitude the other terms in the axial momentum equation inside the primary zone; in addition, the high generation of turbulence kinetic energy caused high turbulent viscosities (ν_t) and this effectively reduced the local cell Peclet numbers in this region. These suggest that the influence of numerical diffusion is likely to be small in these regions (Green, 1981). The zonal approach and the use of cyclic boundary conditions also contributed to this aspect.

Numerical errors can also occur from the method of correction of the fluxes at the jet entry planes via a false density factor as described in subsections 3.3.3 and 5.2.1. It was found that when these correction factors were higher than about 1.3, a circumferential pressure gradient was created in the vicinity of the hole which lead to increased spread of the jet. In the calculations of zone A, the correction factors were lower than the above value (for grids 2 and 3) and such errors did not influence the solutions. In the calculations of zone B, however, correction factors of about 3 were used due to the non-coincidence of the plane of the hole with the grid surface (as discussed in subsection 3.3.3) and the coarseness of the grid. This point will be addressed again in the presentation and discussion of the results.

5.3 Results

The calculated results for all investigated cases of Table 2.1 are now presented and compared with the measurements in terms of radial profiles and contour plots of the three mean velocities and turbulence kinetic energy. The former type of comparison provides detailed information about the accuracy of the calculation method in predicting the local gradients while the latter provides an evaluation of the overall level of qualitative correspondence between measurements and predictions.

Mean velocity profiles

Figure 5.7 shows the comparison between experiment and calculation for the radial profiles of the axial, azimuthal and radial velocities for the swirler flow level of 10%. In the primary zone, the negative axial velocities near the centre line were underestimated with a maximum discrepancy of about 30% occurring near the primary jet impingement position (plane d). The level of agreement improves within the recirculation region (plane b) and in the intermediate zone, planes f, h, k. The radial velocity distribution at plane d is, however, predicted well indicating the correctness of the jet entry boundary condition. The increased discrepancy in the prediction of the axial velocity in the vicinity of the primary jet impingement position is related to the performance of the turbulence model and will be discussed further in the presentation of the turbulence results.

Swirl velocities are predicted fairly accurately up to station d but thereafter the shift of the swirl peak towards the combustor wall is not predicted correctly and the Rankine vortex type of profile is retained in the calculation in contrast to the measured solid body rotation type of distribution (planes f, h). Larger swirl velocities are predicted in the vicinity of the wall as the flow enters the intermediate zone, but the peak velocity still remains near the centre line.

As discussed in subsection 5.2.1, due to the overlap of the two calculation domains, the dilution region profiles were calculated in both zones and the results of each calculation have been plotted at stations l and m. In the calculation of zone A, the radial velocity gradient at plane l (Figure 5.7c) is predicted correctly near the dilution hole indicating that the jet entry boundary conditions are correct. The penetration of the dilution jets near the axis is, however, underestimated and this allows the bulk flow, in the calculation, to exit from the dilution jet plane through the centre line region leading to a large overestimation of the axial velocities at this position (Figure 5.7a, plane l). In contrast, in the calculation of zone B, although $\partial V/\partial r$ is initially underestimated at this station (due to the coarse representation of the holes in the zone B calculations) the penetration of jet fluid to the centre line is predicted correctly. The calculation in zone B clearly shows improvements in the qualitative features of the axial velocity profiles (eg the off centre line axial velocity peaks at plane m and the low centre line axial velocity at plane l). The maximum level of disagreement in this region is about 50%. The results also indicate that the variation in the pressure field caused by the acceleration induced by the nozzle does influence the flow in the upstream region. In this zone, discrepancies also stem from the asymmetric behaviour of the dilution jets, as discussed in subsection 2.3, and this can explain the differences in the prediction of the swirl velocity; the use of large density correction factors at the jet holes in the calculation of zone B is also thought to contribute to the inaccuracies.

The calculated results for the 15% swirler flow level (Figure 5.8) generally exhibit levels of agreement with the experiment similar to the previous case. This implies that all the relative changes that have occurred in the flow pattern due to the increase in swirler flow (ie increased swirl velocity levels, decrease in primary jet trajectory and primary zone maximum negative axial velocities) have been simulated correctly. Comparison between measurements and predictions at the various θ planes where measurements were taken (Figure 5.9) and at selected positions where the azimuthal variation was large showed very similar levels of three-dimensionality which in both experiments and predictions was confined to the vicinity of the primary and dilution holes.

Figure 5.10 displays the predicted flow field for the swirler flow of 20%. The comparison shows that the steep primary zone flow variations and overall trends throughout the combustor, identified in the measurements, have been predicted well. Inside the primary vortex, the calculated axial and radial velocity profiles at plane b indicate the correct upstream contribution of the primary jets; this is related to the accurate prediction of the primary jet trajectory at plane d (Figure 5.10c). Although the calculated swirl profile is now in qualitative agreement with the measurements at exit from the primary zone (Figure 5.10b, plane f) in the downstream development, discrepancies similar to those found in the lower swirler flows arise and remain throughout the intermediate zone. In the dilution zone agreement with experiment has now generally improved, as compared to the previous cases. One reason for the improvement is thought to be the higher axial and azimuthal momentum of the cross-flow which is now able to deflect the dilution jets strongly and suppress any influences arising from the unsteady annulus flow; improvements in the predicted turbulence field (see discussion below) also contribute to the above.

The predicted velocity field for 25% swirler flow level is depicted in Figure 5.11. Comparison between the predicted and measured axial velocity profiles at planes c and d for the successive swirler flows of 10, 15, 20 and 25% clearly illustrates that the underlying trend of a decrease in the strength of the primary vortex has been calculated qualitatively and quantitatively correctly. This can be attributed to the consistently accurate prediction of the primary jet penetration (Figures 5.7, 5.8, 5.10, 5.11c, plane d). In common with the measurements, a positive axial velocity has now been calculated on the centre line within the primary zone at planes c and d. It seems, however, that the predicted length of the recirculation region adjacent to the swirler hub is too long, as implied by a calculated negative axial velocity found on the centre line at plane b. The axial velocity peaks measured on the combustor axis, due to the precessing motion, were not predicted by the calculation scheme although a slight tendency for an axial velocity peak may be observed in the zone B calculations. This causes the large discrepancies near the centre line at planes h, k. The prediction of the swirl velocity profiles in the intermediate zone has now improved significantly as compared to the previous cases and this is also related to improvements in the prediction of the turbulence field as discussed below. In the dilution region, the differences between the predicted profiles in zone A and zone B at plane m are generally reduced; this denotes that the upstream effect of the nozzle decreases with increasing bulk flow and shallower penetration of the dilution jets.

As the swirler flow increases to 28% (Figure 5.12) and then to 35% (Figure 5.13), the overall level of agreement generally remains similar to that of the previously examined cases. In the intermediate zone, however, the discrepancy in both axial and azimuthal velocities near the centre line has now increased further due to the inability of the numerical method to predict the increasing effect of the strong rotation and precession in this region. (Note non-zero swirl velocities on the axis in the measurements, eg Figure 5.12, plane h onwards).

The calculation of the flow patterns obtained with swirler 2 operating with 15% swirler flow is shown in Figure 5.14. Comparison between Figures 5.8 and 5.14 reveals that the variations in the primary zone flow pattern caused by the introduction of swirler 2 are well reproduced by the calculations. The decrease in primary jet penetration

(Figures 5.8, 5.14, plane d) and the resulting reduction in the maximum axial negative velocity in the primary zone were calculated to within 20%. In common with the measurements, the predictions show that in the intermediate zone swirler 2 reduces the levels of axial velocity while increasing the angular component. Similar levels of agreement were obtained in the calculation of cases 7 and 9.

Turbulence kinetic energy profiles

The predicted turbulence kinetic energy distributions for the various swirler flow levels are depicted in Figure 5.15. At the lower swirler flow of 15% (Figure 5.15a), turbulence kinetic energy profiles are predicted well inside the primary zone, plane b, while the discrepancy increases in the vicinity of the primary jet entry plane where turbulence energy levels are underestimated by about 40%. In the discussion of the measuremetns in Chapter II, it was suggested that the anisotropy of turbulence and the increase in $\sqrt{\overline{u^2}}$, $\sqrt{\overline{v^2}}$, $\sqrt{\overline{w^2}}$ and hence k in this position was mainly due to normal stress ~ normal strain generation terms; this implies that transport of each component of Reynolds stresses should receive separate consideration if correct levels and partitioning of turbulence kinetic energy were to be calculated. The underestimation of turbulence levels in this region illustrates the weakness of the k-ϵ turbulence model and this deficiency is likely to be responsible for the increased discrepancy in the mean flow prediction in the primary jet impingement region. As the individual normal stress distributions become more uniform and of similar magnitude at the later stages of the intermediate zone, the calculation of turbulence energy levels improves (Figure 5.15a, planes h, k). The prediction of turbulence kinetic energy again deteriorates in the dilution region where turbulence is generated by both shear and normal stresses due to the steep penetration of the dilution jets at this swirler flow.

Better agreement between measured and predicted turbulence levels is seen at the swirler flow of 20% over the whole combustor flow field. Maximum discrpancies are now found at plane f (about 30%) where primary jet fluid continues its penetration to the centre line and at plane l (about 60%) where the dilution jets enter the combustor. Further improvements are obtained at 28% swirler flow with the level of discrepancy in the primary zone now reduced to about 25% (plane f). The centre line peaks in the turbulence kinetic energy distribution due to non-turbulent contribution from the processing motion are not found in the calculation and this is consistent with the mean flow prediction.

Centre line profiles and contour plots of the mean and turbulence fields

Figure 5.16 illustrates the centre line development of the predicted and measured axial velocity and turbulence kinetic energy for 15, 20 and 25% swirler flow rates. In the lower swirler flows, maximum discrepancies are found near the jet entry planes (d, l) and are associated with jet impingement. Consistent improvements in the prediction of both the mean and turbulence profiles are shown in the higher swirler flows (Figure 5.16, b, c) whilst the precession of the vortex core is the main reason for the underestimation of the flow development at the later stages of the intermediate zone.

An overall evaluation of the degree of correspondence between experiment and calculation, as the flow patterns change due to the variation of the swirler flow, can be gained by comparing on the basis of contour plots (Figures 5.17 - 5.20). In these, the measured data are on the upper half while the predicted data are on the lower half; the results of zone B calculation were also included for the dilution zone. At the lower swirler flow of 10% (Figure 5.17a) the steep penetration and dominance of the primary jets in creating the upstream recirculation is evident in both the measurements and the predictions. The length of the primary vortex is calculated correctly while its width is slightly underestimated. The ability of the method to predict the small recirculation regions near the combustor wall downstream of the primary holes is encouraging for its use in the design process, since the designer wishes to know of such small stagnation regions which cause overheating, hot spots and influence critically the life of the chamber. The predicted swirl velocity contours near the centre line (Figure 5.17b), associated with the maximum swirl velocities, project deeper into the intermediate zone than the measured ones, indicating that radial transfer of angular momentum is underpredicted in this region. This can be related to the underestimation of turbulence energy in the primay jet impingement region as shown in Figure 5.17c; the locations of intense turbulence generation are predicted well in both primary and dilution regions. Similar correspondence between jet penetration and high generation of turbulence has been found in the computational investigations of Green (1981) and Bruce et al (1979). In the dilution zone, the differences in the radial location of the measured and predicted maxima in the axial velocity contours (Figure 5.17a) indicates that the dilution jet penetration is underestimated. The swirl velocities in this zone are also significantly underpredicted (Figure 5.17b).

The steep reduction in the strength of the primary zone vortex as the swirler flow level increases to 20% is evident in Figure 5.18a. The levels of negative velocity inside the vortex are predicted well although its size is again underestimated. The penetration of the dilution jets is also underpredicted as indicated by the quantitative differences of the axial velocity contours in that region. The predictions of the turbulence field is now in better agreement with the measurements as compared to the previous case.

The complex primary zone flow pattern measured at 25% swirler flow level is predicted accurately as illustrated in Figure 5.19a. The strength and location of the centre of the vortex is calculated correctly. The predicted swirl velocity contours in this case (Figure 5.19b) are in better agreement with the measurements downstream of the primary jet entry plane and this can be associated with the improvements in the calculation of the turbulence kinetic energy in this region, as shown in Figure 5.19c.

Predicted radial velocity contours for the 15% and 25% swirler flow levels are depicted in Figures 5.20a and b respectively. In the lower swirler flow case, the location and spacing of the high radial velocity contours implies that the lateral spread and depth of penetration of the primary jets is predicted well. The dilution jet penetration, however, is underpredicted as indicated by the position of the zero and negative velocity contours in this region. As the velocity ratio jet/cross-flow increases (Figure 5.20b), the trajectories of the primary and dilution jets decrease in both the measurements and calculation. The similarity in the predicted and measured lateral spread of the primary jets in the azimuthal direction is shown in Figure 5.20c.

Calculation of the flow inside the nozzle and at the exit from the combustor

Figure 5.21 illustrates predicted axial velocity profiles at six axial locations inside the dilution zone and nozzle section. These were obtained from the calculation of zone B at the 90^{o} and 0^{o} planes, passing through the combustor centre line. In the vertical mid-plane, the acceleration caused by the contracting nozzle is evident in the flow development at the three downstream stations. The presence of the dilution jets (entering at $x/D_C=1.7$) is reflected by the peaks at $x/D_C=1.93$. Comparison of the flow development between the two planes reveals that small but noticeable asymmetries intrude at $x/D_C=1.93$ as the differences in the velocity peaks at this station show. Large deviations from cyclic behaviour, however, occur only at $x/D_C=2.16$. This demonstrates the predicted upstream influence of the nozzle. The small negative velocity region found at $x/D_C=2.43$ ($\theta=0^o$) is the result of a local adverse pressure gradient on the expanding walls of the nozzle (local angle of expansion 15^o) and its existence was suggested in subsection 2.3. These low velocities near the wall contribute to the axial velocity deficit found in both the measured and calculated exit profiles. Although no measurements were obtained inside this region, due to beam interference with the curved walls, the calculation of the flow inside the nozzle provided useful indications about the flow development in this region and contributed to the interpretation of the exit profiles.

Detailed comparisons between the predicted and measured axial velocity distributions at the exit for 15 and 25% swirler flow level are shown in Figure 5.22, while the overall level of qualitative agreement can be seen in the comparison of the corresponding contours (Figure 5.23). In the lower swirler flows (Figure 5.22a, 5.23a), maximum discrepancies of order of 35% are found near the sides of the nozzle walls and in the region where the flow accelerates near the bottom of the cross-section. The higher velocities identified in the predictions near the walls can be attributed to an underestimation of the adverse pressure gradient on the expanding nozzle walls. Slightly better agreement is obtained at 25% swirler flow level (Figure 5.22b, 5.23b) with the maximum discrepancy reduced to about 25% and found near the centre of the nozzle. This is consistent with the improved agreement obtained in the prediction of the dilution zone profiles as discussed previously. Overall, the qualitative agreement (which is perhaps all which can be expected due to the coarseness of the grid used for the calculations of zone B) can be considered as fair. Although the predicted axial velocity fields for both cases are more uniform than the measurements they clearly indicate regions of local acceleration as can be seen by the location of the contours 2.15 (predicted) and 2.75

(measured, case 2) and 2.0 (predicted) and 2.4 (measured, case 4) shown in Figure 5.23a, b.

5.4 Assessment

The results presented in the previous subsection showed that good qualitative agreement was obtained between measurements and calculations for the range of flows investigated. Quantitative discrepancies were highest in regions of strong impingement of primary and dilution jets where anisotropy of the turbulence field was identified; in such locations, underestimation of the turbulence kinetic energy was found to influence the prediction of the mean flow. Improvements in these regions were identified at higher swirler flows when anisotropy was reduced. The range of investigations clearly illustrated the failure of the $k-\epsilon$ turbulence model to predict accurately flow regions which are strongly anisotropic and possess rapid spatial changes in the turbulence structure and confirms similar criticisms by various workers (Bradshaw, 1973; Leschziner and Rodi, 1980; Taylor and Whitelaw, 1984).

Although the poor performance of the turbulence model is primarily responsible for the inaccuracies identified in the primary zone, in the dilution region additional errors were introduced due to the asymmetric behaviour of the dilution jets. The unsteady annulus flow and the random circulations in the vicinity of the dilution holes, as discussed in subsection 2.3, are expected to affect the jet entry conditions (eg by altering the velocity field and mass flow rate at the hole in an intermittent manner) and consequently influence the dilution jet development inside the combustor in a different manner than that implied by the boundary conditions used in the present calculation. The high W velocities measured in the dilution zone (planes l and m) could be associated with this behaviour (as discussed in subsection 2.3, case 1) and the large underprediction of the W component in the dilution zone can be partly related to this effect. These effects were generally seen to be smaller as the cross-flow increased at the higher swirler flows. Further, the use of large density correction factors for the dilution jet fluxes (zone B only) has been found to increase the spreading rate of the jets, as discussed in subsection 5.2.3, and this can be considered partly responsible for the underprediction of the radial gradient of the radial velocity near the dilution hole (Figure 5.7c, plane l). Numerical diffusion errors are also possible in the calculation of zone B due to the coarseness of the grid used. The favourable agreement between the calculated results of this zone with those obtained with the finer meshes of zone A and the dominance of large pressure gradients on the flow development, as discussed in subsection 5.2, suggests that their effect is likely to be small. Nonetheless, a complete evaluation of this type of error in this zone must wait until a finer mesh is used.

The present work also showed that the numerical model becomes inaccurate in regions where instabilities and periodic oscillations induced by the stongly swirling flow field contribute significantly to the flow field development and substantiates similar suggestions by Gupta et al (1984) and Gouldin et al (1985).

The extensive comparisons between measurements and predictions showed that despite the above discussed deficiencies the calculation method is capable of providing accurate qualitative and useful quantitative information about the detailed flow development over a wide range of flow patterns and boundary conditions. Important aspects of the flow, such as large scale recirculations, regions of high turbulence generation, jet penetration and trajectories and interaction between swirler and primary jets were predicted adequately for preliminary design purposes.

Apart from the detailed information, overall quantities of importance to design, such as the primary zone recirculation ratio, can also be extracted from the calculated results. The primary zone recirculation ratio was evaluated from the predictions in the same manner as that described in subsection 2.4, and is shown in Figure 5.24, compared with the experiment. Good qualitative similarity is exhibited for the range of swirler/primary jets mass flow ratios. Maximum discrepancies of about 17% are found at the lower swirler/primary jets mass flow ratios while a slight improvement is observed for the higher swirler flow ratios consistent with the discussions of the previous subsection. The observed good correspondence between experiment and calculation illustrates the potential usefulness of the method in estimating the primary zone recirculation ratio in configurations which combine swirler and primary jets for which no information currently exists.

5.5 Further calculations

In the preceding sections, the ability of the calculation method to provide useful results on the influence of swirler/primary jets mass flow ratio for the specific configuration investigated experimentally was demonstrated. It is clear, however, that the primary zone flow pattern is also dependent on several geometric features such as the distance from primary jets to swirler exit and the combustor/swirler diameter ratio (Lefebvre, 1983). Bearing the limitations of the predictions in mind, the calculation scheme was used to quantify the effect of the swirler/primary jets mass flow ratio on the flow pattern (under isothermal conditions) inside a geometrically different configuration with swirler/combustor diameter ratio twice that of the water model and where the distance from the primary jets to swirler exit was increased by 40%; this could be evaluated by experiment but at greater inconvenience and cost.

The geometry chosen for investigation is shown in Figure 5.25a and closely resembles in its dimensions that of *current production* can-type combustors; it comprises a swirler (the same as swirler 2 of Figure 2.4) and two rows of primary and dilution holes; wall transpiration flow is also introduced between the two rows of holes. It was assumed that the fluid was air and 790^{o}k and 315 psia were the conditions at inflow to the chamber (these are typical conditions at a compressor outlet). Since only the primary zone flow was to be investigated, the calculation domain excluded any downstream nozzle and a cylindrical polar mesh of 45 x 18 x 15 (x, r, θ) grid nodes was used; the periodic nature of the geometry allowed cyclic boundary conditions to be used on the bounding planes of the 60^{o} sector considered.

Figure 5.25b shows the axial development of the flow inside the primary and initial stages of the intermediate zones. The three operating conditions chosen for study have swirler/primary jets mass flow ratios similar to those used in the water model investigation and are depicted in Table 5.3.

TABLE 5.3

OPERATING CONDITIONS FOR CONFIGURATION OF FIGURE 5.25a

	$\dot{m}_{sw}$	$\dot{m}_{pr}$	$\dot{m}_{tr}$	$\dot{m}_{d}$	$\dot{m}_{tot}$	$\dot{m}_{sw}/\dot{m}_{pr}$
case a	0.088	0.2345	0.182	0.494	1.97	0.375
case b	0.1336	0.2228	0.173	0.469	2.073	0.6
case c	0.175	0.216	0.131	0.476	1.3695	0.81

As the swirler flow increases trends similar to those found inside the primary zone of the water model combustor can be seen. At station $x/D_c=0.538$ (through the geometric axis of the primary jets) the gradual increase in the positive axial velocities suggests a decrease in the primary jet trajectory. This results in a shift in the location and decrease in the magnitude of the maximum negative and positive axial velocities at planes $x/D_c=0.419$ and 0.711; the above variations can be compared with the changes in the axial velocity profiles at planes c, d, f inside the water model. The backflow near the swirler increases with swirler flow and a region of recirculation is identified near the curved combustor head due to the flow expansion and swirl effect (Altgeld et al, 1983; a similar small recirculation had been predicted in the water model for the high swirler flows but was not shown in the comparisons of subsection 5.3 due to lack of measurements near the swirler). The predicted primary zone recirculation ratio for the above configuration (calculated from the integration of the negative part of the axial velocity profile at $x/D_c=0.39$) is compared against that obtained from the prediction of the water model combustor operating with the same swirler, in Figure 5.25c. The comparison indicated that the configuration of Figure 5.25a results in a less steep variation in the range $0.3<\dot{m}_{sw}/\dot{m}_{pr}<0.65$ and produces a primary zone recirculation ratio which is higher by 25% than that of the water model combustor. This can be attributed to the reduced influence of the swirler flow on the primary jets due to the greater distance between swirler and primary holes.

5.6 Summary

The calculation of the turbulent isothermal flow inside a model of a can-type gas turbine combustion chamber was obtained by using a numerical model based on the finite-difference solution of the three-dimensional time-averaged equations governing the transport of mass, momentum, turbulence kinetic energy and energy dissipation rate. The economic and efficient calculation of the flow inside the complex model geometry was achieved by splitting the whole combustor into two overlapping zones: zone A comprising the can section and the two rows of holes and zone B made up of the exit nozzle and part of the upstream cylindrical barrel including the dilution holes. The flow in the first was calculated with a cylindrical polar grid and cyclic boundary conditions were used in the 60° sector considered. The computation of the nozzle was made possible by using a general method capable of handling three-dimensional geometries with arbitrary boundaries within finite-difference methods based on simple co-ordinate systems.

1. The range of investigations showed that the calculation method was capable of predicting qualitatively and quantitatively the effect of the variation of the flow split between swirler and ports and the influence of swirler geometry on the flow development.

   (a) In the primary zone, in the lower swirler flows, the maximum levels of discrepancy were found in the vicinity of the primary jet impingement region and were of order 40%. These were attributed to the failure of the $k-\epsilon$ turbulence model to describe accurately the turbulent transport in this region of high anisotropy, as indicated by the underestimation of the turbulence kinetic energy by about 40%. At higher swirler flows, due to shallower penetration of the primary jets, anisotropy was reduced, turbulence was generated predominantly through shear and the prediction of the mean and turbulence fields was improved. In general, important variations in detailed and global features of the flow (eg decrease in primary jet trajectory, levels of negative axial velocity, increase in swirl velocities, reduction in primary zone recirculation ratio) were correctly reproduced by the calculation method.

(b) In the intermediate zone, discrepancies found at the initial stages were attributed to inaccuracies in the prediction of the flow in the primary jet impingement region. Agreement between measurements and predictions improved significantly at the later stages where the measured distributions of the three normal stresses became uniform; for the higher swirler flows, the effects of the central precessing core on the flow development were not predicted and this lead to increased discrepancies in the axial and azimuthal velocities near the centre line.

(c) The discrepancies were observed to increase in the dilution zone which was calculated in both zone A and B. Comparison between the results obtained from the two zones showed that under conditions of dilution jet impingement the upstream effect of the nozzle extended up to the dilution jet entry plane while at higher swirler flows this effect was reduced. Apart from the deficiencies due to the turbulence model which were particularly evident in the lower swirler flows when the dilution jets penetrated and formed a backflow, additional error sources were identified in this zone. The observed unsteady annulus flow near the dilution holes is thought to influence the dilution jet entry conditions and their subsequent development inside the combustor in a manner not described by the boundary conditions used in the calculations; this effect was observed to be smaller in the higher jet/cross-flow velocity ratios. In addition, the use of high density correction factors to obtain the appropriate dilution jet fluxes in the calculation of zone B is also expected to influence the dilution jet spread.

(d) The calculation of the flow development inside the nozzle indicates its effect on the upstream flow as discussed above and revealed flow separation from the expanding nozzle walls;

this was contributing to the low velocities near the wall at the exit cross-section in both measurements and calculations. At the combustor exit for the lower swirler flows (eg 15%) the maximum discrepancy between the predicted and measured axial velocity profiles was 35% while this improved to 25% at higher swirler flows. Overall, although the predicted axial velocity distributions at the exit were much more uniform than the measurements, they provided useful indications of the regions of local acceleration.

2. The observed maximum discrepancies are slightly larger than those found in the calculation of axisymmetric swirl stabilised combustors (eg Whilelmi, 1984); this is not surprising, however, since the differences are concentrated in regions where the present flow is significantly more complex, ie primary jet impingement position, dilution zone. The level of agreement between measurements and calculations in the present study is similar to that found in the computational investigation of a geometrically simpler model combustor without swirl by Green (1981).

3. The parametric study over the wide range of operating conditions appropriate of gas turbine practice (particularly the lower swirler flows) has shown that this type of numerical approach can provide useful qualitative and quantitative results about the details and global aspects of the flow for practical combustion chamber designs at least under isothermal conditions. It was also demonstrated that such methods can be applied conveniently and economically for the complex geometries as found in practice.

CHAPTER VI

CLOSURE

6.1 Achievements and conclusions

This chapter outlines the main findings and contributions of the present thesis and puts forward some recommendations for future work. Contributions are classified under the categories of experimental and computational work.

6.1.1 Experimental work

Laser Doppler velocimetry was used to obtain velocity and turbulence data inside a water model of a can-type combustion chamber comprising a swirler, annulus fed primary and dilution ports and an exit contraction nozzle. The effect of the variation of the flow split between swirler and ports and the influence of swirler geometry on the flow field were investigated.

An increase in swirler flow decreased the trajectory and penetration of the primary jets and this resulted in a reduction in the strength and size of the primary zone vortex. This increase in swirler/primary jets mass flow ratio was, therefore, accompanied by a reduction in the primary zone recirculation ratio; the variation was almost linear for $0.2<\dot{m}_{sw} / \dot{m}_{pr}<1.0$ (for swirler 1). For swirler flows higher than 25% of the total flow rate, a central precessing core was observed on the can axis. A change in swirler geometry, comprising a decrease in swirler exit area and an increase in swirl number, resulted in a reduction of the primary jet trajectory and levels of maximum negative velocity and turbulence energy inside the primary zone. Maximum levels of turbulence energy and anisotropy were associated with strong jet impingement and were reduced with increasing swirler flow. Overall, the steep variations in the primary zone flow pattern had a smaller effect on the combustor exit profiles due to strong and efficient mixing in the dilution zone.

The investigation provided quantitative information about the interaction between swirler and primary jets and quantified the effect of swirler flow on jet penetration, regions of recirculation and intense turbulence generation. Very little information inside a realistic geometry existed on the above aspects of the flow which are important in the design of actual combustion chambers. Since the measurements were obtained inside a practical configuration under operating conditions which are representative of gas turbine practice (particularly the lower swirler flows) they are of direct relevance to the flow fields inside actual combustion chambers. The data taken were also sufficiently comprehensive to be suitable for the appraisal of combustor prediction methods.

6.1.2 Computational work

As a first step in assessing the capability of the numerical calculation method to predict the complete diffuser-annulus-combustor system, the two-dimensional flow inside a practical dump diffuser geometry for an annular combustor and the three-dimensional flow inside the water model combustor were investigated; errors that could arise from the interaction between the internal and external calculation domain were thereby eliminated in this separate investigation.

In the former calculation, the numerical solution of the governing equations was achieved on a boundary-fitted mesh necessary to represent correctly the flow around the curved combustor head. Due to the very fine meshes required to minimise numerical diffusion errors arising from the hybrid differencing scheme presently used, adoption of a higher order finite-difference scheme was recommended for the efficient calculation of this type of diffuser. The investigation showed that trends in the variation in the details of the flow and in the overall performance caused by changes in diffuser design features (eg inner/outer annulus flow split or dump gap) were predicted adequately for engineering design purposes. The accuracy of the prediction of the flow in the annulus was also encouraging for their eventual use as boundary conditions in the calculation of the flow inside the combustor.

A zonal approach was adopted for the calculation of the water model combustor. A cylindrical polar grid was used to calculate the can section and a general method for handling three-dimensional geometries with arbitrary boundaries was further developed and employed to calculate the flow inside the exit nozzle. Calculated results were in favourable agreement with measurements in the primary and intermediate zones with the maximum discrepancy in the prediction of the mean flow of 40% (at the lower swirler flows) found at the primary jet impingement position. This was attributed to the poor performance of the turbulence model in this region of high anisotropy, as indicated by the underestimation of turbulence energy also by 40%. The prediction of the mean and turbulent fields was generally improved at higher swirler flow levels. The discrepancies were higher in the dilution region, where in addition to the turbulence model deficiencies, the asymmetric behaviour of the dilution jets and the use of high density correction factors for the dilution jet fluxes, in the calculation of the nozzle, contributed to the inaccuracies. The calculation of the exit nozzle showed that its upstream effect extended up to the dilution jet entry plane and decreased as the dilution jet penetration was reduced; maximum discrepancies at the combustor exit axial velocity profiles were of order 30%.

The extensive comparison with measurements showed that the numerical calculation method was capable of predicting the effect of the variation of the flow split between swirler and ports, and the influence of swirler geometry on the flow development. Detailed aspects of the flow, such as the primary and dilution jet trajectory, the primary zone flow distribution and the location of regions of intense turbulence generation, were also predicted adequately for preliminary design purposes. Overall, the parametric study over a range of operating conditions appropriate to gas turbine practice showed that, at least under isothermal conditions, this type of approach can provide useful qualitative and quantitative information about the effect of geometric and flow variables for the flows inside practical gas turbine combustion chambers. The further development of the general arbitrary boundary method was also a significant step in removing the limitations in the application of this type of method to the complex geometries found in practice.

6.2 Future work

Several categories of future work are envisaged for the application of laser Doppler anemometry and numerical calculation techniques in the design of practical combustion chambers.

The laser Doppler anemometer is now a widely used instrument for the measurement of mean velocity and turbulence quantities inside a range of practical flow configurations. In the design and development of gas turbine combustion chambers, the application of LDA in conjunction with the use of the well established water and cold air models can provide quantitative information in cases where the degree of accuracy and resolution required is greater than that achieved by flow visualization and pitot probe measurements. For example, accurate quantification of the highly turbulent primary zone flow pattern would be very difficult to achieve with a probe as the steep variations inside the water model suggest. The detailed data provided by this approach are also suitable for subsequent comparison with calculations.

With reference to the experimental investigation of Chapter II, the present work can be extended in several areas. The present measurements examined the influence of the flow split between swirler and ports and focussed attention on a specific combustor design. As mentioned in subsection 5.5, the flow pattern inside the combustor also depends on the particular chamber geometry. The work can be extended to investigate the effects of geometric features such as combustor/swirler diameter ratio and the location and size of primary and dilution holes. The realism of the model can also be increased by including cooling rings, trimmer holes and different port configurations (chutes, plunged holes). The choice of suitable geometry can be made by reference to current practice or the numerical approach can be used to provide preliminary indications as demonstrated in subsection 5.5. Attention should also be paid to reduce or, if possible, eliminate any influence of the unsteady annulus flow near the dilution holes, on the dilution jet entry conditions; this could be achieved with flow bleed at the downstream end of the combustor. Elimination of the above uncertainty is particularly important when the data are compared with calculations. Care, however, should be taken so that any of the above modifications does not render important regions of the combustor inaccessible to the laser beams. The present measurements could also be extended to include measurements of concentration and its fluctuation, obtained simultaneously with the velocity and turbulence data, possibly by use of the laser induced fluorecence technique (see Johnson and Bennet, 1981). This type of data is required for the evaluation of current calculation procedures for combusting flows (Jones and Priddin, 1978).

In the application of the numerical approach to the calculation of the flows inside the dump diffuser geometry and the model combustor, the quantitative agreement with measurements was good enough to encourage further work in various areas. In the dump diffuser investigation, a more accurate method for generating orthogonal curvilinear meshes could be used (eg the analytic solution of the inviscid flow aroung a cylinder). This and the use of a higher order finite-difference scheme, as suggested in subsection 6.1.2, would remove the remaining errors in the solution and allow a fuller assessment of the turbulence model. It is also possible to increase the realism of the geometry by introducing flow through the combustor via the head, primary and dilution holes and examine their influence on performance. The representation of the dilution holes would then require the use of the three-dimensional equations and this would increase the computer storage requirements.

The favourable level of agreement between measurements and predictions in the calculation of the water model combustor suggests that the calculation method can be used in practical situations. Parametric studies can be undertaken to investigate qualitatively the effect of geometric and flow variables (ie location and size of ports, swirler/combustor diameter ratio, simulated fuel injection) on the flow pattern. The method can also be used in parallel with the experimental approach as suggested above. The limitations of the present model in predicting the present flow or the equivalent combusting flow with little quantitative error concern each of the component parts of the calculation scheme; the grid system, the finite-difference scheme and the turbulence and (eventually) the combustion models. The general arbitrary boundary method presented here significantly broadens the applicability of the method but requires further testing in a range of flows and geometries; in particular, the errors arising from the use of high correction factors should be quantified. The use of a finer mesh to calculate the present nozzle geometry could possibly reduce these correction factors. Because of the inefficiency of the method in the use of grid nodes, as discussed in subsection 3.3.1, it is recommended that work should be directed towards the development of a three-dimensional approach that makes use of non-orthogonal boundary fitted meshes (see Gosman and Issa, 1984) which may be a more economic alternative. It was also suggested, in subsection 5.6, that the use of improved finite-difference techniques and turbulence models could help to reduce the present level of discrepancy (which is likely to increase in the combusting calculation, Green and Whitelaw (1983)) and the present isothermal type of flow is a most convenient case to test their performance. In general, the above improvements in the model will undoutedly broaden the scope of the calculation method as a reliable design tool.

REFERENCES

ADKINS, R. C. (1978)
"The effect of compressor exit flow distribution on air placement in annular combustors"
J. of Engineering for Power, 100, 444

ALTGELD, H., JONES, W. P. and WHILELMI, J. (1983)
"Velocity measurements in a confined swirl driven recirculating flow"
Exp. in Fluids, 1, (2), 73

ATKINSON, K. N., KHAN, Z. A. and WHITELAW, J. H. (1980)
"Experimental investigation of opposed jets discharging normally into a cross-stream"
Report FS/80/40, Mech. Eng. Dept., Imperial College, London

BEER, J. M. and CHIGIER, N. A. (1972)
"Combustion Aerodynamics"
Applied Science, London

BHANGU, J. K., SNAPE, D. M. and EARDLEY, B. R. (1983)
"The design and development of a low emissions transply combustor for the civil Spey engine"
AGARD No. 353

BICEN, A. F. and JONES, W. P. (1985)
"Velocity characteristics of isothermal and combusting flows in a can-type combustor"
Report FS/85/04, Mech. Eng. Dept., Imperial College, London

BOUSSINESQ, J. (1877)
"Theorie de l'ecoulement tourbillant"
Mem. Acad. Sci., 23, No. 46

BRADSHAW, P. (1976)
"Turbulence" (Ed. P. Bradshaw)
Springer-Verlag, Berlin

BRADSHAW, P. (1973)
"Effects of streamline curvature on turbulent flow"
AGARD No. 169

BRIGHTON, J. A. and JONES, J. B. (1964)
"Fully developed turbulent flow in annuli"
J. of Basic Engineering, 86, 835

BRUCE, T. W., MONGIA, H. C. and REYNOLDS, R. S. (1979)
"Combustor design criteria validation"
USARTL-TR-78-55, 1-3

CLARKE, A. E., GERRARD, A. J. and HOLLIDAY, L. A. (1963)
"Some experiences in gas turbine combustion chamber practice using water flow visualization techniques"
9th Int. Combustion Symp., New York

"Computer program for the analysis of annular combustors" (1968),
1-2, NASA CR-72374 and CR-72375

DEMIRDZIC, I. A. (1982)
"A finite-volume method for computation of fluid flow in complex geometries"
Ph.D Thesis, University of London

DRAIN, L. (1980)
"The laser Doppler technique"
Wiley, New York

DURAO, D. F. G. and WHITELAW, J. H. (1974)
"Performance characteristics of two frequency tracking demodulators and a counting system: *measurements in an air jet*"
Report HTS/74/12, Mech. Eng. Dept., Imperial College, London

DURST, F., MELLING, A. and WHITELAW, J. H. (1981)
"Principles and practice of laser Doppler anenometry"
Academic Press, New York

DURST, F. and ZARE, M. (1974)
"Removal of pedestals and directional ambiguity of optical anenometer signals"
Appl. Optics, 13, 11

EDWARDS, R. V., ANGUS, J. C., FRENCH, M. J. and DUNNING, J. W. (1971)
"Spectral analysis of the signal flow from the laser Doppler flow meter: time independent signal"
J. Appl. Phys., 42, 837

ESCUDIER, M. P. and KELLER, J. J. (1985)
"Recirculation in swirling flow: A manifestation of vortex breakdown"
AIAA, 23, (1), 111

FISHENDEN, C. R. (1974)
"The performance of a branched annular diffuser system"
Ph.D Thesis, University of Technology, Loughborough, England

FISHENDEN, C. R. and STEVENS, S. J. (1977)
"The performance of annular combustor dump diffusers"
J. of Aircraft, 10, 60

GEORGE, W. K. and LUMLEY, J. L. (1973)
"The laser Doppler velocimeter and its application to the measurement of turbulence"
J. Fluid Mech. 60, 321

GIBSON, M. M., JONES, W. P., McGUIRK, J. J. and WHITELAW, J. H. (1984)
"Post experience course in turbulence models for computational fluid dynamics"
Lecture notes, Mech. Eng. Dept., Imperial College, London

GIBSON, M. M. and RODI, W. (1981)
"A Reynolds-stress closure model of turbulence applied to the calculation of a highly curved mixing layer"
J. Fluid Mech., 103, 161

GOSMAN, A. D. and ISSA, R. I. (1984)
"Post experience course in computational fluid mechanics and heat transfer"
Lecture notes, Mech. Eng. Dept., Imperial College, London

GOSMAN, A. D. and JOHNS, R. J. R. (1979)
"A simple method for generating curvilinear orthogonal grids for numerical fluid mechanics calculations"
Report FS/79/23, Mech. Eng. Dept., Imperial College, London

GOSMAN, A. D., PUN, W. M., RUNCHAL, A. K., SPALDING, D. B. and WOLFSTEIN, H. (1969)
"Heat and mass transfer in recirculating flows"
Academic Press, London

GOULDIN, F. C., DEPSKY, J. S. and LEE, S. L. (1985)
"Velocity field characteristics of a swirling flow combustor"
AIAA, 23, (1), 95

GRADON, K. and MILLER, S. C. (1968)
"Combustion development on the Rolls-Royce Spey engine"
Cranfield Int. Symp. Series Vol. 10, Combustion in advanced gas turbine systems (Ed. Smith, I. E.), Pergamon Press

GREEN, A. S. (1981)
"Isothermal models of combustion chamber flows"
Ph.D Thesis, University of London

GREEN, A. S. and WHITELAW, J. H. (1983)
"Isothermal models of gas turbine combustors"
J. Fluid Mech., 126, 399

GUPTA, A. K., LILLEY, D. G. and SYRED, N. (1984)
"Swirl flows"
Abacus Press, Tunbridge Wells, England

HABIB, M. A. and WHITELAW, J. H. (1982)
"The calculation of turbulent flow in wide angle diffusers"
Num. Heat Transfer, 5, 145

HAH, C. (1983)
"Calculation of various diffuser flows with inlet swirl and inlet distortion effects"
AIAA, 21, (8), 1127

IRWIN, H. P. A. H. and ARNOT-SMITH, P. (1975)
"Prediction of the effect of streamline curvature on turbulence"
The Physics of Fluids, 18, 624

JOHNS, R. J. R. (1980)
Prediction of flow in Diesel engine cylinders"
Ph.D Thesis, University of London

JOHNSON, B. V. and BENNET, J. C. (1981)
"Velocity and concentration characteristics and their cross correlations for coaxial jets in a confined sudden expansion Part 1: experiments"
Int. Symp. on Fluid Mechanics of Combustion Systems, Boulder, Colorado, U.S.A.

JONES, W. P. and LAUNDER, B. E. (1973)
"Prediction of low Reynolds number phenomena with a two equation model of turbulence"
Int. J. of Heat and Mass Transfer, 16, 1189

JONES, W. P. and McGUIRK, J. J. (1979)
"Mathematical modelling of gas turbine combustion chambers"
AGARD CP 275

JONES, W. P. and PRIDDIN, C. H. (1978)
"Predictions of the flow field and local gas composition in gas turbine combustors"
17th Int. Combustion Sym., Leeds, U.K.

JONES, W. P. and TORAL, H. (1983)
"Temperature and composition measurements in a research gas turbine combustion chamber"
Combustion Science and Technology, 31, 249

KHAN, Z. A., McGUIRK, J. J. and WHITELAW, J. H. (1981)
"A row of jets in a cross-flow"
AGARD CP 308

KILIK, E. (1976)
"The influence of swirler design parameters on the aerodynamics of the downstream recirculation region"
Ph.D Thesis, School of Mechanical Engineering, Cranfield Institute of Technology, England

KLEIN, A., KATHEDER, K. and ROHLFFS, M. (1974)
"Experimental investigation of the performance of short annular combustor dump diffusers"
2nd Int. Symp. on Air breathing engines, University of Sheffield, England

KOUTMOS, P. and McGUIRK, J. J. (1983)
"Numerical calculations of the flow in annular combustor dump diffuser geometries"
Report FS/83/36, Mech. Eng. Dept., Imperial College, London

LAUNDER, B. E. (1982)
"A generalised algebraic stress hypothesis"
AIAA, 20, 436

LAUNDER, B. E., PRIDDIN, C. H. and SHARMA, B. I. (1977)
"The calculation of turbulent boundary layers on spinning and curved surfaces"
J. of Fluids Engineering, 99, 231

LAUNDER, B. E., REECE, G. J. and RODI, W. (1975)
"Progress in the development of a Reynolds-stress turbulence closure"
J. Fluid Mech., 68, 537

LAUNDER, B. E. and SPALDING, D. B. (1974)
"The numerical computation of turbulent flow"
Computer Methods in Applied Mechanics and Engineering, 3, 269

LEFEBVRE, A. H. (1968)
"Design cosiderations in advanced gas turbine combustion chambers"
Cranfield Int. Symp. Series Vol. 10, Combustion in advanced gas turbine systems (Ed. Smith, I. E.), Pergamon Press

LEFEBVRE, A. H. (1983)
"Gas turbine combustion"
Hemisphere Publishing Corporation

LEONARD, B. P., LESCHZINER, M. A. and McGUIRK, J. J. (1978)
"Third order finite-difference method for steady two-dimensional convection"
Proc. 1st Int. Conf. on numerical methods in laminar and turbulent flows, C. Taylor (Ed.), Pentech. Press, London

LESCHZINER, M. A. (1980)
"A comparison between three finite-difference schemes for the computation of steady-state recirculating flows"
Report No. SFB 80/T/149, University of Karlsruhe

LESCHZINER, M. A. and RODI, W. (1981)
"Calculations of annular and twin parallel jets using various discretization schemes and turbulence model variants"
J. Fluids Engineering, 103, 352

LIVESEY, J. L., JONES, P. K., PARKER, E. and SHAW, J. P. (1960)
"Aerodynamics of tube type gas turbine combustion chamber entry sections"
J. of Mech. Engineering Science, 2, (3), 202

MATHUR, M. L. and MACCALUM, N. R. L. (1967)
"Swirling air jets issuing from vane swirlers"
J. Inst. of fuel, 40, 214

McGUIRK, J. J. and RODI, W. (1978)
"A depth-averaged mathematical model for the near field of side discharges into open channel flow"
J. Fluid Mech., 86, 761

McGUIRK, J. J. and SPALDING, D. B. (1973)
"The treatment in three-dimensional boundary layer program of walls which do not pass through grid nodes"
Report HTS/73/13, Mech. Eng. Dept., Imperial College, London

McGUIRK, J. J. TAYLOR, A. M. K. P. and WHITELAW, J. H. (1981)
"The assessment of numerical diffusion in upwind difference calculations of turbulent recirculating flows"
Paper presented at Third Symposium on Turbulent Shear Flows, U.C. Davis, Ca., September 1981

McGUIRK, J. J. and WHITELAW, J. H. (1983)
"Internal flows of relevance to gas turbines"
Report FS/83/25, Mech. Eng. Dept., Imperial College, London, Invited Paper at the ASME Fluids Engineering Meeting Symposium on Computation of Internal Flows, New Orleans, February 1984

MELLING, A. (1975)
"Investigation of flow in non-circular ducts and other configurations by laser Doppler anenometry"
Ph.D Thesis, University of London

MELLING, A. and WHITELAW, J. H. (1973)
"Measurements in turbulent water flows by laser anenometry"
Proc. of 3rd Biennial Symp. on Turbulence in Liquids, Rolla, 115

MULARZ, E. J., WEAR, J. D and VERBULECZ, P. W. (1975)
"Pollution emissions from single swirl can combustor modules at parametric test conditions"
NASA TM X-3167

MULARZ, E. J., WEAR, J. D. and VERBULECZ, P. W. (1975a)
"Exhaust pollutant emissions from swirl can combustor module arrays at parametric test conditions"
NASA TM X-3237

NIEDZWIECKI, R. W. and JONES, R. E. (1974)
"Pollution measurements of a swirl can combustor"
AIAA, 12, (6), 844

NOVICK, A. S., ARVIN, J. R. and QUINN, R. E. (1980)
"Development of a gas turbine combustor dilution zone design analysis"
J. of Aircraft, 17, (10), 712

NOVICK, A. S., MILES, G. A. and LILLEY, D. G. (1979)
"Numerical simulation of combustor flow fields: a primitive variable design capability"
J. of Energy, 3, (2), 95

NOVICK, A. S., MILES, G. A. and LILLEY, D. G. (1979a)
"Model parameter influences in gas turbine combustor design"
J. of Energy, 3, (5), 257

ODGERS, J. (1979)
"Combustion modelling with gas turbine engines, some applications and limitations"
AGARD CP 275

OLDENGARM, J., van KRIEKEN, A. H. and RATERINK, H. J. (1976)
"Development of a rotating grating and its use in laser velocimetry"
Bericht R117/76, ISL, St. Louis, France. Proceedings of the ISL/AGARD workshop on laser anemometry, May 5-7, 1976

OSGERBY, I. T. (1974)
"Literature review of turbine combustor modelling and emissions"
AIAA, 12, (6), 743

PATANKAR, S. V. (1980)
"Numerical heat transfer and fluid flow"
Hemisphere Publishing Corporation, Washington

PATANKAR, S. V. and SPALDING, D. B. (1972)
"A calculation procedure for heat, mass and momentum transfer in three-dimensional parabolic flows"
Int. J. Heat and Mass Transfer, 15, 1787

POPE, S. B. and WHITELAW, J. H. (1976)
"The calculation of near wake flows"
J. Fluid Mech., 73, 1

PRIDDIN, C. H. (1979)
"A version of PACE with arbitrary boundary capability"
Rolls-Royce internal report (not for general publication)

RAITHBY, G. D. (1976)
"Skew upstream differencing scheme for problems involving fluid flow"
Comp. Meth. in Applied Mech. and Engineering, 9, 153

REECE G. J. (1976)
"Development and applications of a generalised Reynolds-stress model of turbulence"
Ph.D Thesis, University of London

RHODE, D. L., LILLEY, D. G. and McLAUGHLIN, D. K. (1983)
"Mean flow fields in axisymmetric combustor geometries with swirl"
AIAA, 21, (4), 593

ROACHE, P. J. (1976)
"Computational fluid dynamics"
Hermosa Publishers, New Mexico

RODI, W. (1979)
"Influence of boyancy and rotation on equations for the turbulent length scale"
2nd Symp. on Turbulent Shear Flows, Imperial College, London

RODI, W. (1970)
"Basic equations for turbulent flow in cartesian and cylindrical co-ordinates"
Report BL/TN/A/36, Mech. Eng. Dept., Imperial College, London

ROSENTHAL, J. (1959)
"Exploring methods for the determination of gas flow and temperature pattern in gas turbine combustors"
ARL/ME Note 235, Aeronautical Research Laboratories, Australia

SALA, R., VIVARELLI, P. L. and GANITI, G. (1980)
"Numerical analysis of wide-angled diffusers in turbulent flows"
ASCE J. Hydraulics Div., 106, 629

SCHLICHTING, H. (1968)
"Boundary layer theory"
McGraw Hill, New York

SERAG ELDIN (1977)
"The numerical prediction of the flow and combustion in a three-dimensional can combustor"
Ph.D. Thesis, University of London

SERAG ELDIN, M. A. and SPALDING, D. B. (1979)
"Computations of three-dimensional gas turbine combustion chamber flows"
J. of Engineering for Power, 101, 326

SIMPSON, R. L., STRICLAND, J. H. and BARR, P. W. (1976)
"Features of a separating, turbulent boundary layer in the vicinity of separation"
J. Fluid Mech., 79, 553

SMITH, J. M. (1979)
"Performance of a vortex-controlled diffuser in an annular swirl can combustor at inlet Mach numbers up to 0.53"
NASA TP-1452

SOVRAN, G. and KLOMP, E. D. (1967)
"Experimentally determined geometries for rectilinear diffusers with rectangular, conical or annular cross-section"
Fluid mechanics of internal flow, Elsevier, New York, p.270

SPALDING, D. B. (1972)
"A novel finite-difference formulation for differential expressions involving both first and second derivatives"
Int. J. Num. Meth. in Enginering, 4, 551

STEVENS, S. J. and FRY, P. (1973)
"Measurements of the boundary layer growth in annular diffusers"
J. of Aircraft, 10, 73

STURGESS, G. J., SYED, S. A. and SEPULVEDA, D. (1981)
"Application of numerical modelling to gas turbine combustor development problems"
Int. Symp. on Fluid Mechanics of Combustion Systems, Boulder, Colorado, U.S.A.

SWITHENBANK, J., TURAN, A., FELTON, P. G. and SPALDING, D. B. (1979)
"Fundamental modelling of mixing, evaporation and kinetics in gas turbine combustors"
AGARD CP 275

SYRED, N. and BEER, J. M. (1974)
"Combustion in swirling flows: A review"
Combustion and Flame, 23, 143

TACINA, R. R. and GROBMAN, J. (1969)
"Analysis of total pressure loss and airflow distribution for annular gas turbine combustors"
NASA TN D-5385

TAYLOR, A. M. K. P. (1981)
"Confined, isothermal and combusting flows behind axisymmetric baffles"
Ph.D Thesis, University of London

TAYLOR, A. M. K. P. and WHITELAW, J. H. (1984)
"Velocity characteristics in the turbulent near wakes of confined axisymmetric bluff bodies"
J. Fluid Mech., 139, 391

TENNEKES, H. and LUMLEY, J. L. (1972)
"A first course in turbulence"
MIT Press, Cambridge, Mass.

THOMPSON, J. F. (1982)
"Numerical grid generation" (Ed. by J. F. Thompson)
J. of Applied Mathematics and Computation, Vol. 10-11

THOM, A. and APELT, C. J. (1971)
"Field computations in engineering physics"
Van Nostrand

THOMPSON, B. E. (1984)
"The turbulent separating boundary layer and downstream wake"
Ph.D Thesis, University of London

TOWNSEND, A. A. (1980)
"The structure of turbulent shear flow"
2nd Edition, Cambridge University Press, Cambridge, England

VAN DEN BERG, B. (1975)
"A three-dimensional law of the wall for turbulent shear flows"
J. Fluid Mech., 70, 149

VERDUZIO, L. and CAMPANARO, P. (1971)
"The air recirculation ratio in can-type gas turbine combustion chambers"
Proc. Int. Propulsion Symp., Cranfield

VU, B. T. and GOULDIN, F. C. (1982)
"Flow measurement in a model swirl combustor"
AIAA, 20, (5), 642

WAY, S. (1956)
"Combustion in the turbojet engine"
AGARD Combustion Colloquium, Butterworths, London

WHILELMI, J. (1984)
"Axisymmetric swirl stabilised combustion"
Ph.D Thesis, University of London

WINSLOW, A. M. (1967)
"Numerical solution of the quasi-linear Poisson equation in a non-uniform triangular mesh"
J. Comp. Phys., 2, 149

YOUSSEF, T. E. A. (1968)
"Experimental determination of the velocity and pressure profiles in the combustion zone in a model of a gas turbine combustion chamber"
S.A.E. Trans., 76, section 2, 1068

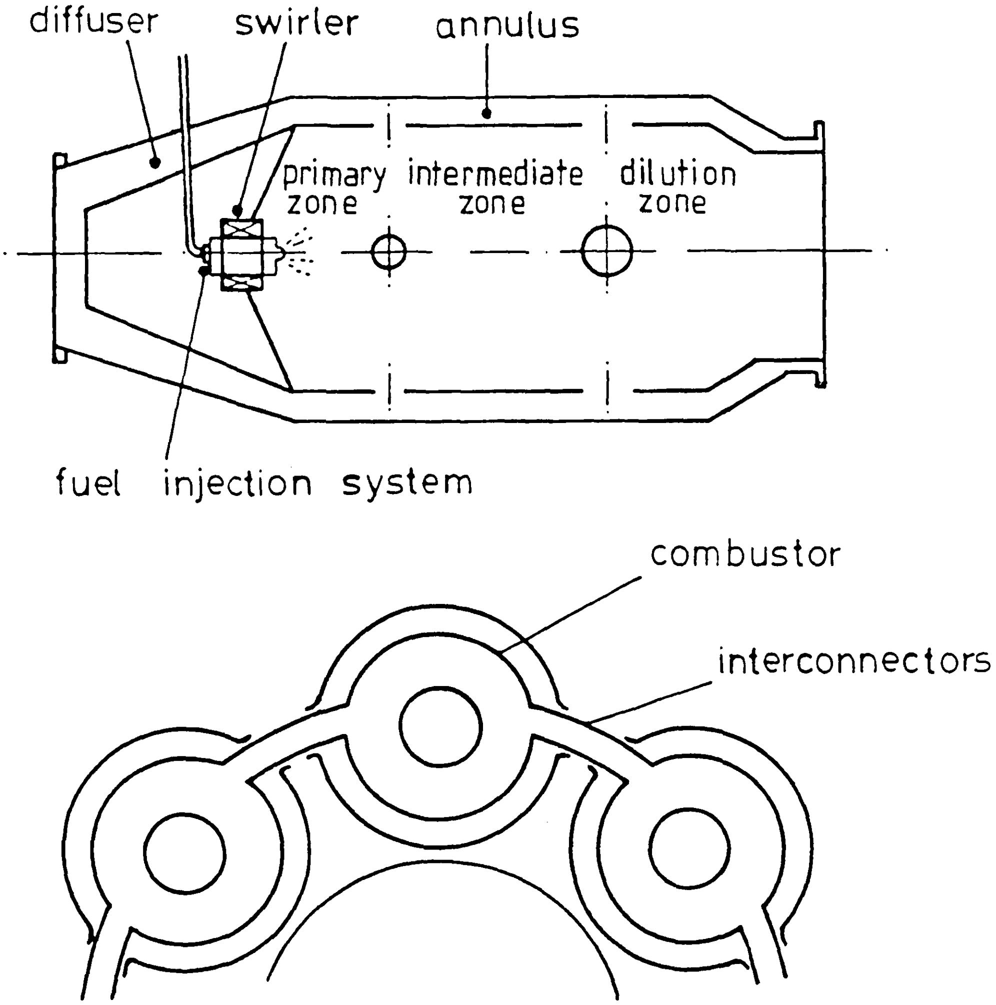

Figure 1.1 Tubular combustion chamber and arrangement

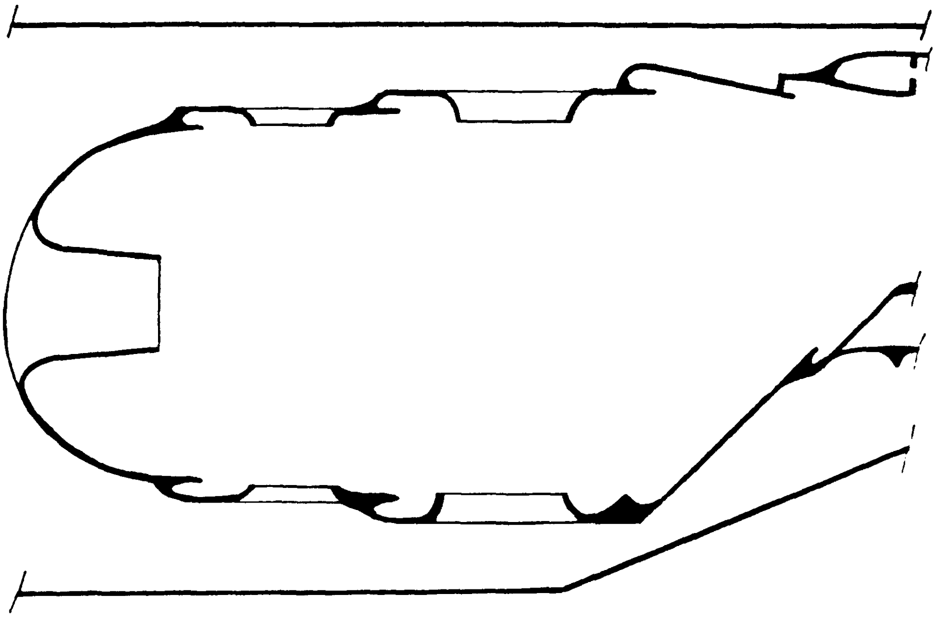

Figure 1.2 Annular combustion chamber

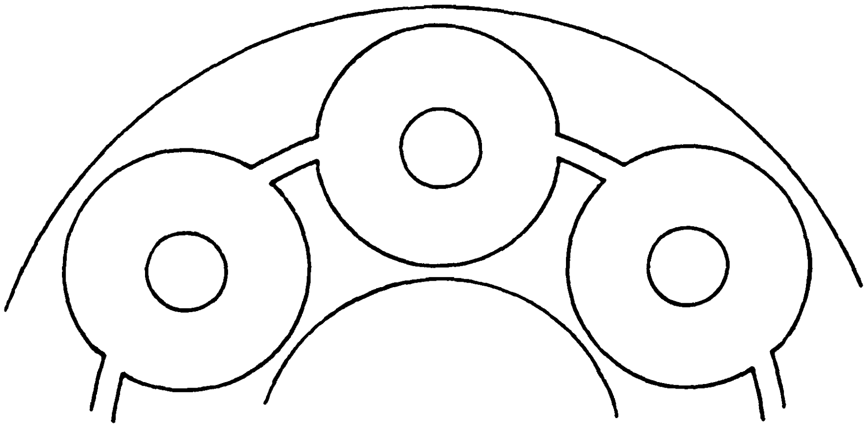

Figure 1.3 Tubo-annular arrangement

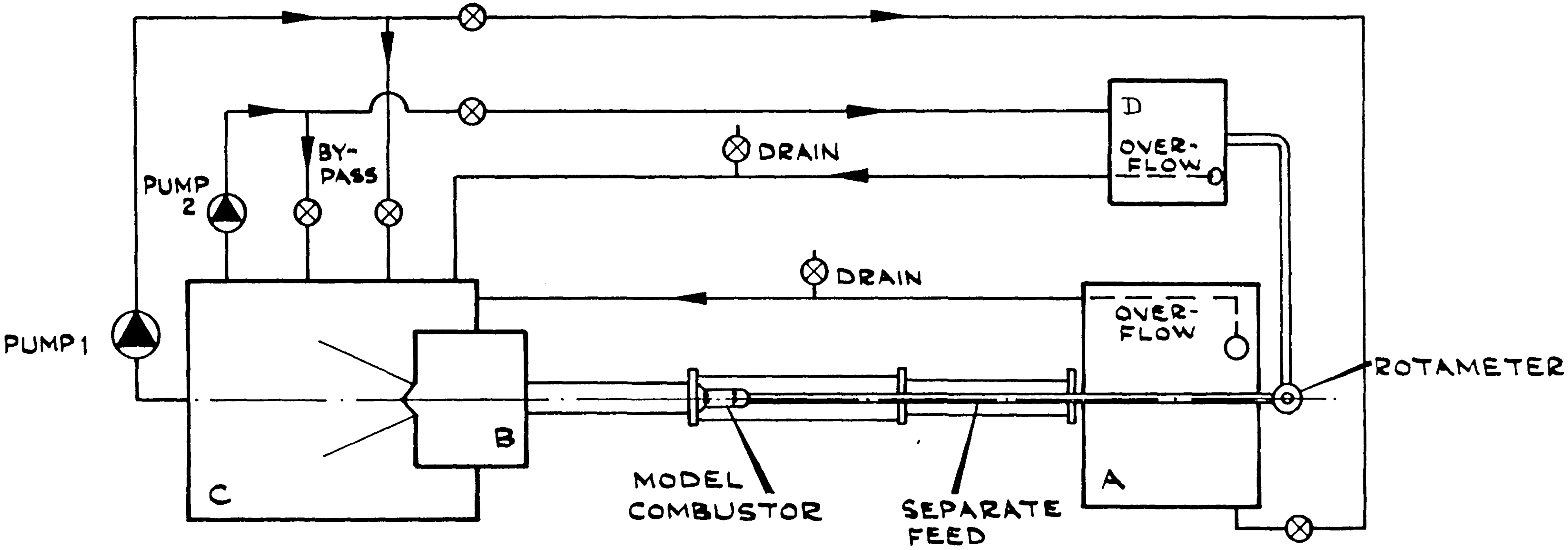

Figure 2.1 Diagram of water tunnel

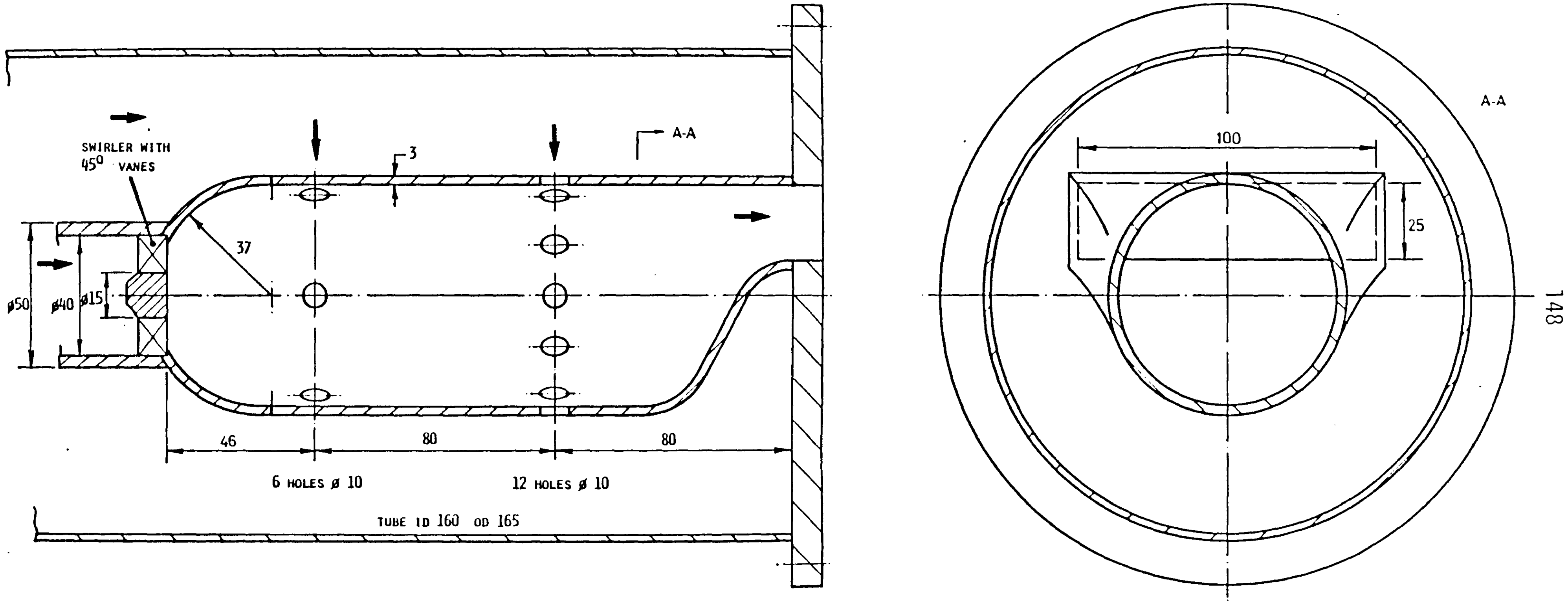

Figure 2.2 Model combustor geometry

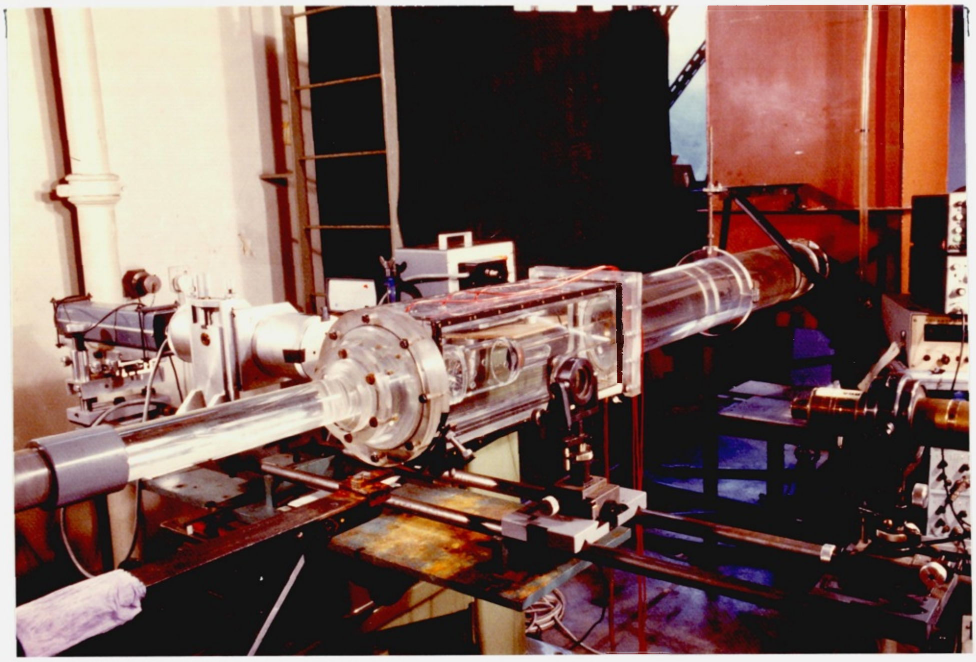

(a)

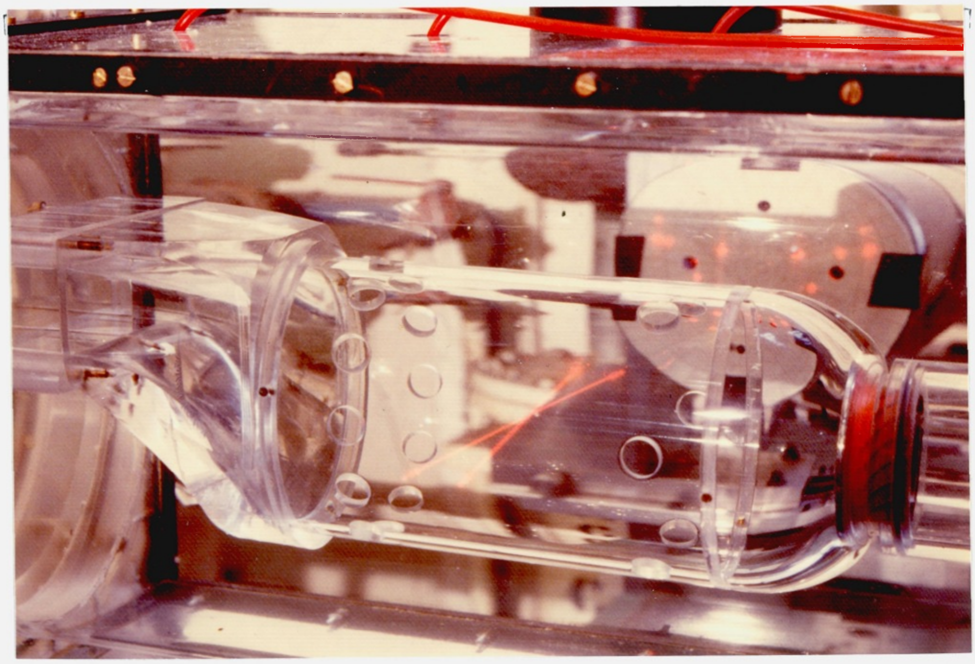

(b)

Figure 2.3 Photographs of

(a) the water flow rig

(b) the model combustor

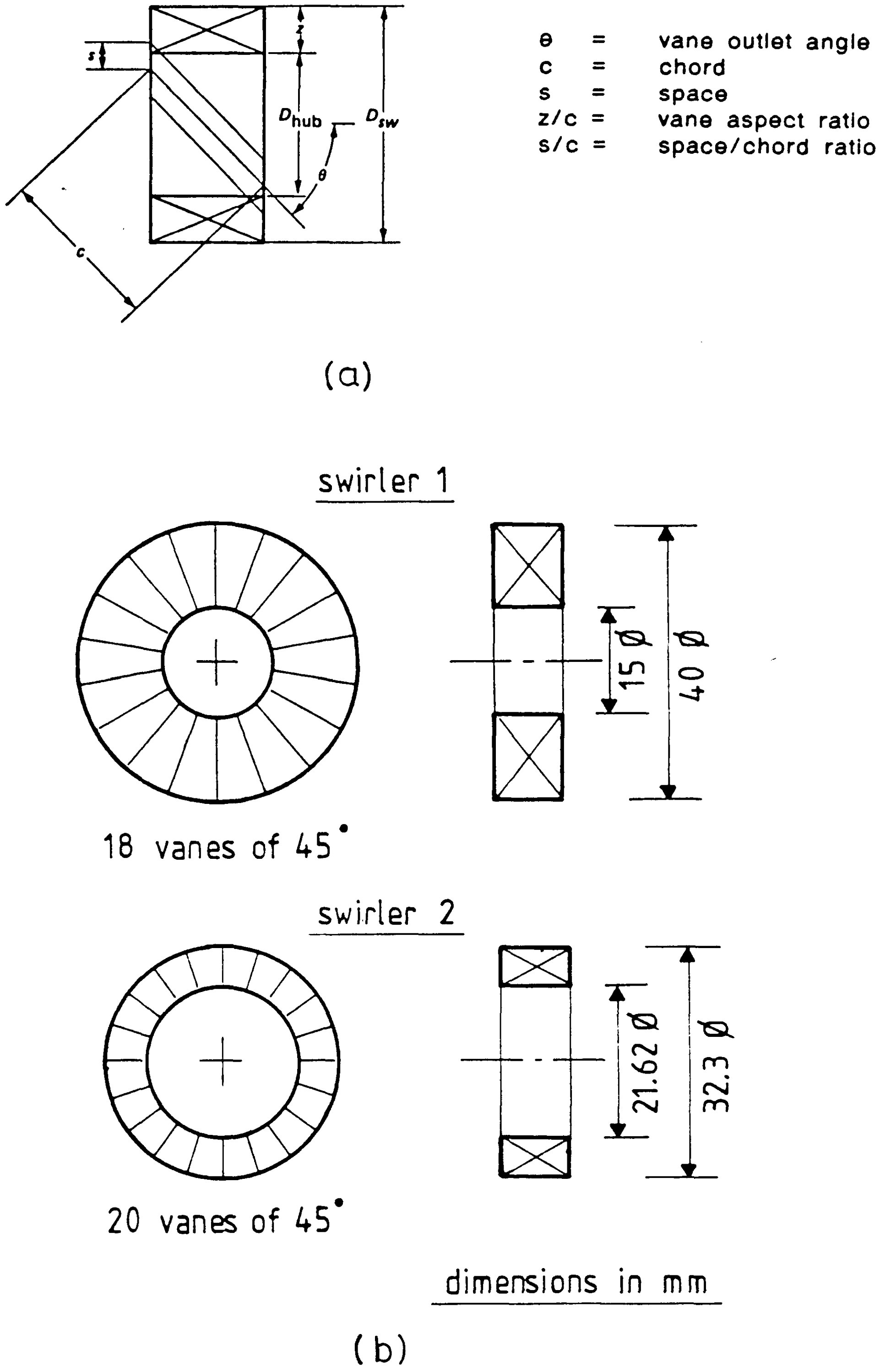

θ = vane outlet angle
c = chord
s = space
z/c = vane aspect ratio
s/c = space/chord ratio

Figure 2.4 (a) Geometrical definitions of flat-vane swirler

(b) Geometry of the two swirlers used in the investigation

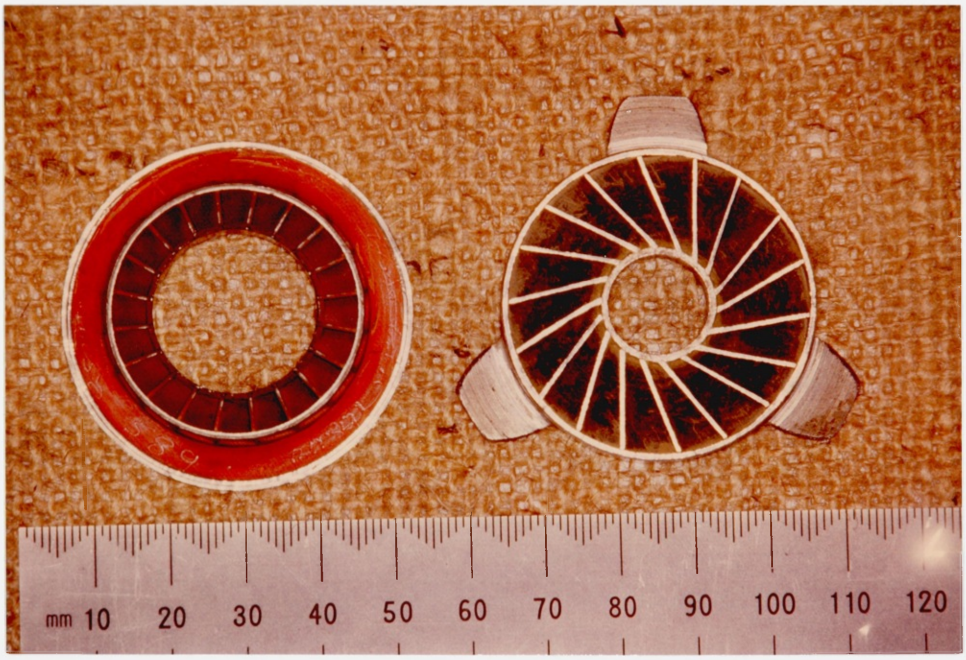

Figure 2.5 Photograph of the two swirlers

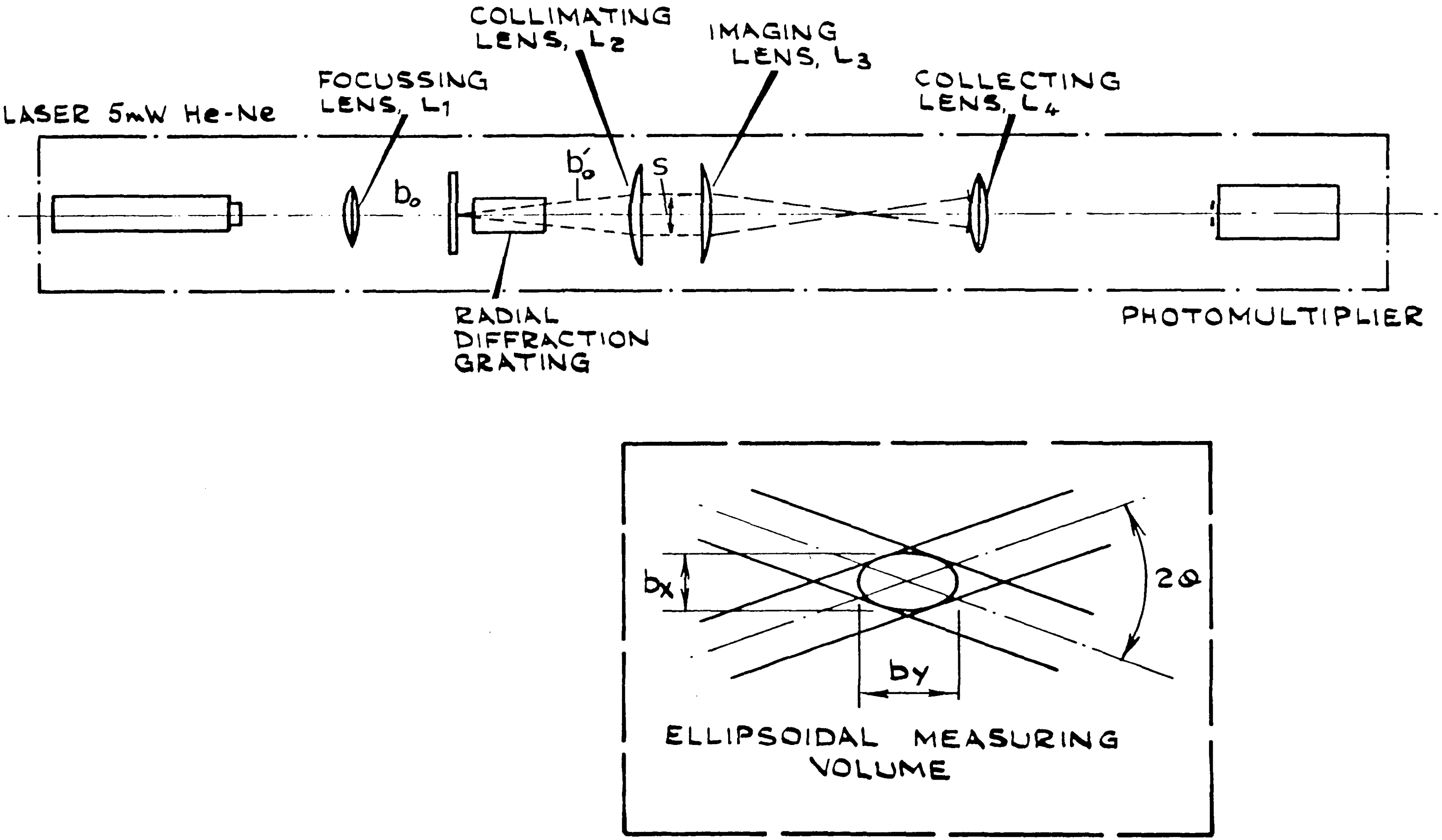

Figure 2.6 Optical arrangement of laser Doppler velocimeter

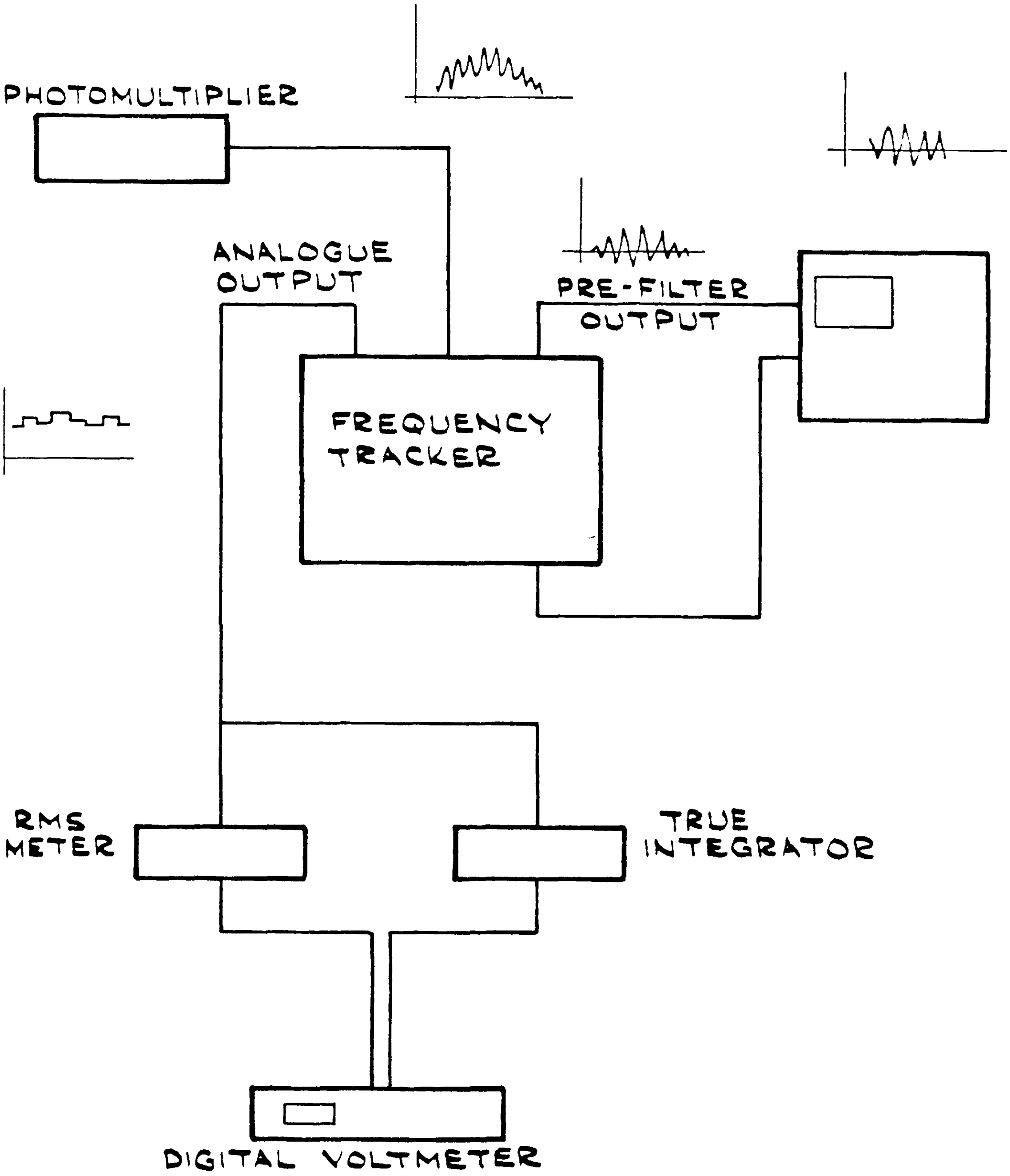

Figure 2.7 Schematic diagram of processing equipment and signal waveforms

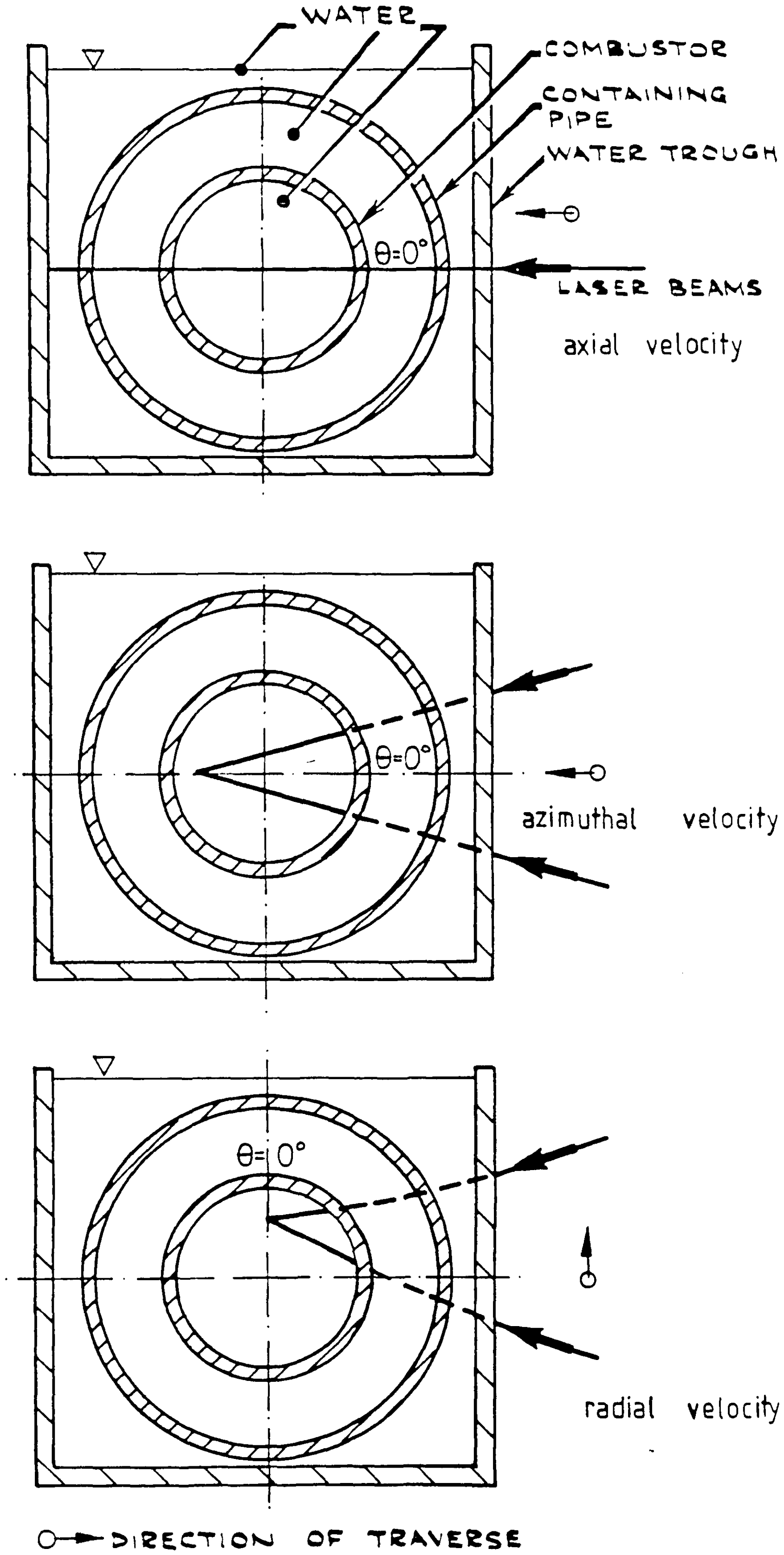

Figure 2.8 Beam orientation and direction of traverse for measurement of velocity components

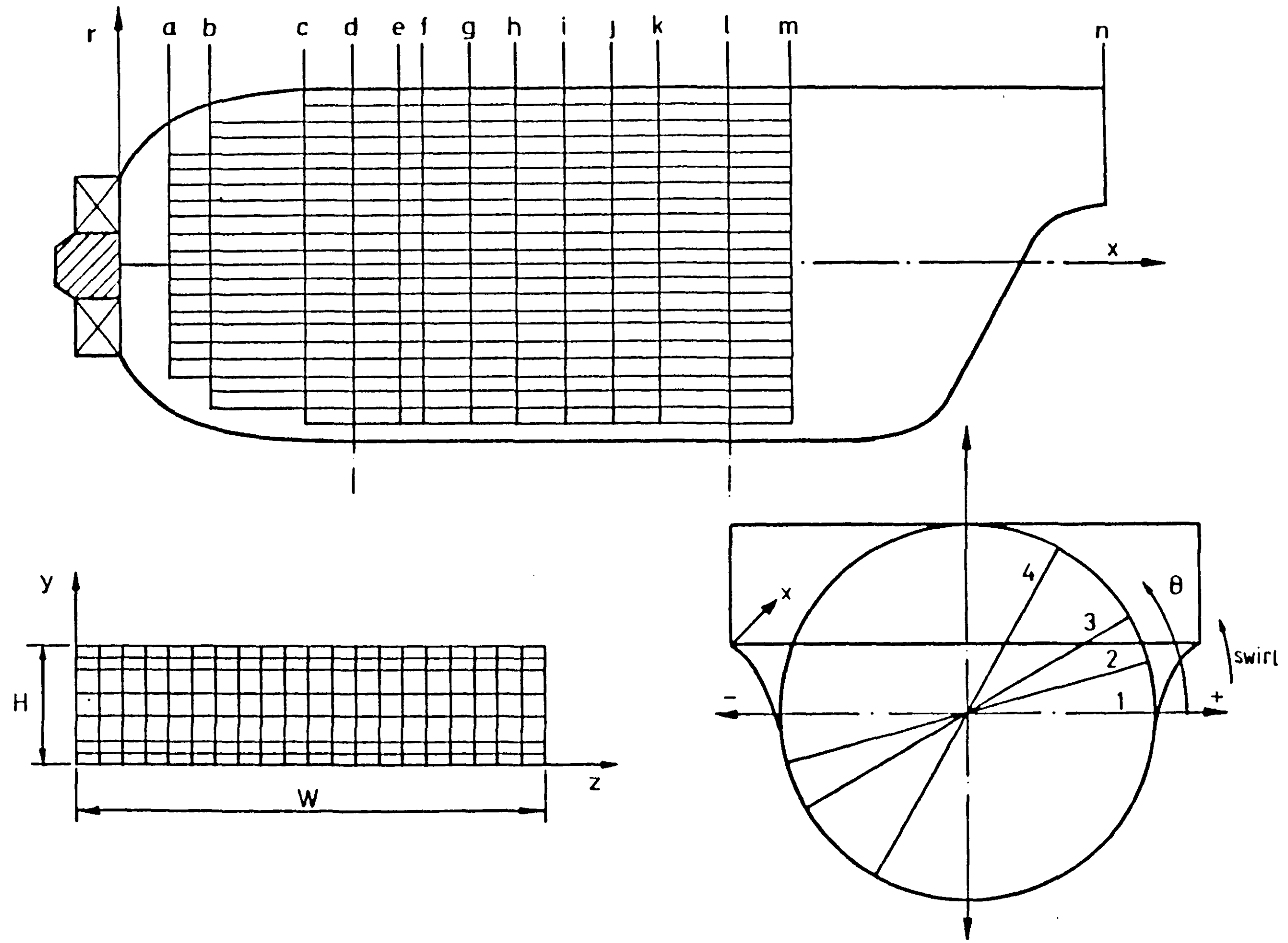

	$\frac{x}{D_c}$
a	0.135 (0.135)
b	0.270 (0.270)
c	0.486 (0.527)
d	0.621 (0.662)
e	0.756 (0.797)
f	0.824 (0.864)
g	0.959 (0.999)
h	1.094 (1.135)
i	1.229 (1.270)
j	1.364 (1.405)
k	1.500 (1.540)
l	1.702 (1.743)
m	1.870 (1.910)

θ plane	
1	0°
2	15°
3	30°
4	60°

axial locations in parentheses are for operation with swirler 2

Figure 2.9 Co-ordinate system and network of measurement points

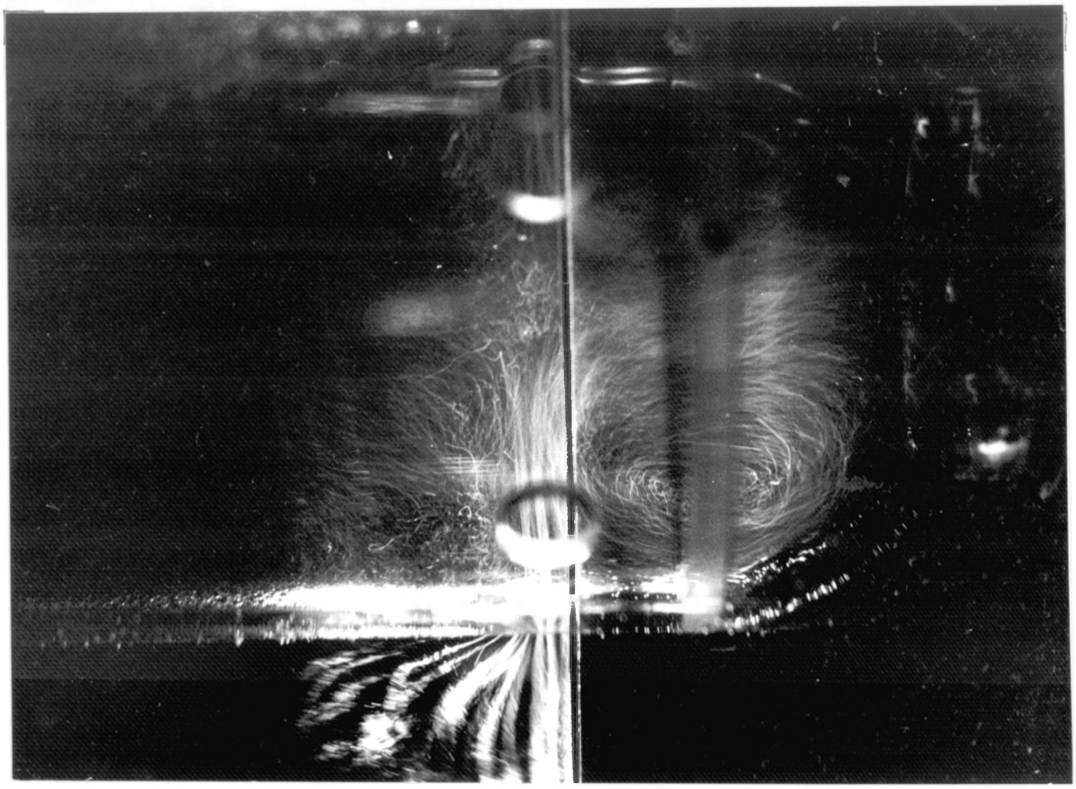

(a) primary jet entry and upstream recirculation (case 2)

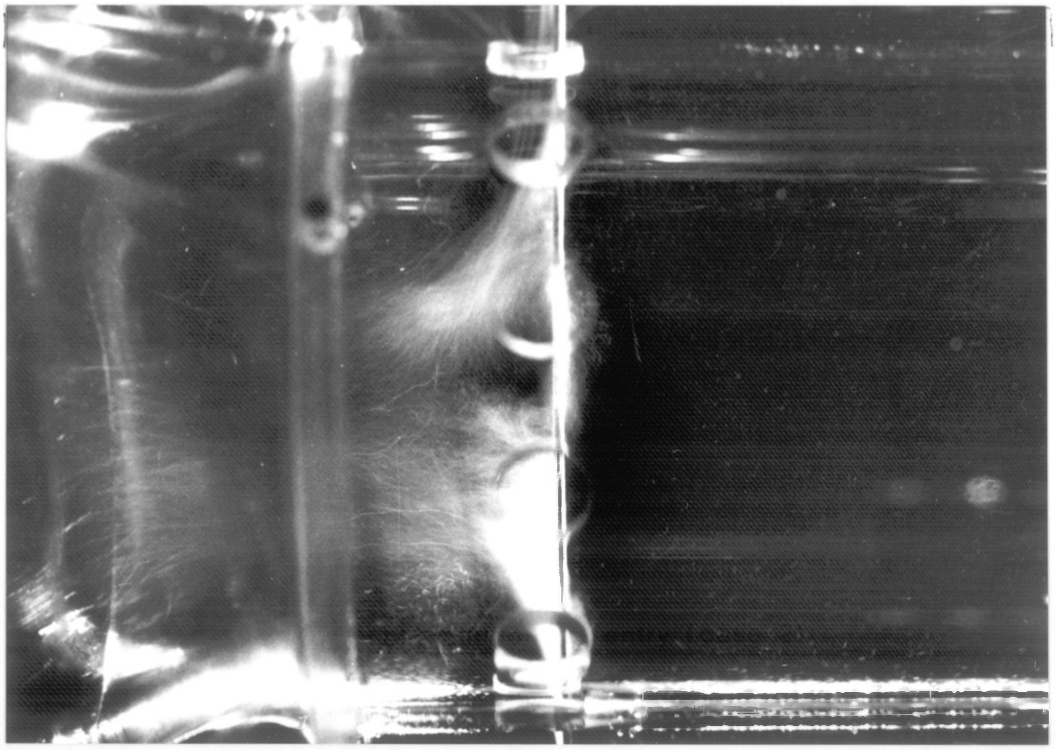

(b) dilution jet entry (case 2)

Figure 2.10 Flow visualization pictures

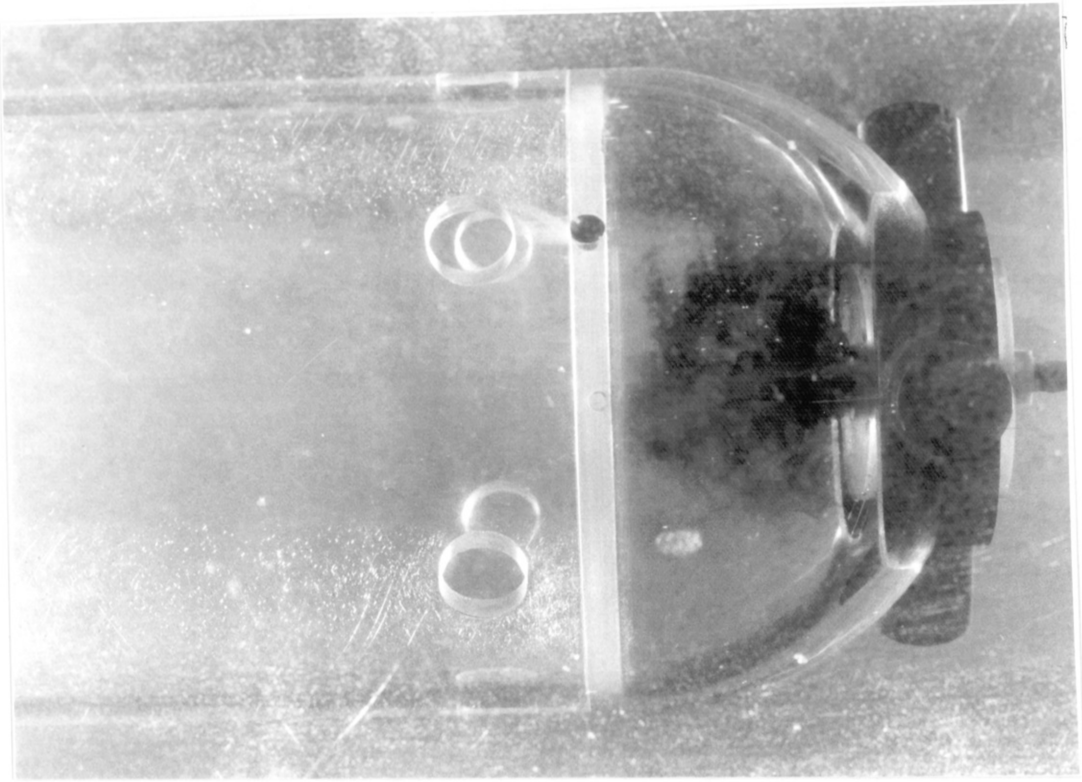

(c) dye flow visualization (case 2)

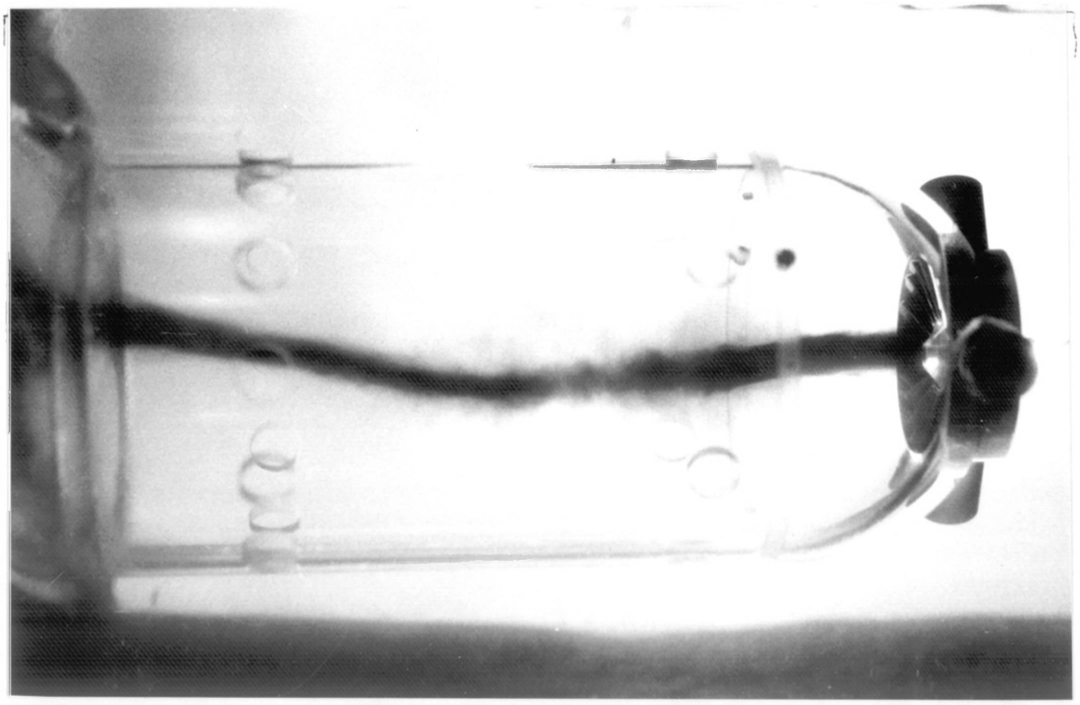

(d) dye flow visualization (case 6)

Figure 2.10 (continued)

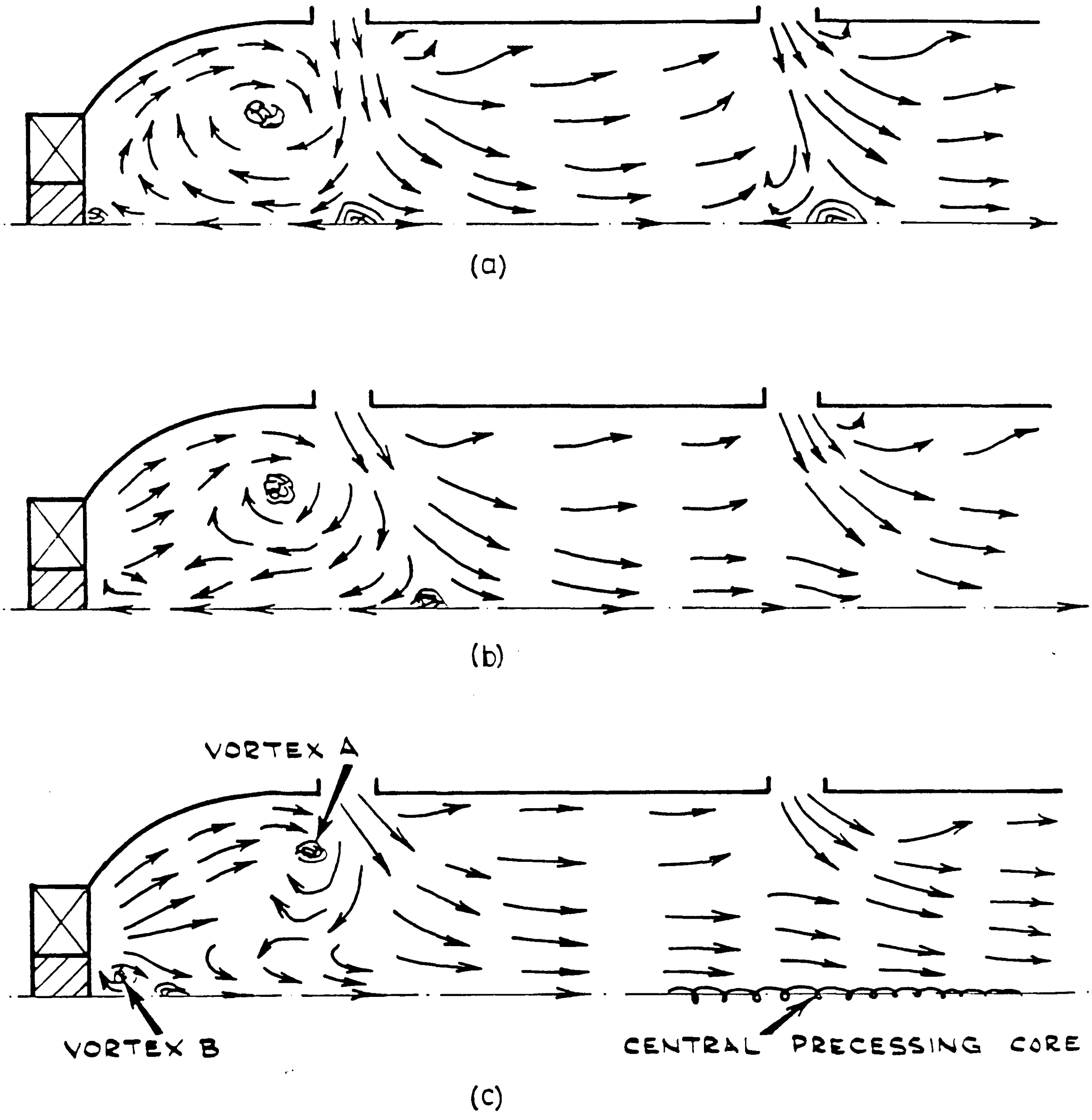

Figure 2.11 Flow pattern deduced from flow visualization

(a) case 2. (b) case 3. (c) case 4

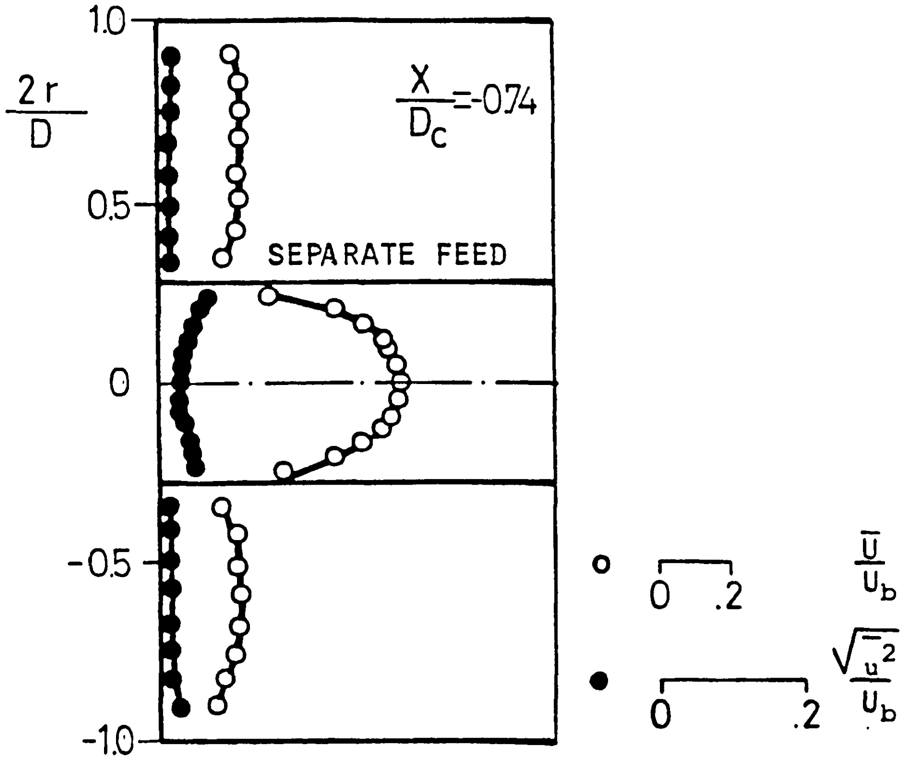

Figure 2. 12 Axial velocity and turbulence intensity profiles upstream of the model combustor

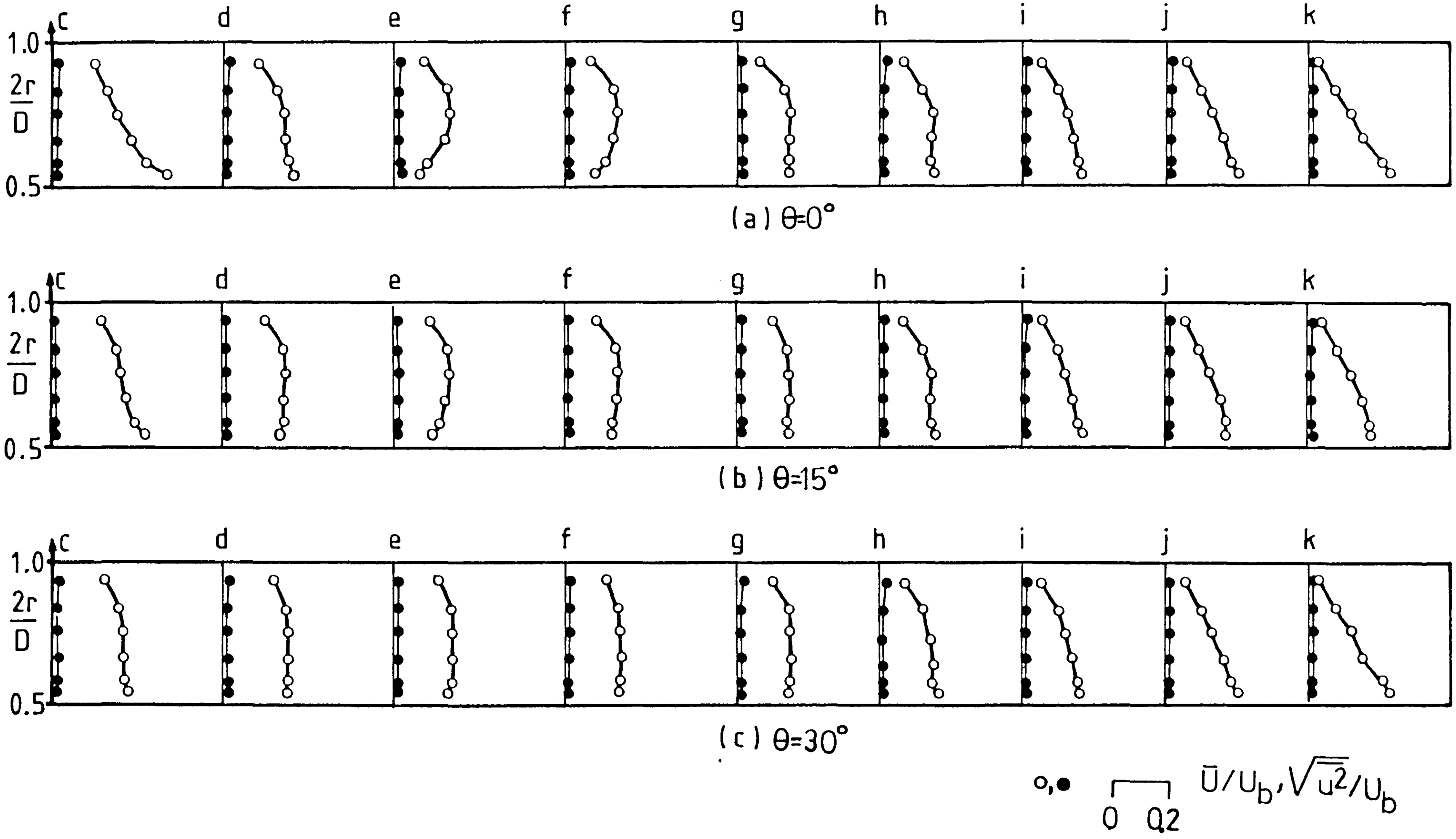

Figure 2.13 Axial velocity and turbulence intensity profiles in the annulus (case 2)

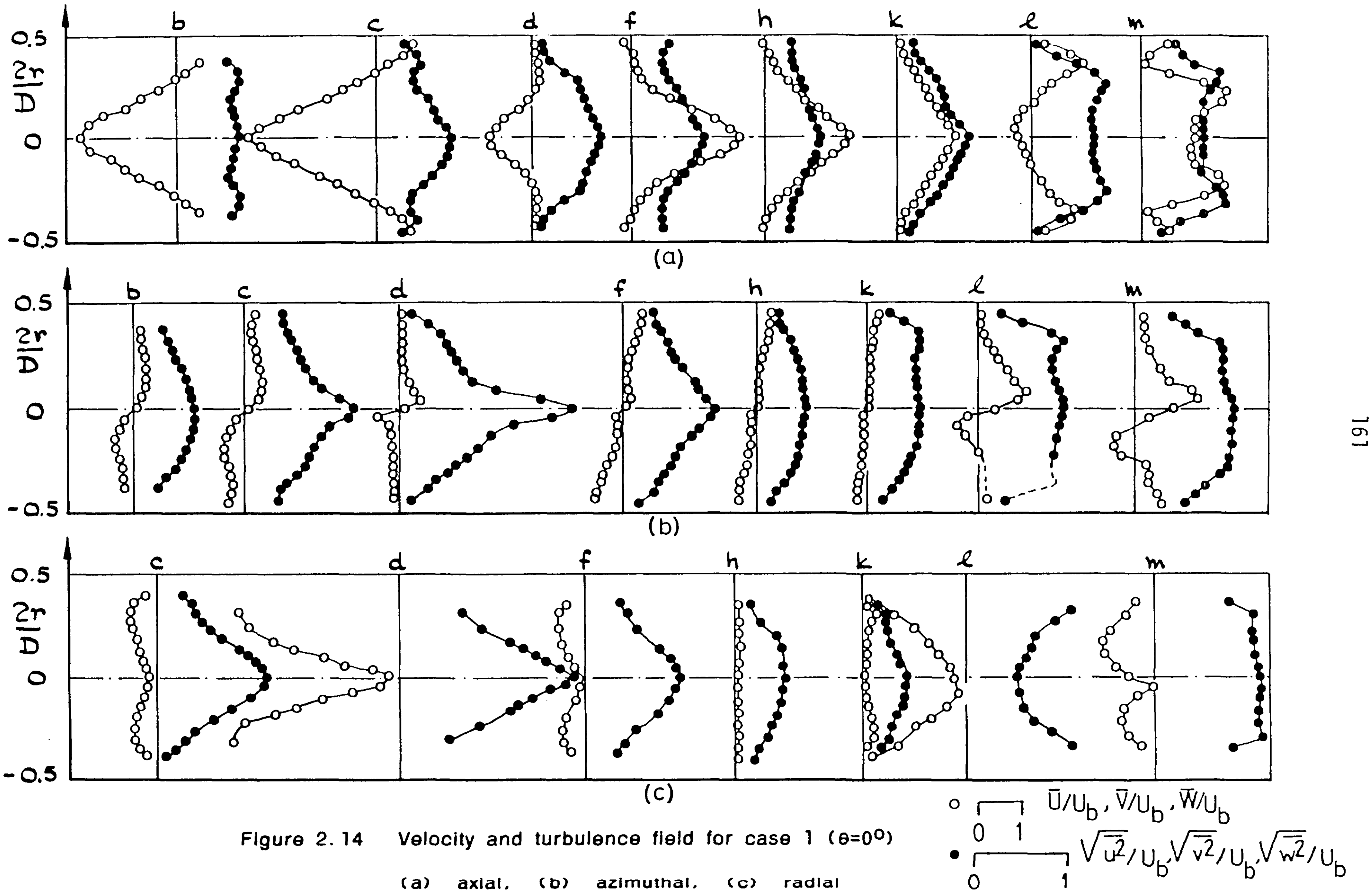

Figure 2.14 Velocity and turbulence field for case 1 ($\theta=0^o$)

(a) axial, (b) azimuthal, (c) radial

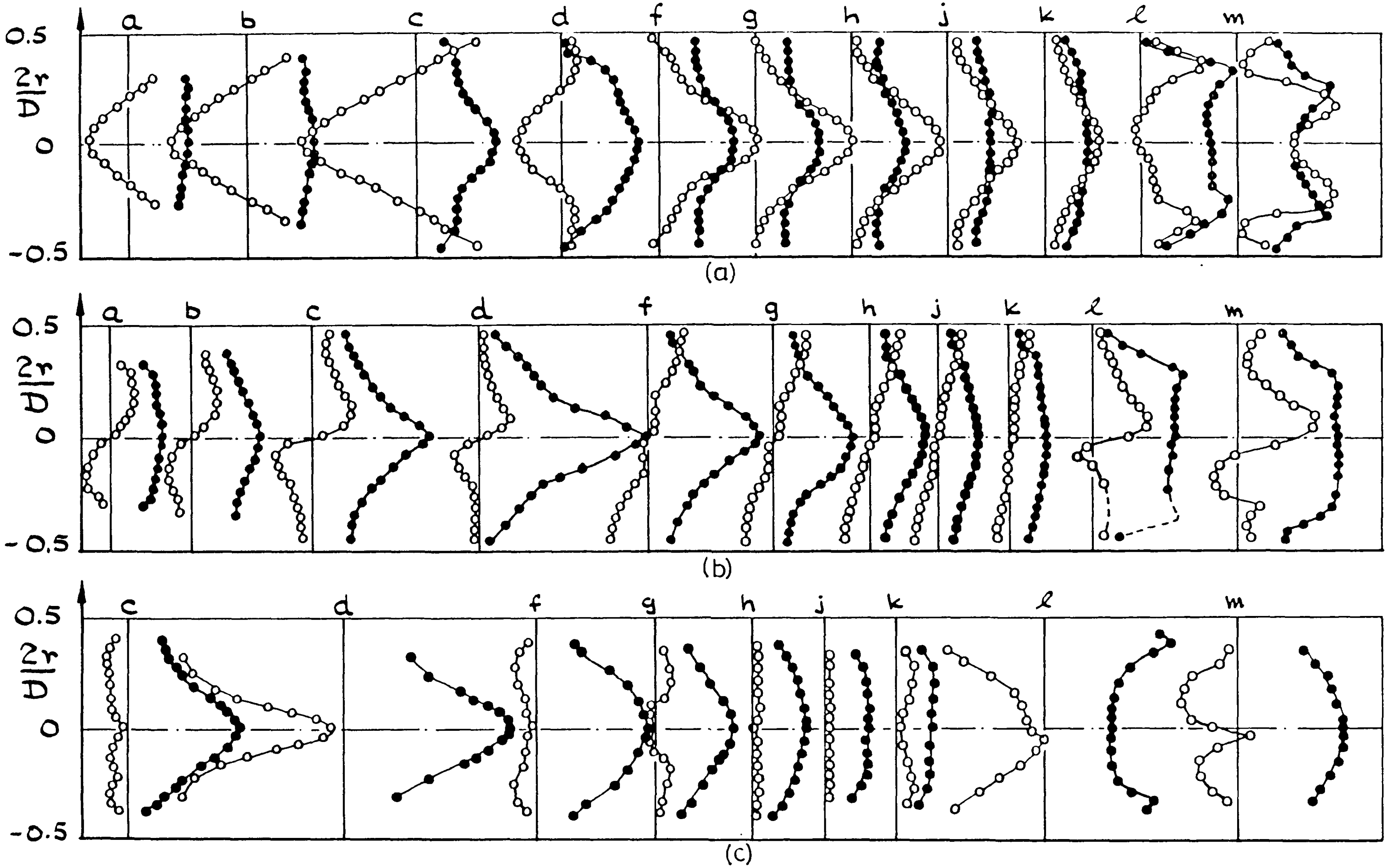

Figure 2.15 Velocity and turbulence field for case 2 ($\theta=0^0$)

(a) axial, (b) azimuthal, (c) radial

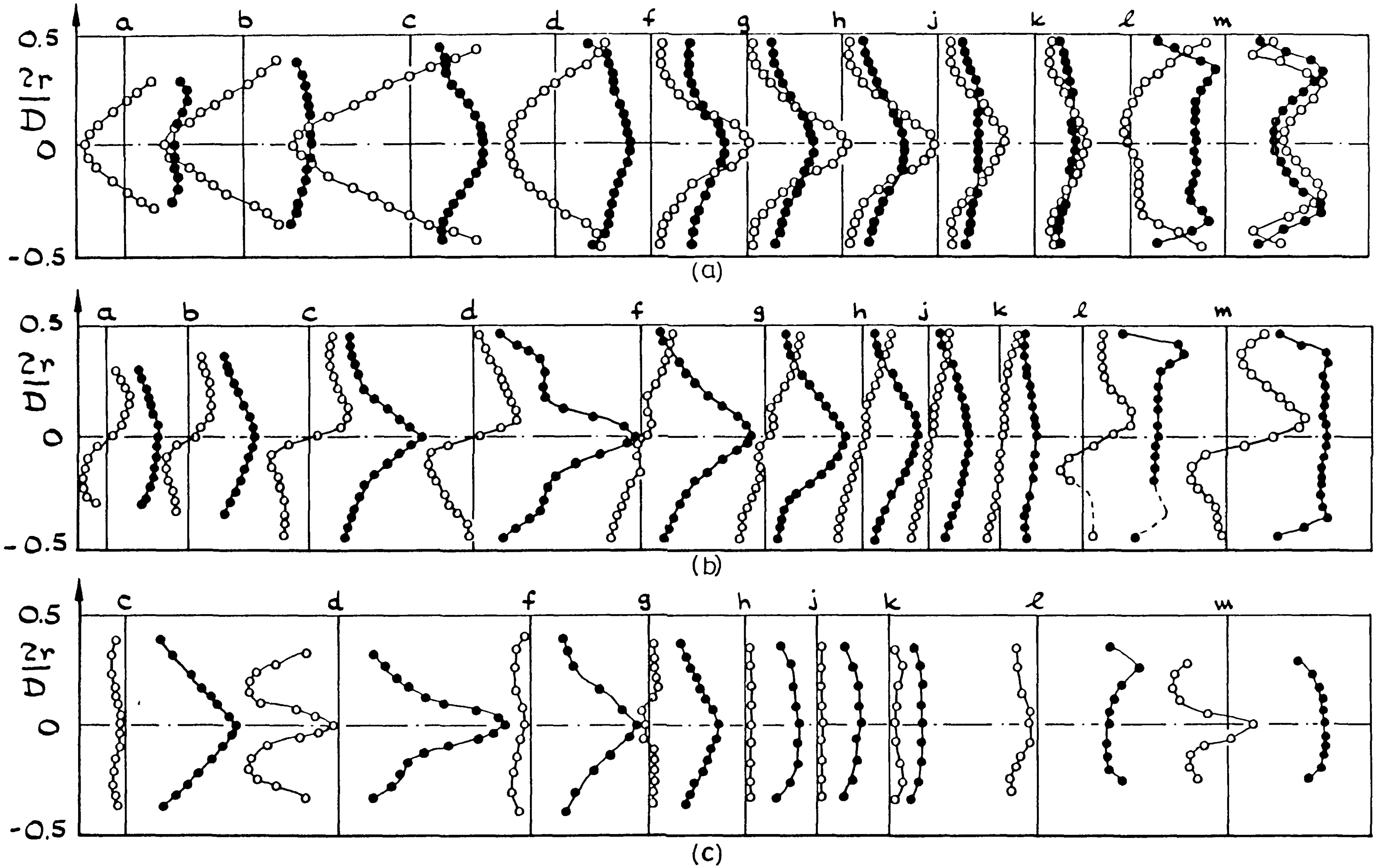

Figure 2.16 Velocity and turbulence field for case 2 (θ=15^{0})

(a) axial. (b) azimuthal. (c) radial

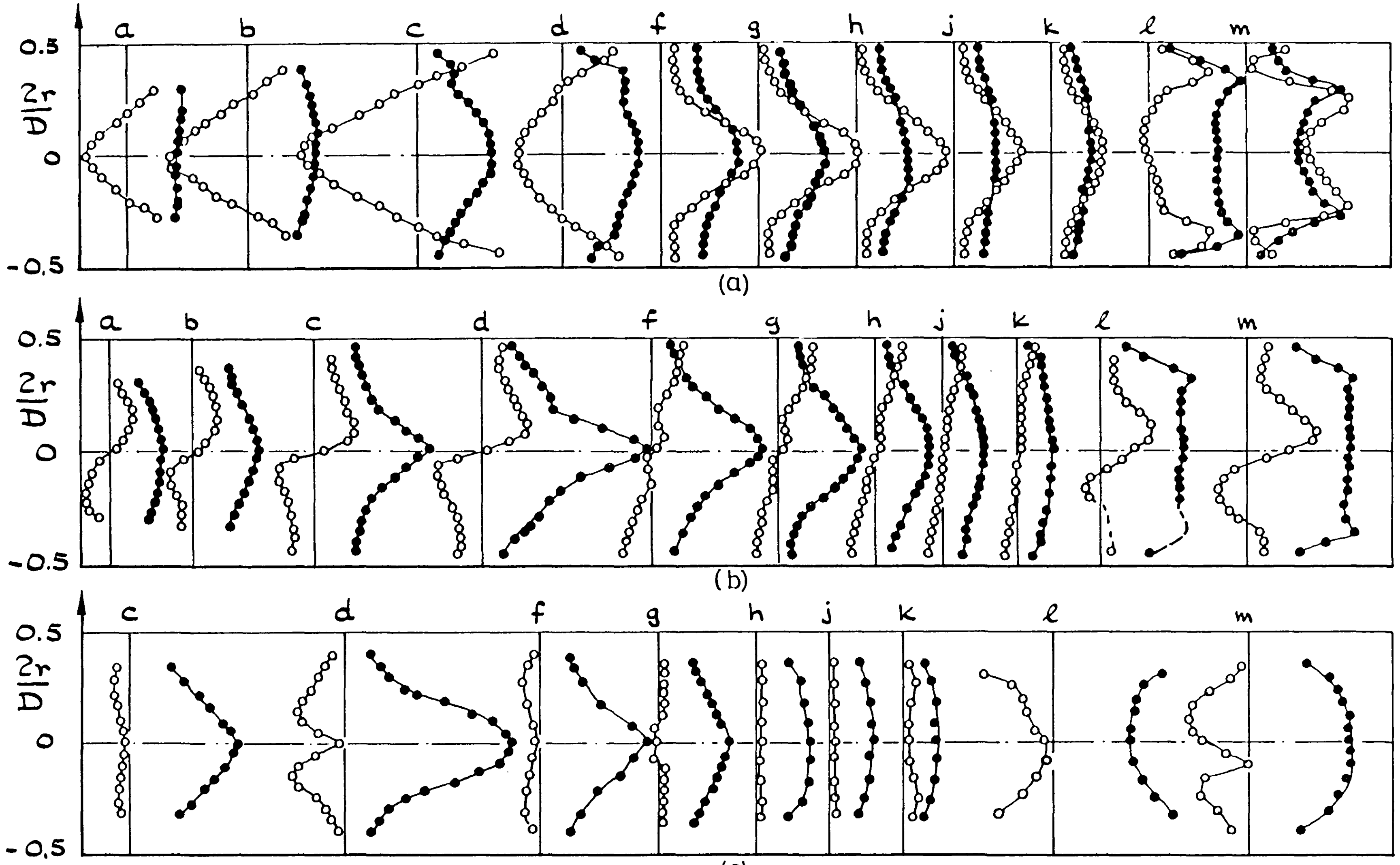

Figure 2. 17 Velocity and turbulence field for case 2 (θ=30°)

(a) axial, (b) azimuthal, (c) radial

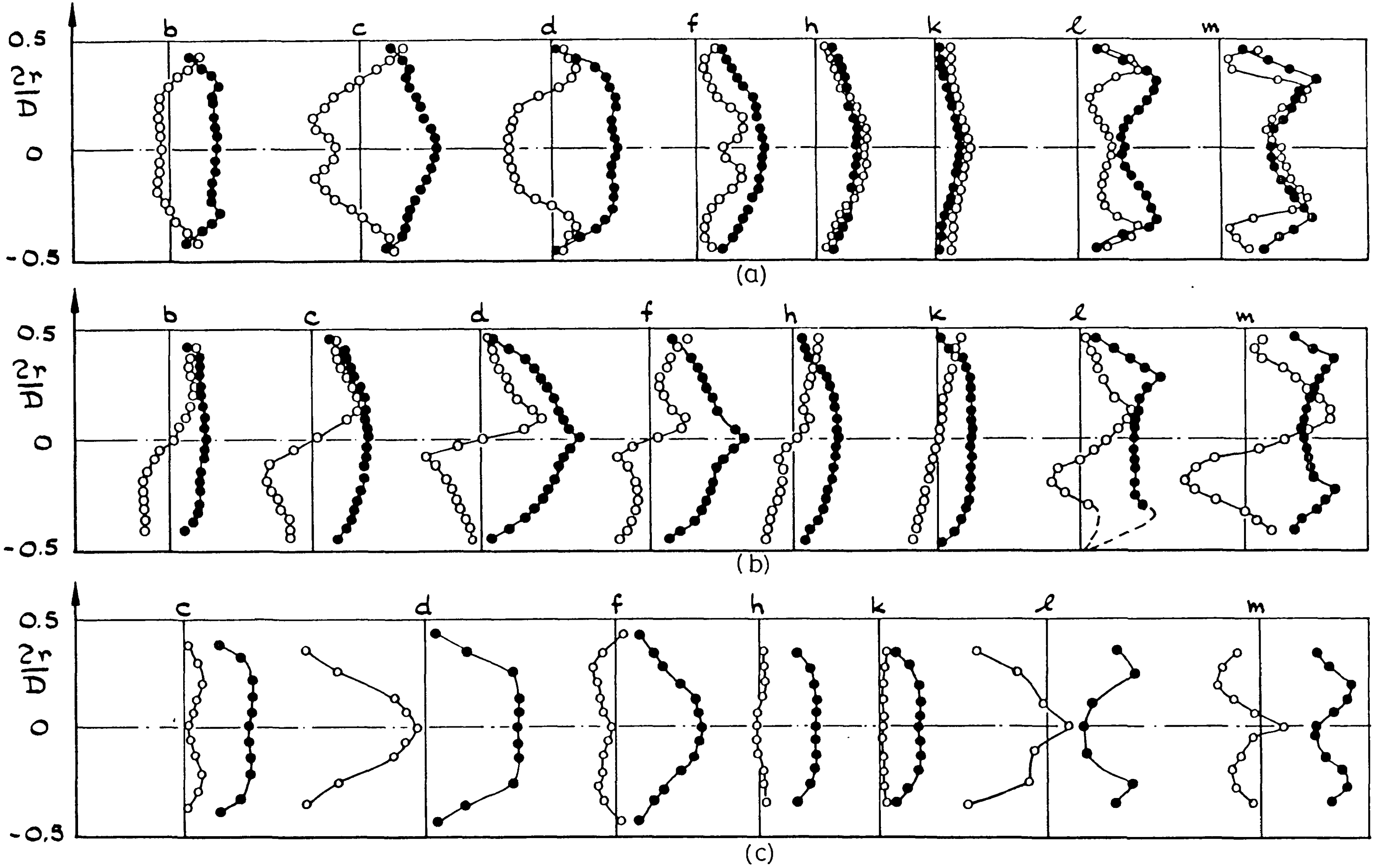

Figure 2. 18 Velocity and turbulence field for case 3 $(\theta=0^{\circ})$

(a) axial. (b) azimuthal. (c) radial

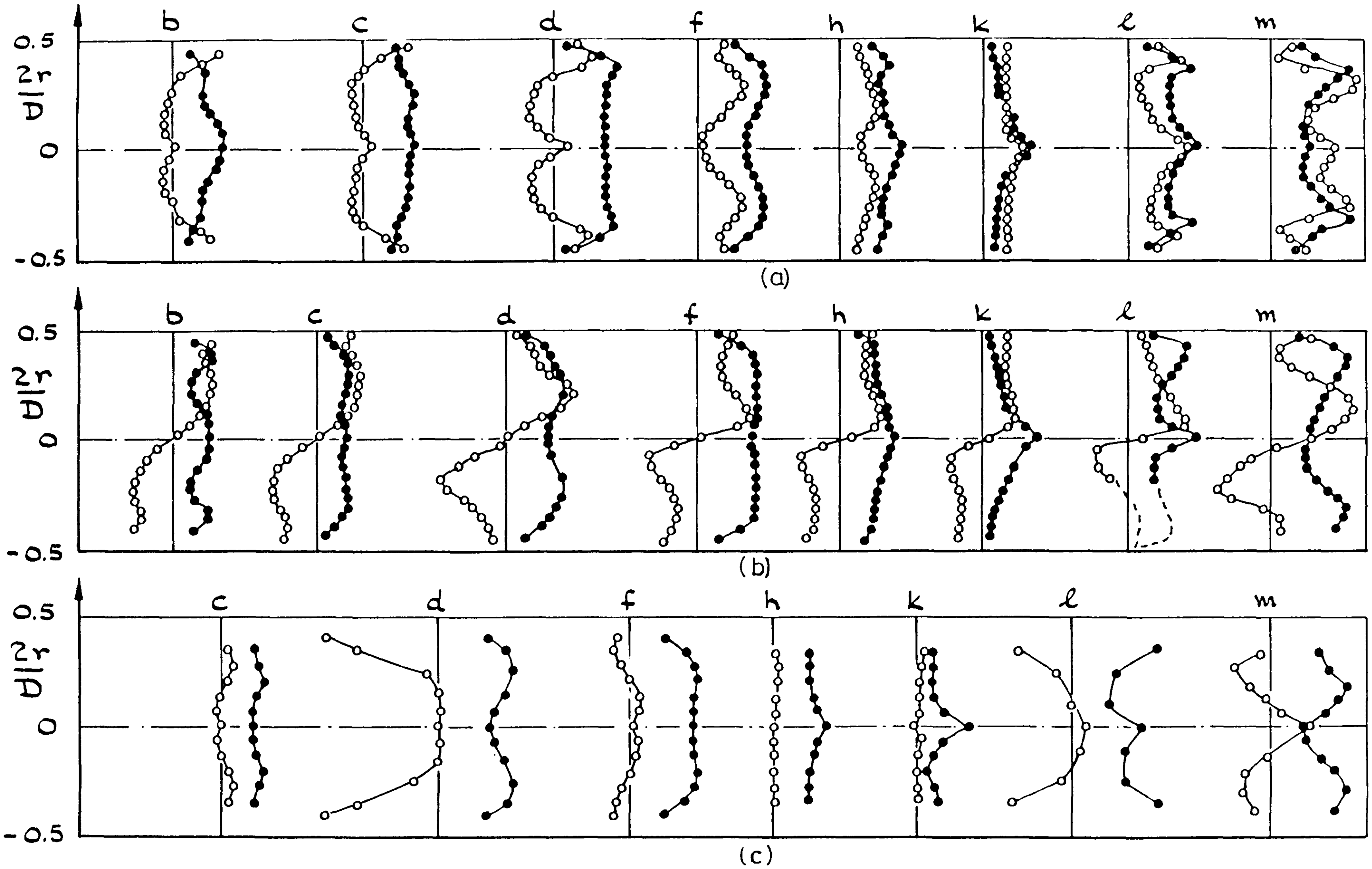

Figure 2. 19 Velocity and turbulence field for case 4 (θ=0°)

(a) axial, (b) azimuthal, (c) radial

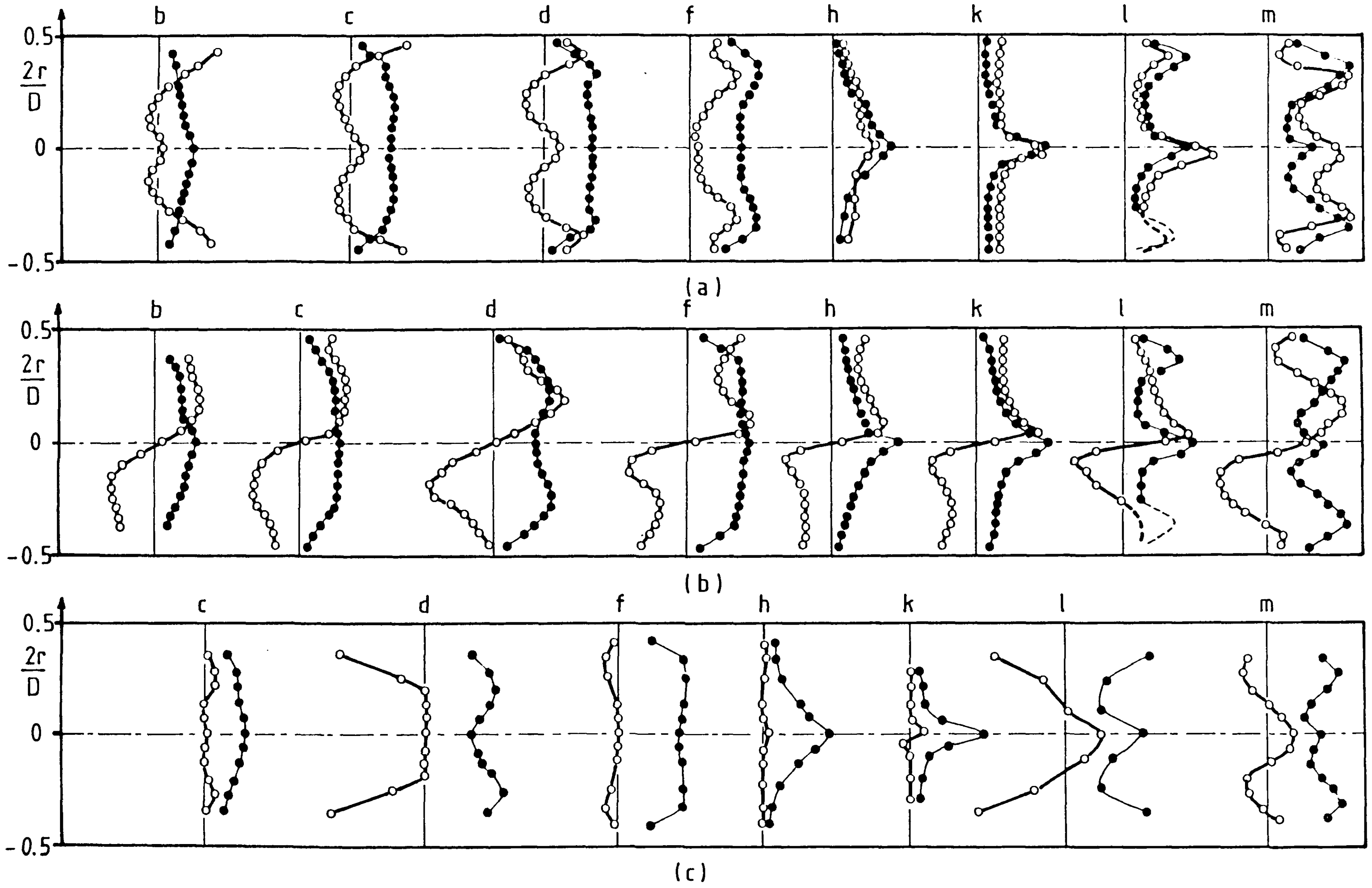

(a)

(b)

(c)

Figure 2.20 Velocity and turbulence field for case 5 (θ=0°)

(a) axial, (b) azimuthal, (c) radial

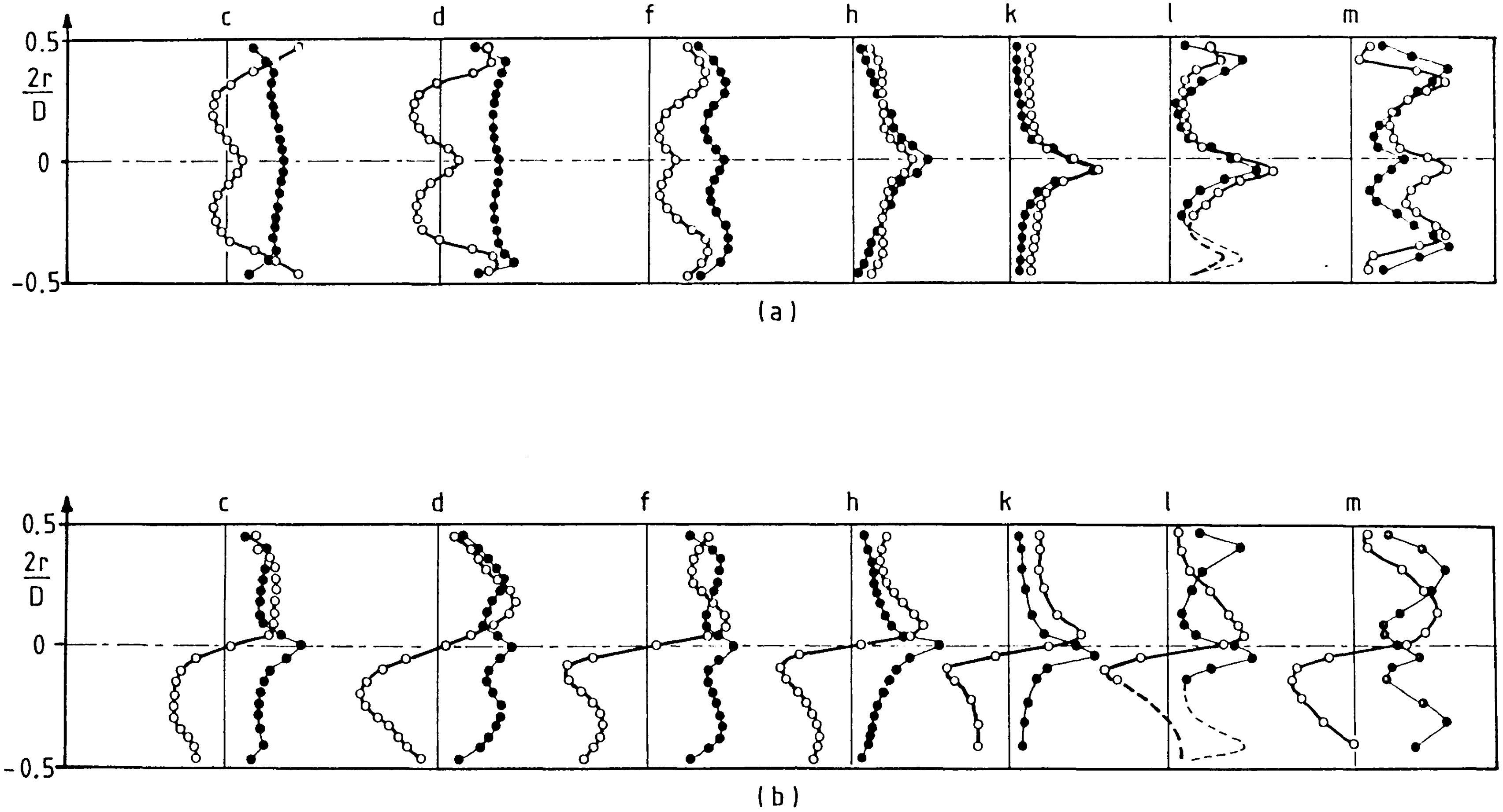

Figure 2.21 Velocity and turbulence field for case 6 (θ=0°)

(a) axial, (b) azimuthal

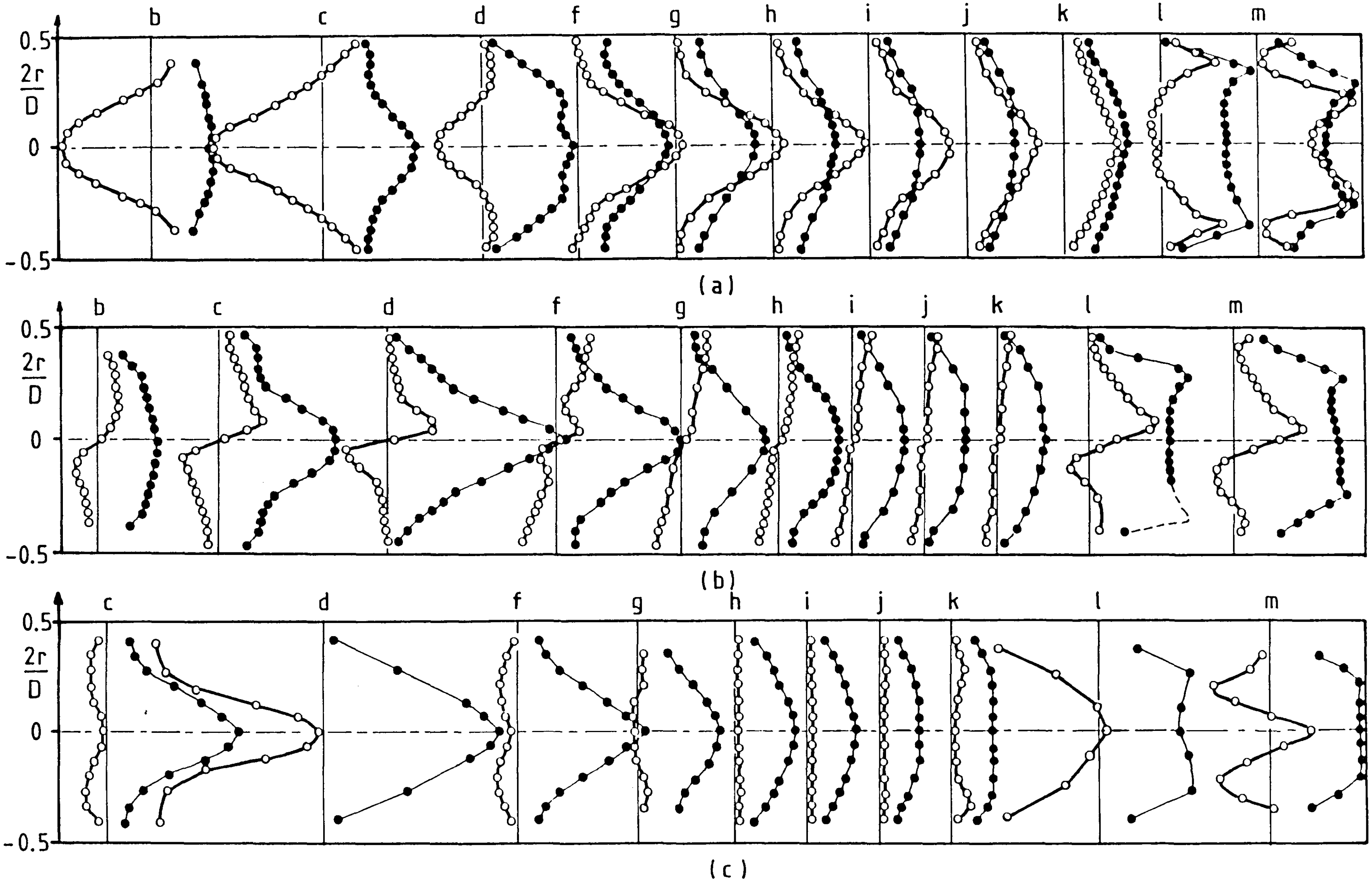

Figure 2.22 Velocity and turbulence field for case 7 ($\theta=0^{\circ}$)

(a) axial. (b) azimuthal. (c) radial

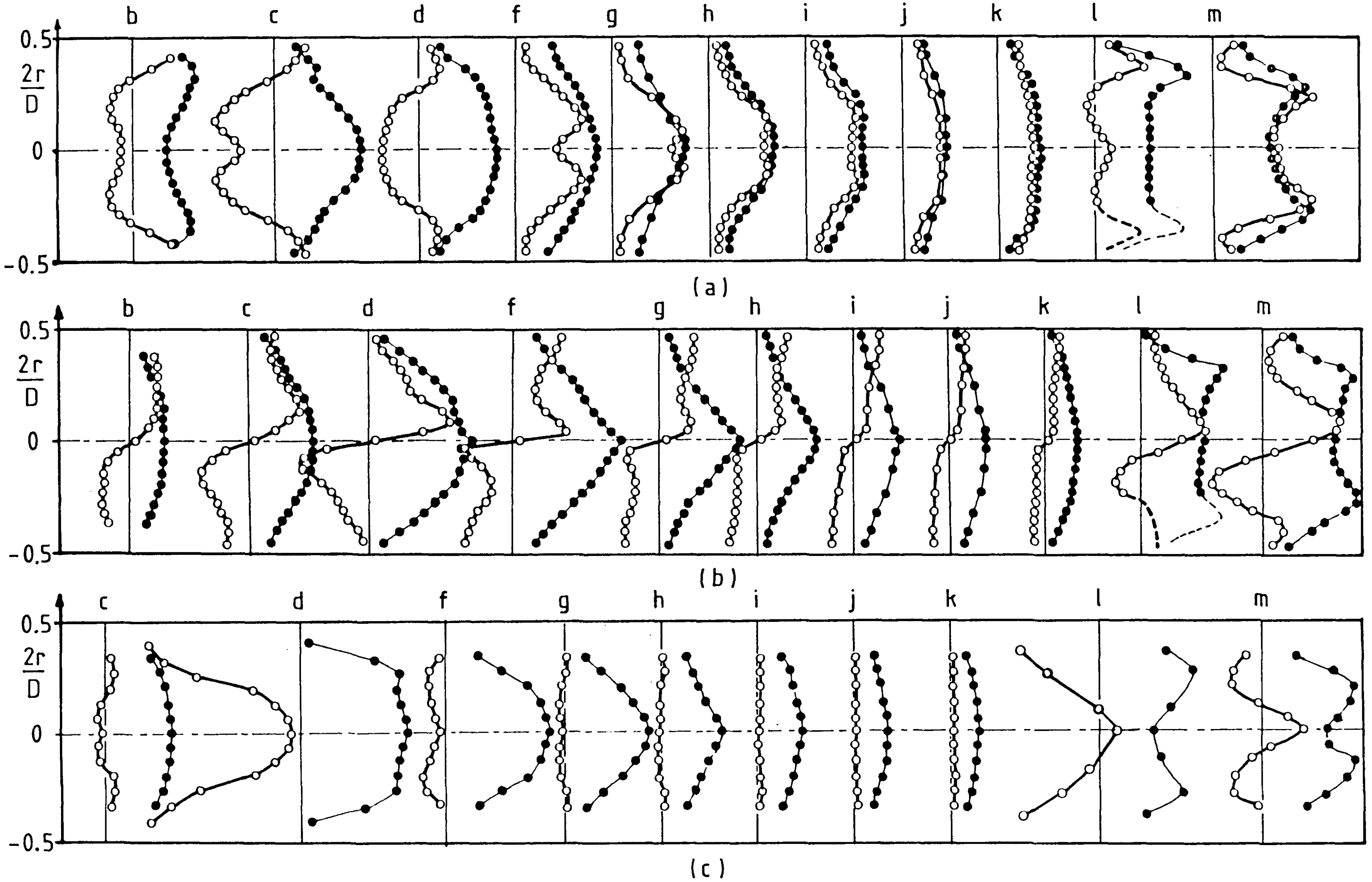

Figure 2. 23 Velocity and turbulence field for case 8 ($\theta=0^0$)

(a) axial, (b) azimuthal, (c) radial

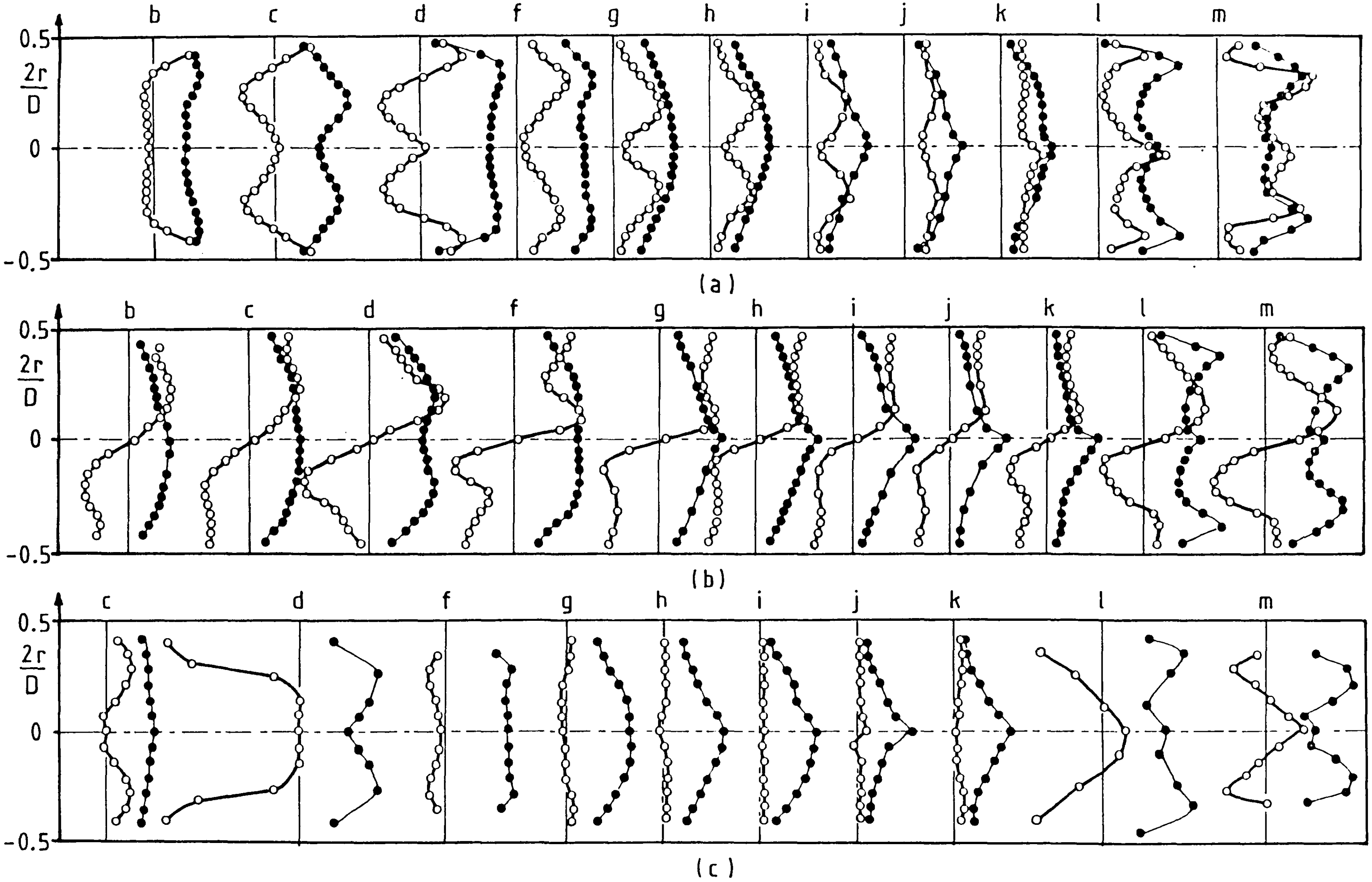

Figure 2.24 Velocity and turbulence field for case 9 ($\theta=0^0$)

(a) axial. (b) azimuthal. (c) radial

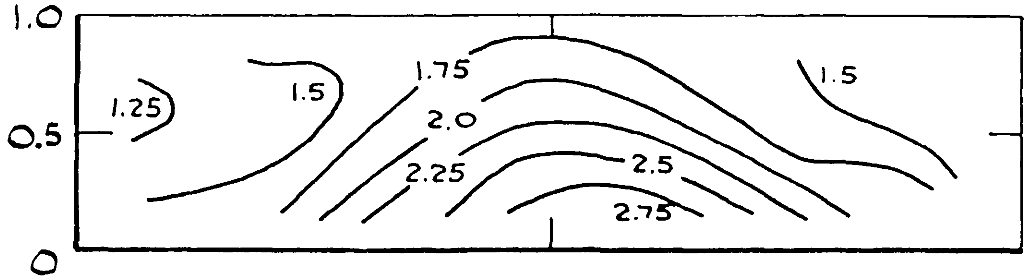

(a) case 1

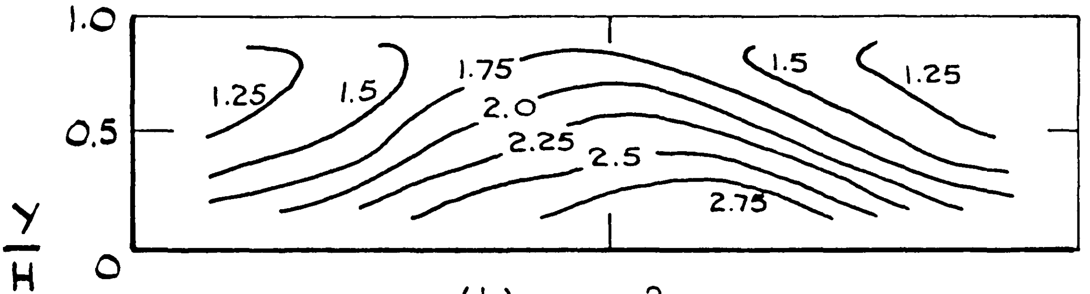

(b) case 2

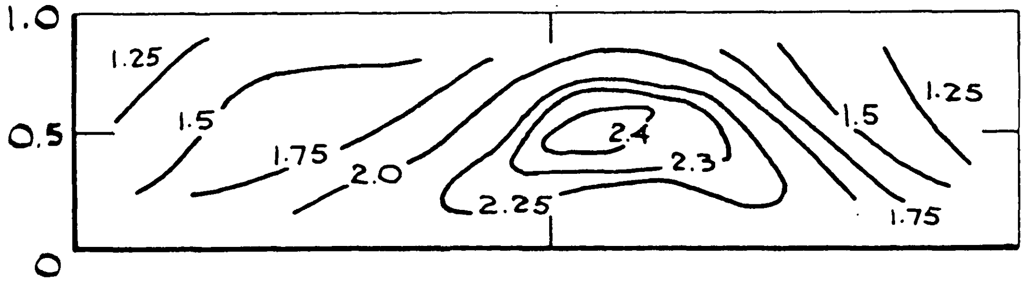

(c) case 3

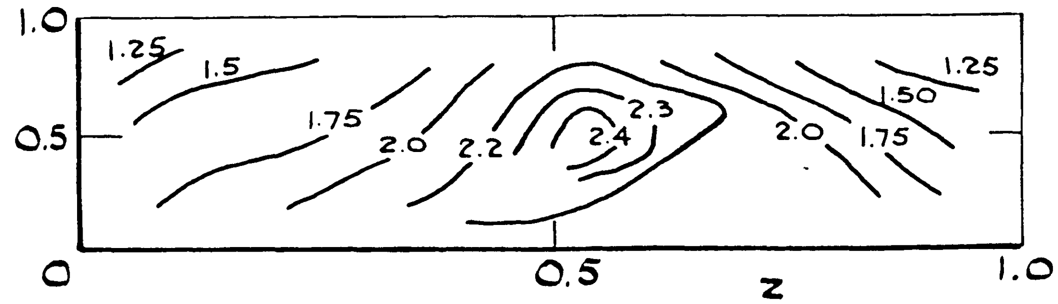

(d) case 4 $\frac{Z}{W}$

Figure 2.25 Axial velocity field at exit from the nozzle contraction

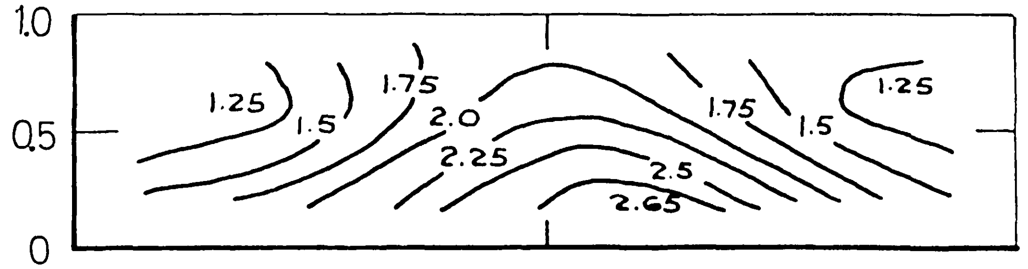

(e) case 7

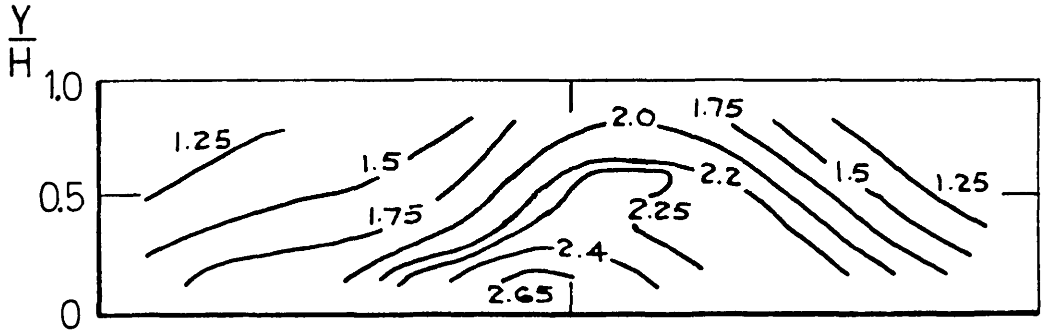

(f) case 8

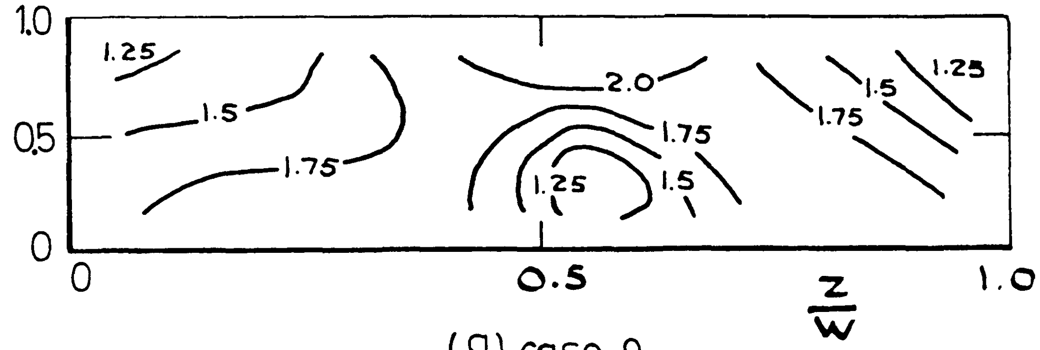

(g) case 9

Figure 2.25 (continued)

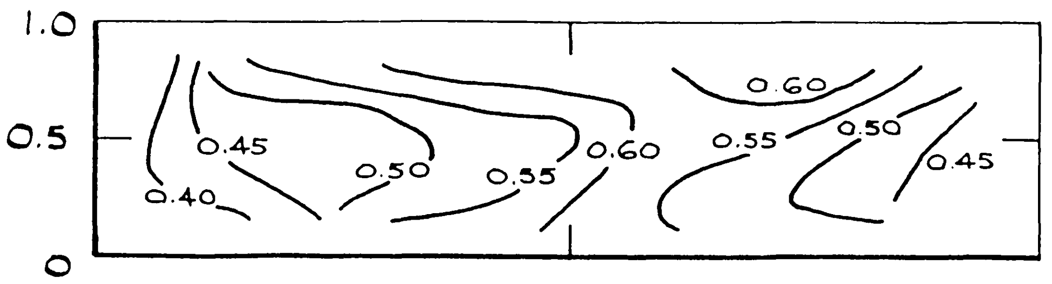

(a) case 1

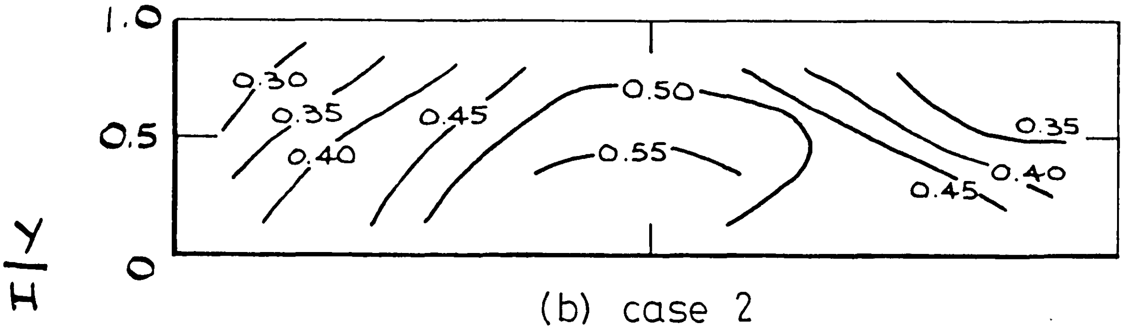

(b) case 2

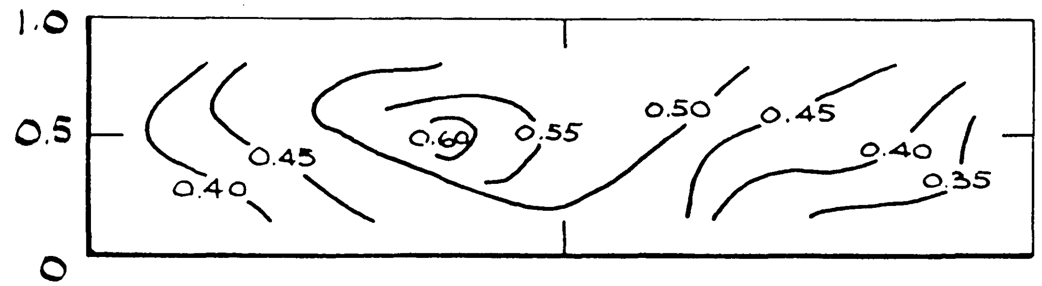

(c) case 3

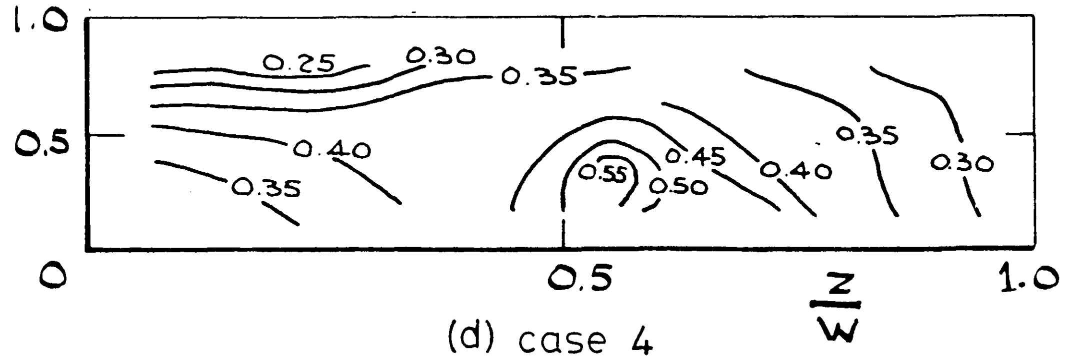

(d) case 4

Figure 2.26 Axial turbulence intensity field at exit from the nozzle contraction

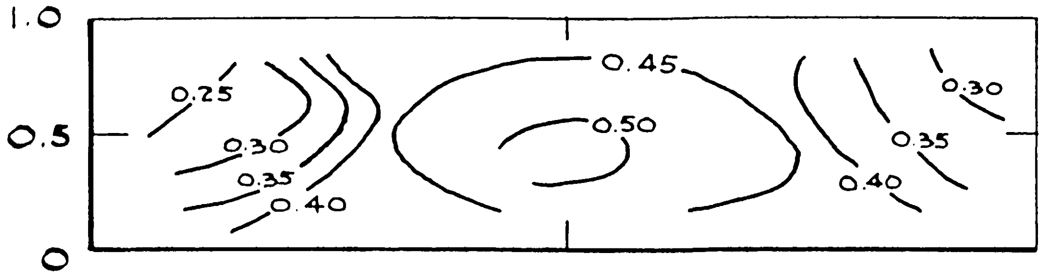

(e) case 7

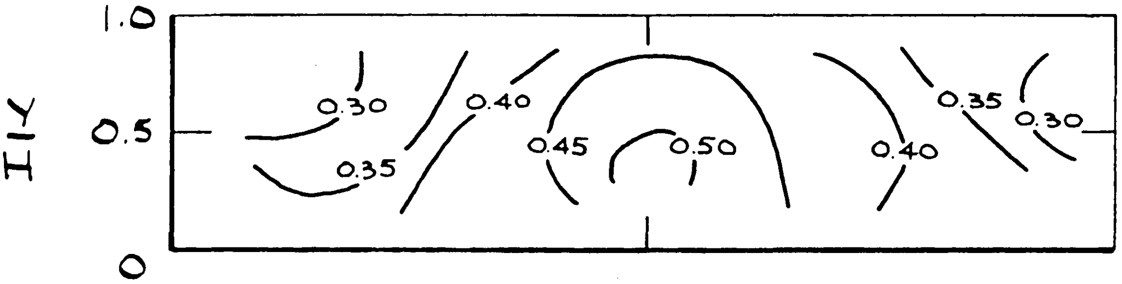

(f) case 8

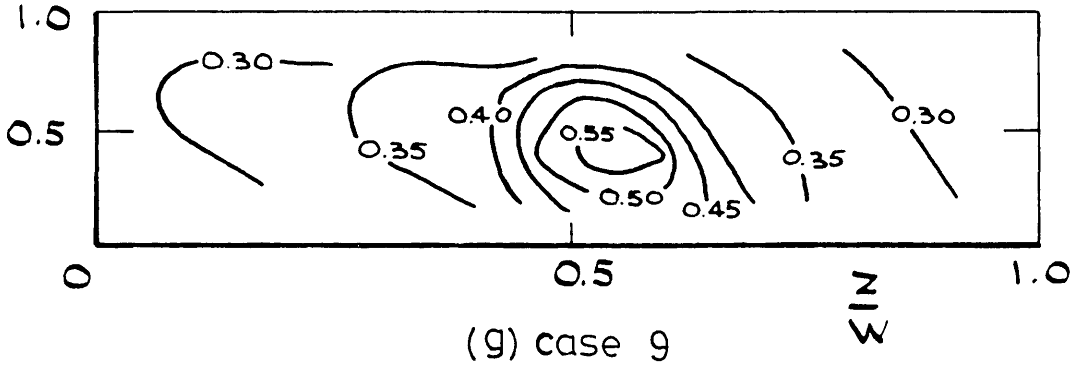

(g) case 9

Figure 2.26 (continued)

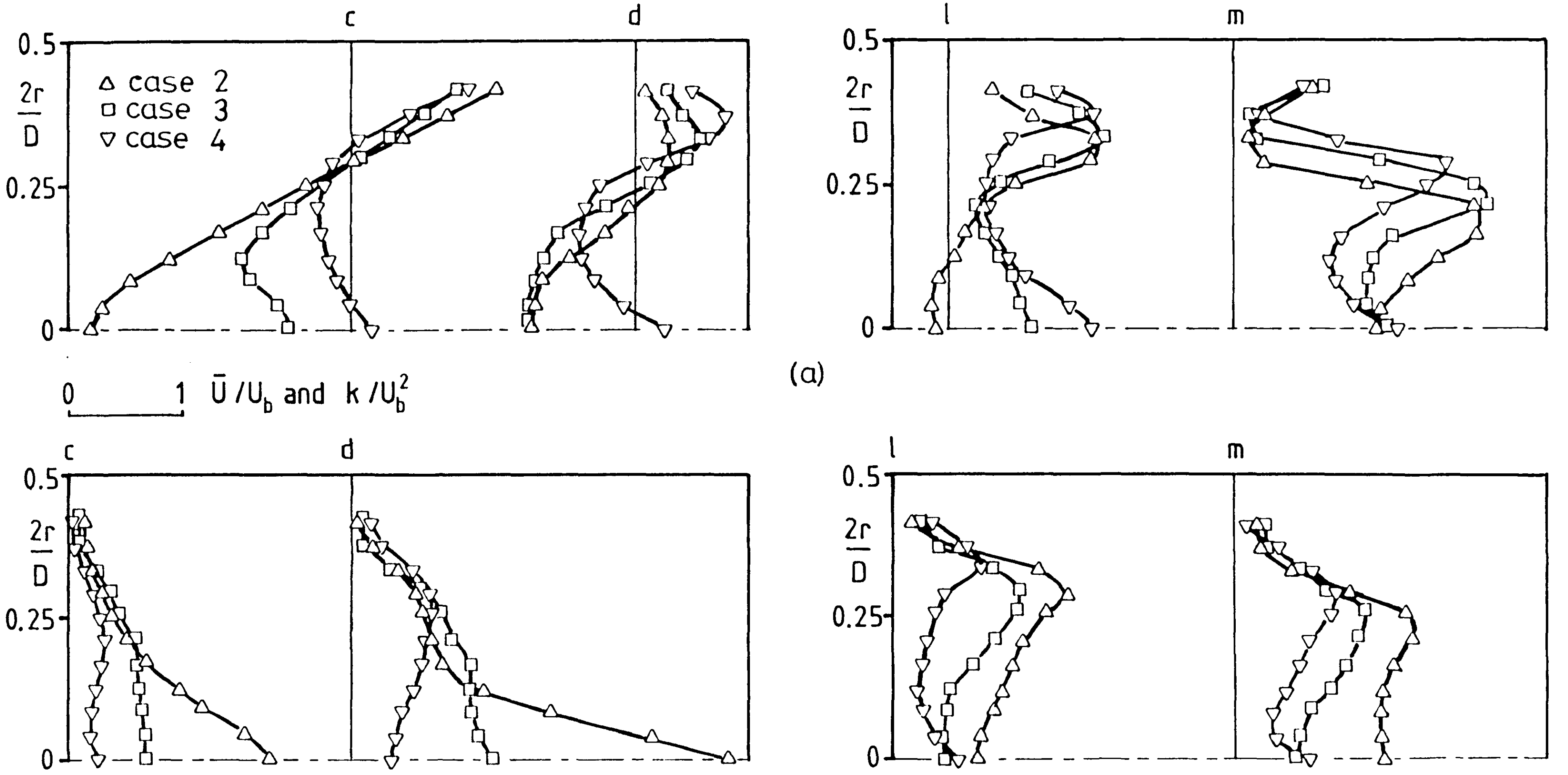

(a)

(b)

Figure 2.27 Influence of flow split on

(a) axial velocity field

(b) turbulence kinetic energy field

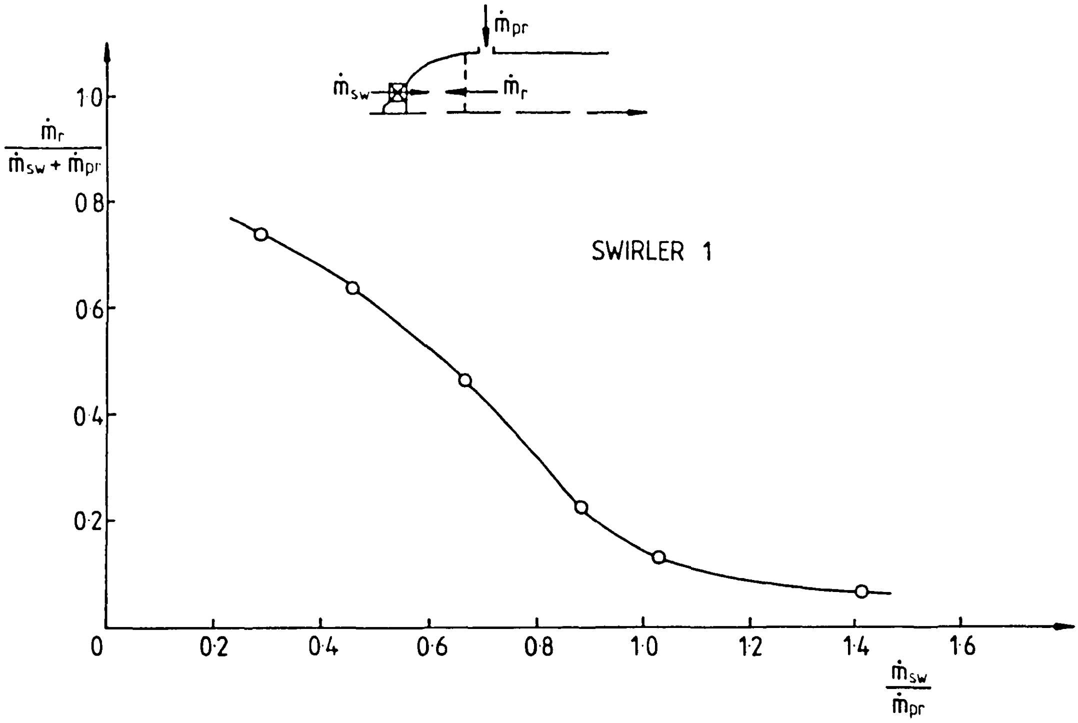

Figure 2. 28 Primary zone recirculation ratio (swirler 1)

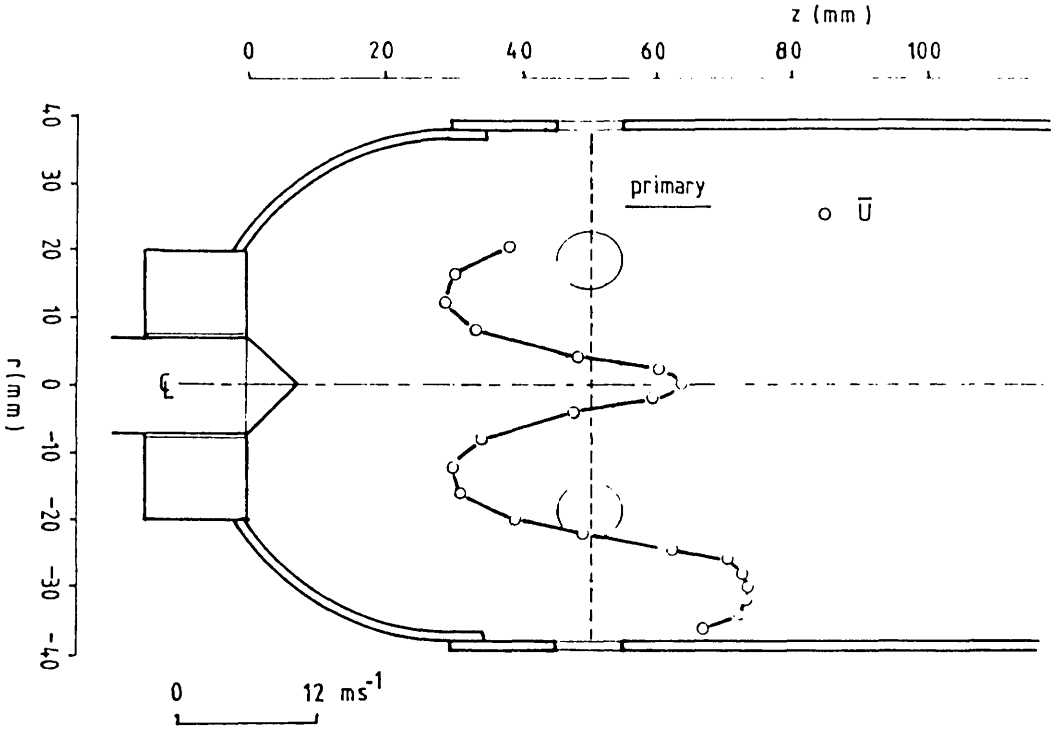

Figure 2.29 Axial velocity distribution obtained inside a can-type combustion chamber geometrically similar to the current water model under combusting conditions (taken from Bicen and Jones, 1985)

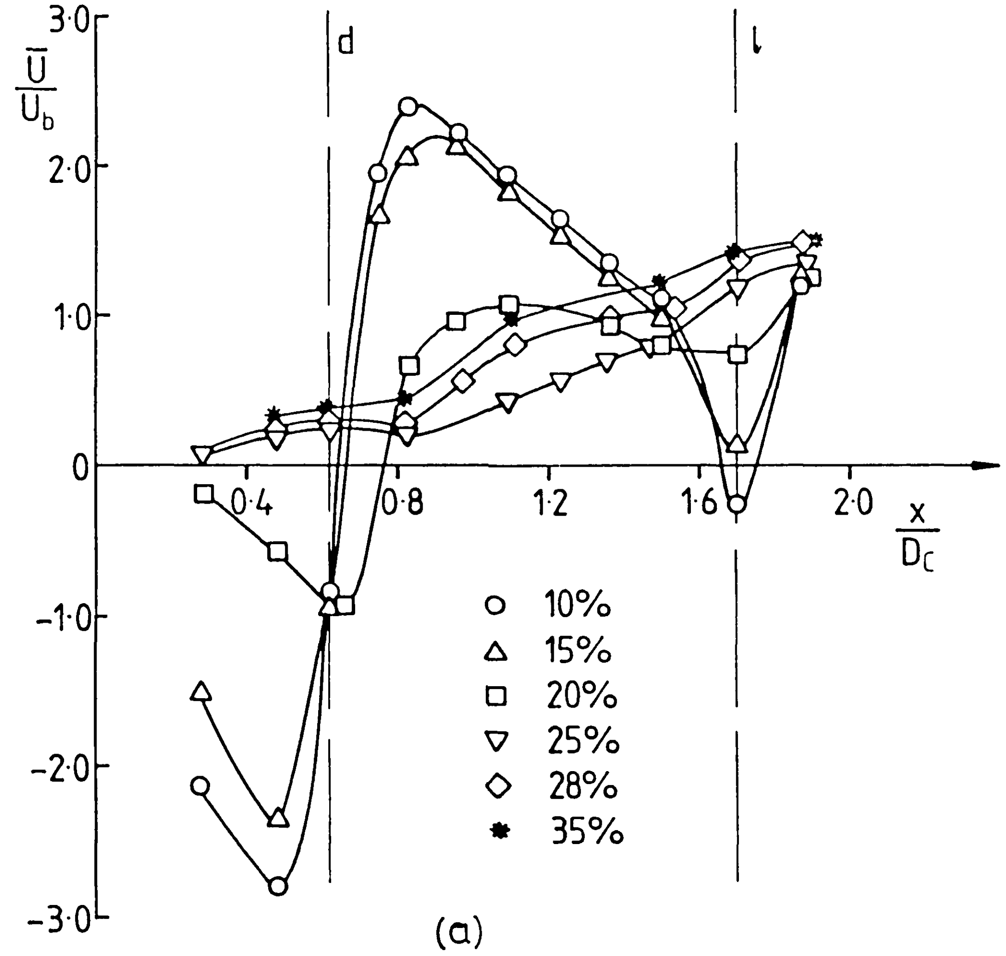

(a)

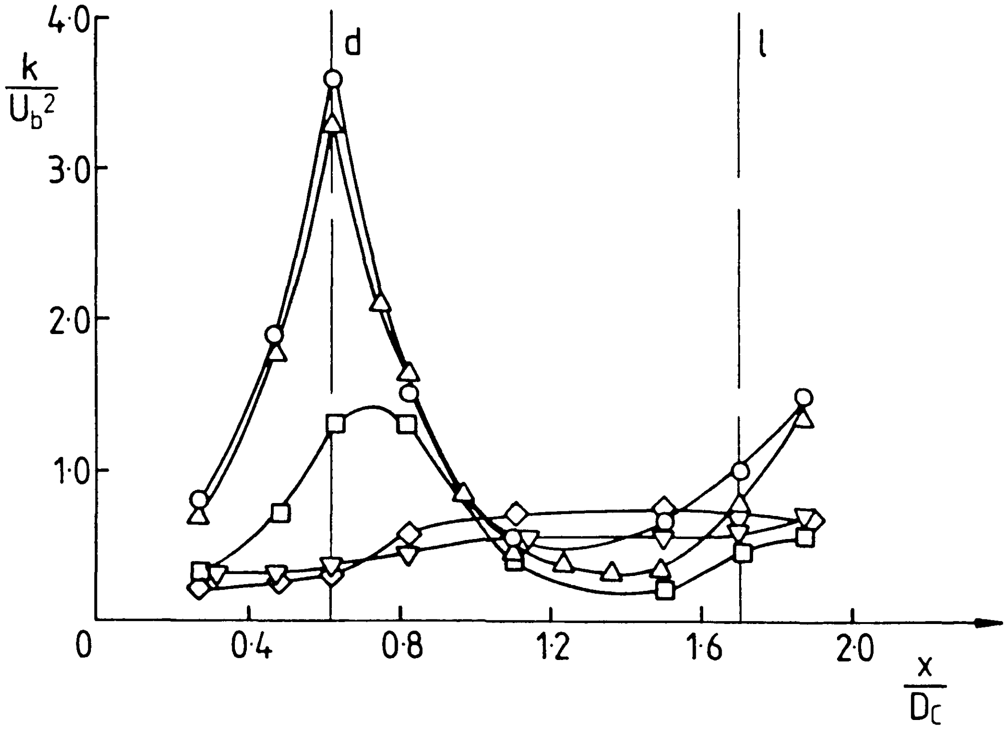

(b)

Figure 2.30 Centre line development of

(a) axial velocity

(b) turbulence kinetic energy (swirler 1)

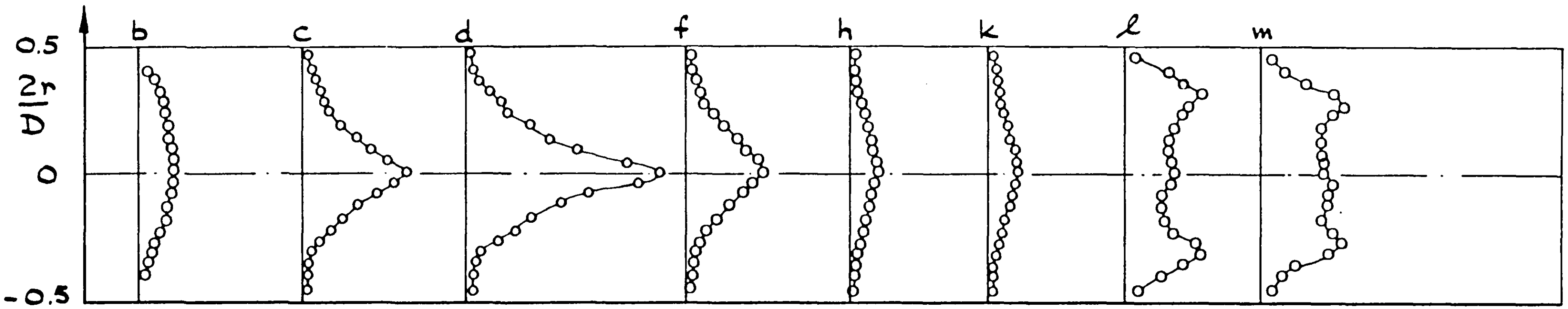

(a) case 1

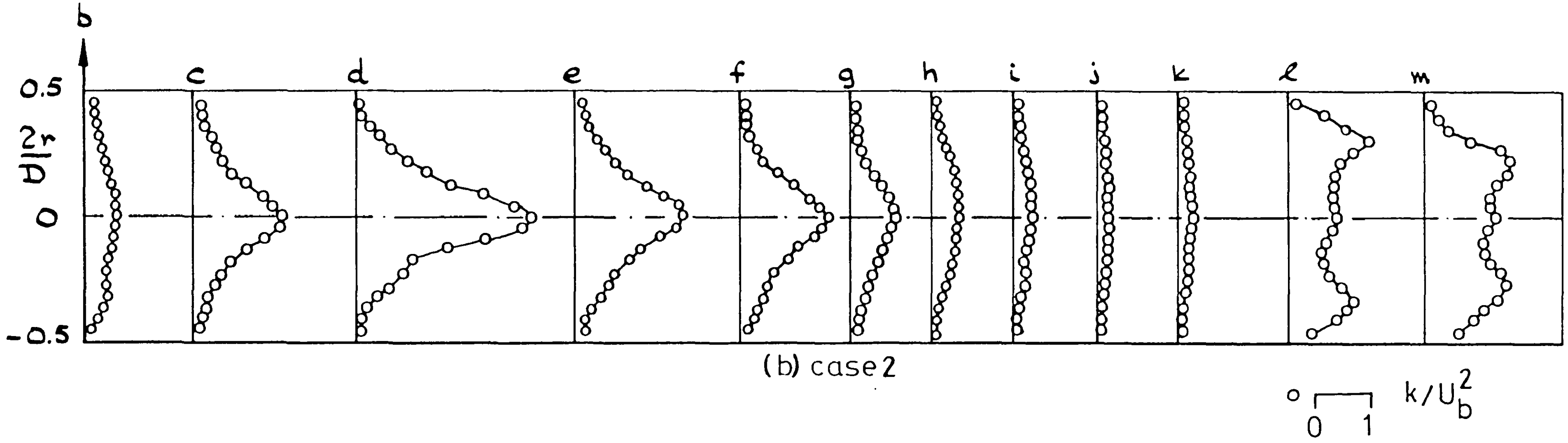

(b) case 2

Figure 2.31 Turbulence kinetic energy field inside the combustor
($\theta=0^\circ$, swirler 1)

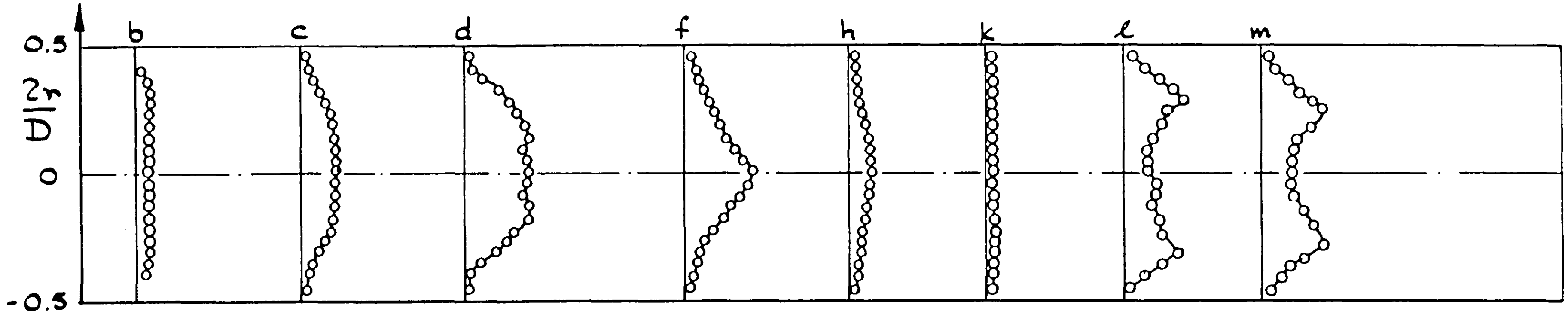

(c) case 3

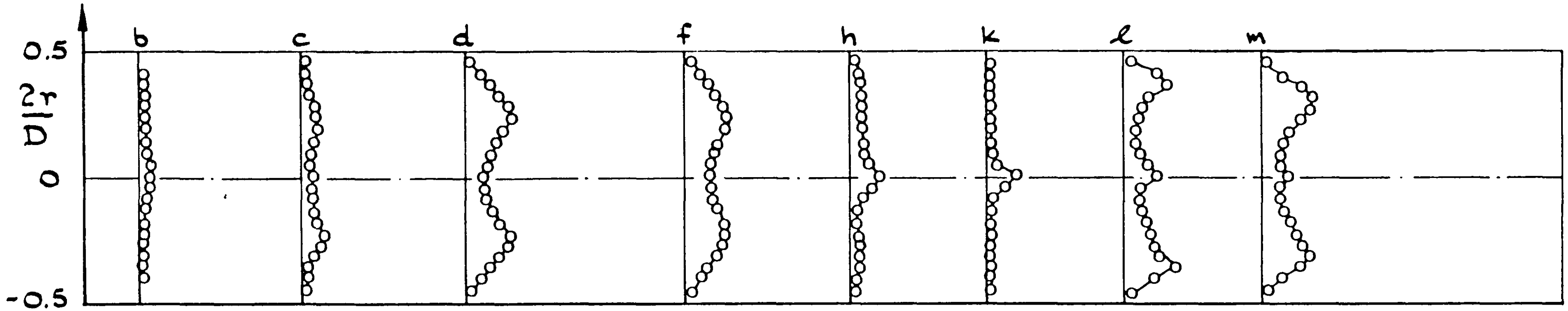

(d)case4

Figure 2.31 (continued)

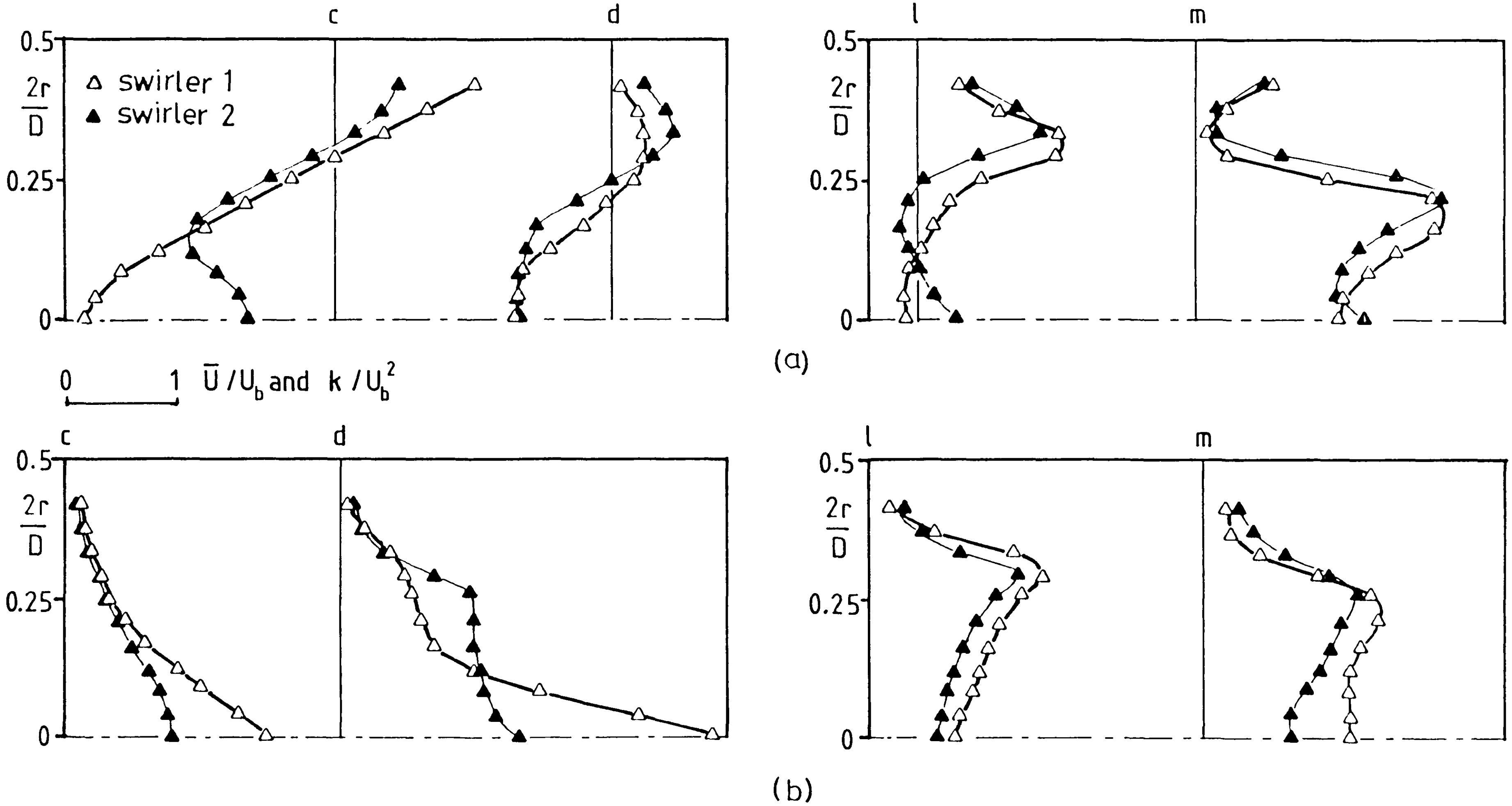

Figure 2. 32 Influence of swirler geometry on

(a) axial velocity field

(b) turbulence kinetic energy field (15% swirler flow level)

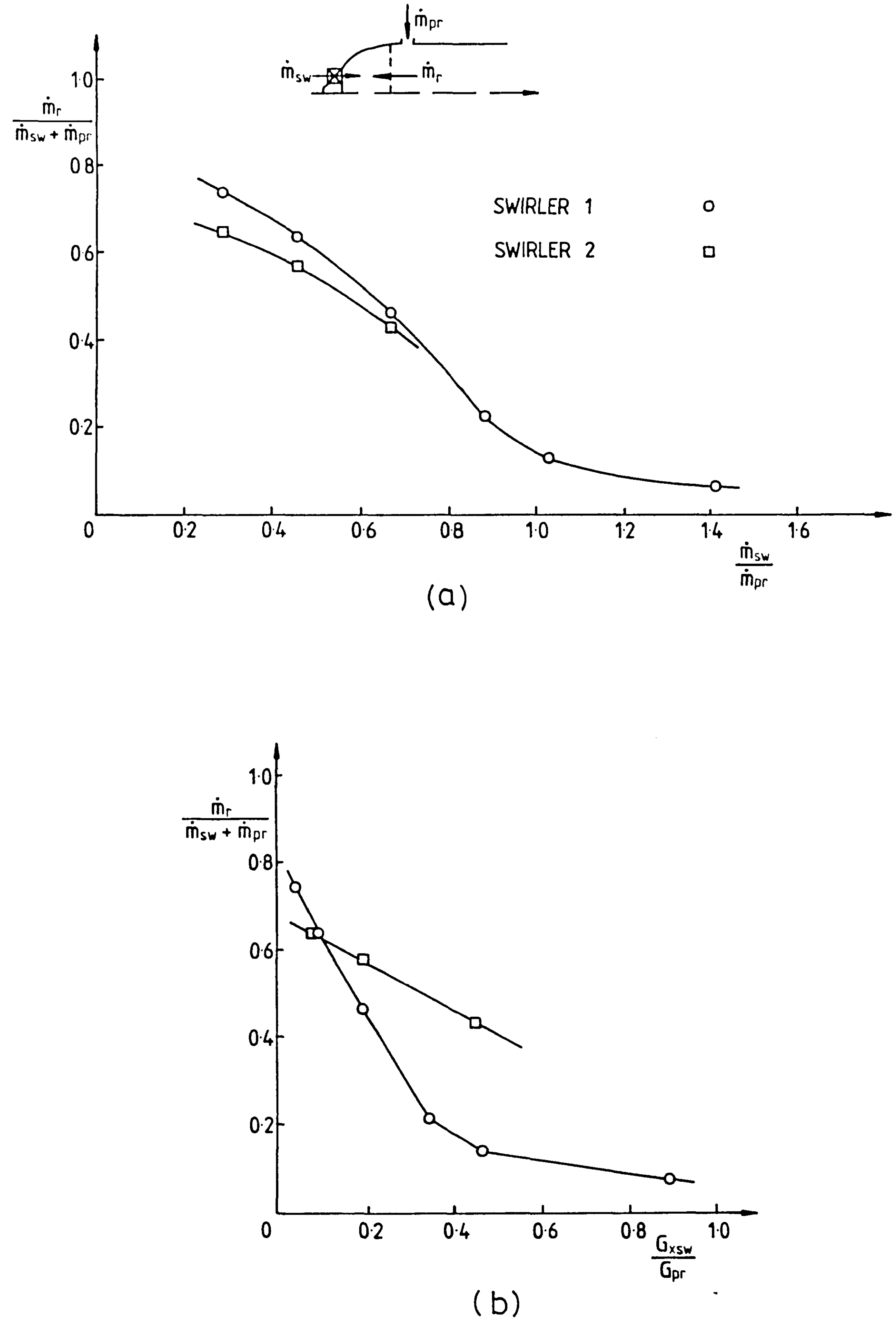

Figure 2.33 (a), (b) Primary zone recirculation ratio and comparison of the performance between swirler 1 and swirler 2

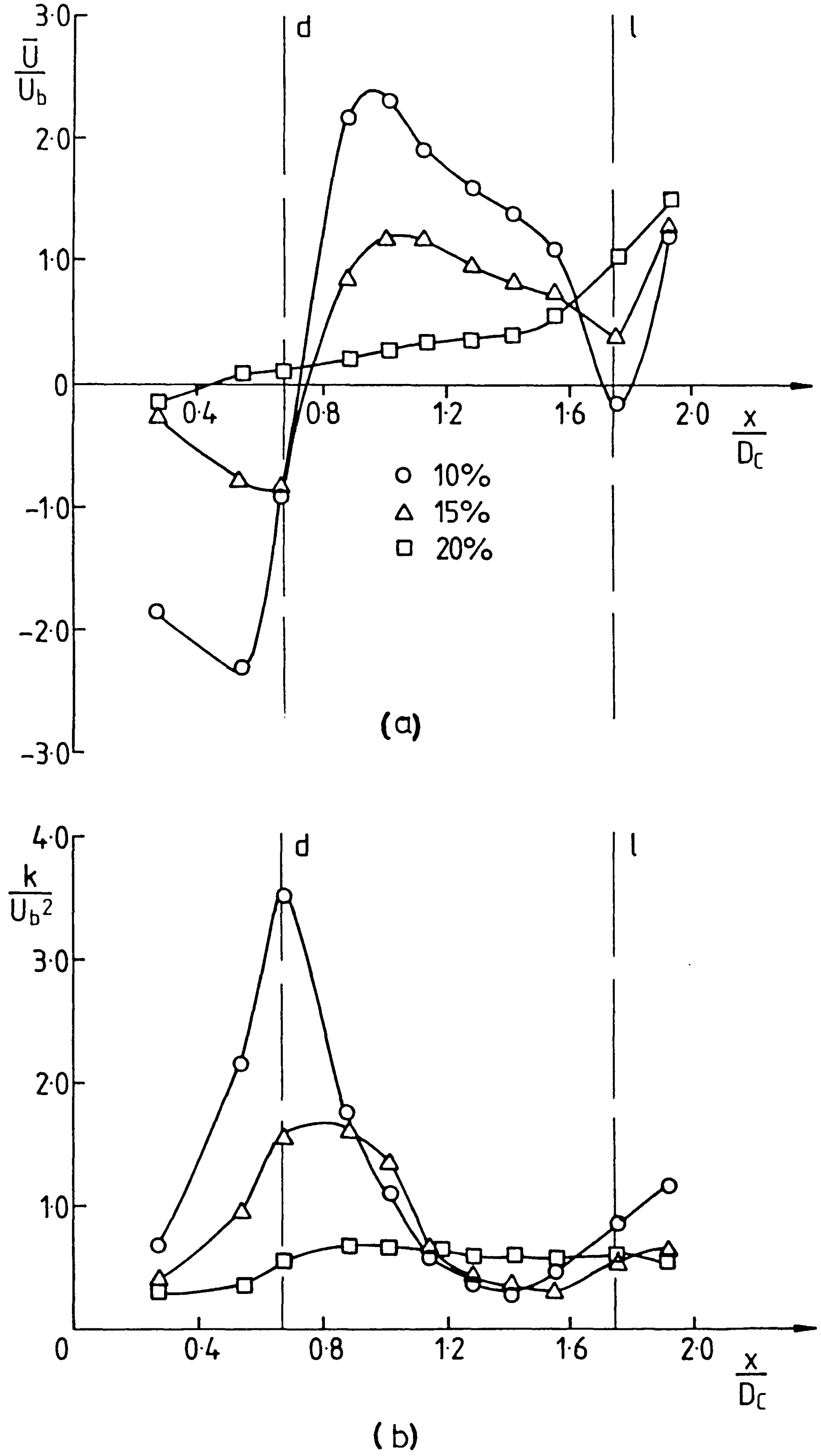

Figure 2. 34 Centre line development of

(a) axial velocity

(b) turbulence kinetic energy (swirler 2)

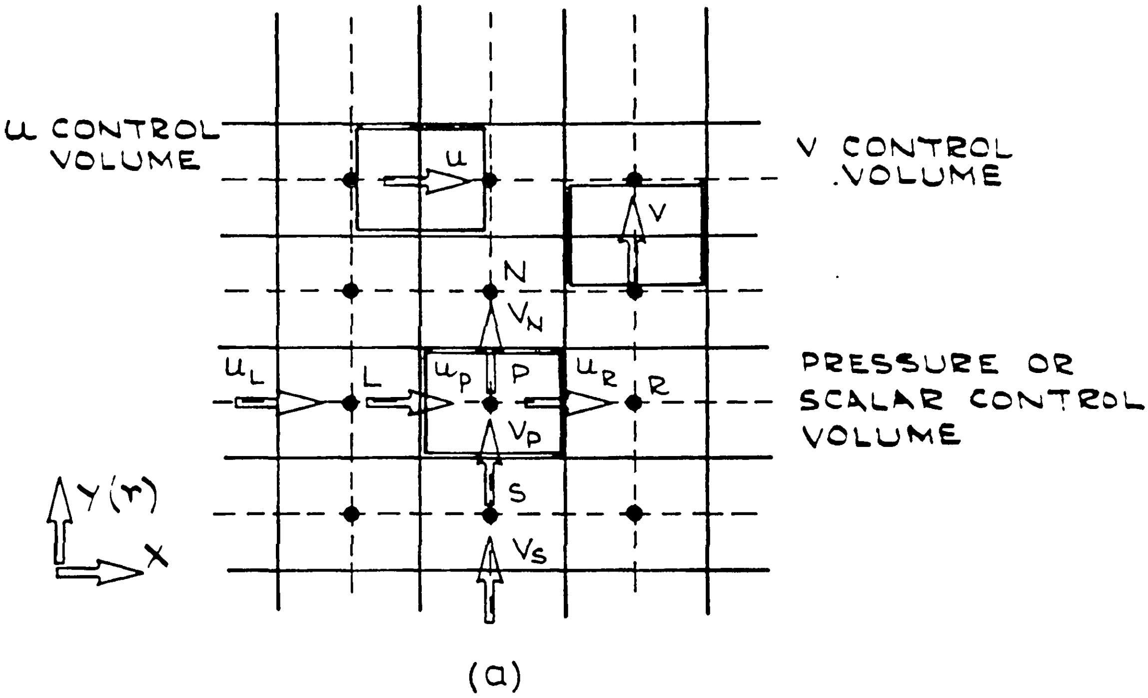

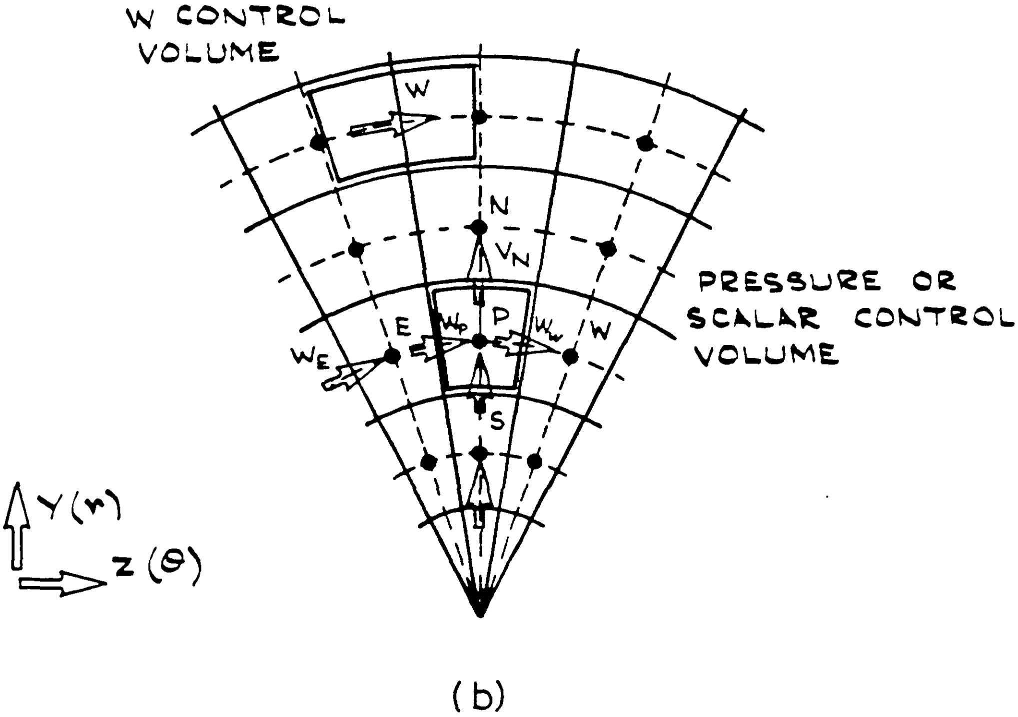

Figure 3.1 Velocity and scalar control volumes for a three-dimensional calculation domain

(a) U, V and scalar control volumes in x-y plane

(b) W and scalar control volumes in y-z plane

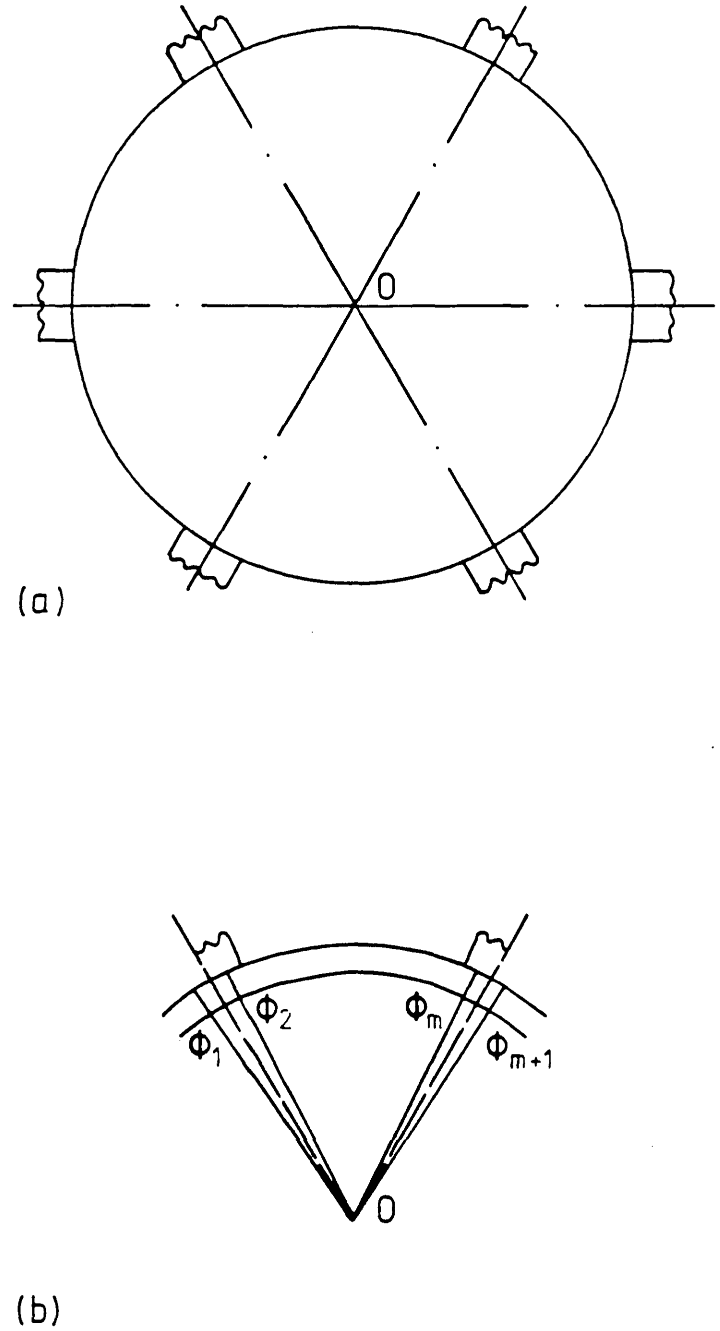

Figure 3.2 Cyclic boundary conditions

(a) Physical domain with periodic repetition

(b) Calculation domain with cyclic boundary conditions applied at periodic axes

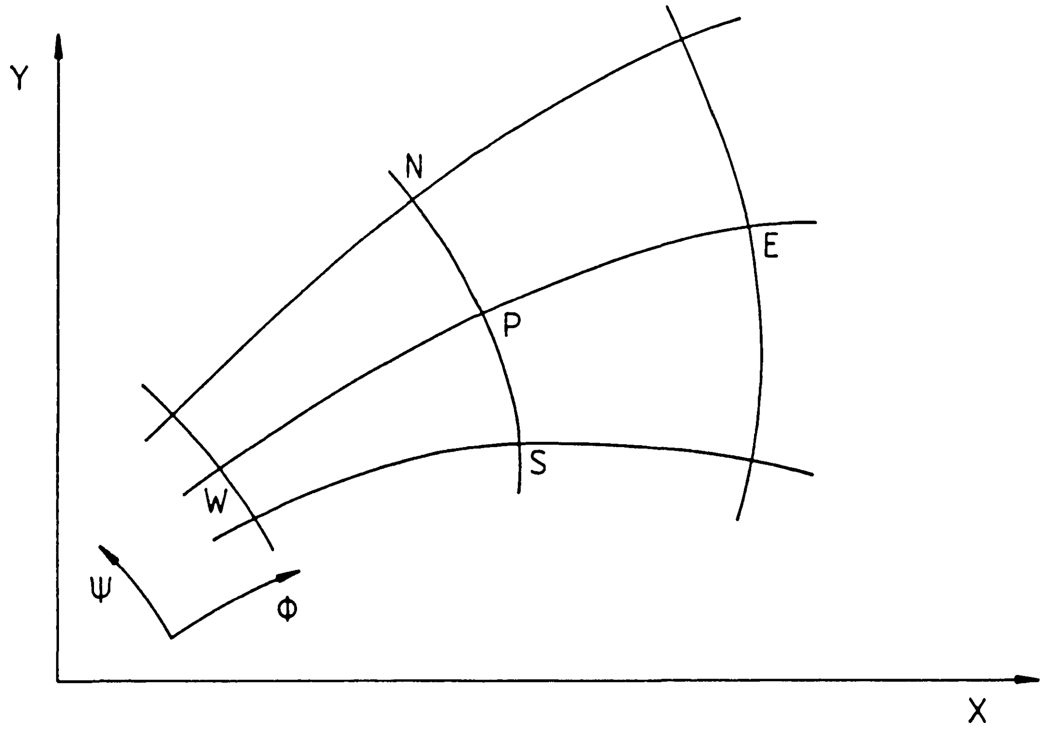

Figure 3.3 Numerical mesh for stream function – velocity potential solution

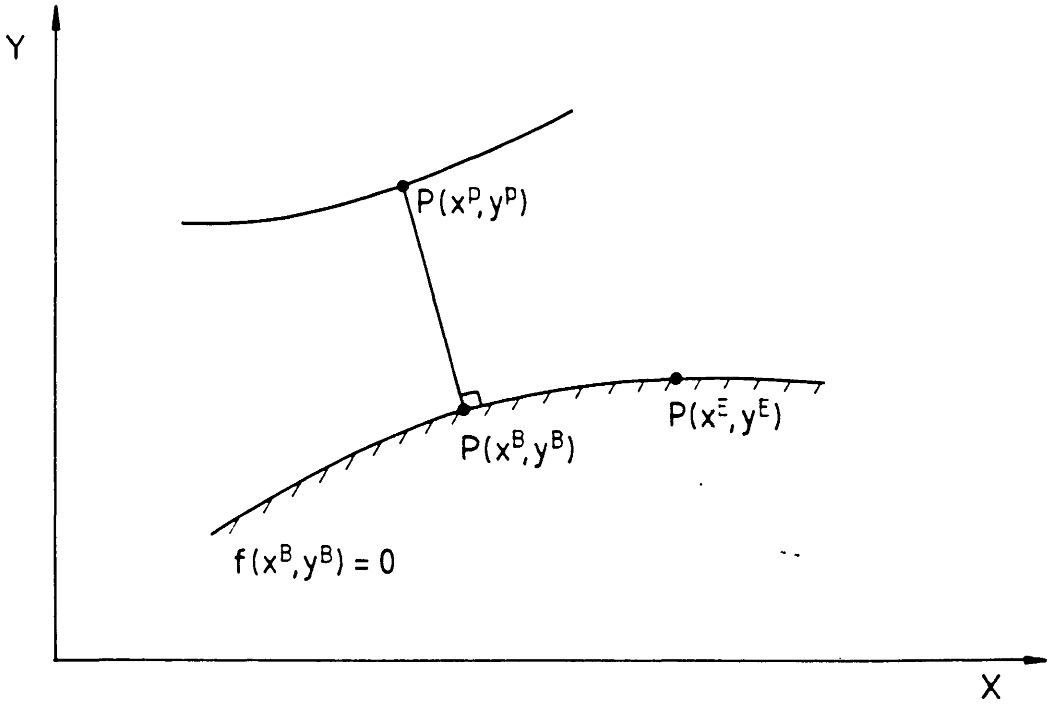

Figure 3.4 Boundary calculations: layout and notation

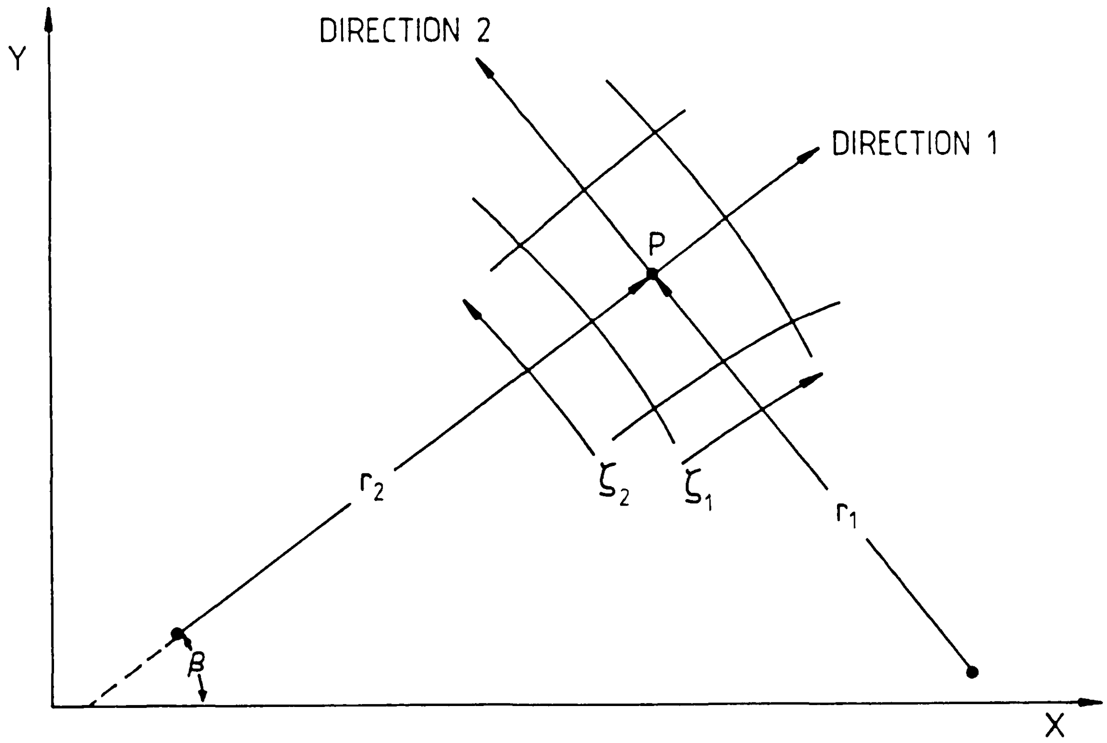

Figure 3.5 Two-dimensional plane of orthogonal curvilinear co-ordinates

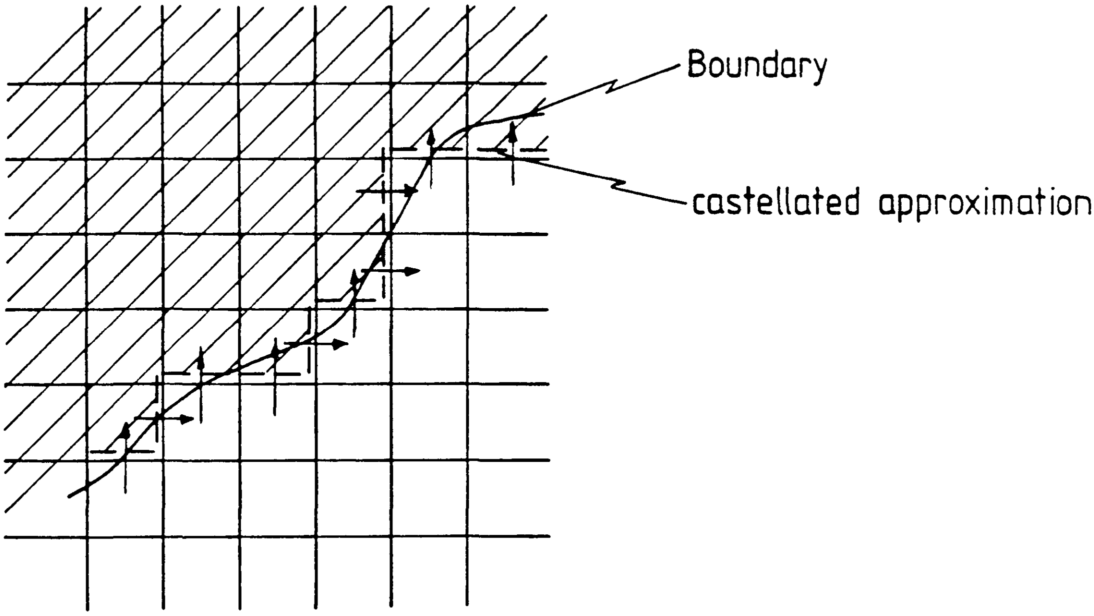

Figure 3.6 Castellated approximation

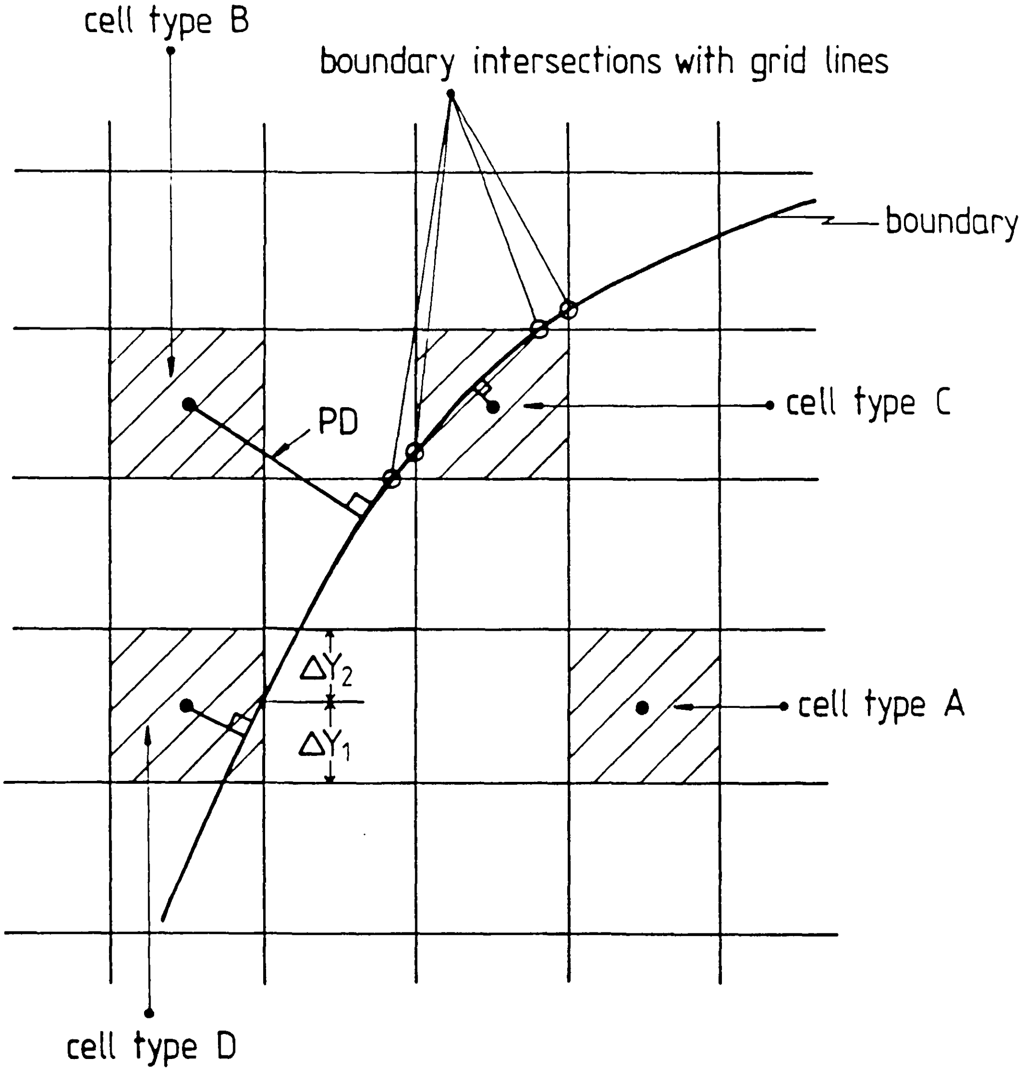

PD: perpendicular distance from cell node to boundary

normalised boundary cell face area of that part of the cell lying inside the boundary:

$$\frac{\Delta Y1 . \Delta Z}{(\Delta Y1+\Delta Y2) . \Delta Z}$$

(in two-dimensions)

Figure 3.7 Boundary cell classification and geometrical quantities

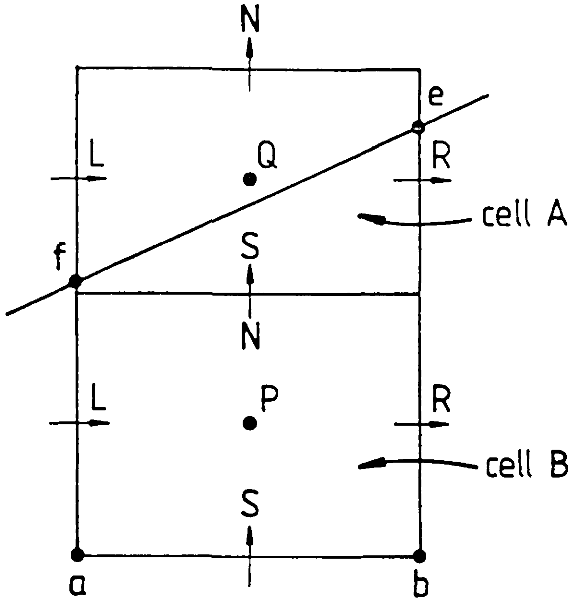

Figure 3.8 Adding on of an external cell

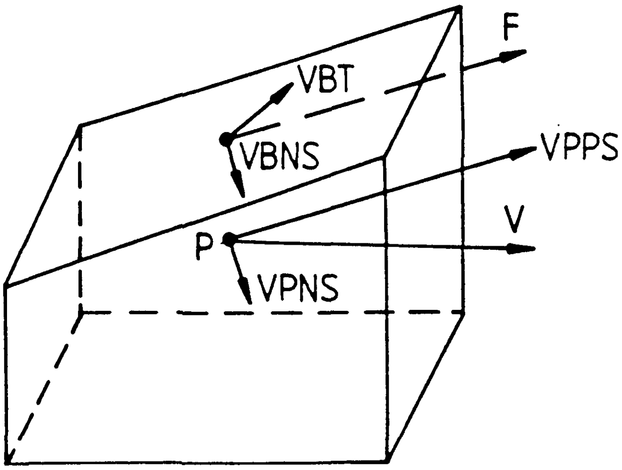

Figure 3.9 Velocity vectors in a boundary cell

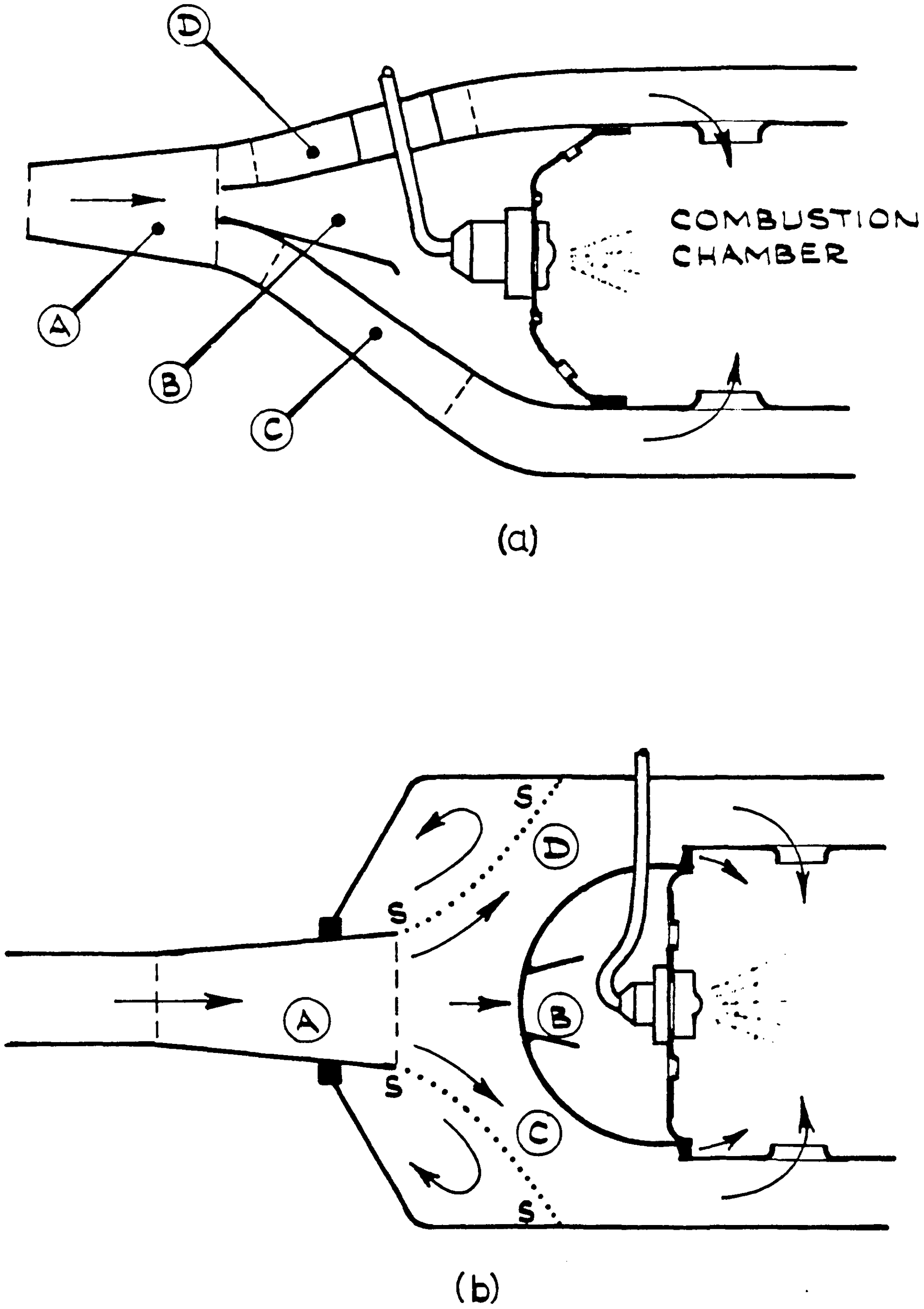

Figure 4.1 Gas turbine combustion chamber diffuser systems

(a) "faired" diffuser

(b) "dump" diffuser

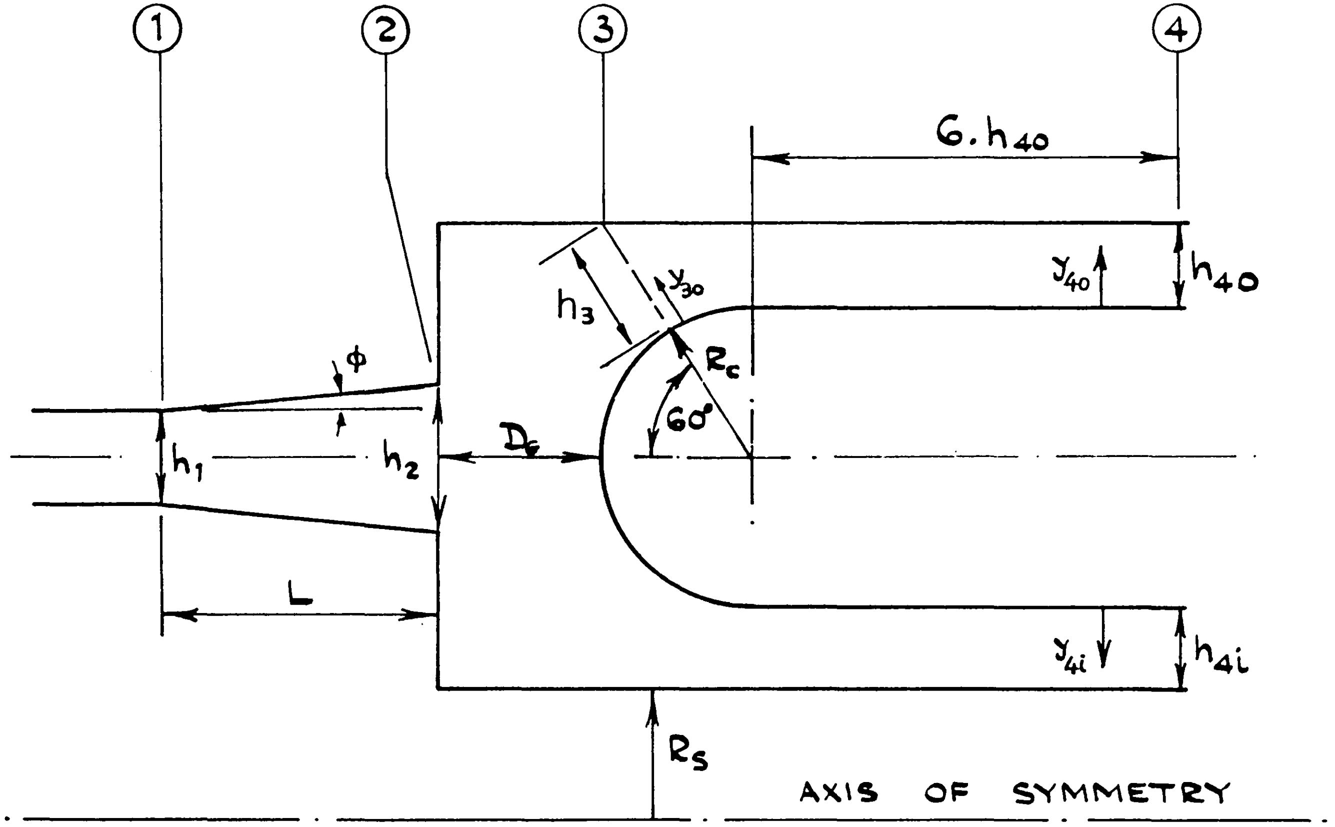

$h_{4o} = h_{4i} = 38.1\,\mathrm{mm}$

$R_S = 130.2\,\mathrm{mm}$

$R = 66.67\,\mathrm{mm}$

Figure 4.2 Flow configuration investigated

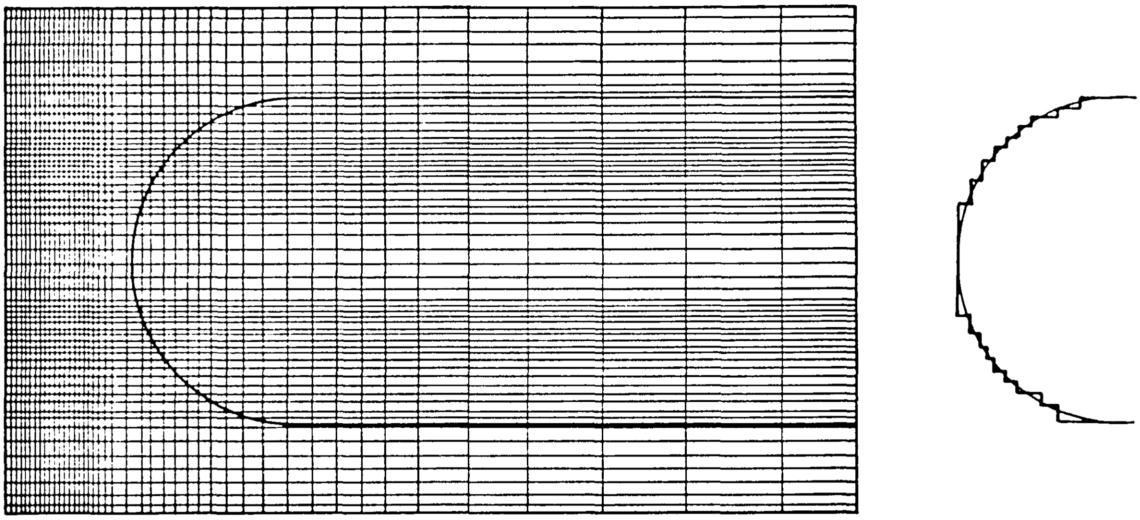

Figure 4.3 Cylindrical polar mesh of 45 x 58 (x, r) grid nodes and castellated approximation of the combustor head

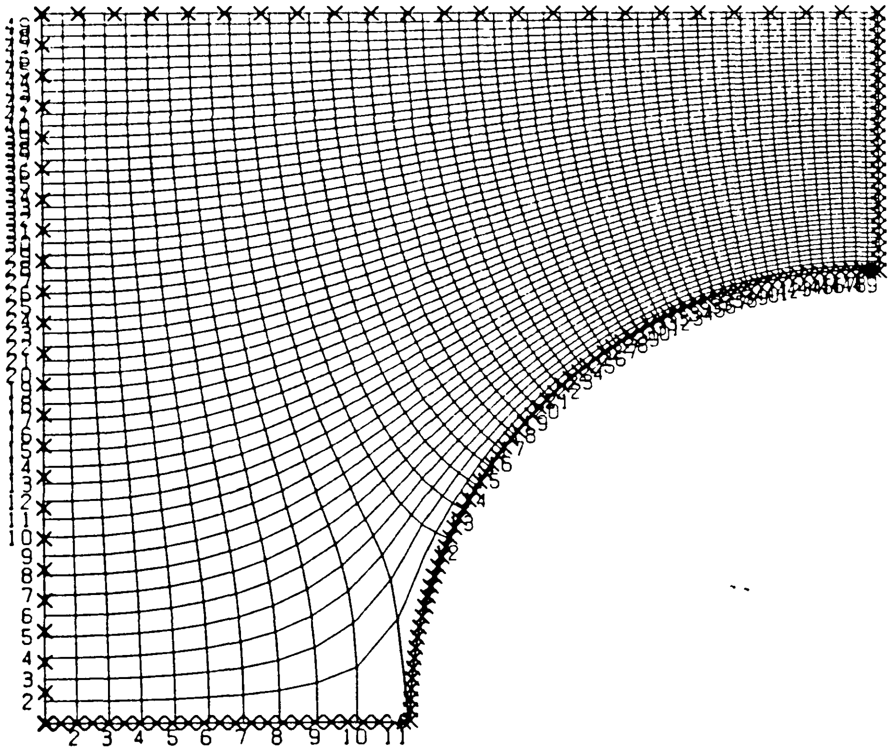

Figure 4.4 Mesh generation

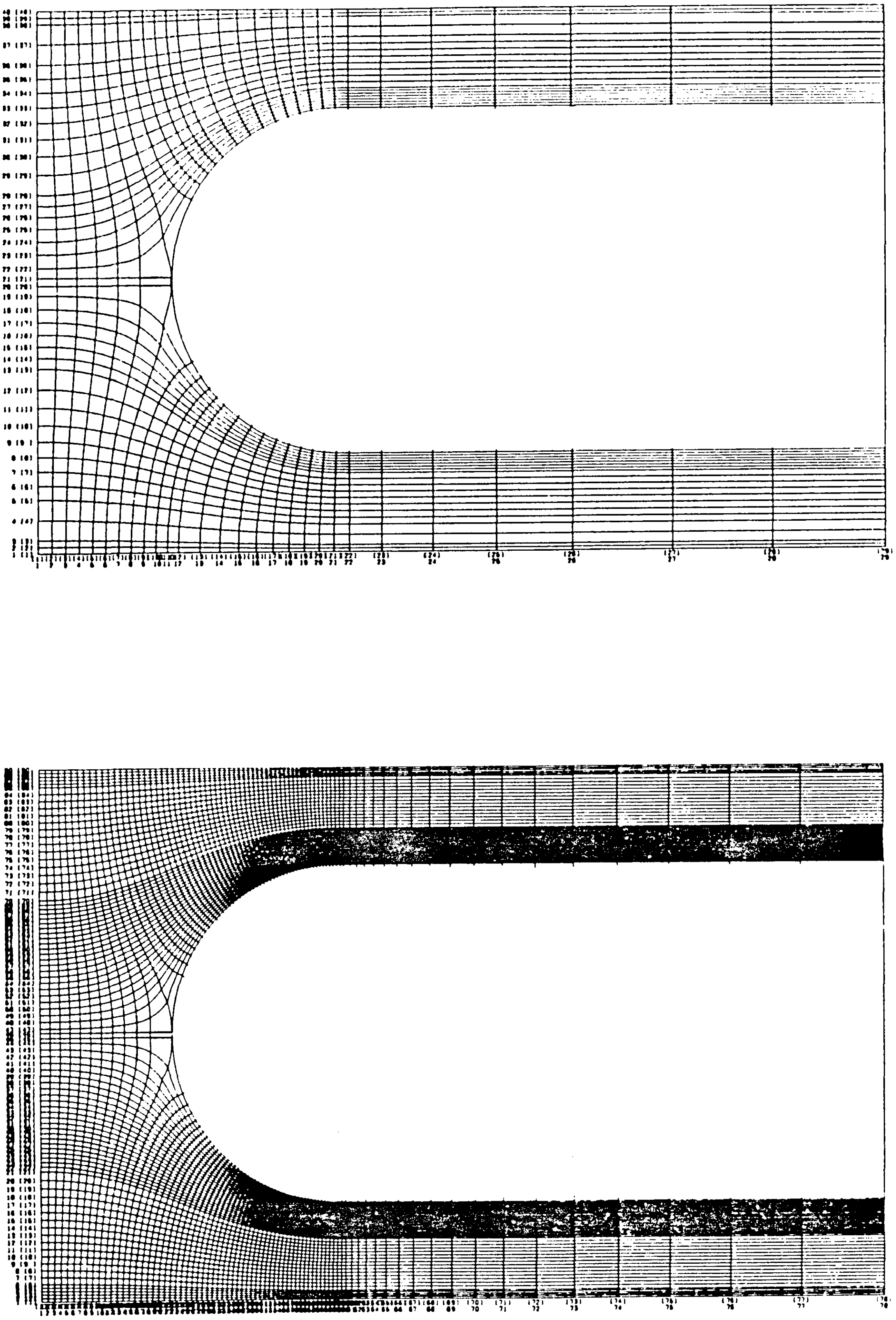

Figure 4.5 Boundary fitted meshes of 31 x 42 and 80 x 92 (ζ_1, ζ_2) grid nodes

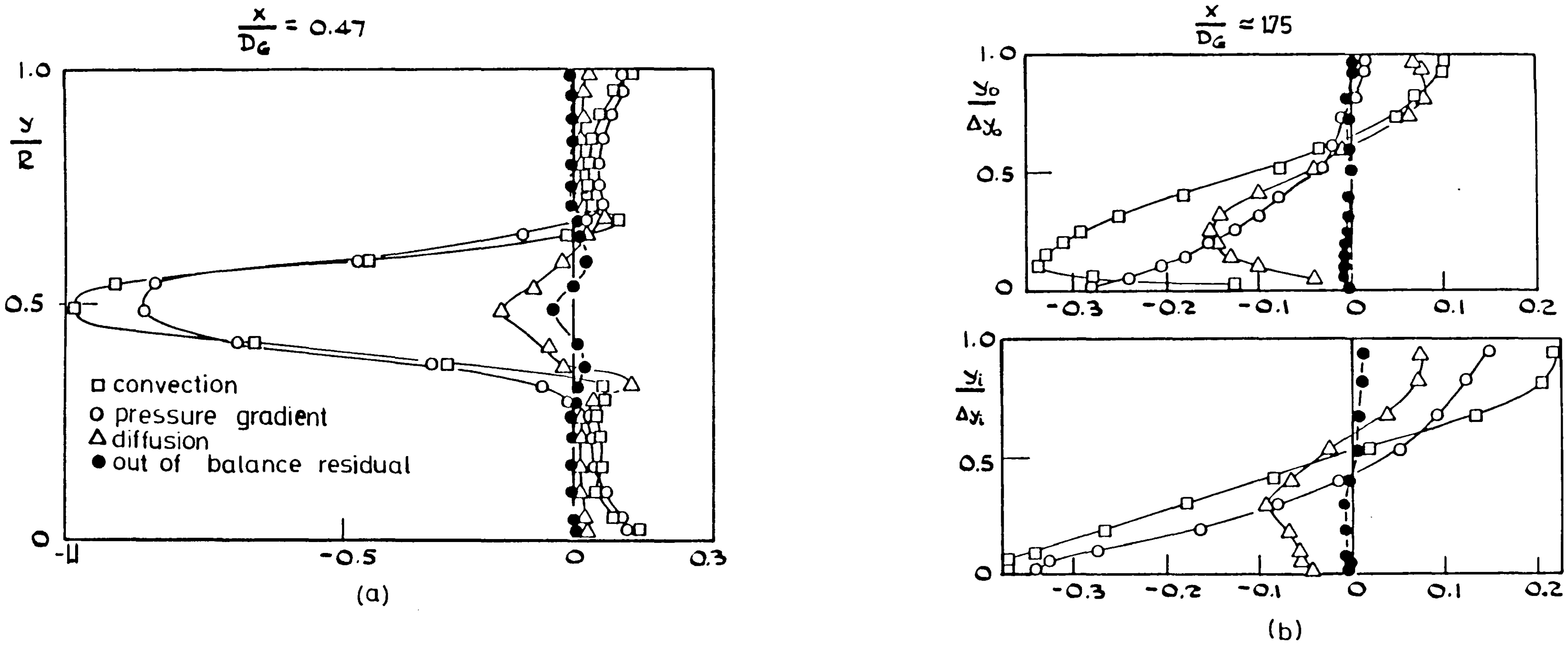

(a)

(b)

y: radial distance of each grid node measured from the bottom casing of the diffuser

R: $2R_c + y_{4o} + y_{4i}$

$y_{o,i}$ radial distance of each grid node measured from the position of intersection of the grid line with the combustor wall

$\Delta y_{o,i}$ radial distance from the combustor wall to the casing

Figure 4.6 Truncation error analysis. Abscissa non-dimensionalised with $\rho U_2^2/D_G$

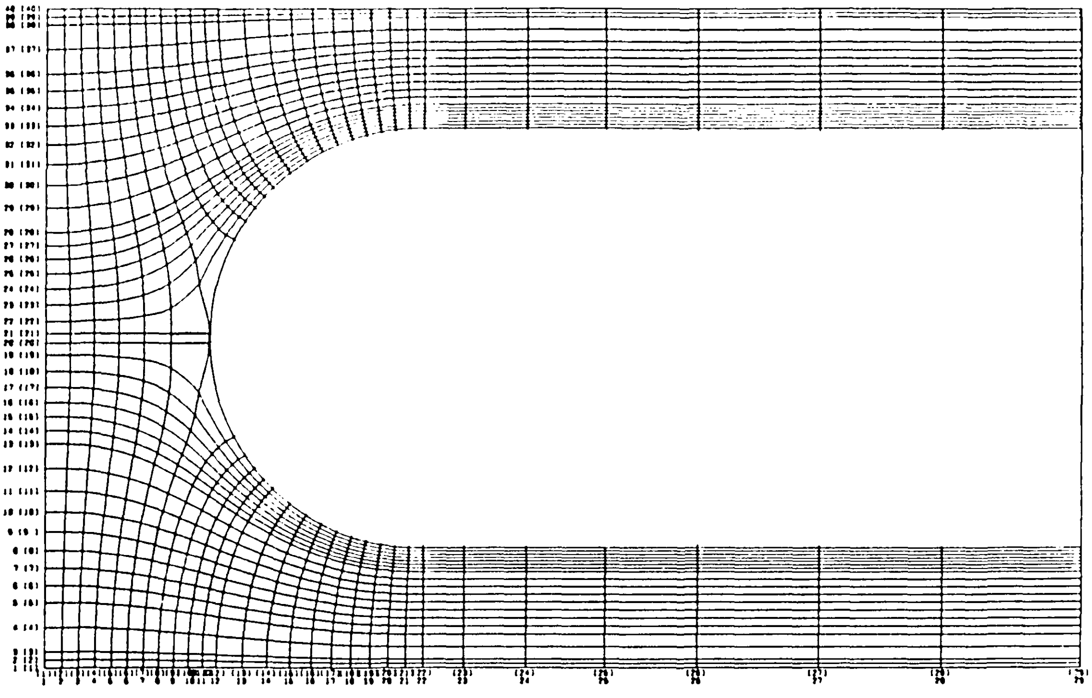

(a) mesh 1

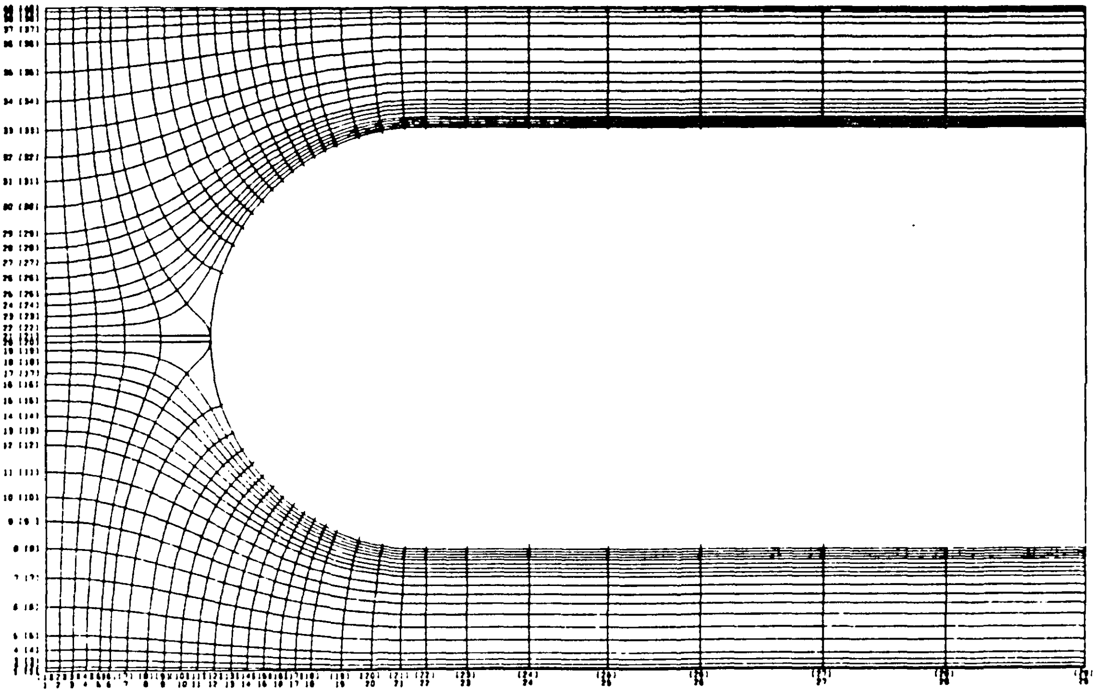

(b) mesh 2

Figure 4.7 Orthogonality error estimates

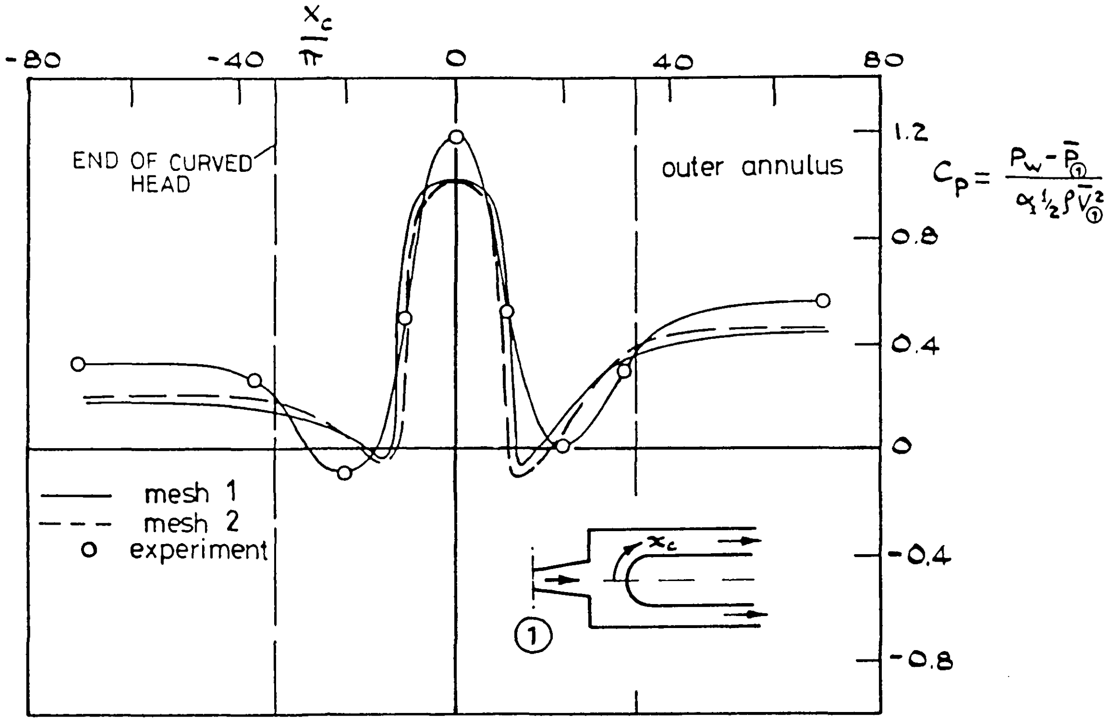

(c) static pressure distribution on combustor wall

Figure 4.7 (continued)

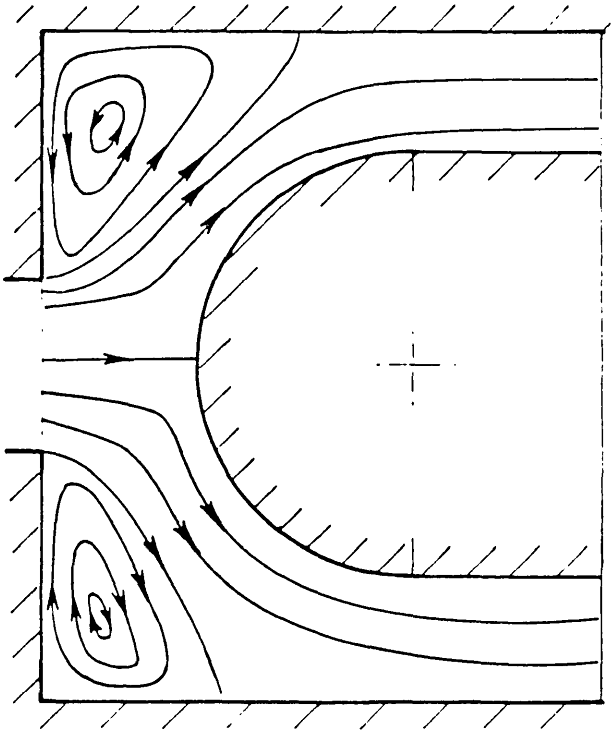

(a) stream function contours

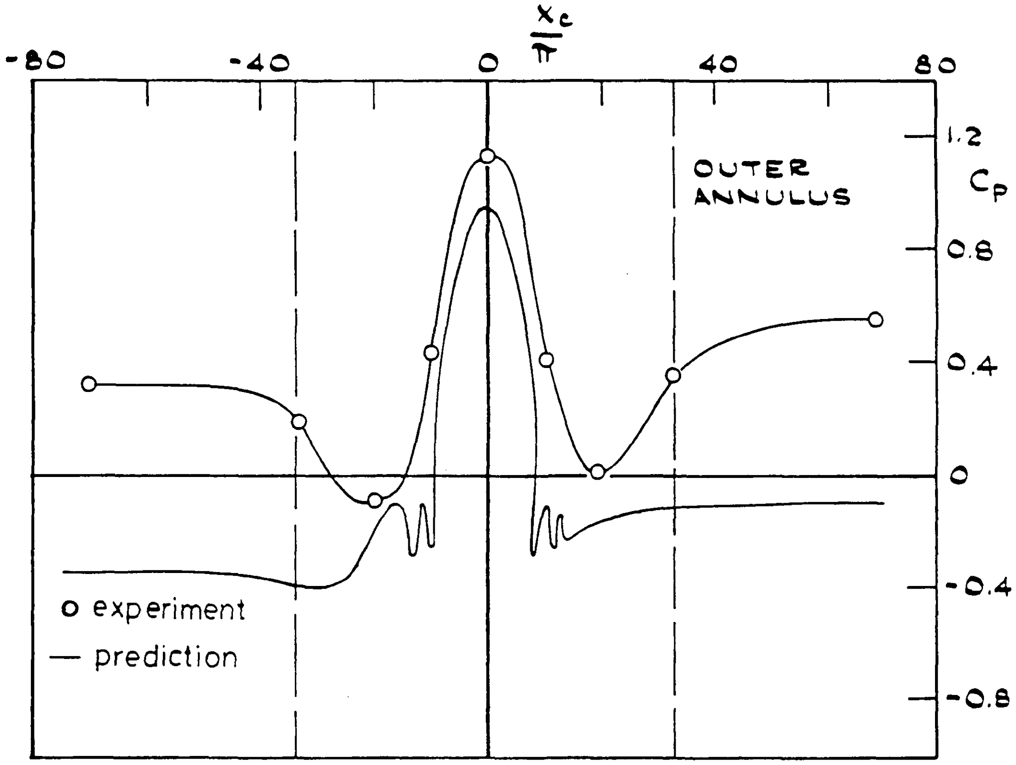

(b) combustion chamber static pressure distribution

Figure 4.8 Cylindrical polar grid results

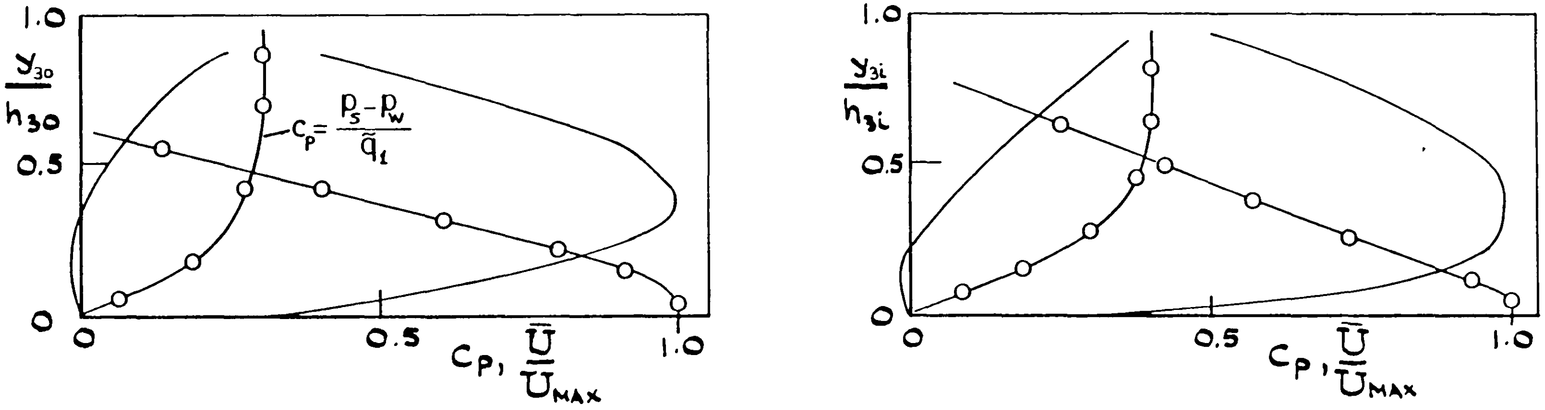

(c) velocity and static pressure profiles at station 3

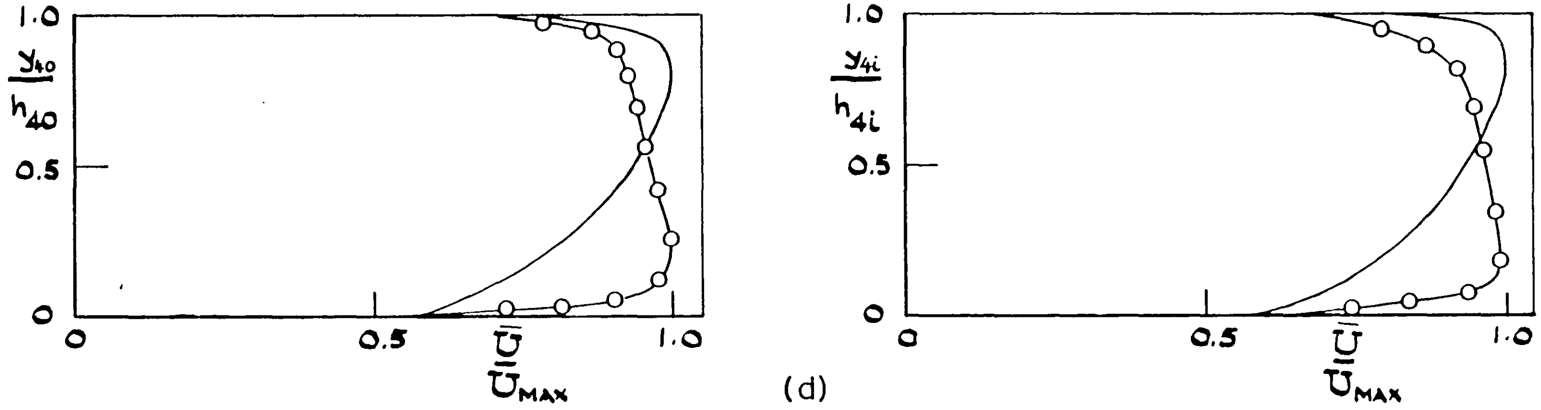

(d) velocity profiles at exit from the settling length

Figure 4.8 (continued)

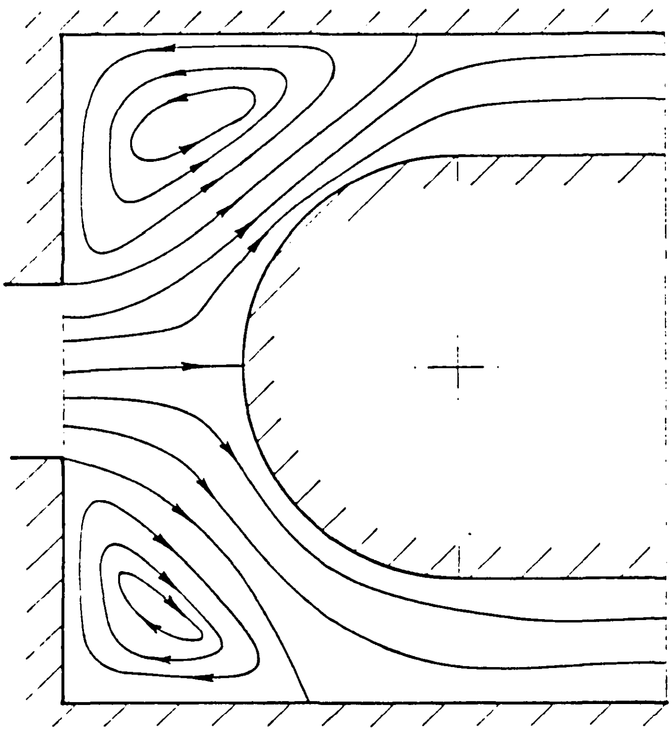

(a) stream function contours

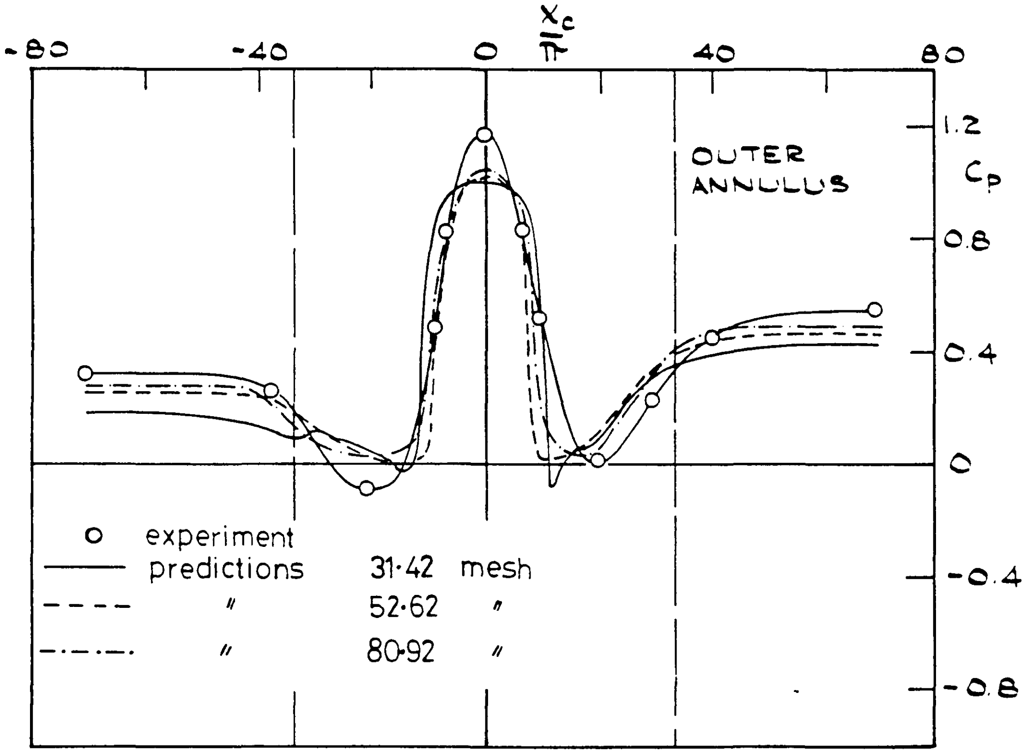

(b) combustion chamber static pressure distribution

Figure 4.9 Results of calculations with boundary fitted meshes

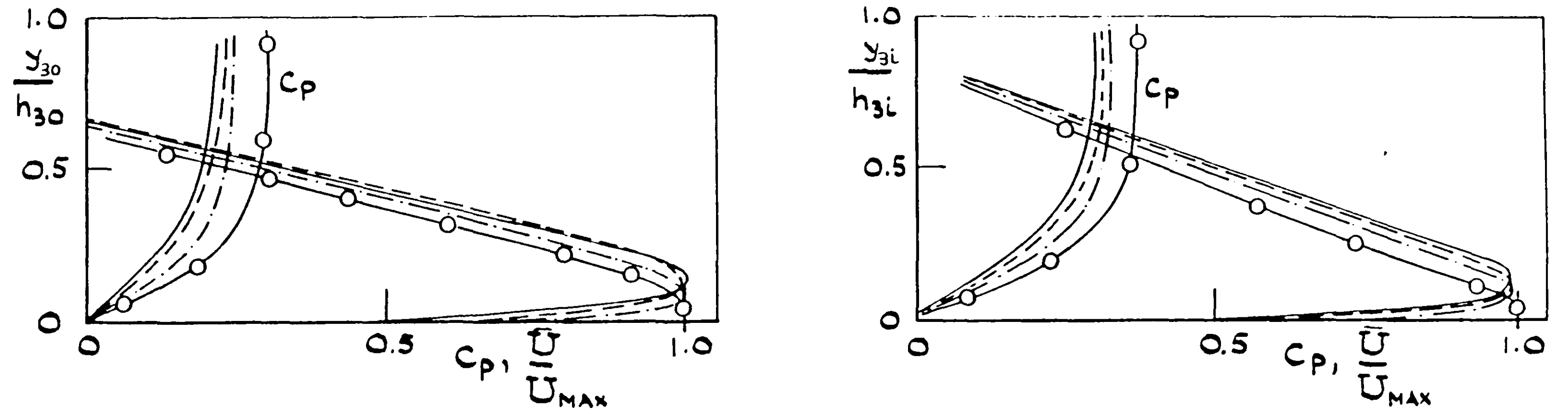

(c) velocity and static pressure profiles at station 3

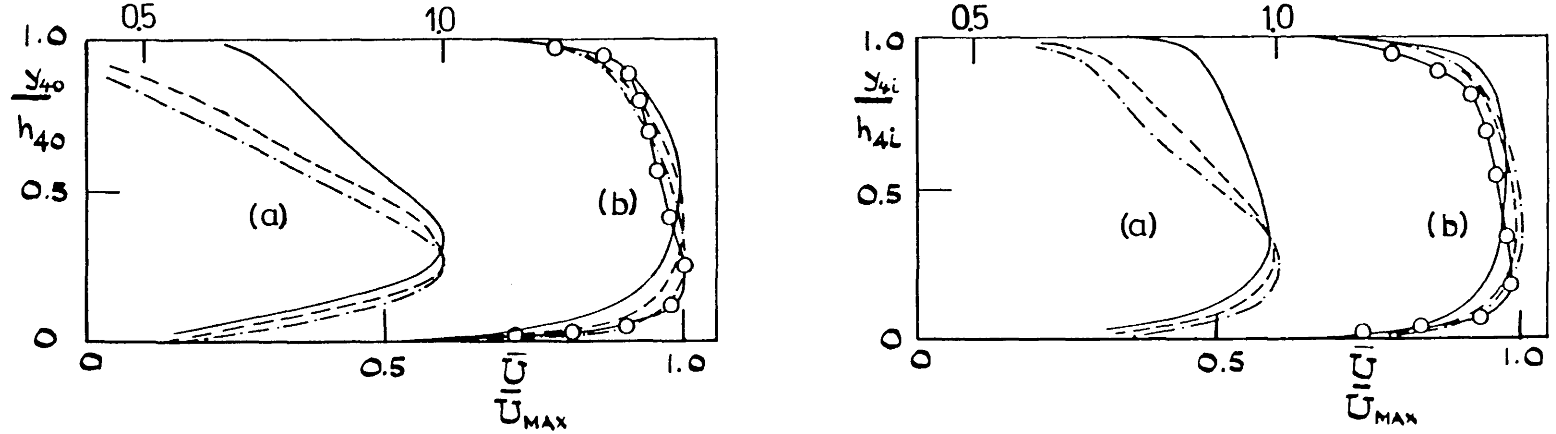

(d) velocity profiles at entry to annuli (a) and exit from the settling length (b)

Figure 4. 9 (continued)

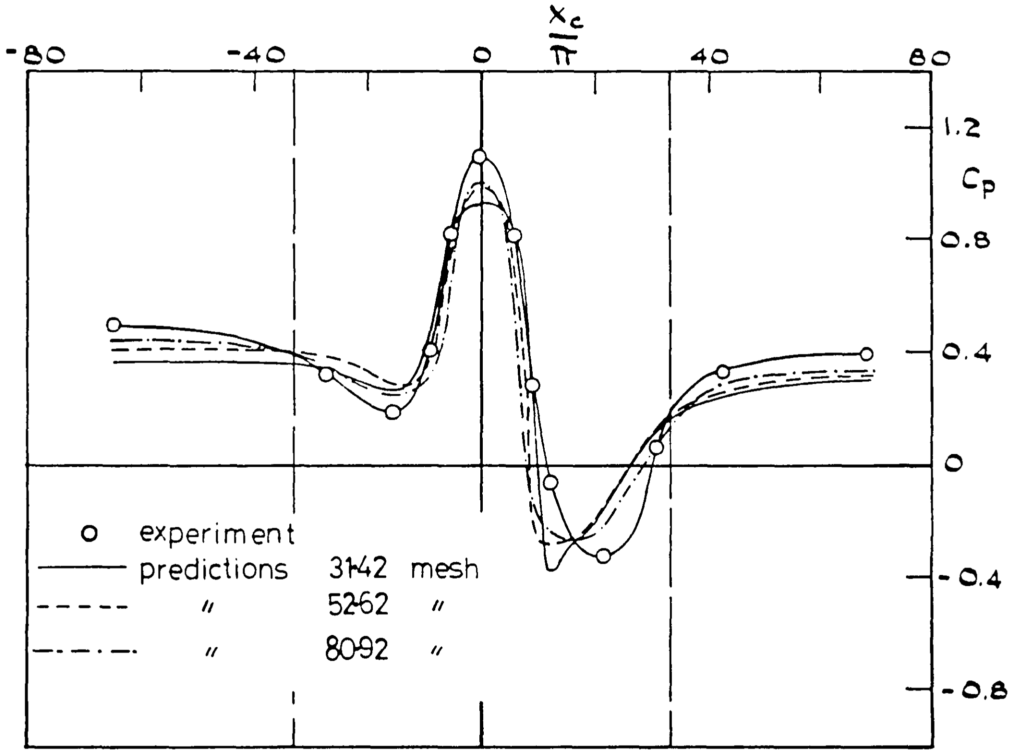

(a)

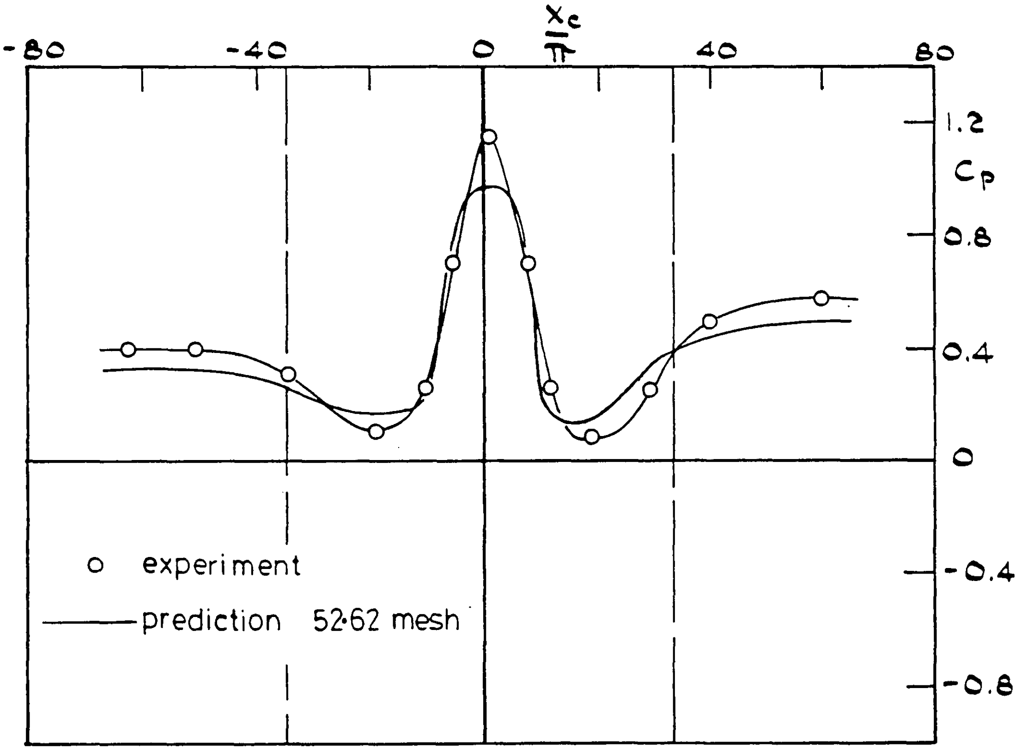

(b)

Figure 4.10 **Predicted and measured combustion chamber static pressure distribution (boundary fitted meshes)**

(a) $D_G/h_2 = 1.0$, $s = 2.57$

(b) $D_G/h_2 = 1.0$, $s = 2.30$

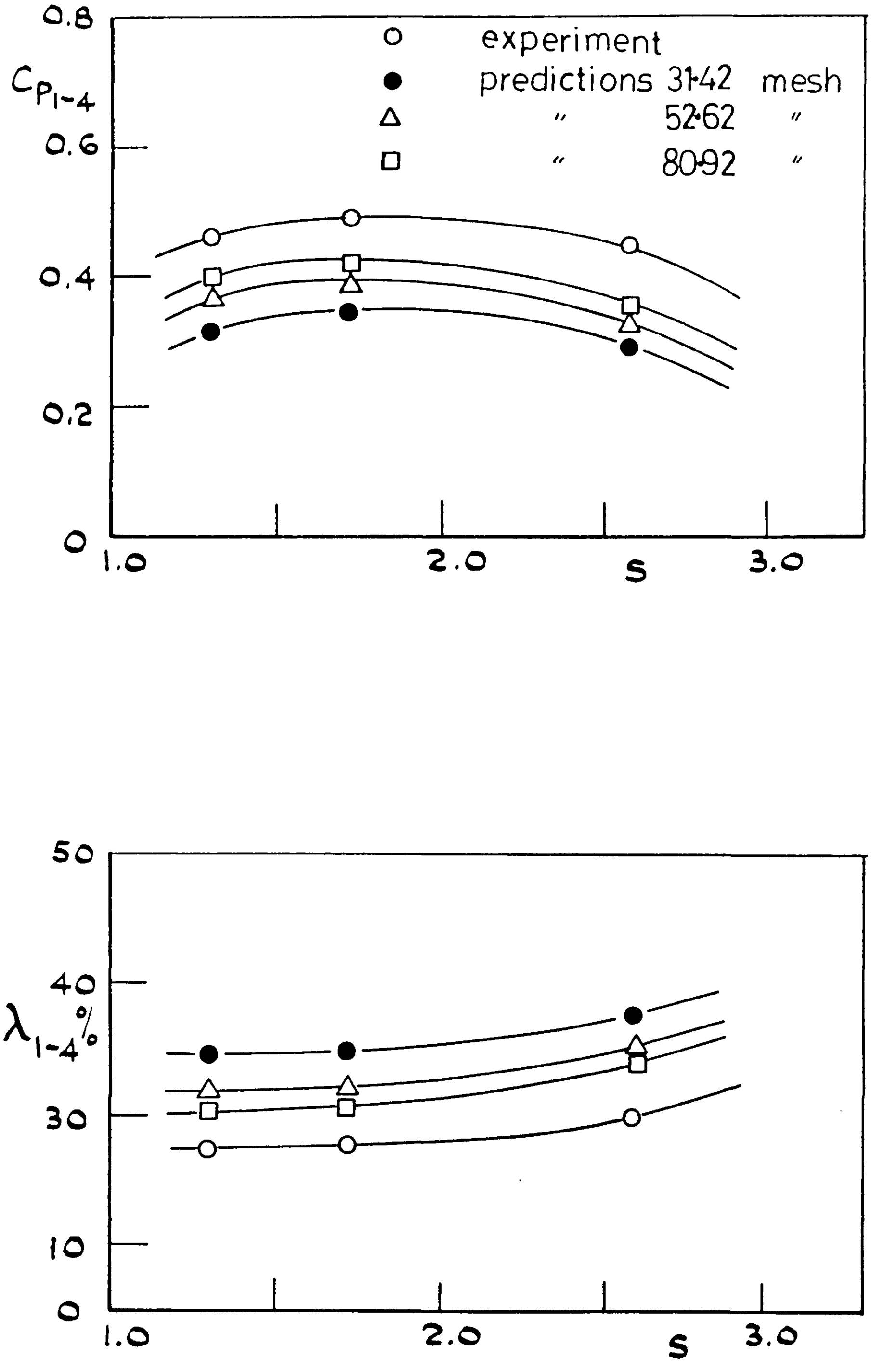

(a)

Figure 4.11 Predicted and measured variation in performance with flow split (D_G/h_2=1.0)

(a) overall static pressure recovery and loss coefficient

(b) velocity profile energy coefficients at station 4

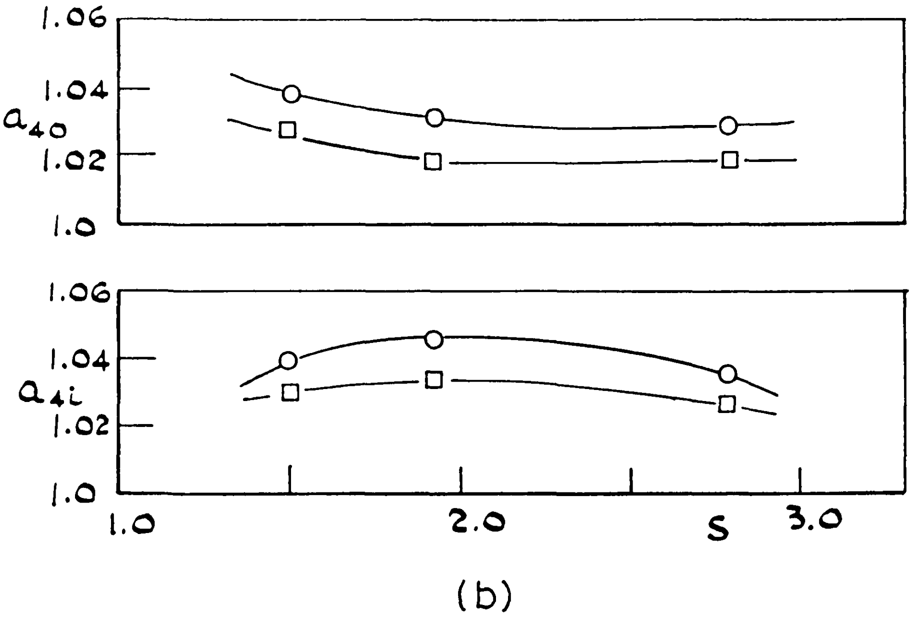

Figure 4.11 (continued)

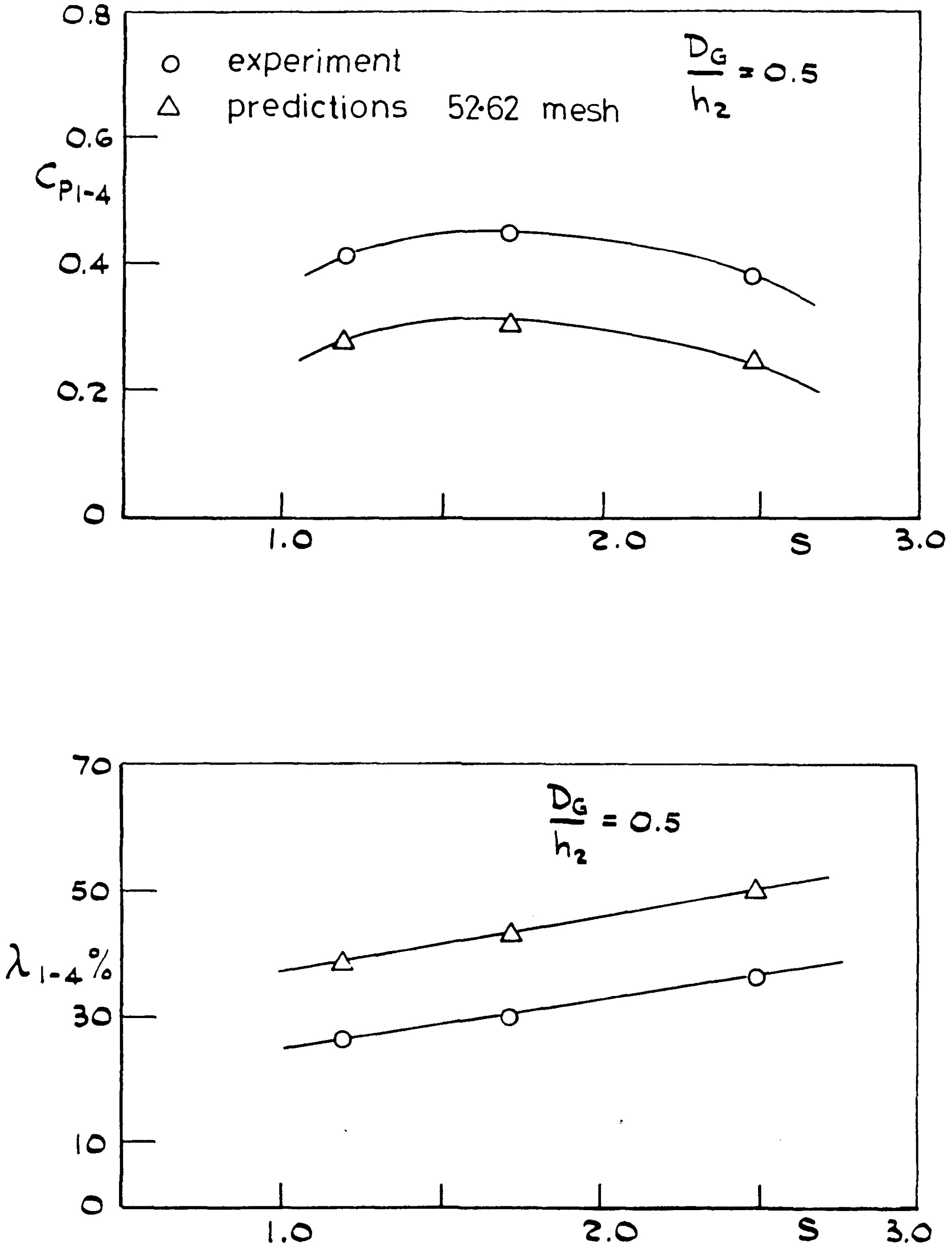

(a)

Figure 4. 12 Predicted and measured variation in performance with (a, b) flow split (c) dump gap

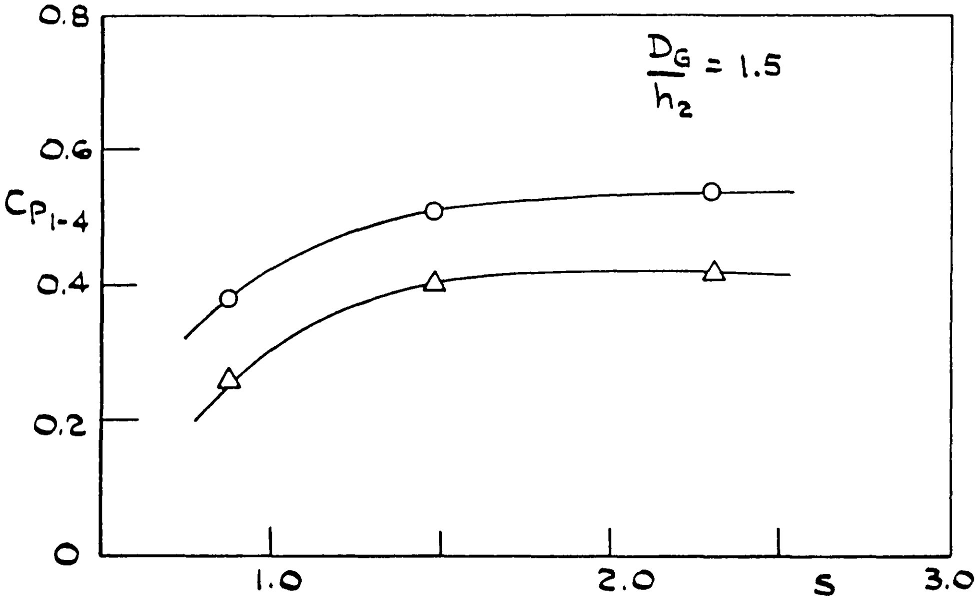

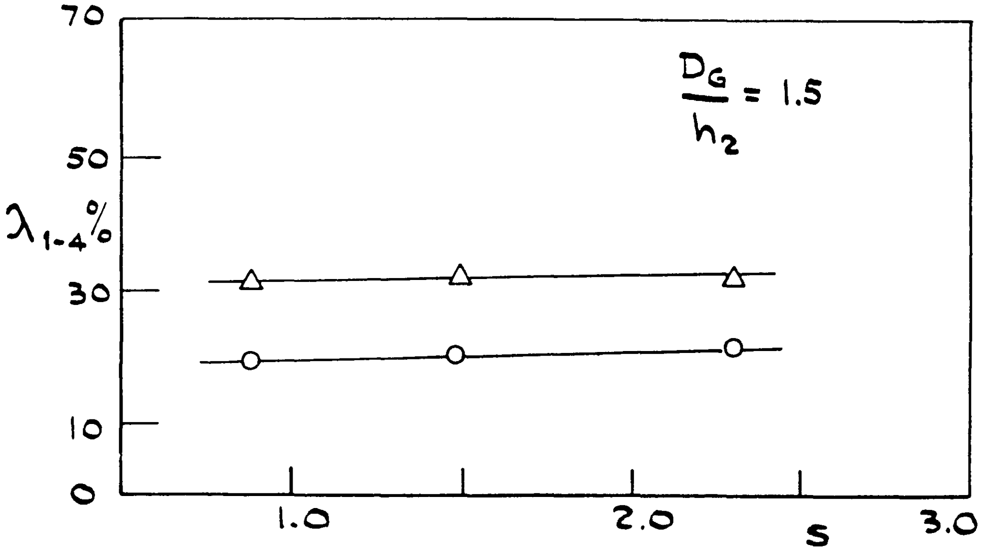

(b)

Figure 4.12 (continued)

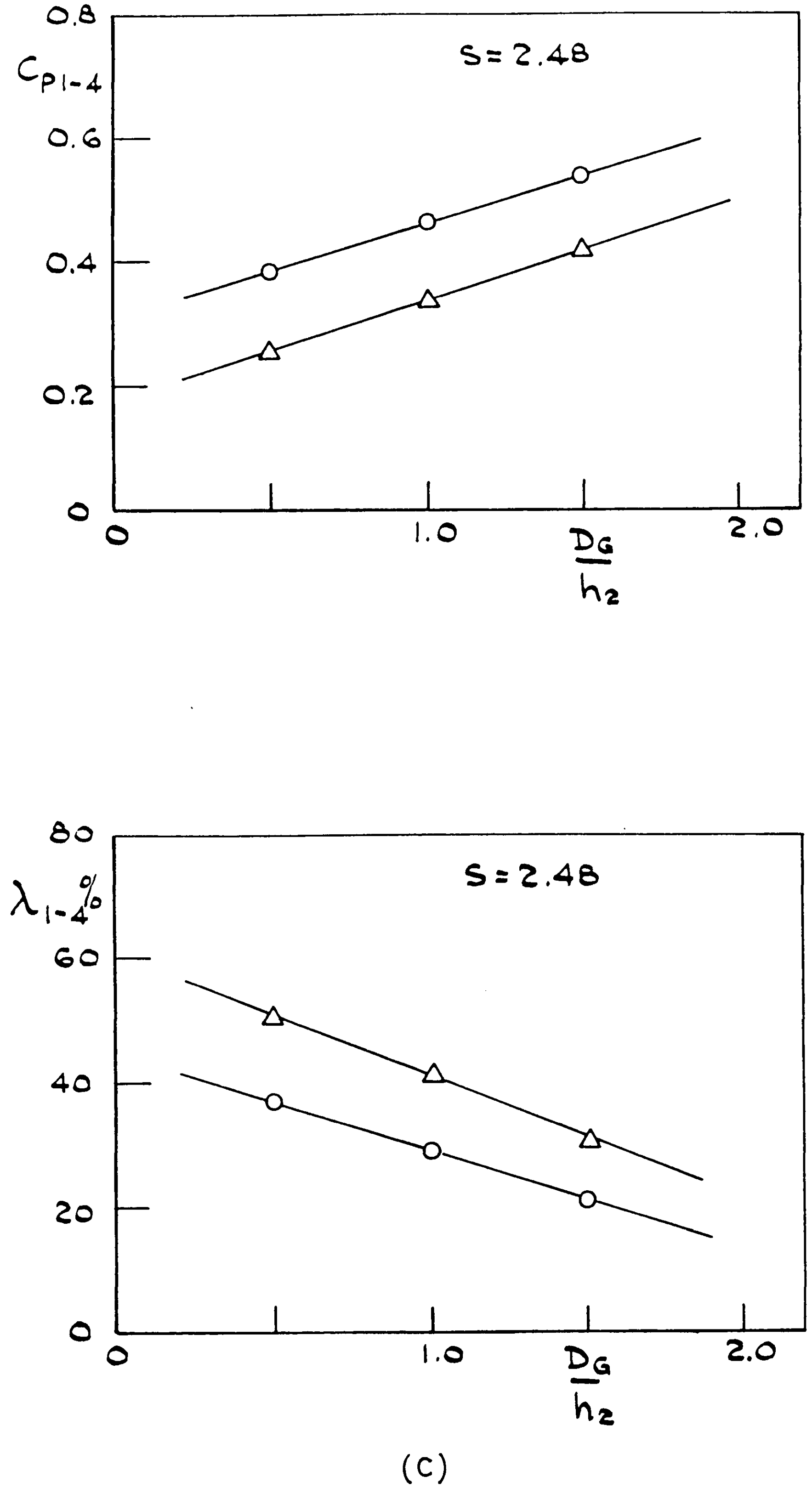

(C)

Figure 4. 12 (continued)

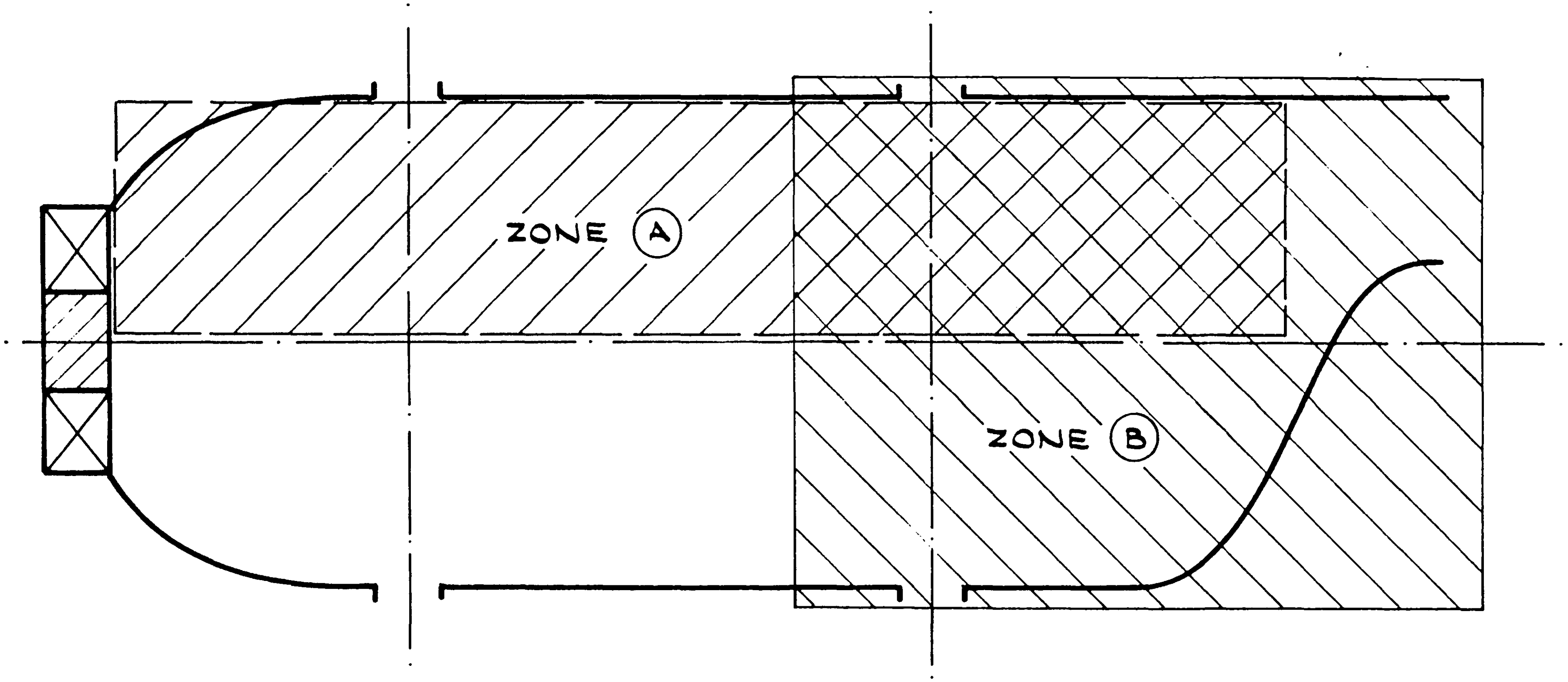

Figure 5.1 Arrangement of calculation for water model combustor

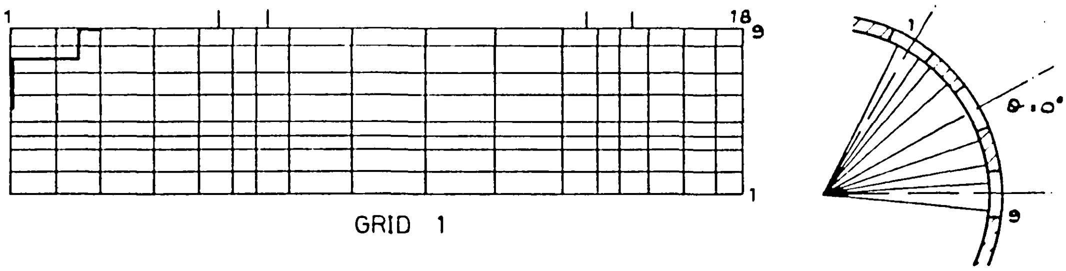

GRID 1

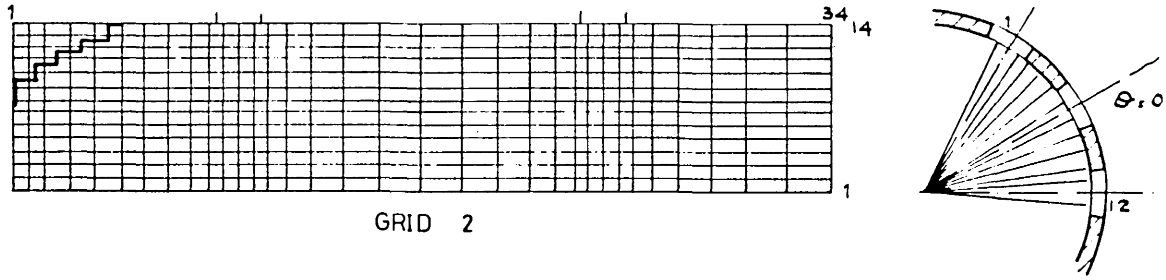

GRID 2

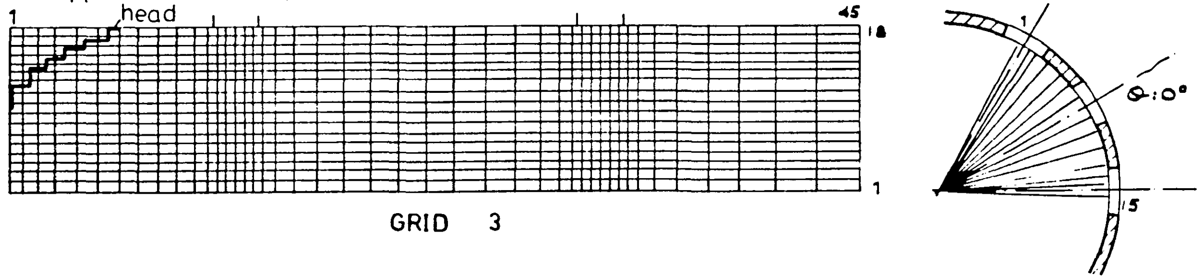

GRID 3

Figure 5.2 Finite-difference meshes used in the calculations of zone A

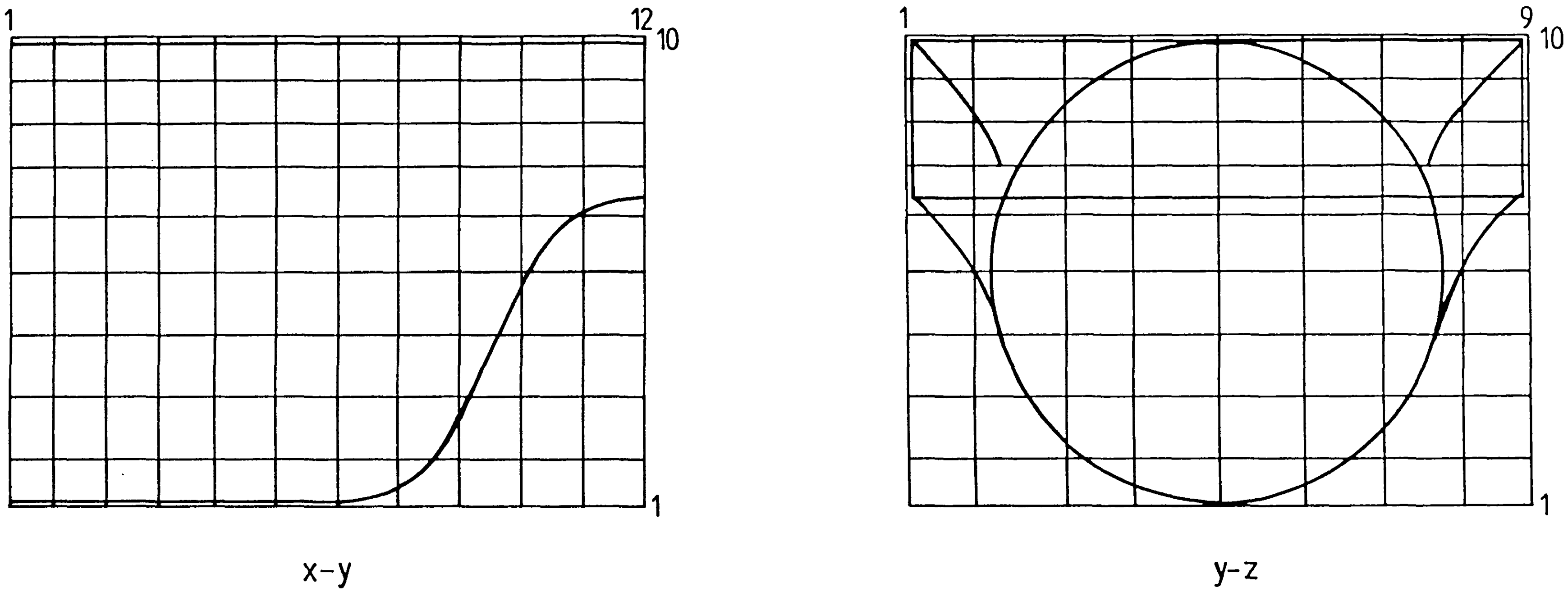

Figure 5.3 Finite-difference mesh used for the calculations of zone B

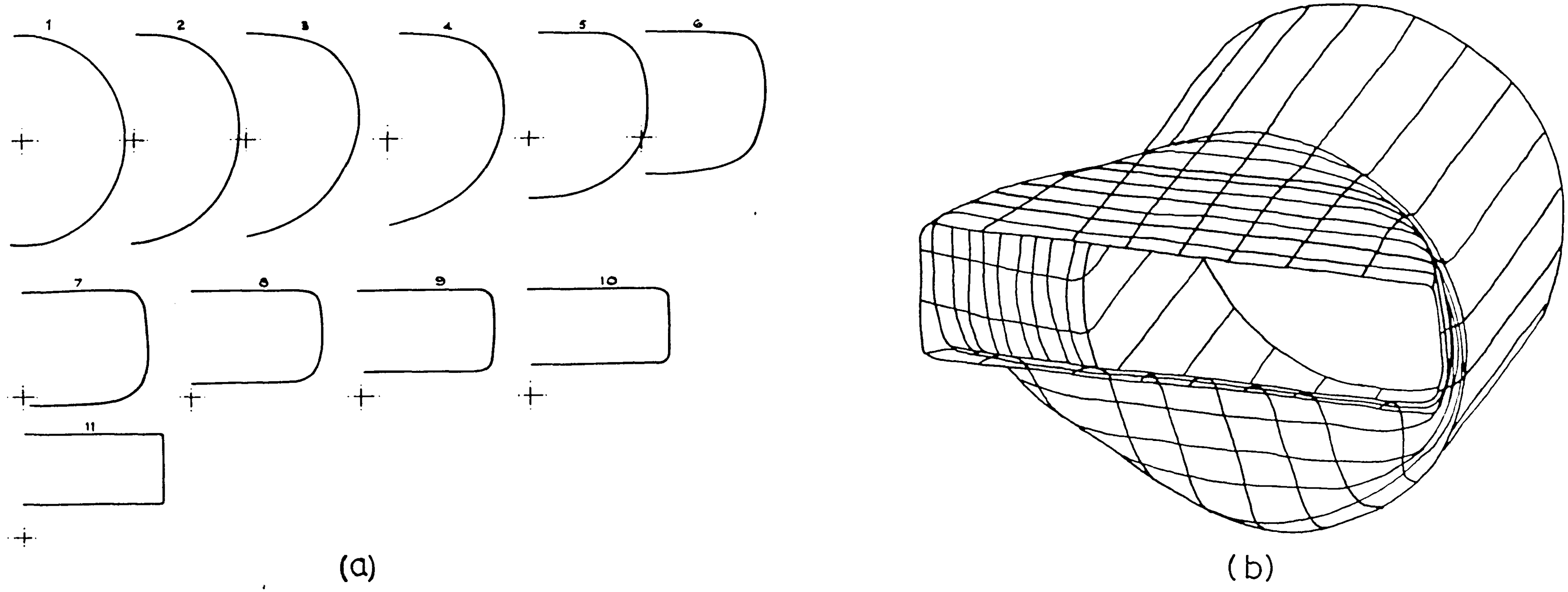

Figure 5.4 (a) Description of the nozzle cross-section at successive axial locations

(b) Surface of the nozzle and adjoining can section comprising the calculation domain for zone B

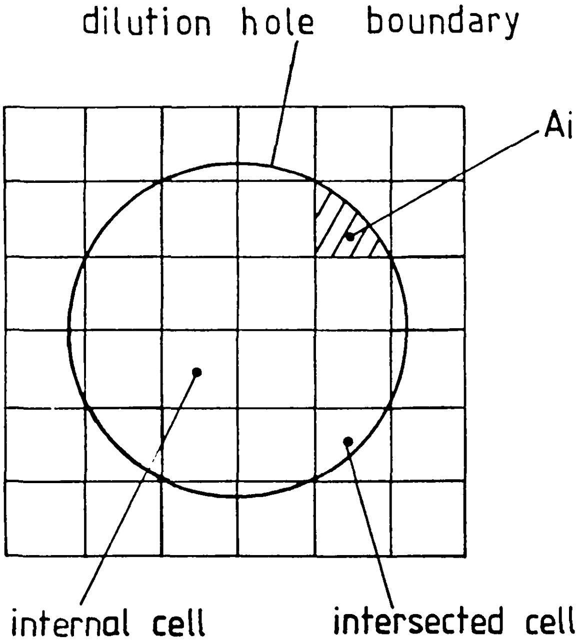

Figure 5.5 Correction of fluxes through the dilution holes

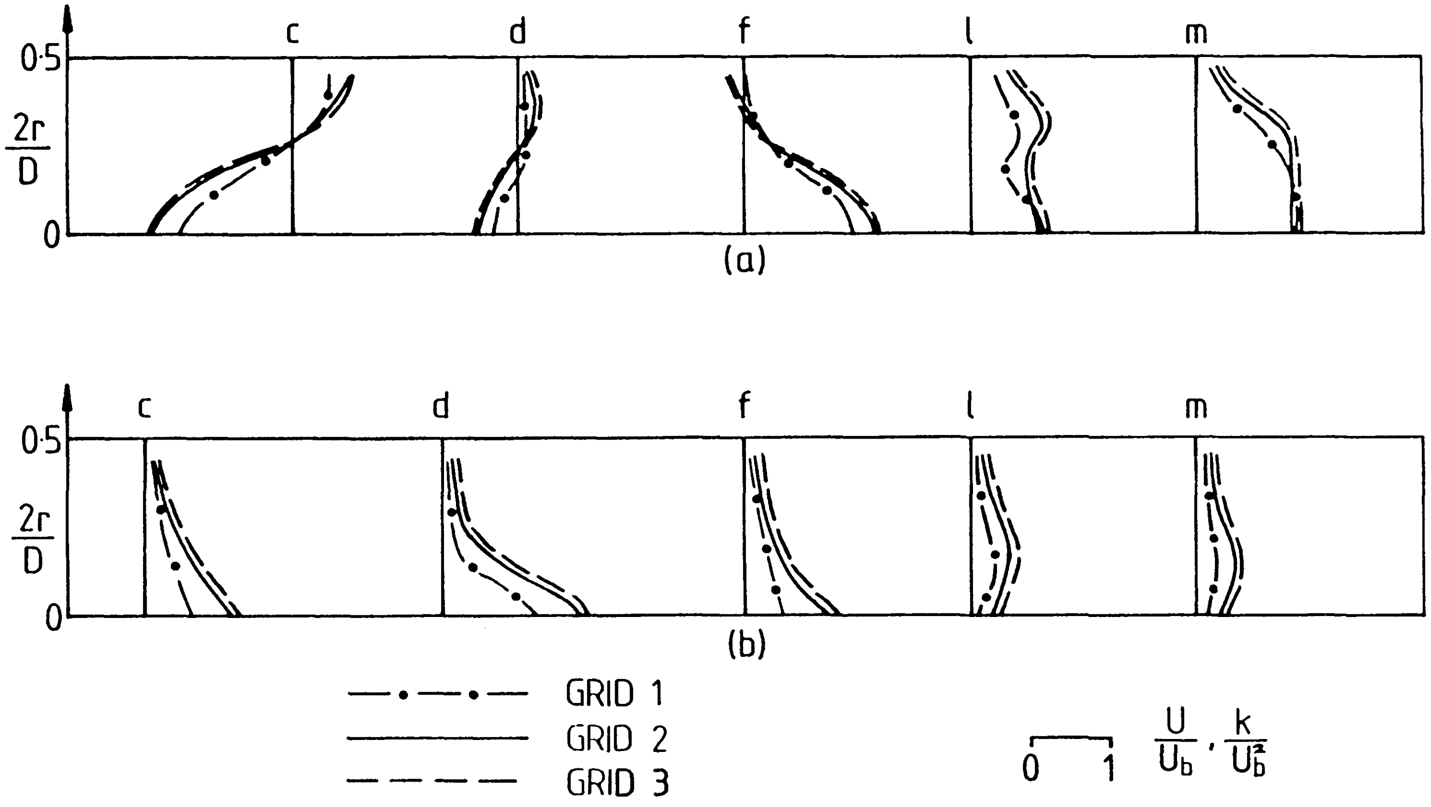

Figure 5.6 Grid refinement process for cylindrical polar meshes used for zone A (a) axial velocity. (b) turbulence kinetic energy

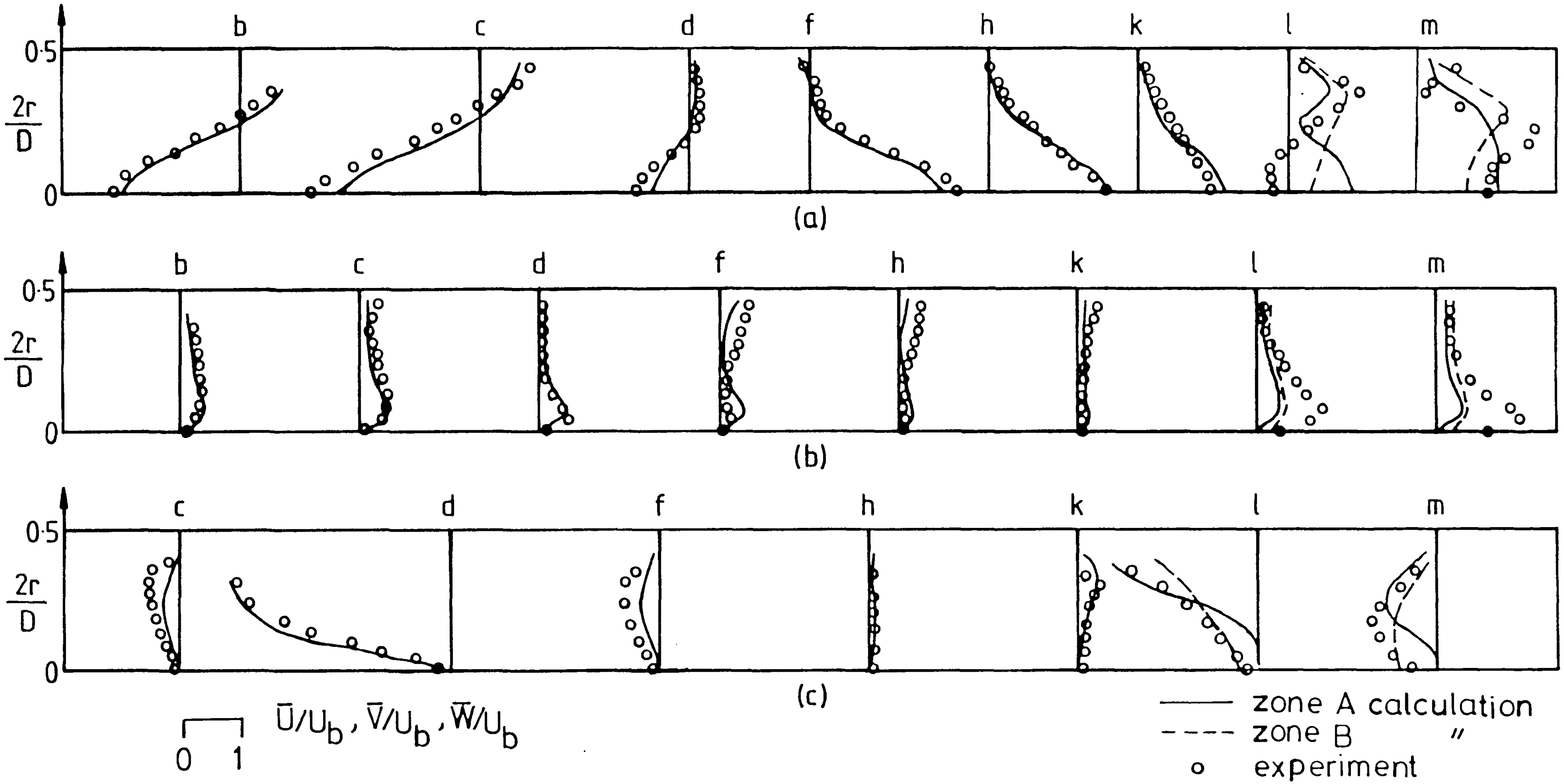

Figure 5.7 Comparison of calculated and measured velocity fields for case 1 ($\theta=0^{\circ}$) (a) axial, (b) azimuthal, (c) radial

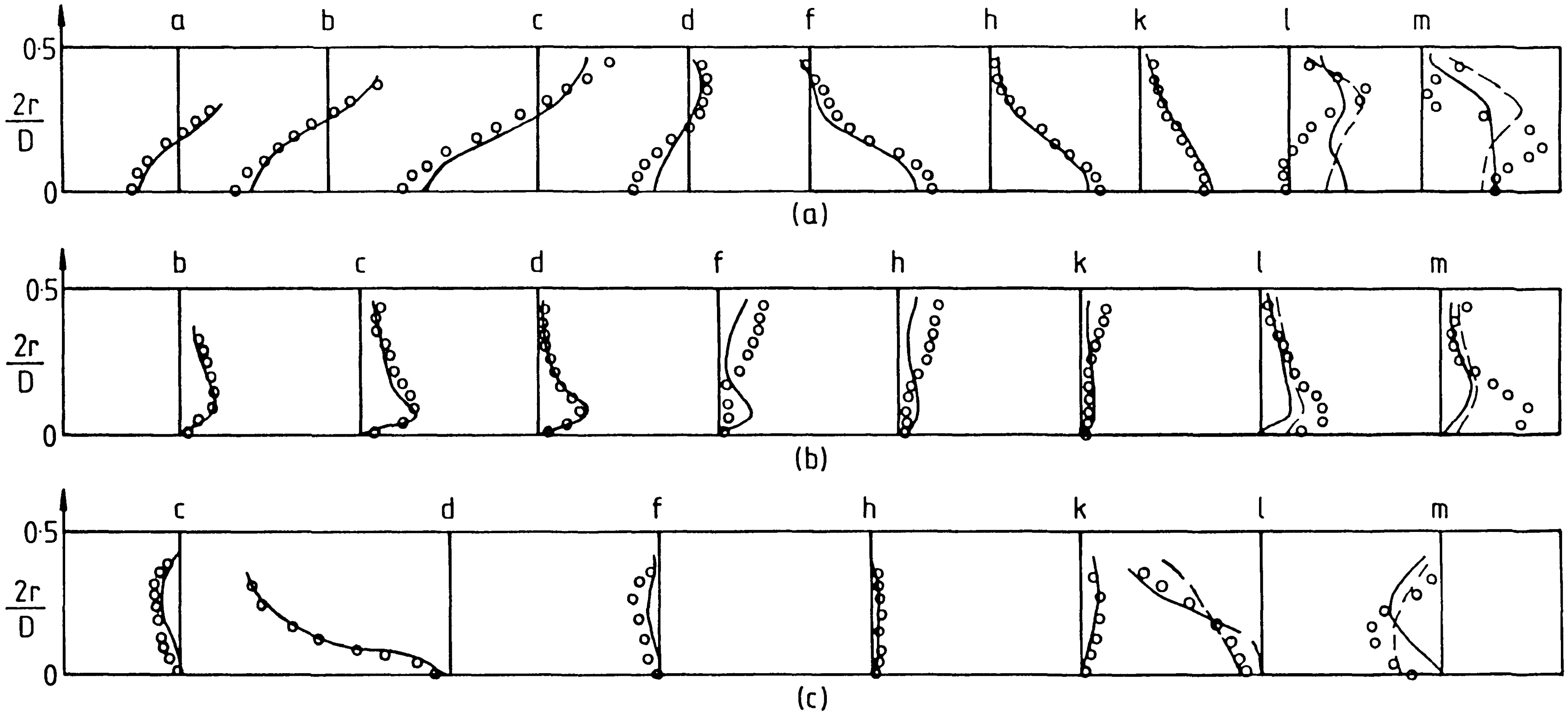

Figure 5.8 Comparison of calculated and measured velocity fields for case 2 ($\theta=0^{\circ}$) (a) axial, (b) azimuthal, (c) radial

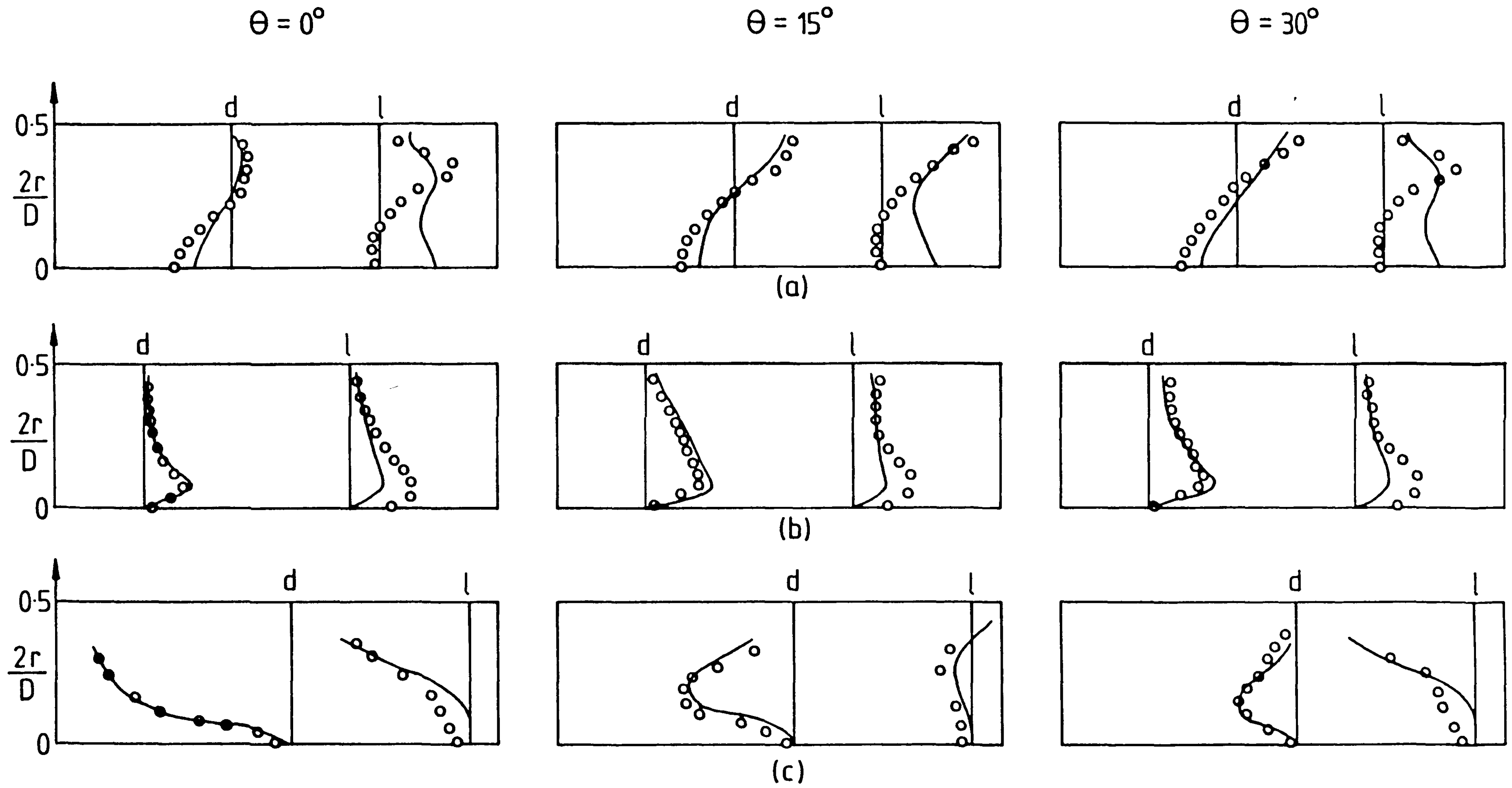

Figure 5.9 Comparison of calculated and measured velocity fields at various θ planes for case 2 (a) axial, (b) azimuthal, (c) radial

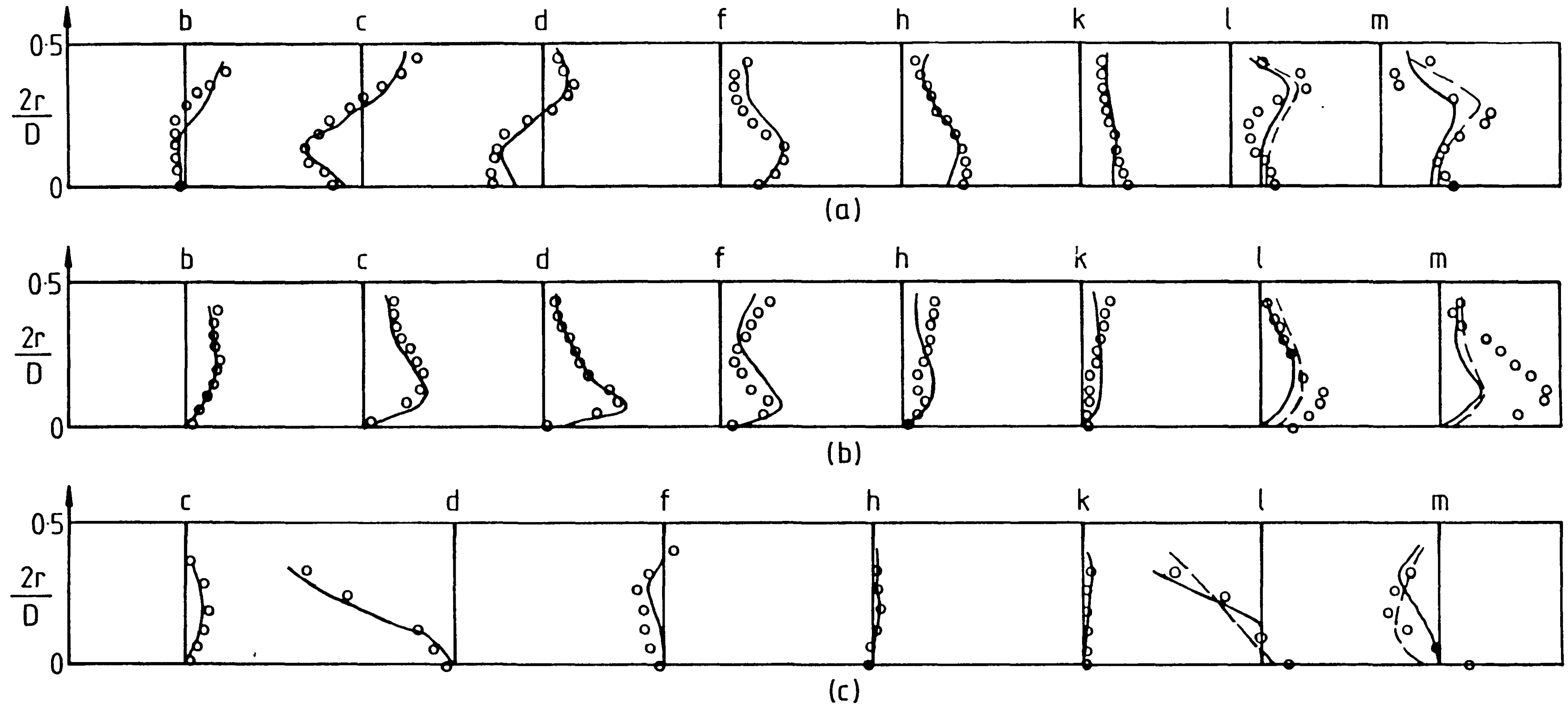

Figure 5.10 Comparison of calculated and measured velocity fields for case 3 (θ=0°) (a) axial. (b) azimuthal. (c) radial

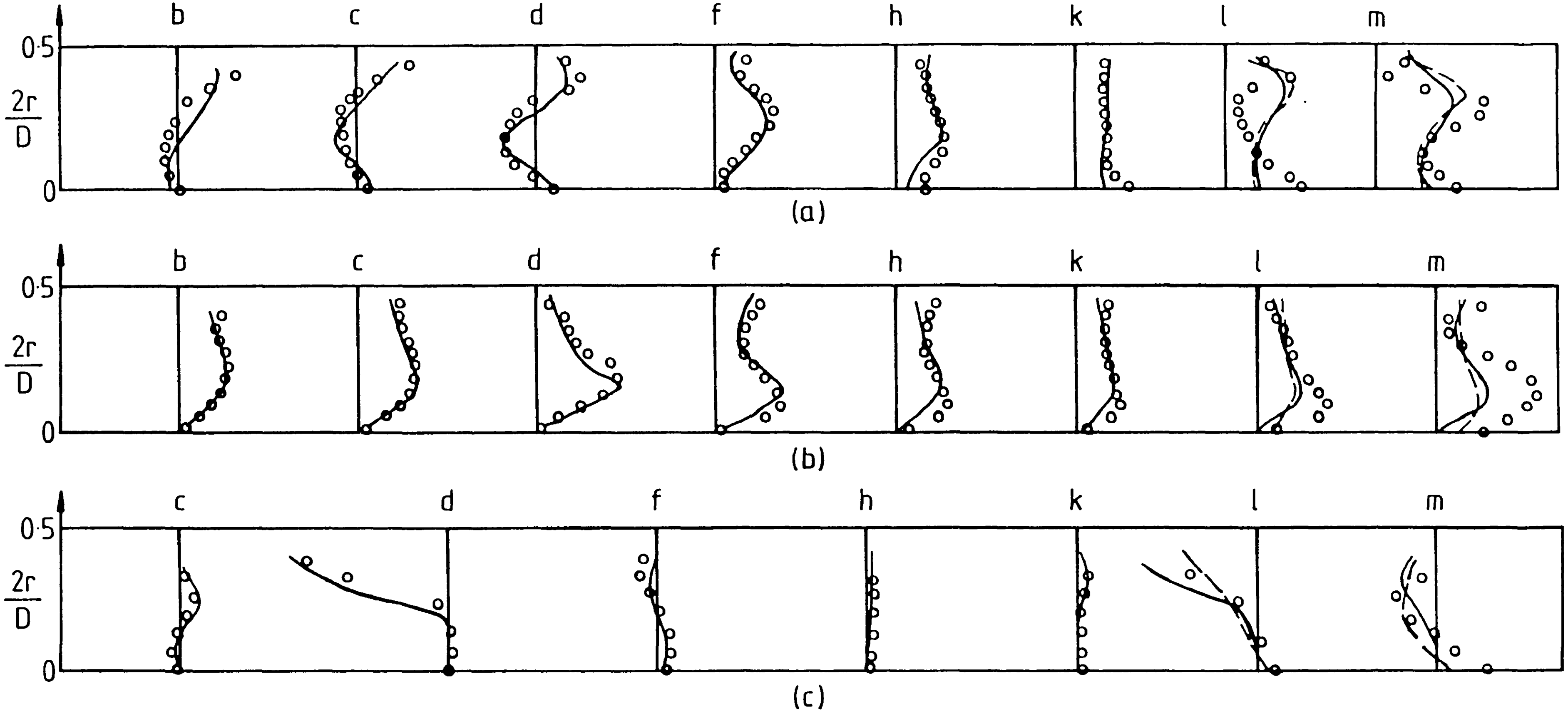

Figure 5.11 Comparison of calculated and measured velocity fields for case 4 ($\theta=0^{o}$) (a) axial, (b) azimuthal, (c) radial

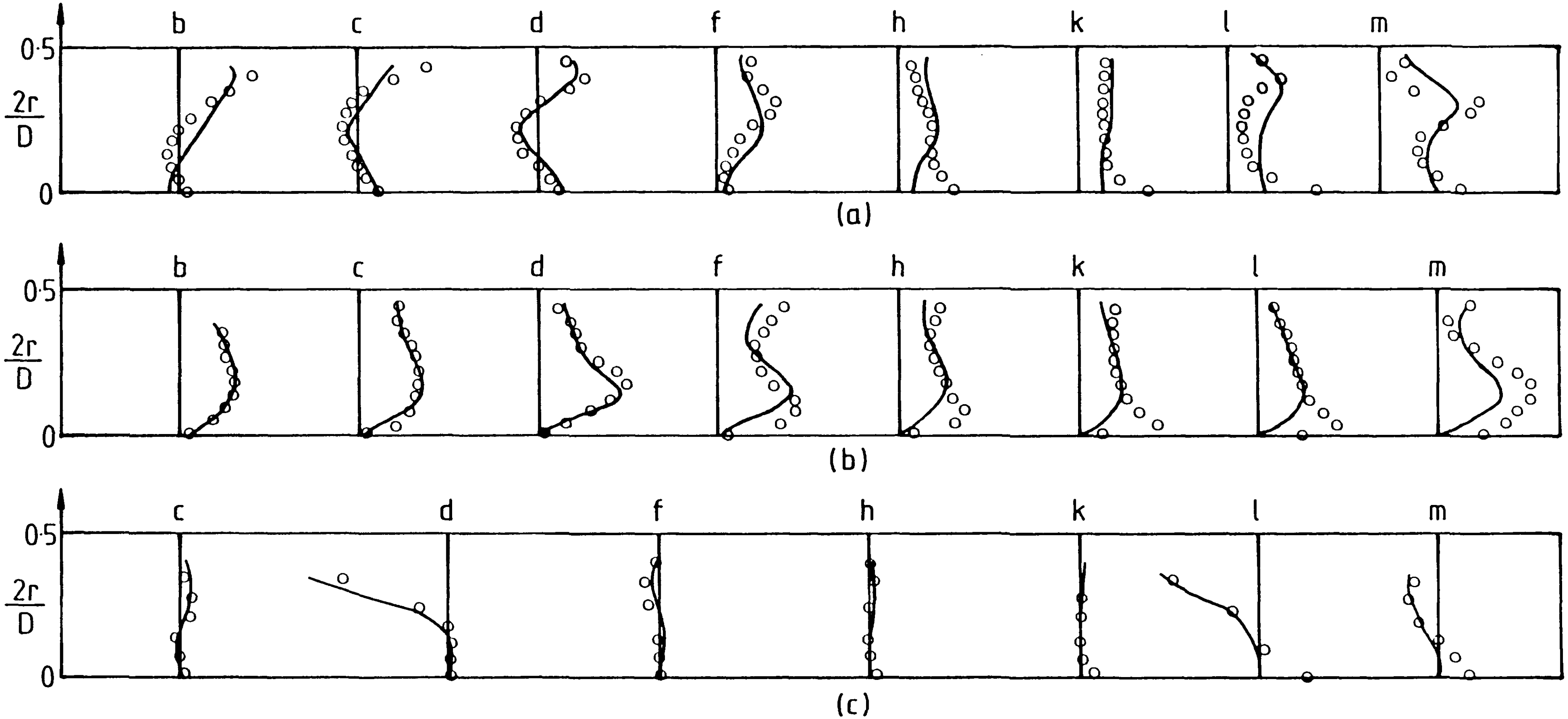

Figure 5. 12 Comparison of calculated and measured velocity fields for case 5 ($\theta=0^{\circ}$) (a) axial, (b) azimuthal, (c) radial

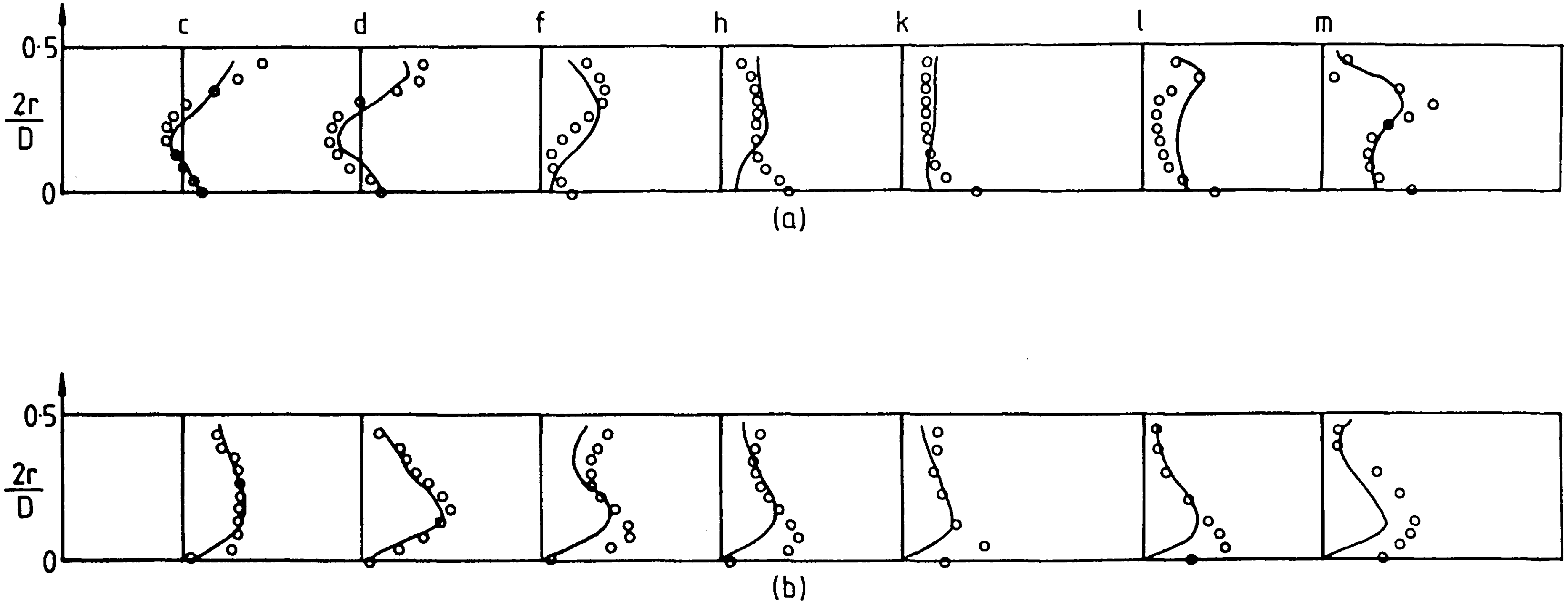

Figure 5.13 Comparison of calculated and measured velocity fields for case 6 (θ=0°) (a) axial, (b) azimuthal

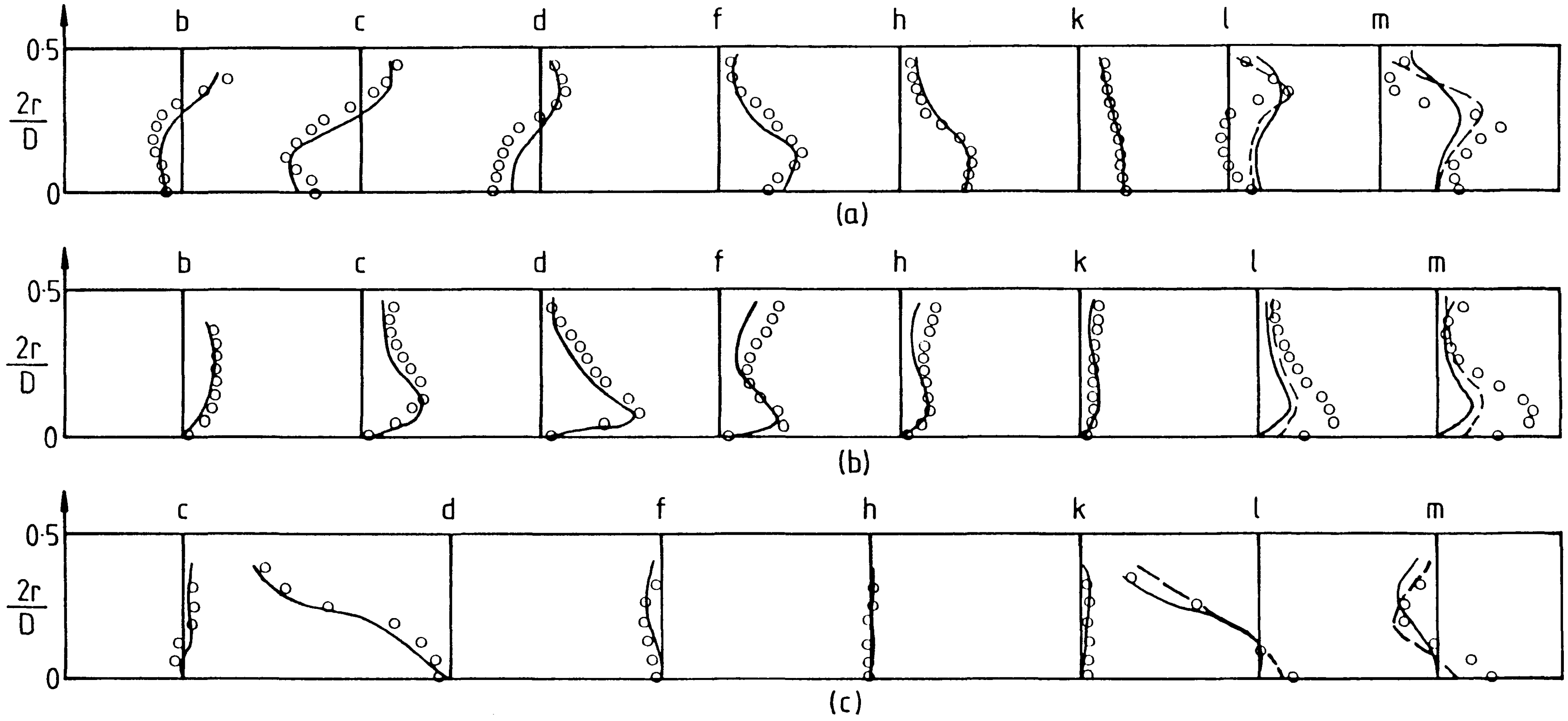

Figure 5. 14 Comparison of calculated and measured velocity fields for case 8 ($\theta=0^{o}$) (a) axial, (b) azimuthal, (c) radial

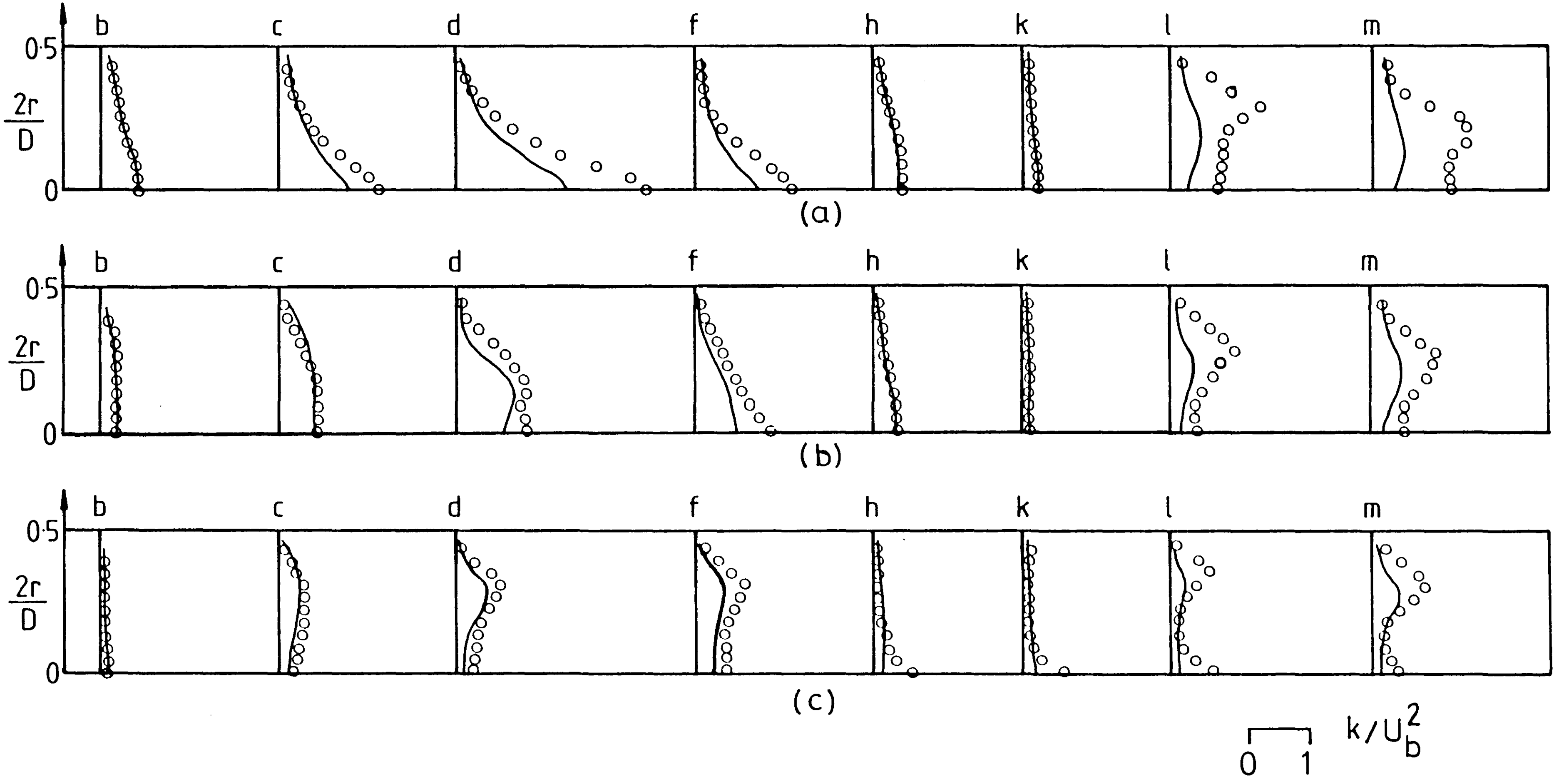

Figure 5. 15 Comparison of calculated and measured turbulence kinetic energy profiles (a) case 2, (b) case 3, (c) case 5

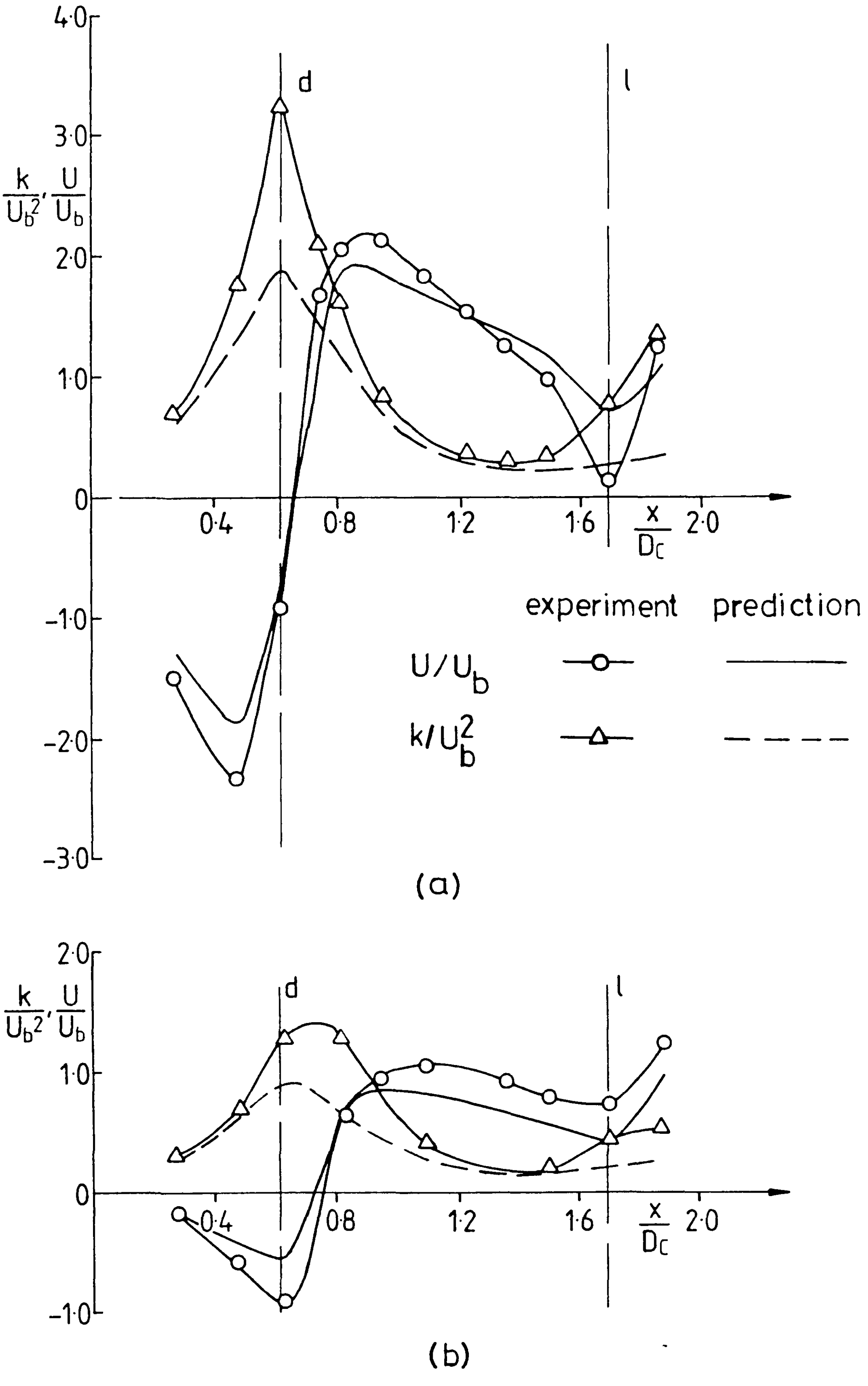

Figure 5. 16 Comparison of calculated and measured centre line axial velocity and turbulence kinetic energy profiles

(a) case 2, (b) case 3, (c) case 4

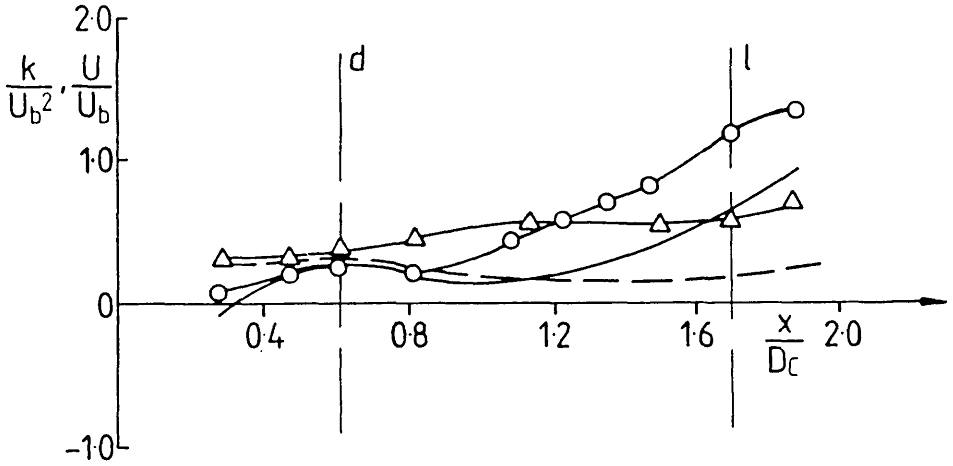

(c)

Figure 5. 16 (continued)

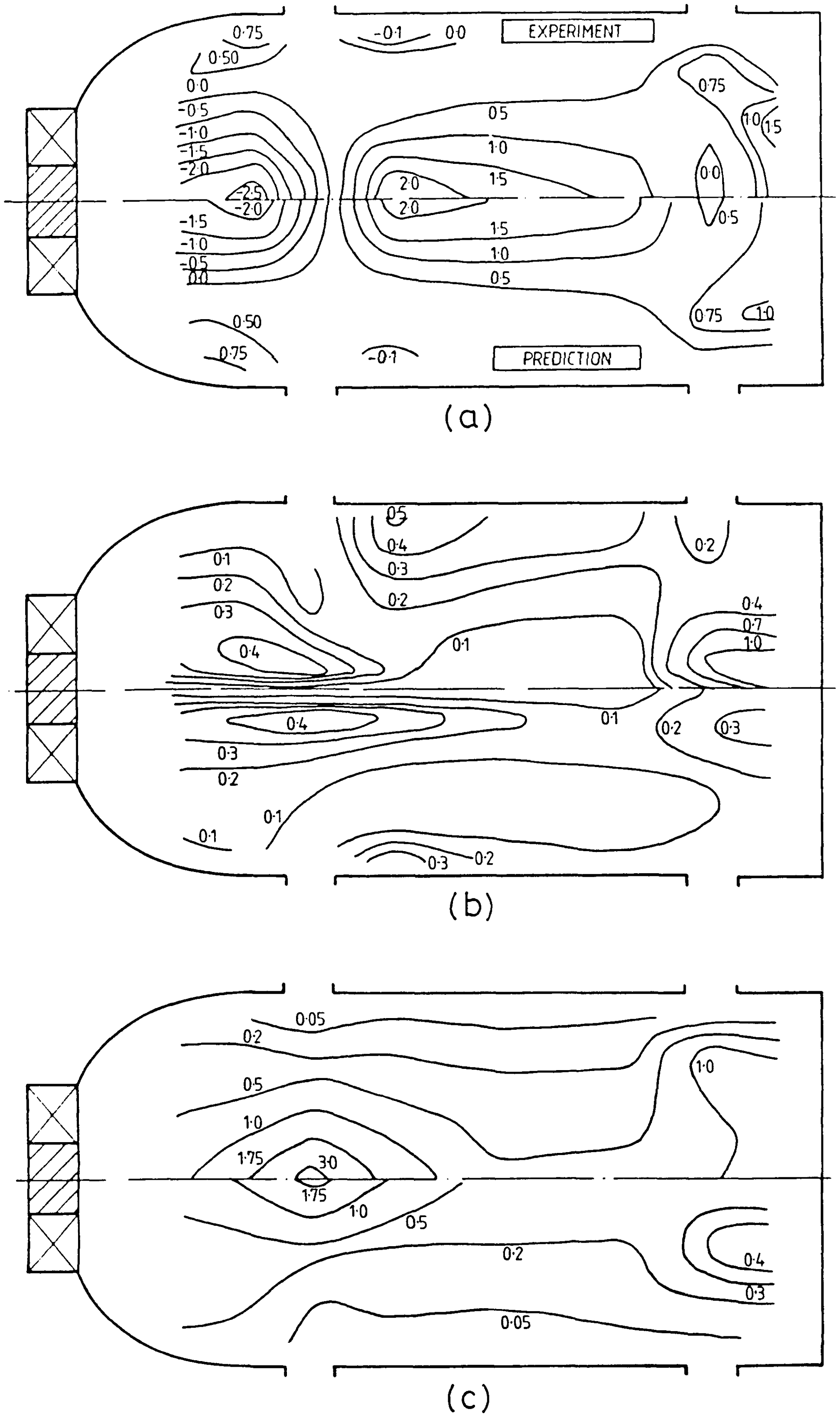

Figure 5.17 Comparison of calculated and measured contours for case 1 ($\theta=0^{o}$) (a) axial velocity, (b) azimuthal velocity, (c) turbulence kinetic energy

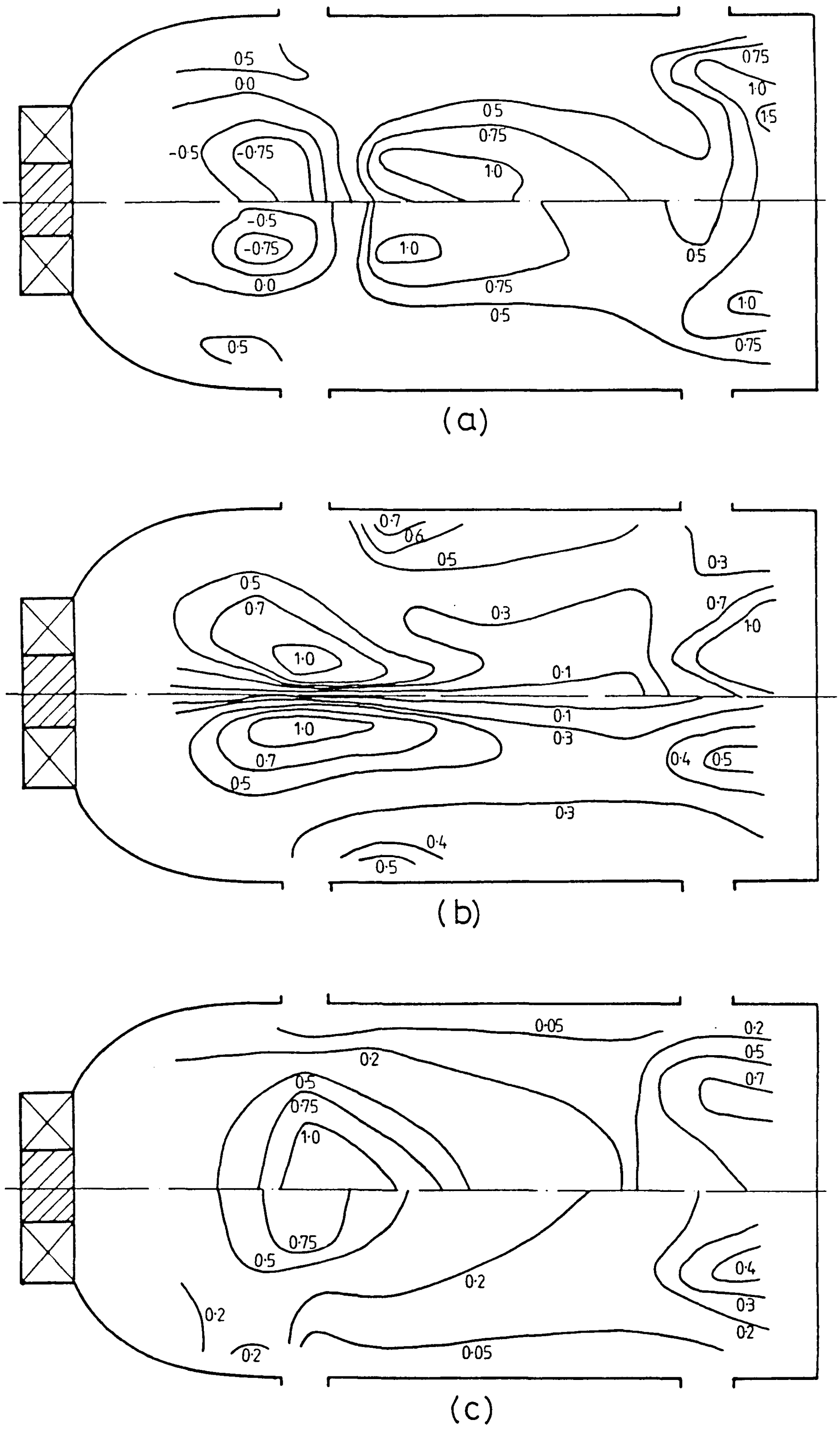

Figure 5. 18 Comparison of calculated and measured contours for case 3 (θ=0°) (a) axial velocity, (b) azimuthal velocity, (c) turbulence kinetic energy

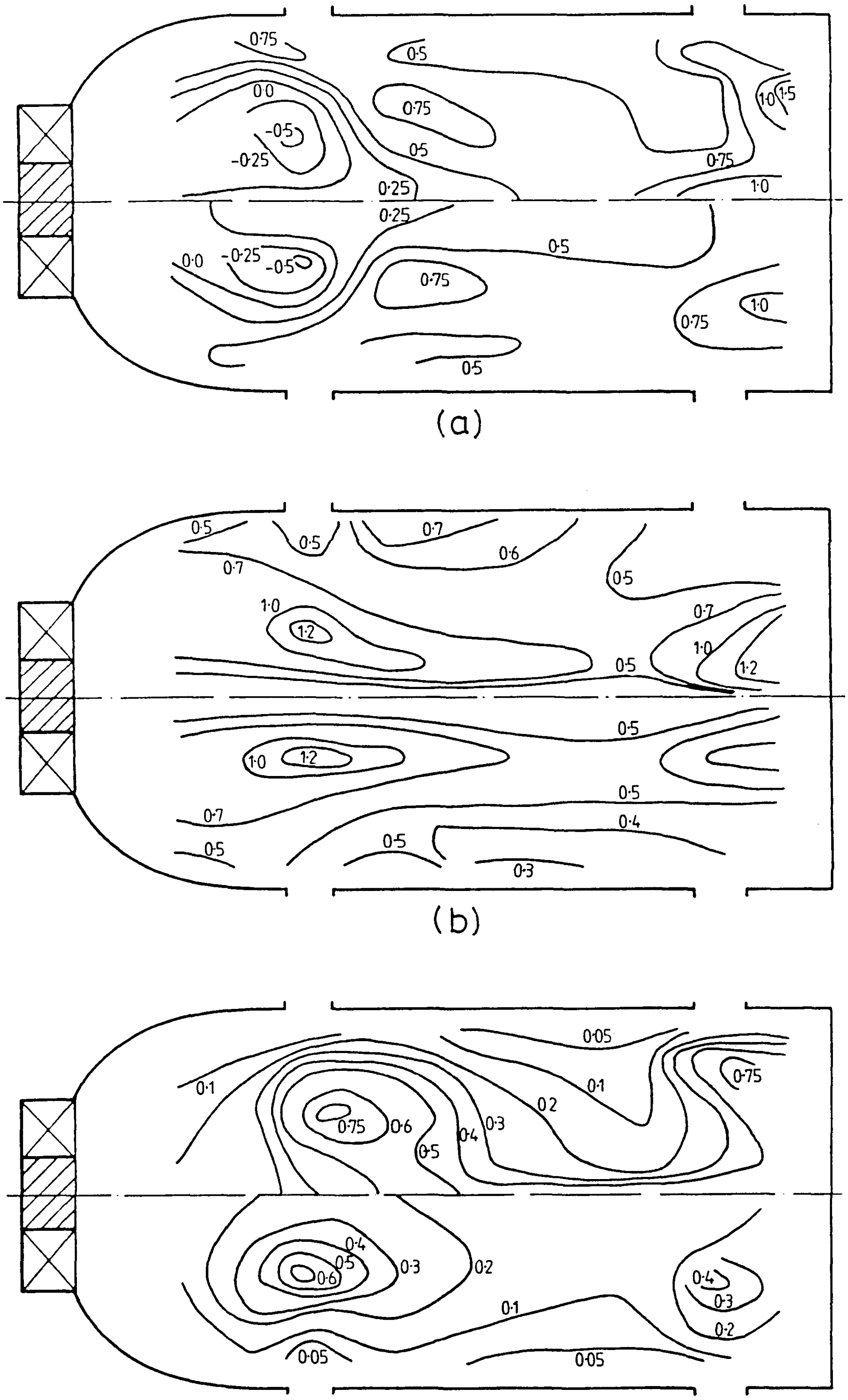

Figure 5. 19 Comparison of calculated and measured contours for case 4 (θ=0°) (a) axial velocity, (b) azimuthal velocity, (c) turbulence kinetic energy

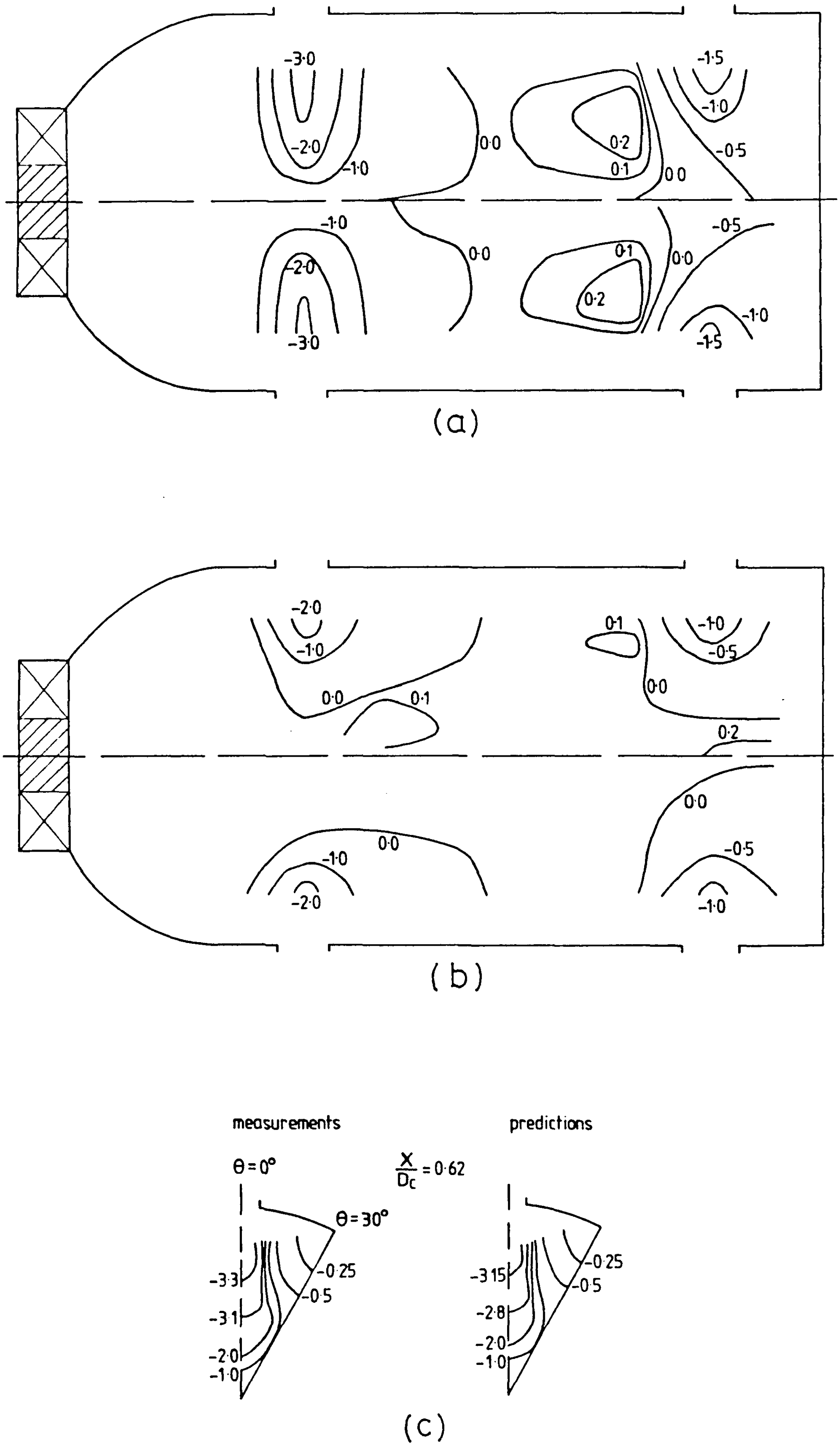

Figure 5.20 Comparison of calculated and measured radial velocity contours

(a) case 2 (θ=0°), (b) case 4 (θ=0°), (c) case 2

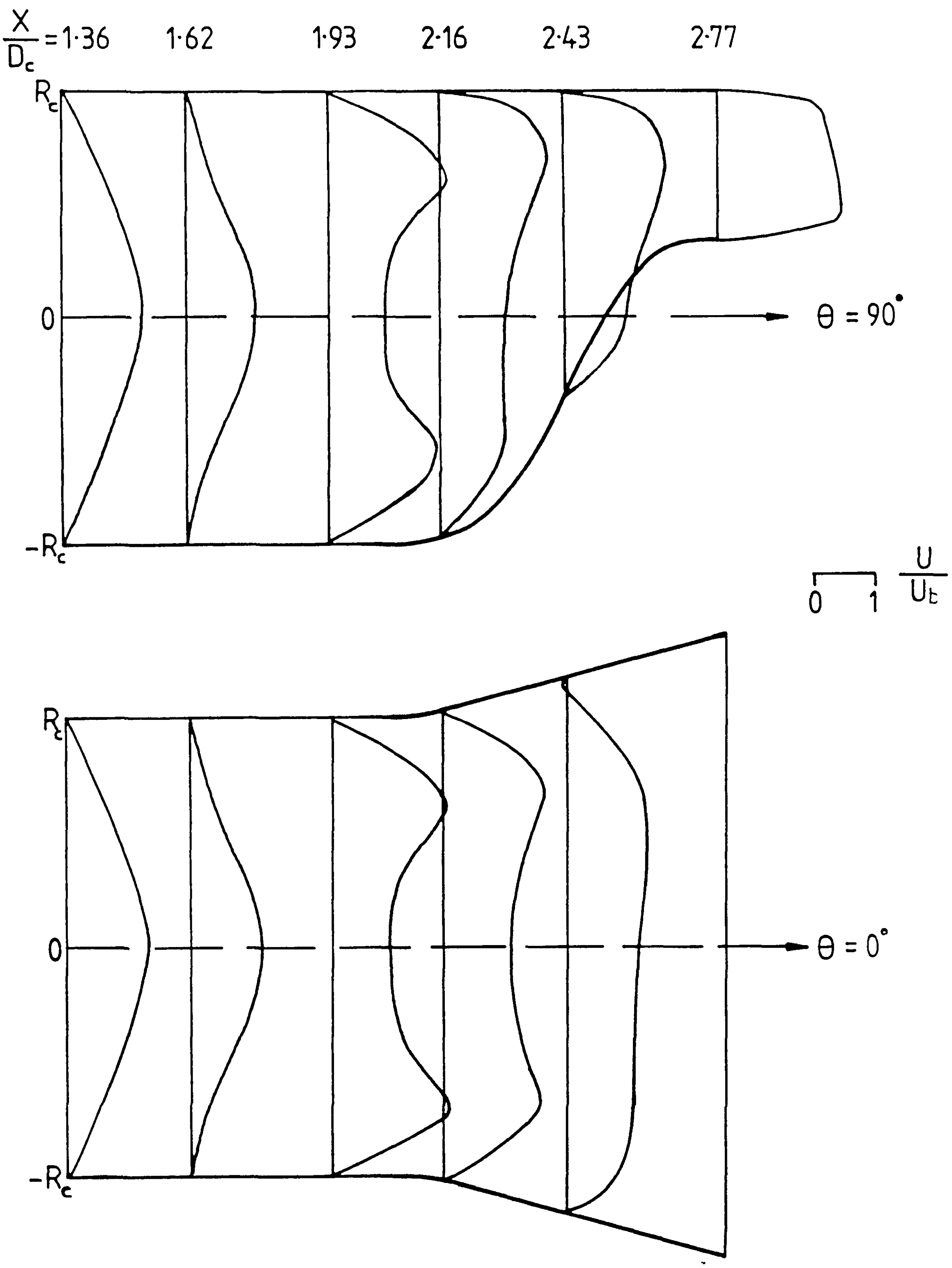

Figure 5.21 Calculated axial velocity field inside the nozzle (case 2)

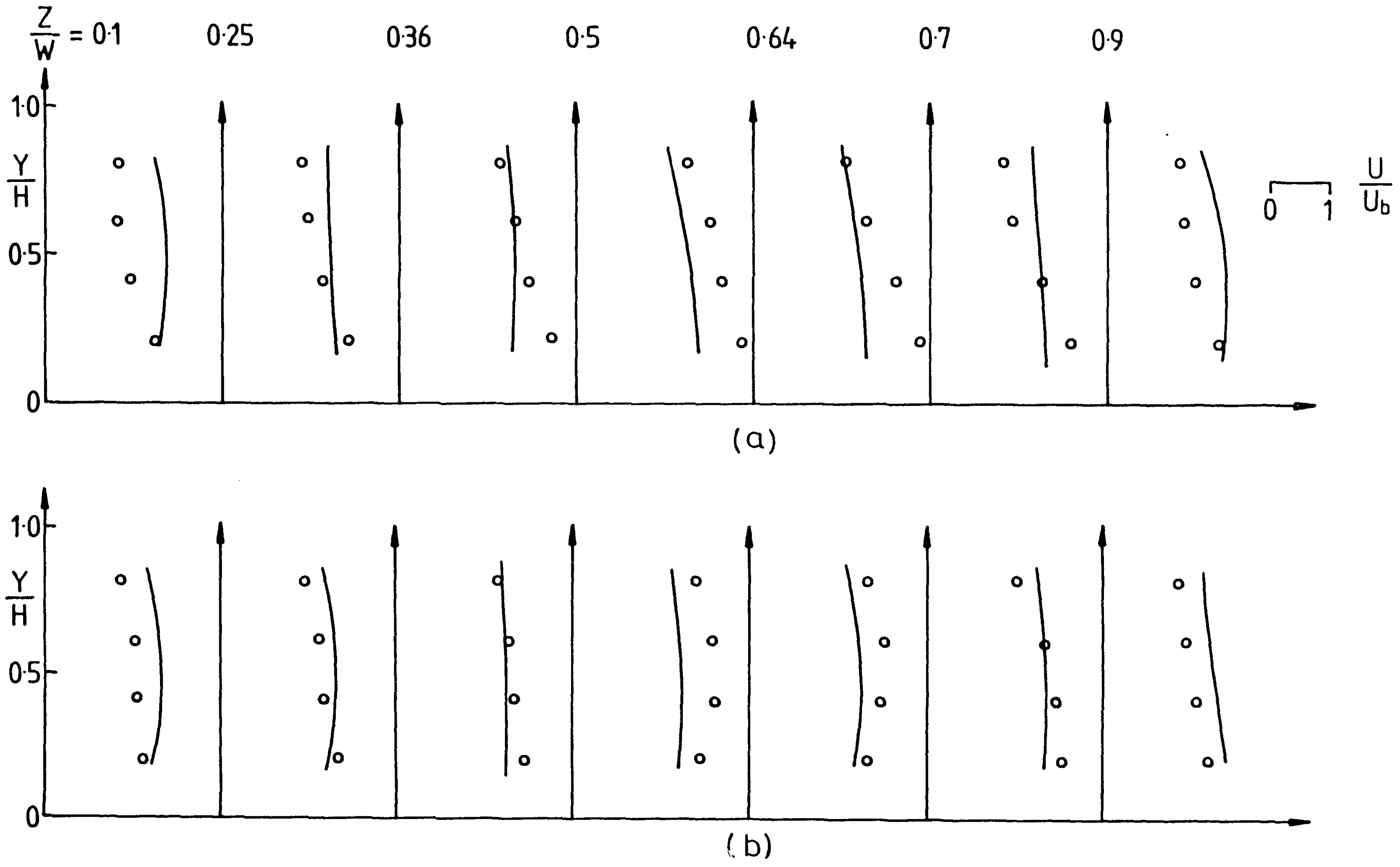

Figure 5.22 Comparison of calculated and measured axial velocity fields at the combustor exit (a) case 2, (b) case 4

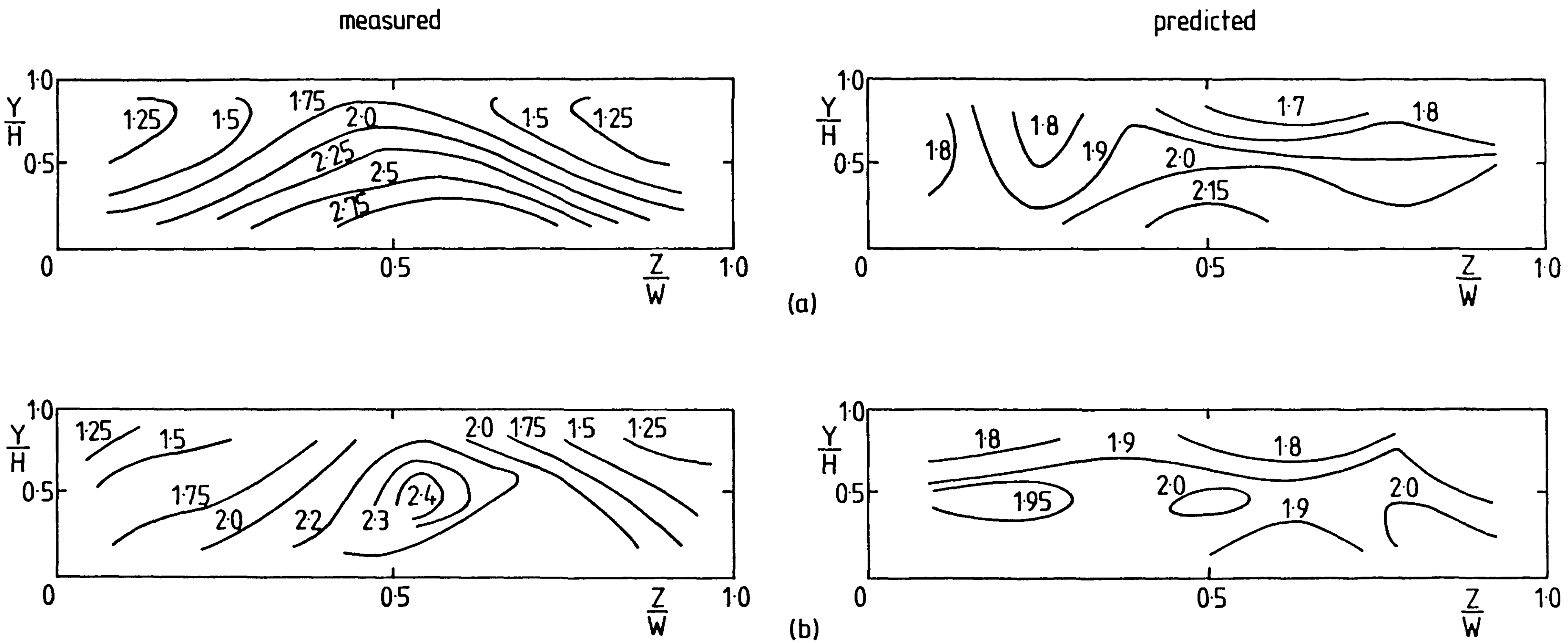

Figure 5.23 Comparison of calculated and measured axial velocity contours at the combustor exit (a) case 2. (b) case 4

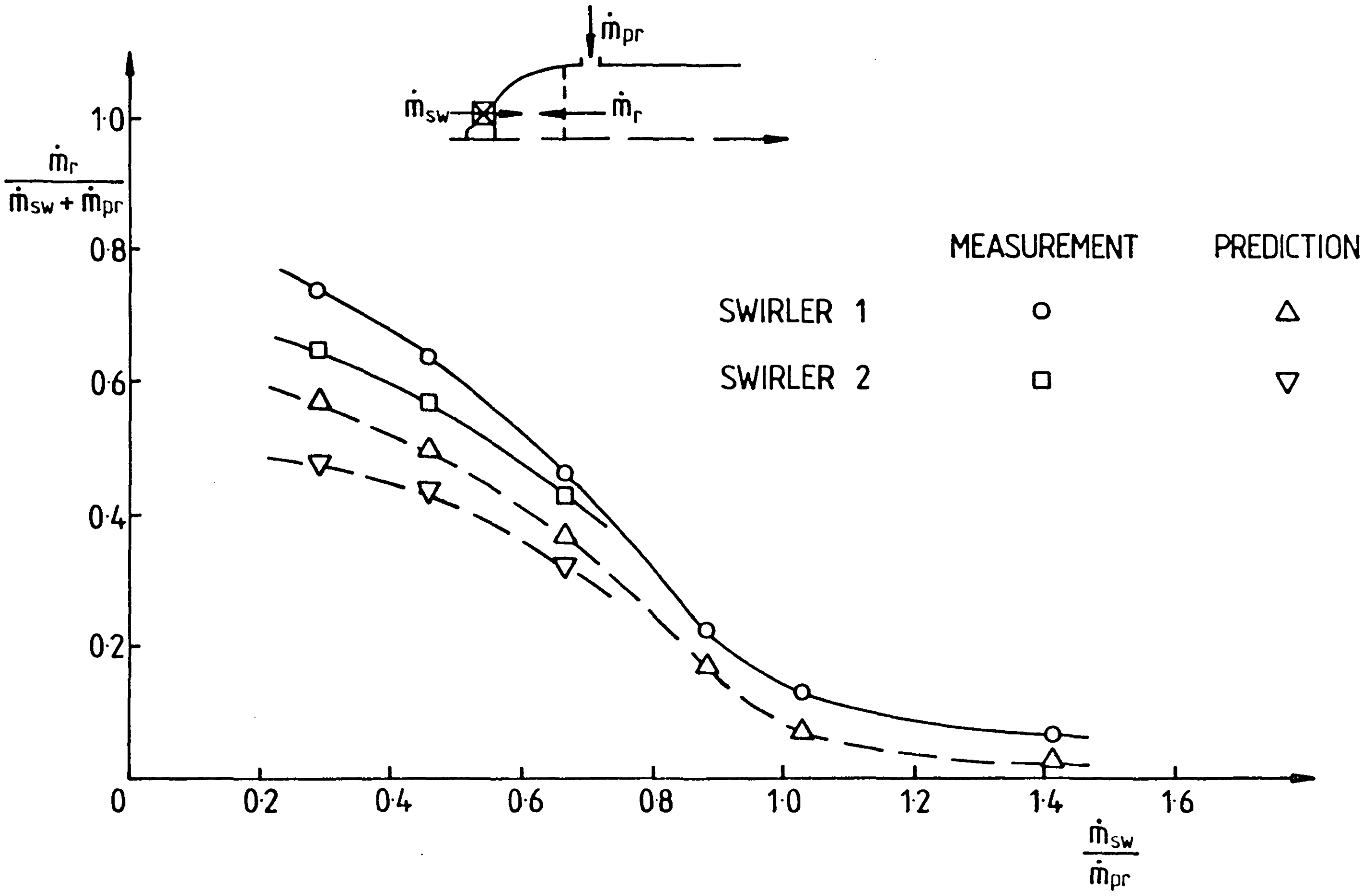

Figure 5. 24 Comparison of calculated and measured variation of the primary zone recirculation ratio

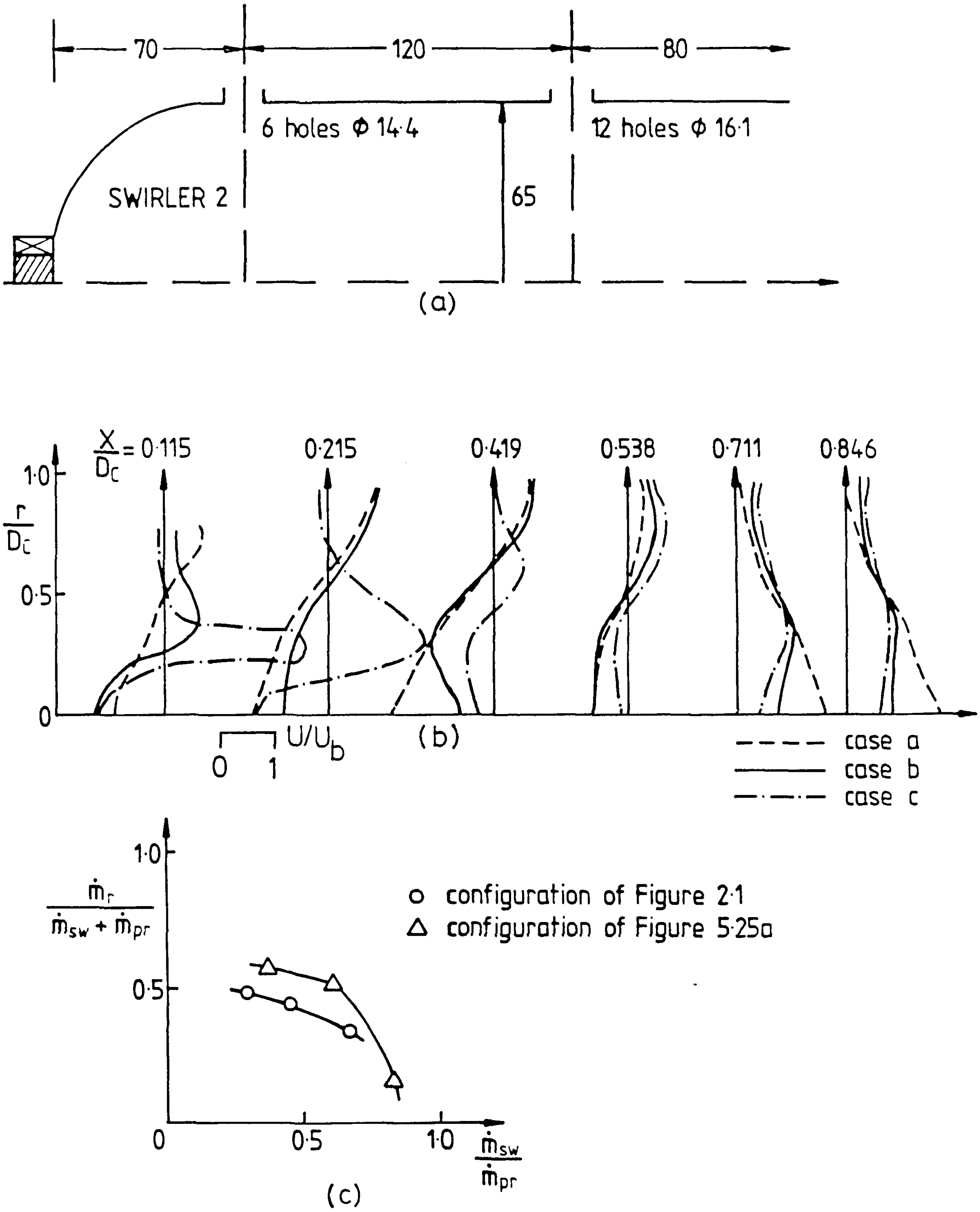

Figure 5.25 (a) combustor geometry

(b) mean velocity field inside the primary zone

(c) primary zone recirculation ratio